

Materials Science and Microfabrication: Key Tools to Develop Microsystems for Chemical and Cellular Monitoring

PhD Thesis

2021

Maite Garcia Hernando

Supervisors:

Assoc. Prof. Fernando Benito López

Ikerbasque Res. Prof. Lourdes Basabe Desmonts



Universidad
del País Vasco Euskal Herriko
Unibertsitatea

MATERIALS SCIENCE AND MICROFABRICATION: KEY TOOLS TO DEVELOP MICROSYSTEMS FOR CHEMICAL AND CELLULAR MONITORING

Maite García Hernando^{1,2}

Thesis submitted for the Degree of Doctor of Philosophy

Supervisors: **Assoc. Prof. Fernando Benito López¹**

Ikerbasque Res. Prof. Lourdes Basabe Desmonts^{2,3}

¹*Microfluidics Cluster UPV/EHU, Analytical Microsystems & Materials for Lab-on-a-Chip (AMMa-LOAC) Group, Analytical Chemistry Department, University of the Basque Country UPV/EHU, Spain.*

²*Microfluidics Cluster UPV/EHU, BIOMICs microfluidics Group, Lascaray Research Center, University of the Basque Country UPV/EHU, Vitoria-Gasteiz, Spain*

³*Basque Foundation of Science, IKERBASQUE, María Díaz Haroko Kalea, 3, 48013 Bilbao, Spain*

"If you believe it will work out, you will see opportunities. If you do not believe it will work out, you will see obstacles" – Wayne Dyer

Declaration

I hereby certify that this material, which I now submit for assessment on the programme of study leading to the award of Doctor of Philosophy is entirely my own work, and that I have exercised reasonable care to ensure that the work is original, and does not, to the best of my knowledge, breach any law of copyright, and has not been taken from the work of others save and to the extent that such work has been cited and acknowledged within the text of my work.

Signed:



Maite García Hernando

ID No.: ____ 44346973-Y _____

Date: ____ 8th April, 2021 _____

Summary

During the last decades, considerable advances have been made towards the development of integrated miniaturised lab-on-a-chip devices able to provide with new chemical or biological information difficult to obtain with conventional techniques. Therefore, easily implementable microfabrication protocols for the generation of these devices would boost their use as enabling technologies for monitoring. In this thesis, materials science and microfabrication have been combined to generate novel microsystems for chemical and cellular monitoring, providing novel sensing strategies based on the integration of functional materials in miniaturised systems.

Resumen

En las últimas décadas, se han realizado avances considerables en el desarrollo de dispositivos miniaturizados “lab-on-a-chip” integrados. Los sistemas miniaturizados pueden aportar información difícil de conseguir con otros medios, por lo que la utilización de protocolos de microfabricación de fácil implementación impulsaría el uso de estas plataformas como tecnologías para monitorización. En esta tesis, se han combinado la microfabricación y la ciencia de los materiales para desarrollar microsistemas para monitorización química y celular, dando lugar a estrategias novedosas como sensores, basadas en la integración de materiales funcionales en sistemas miniaturizados.

Laburpena

Azken hamarkadetan, aurrerapauso garrantzitsuak egin dira lab-on-a-chip gailu miniaturizatu eta integratuak garatzeko bidean. Gailu miniaturizatuek, gainera, teknika konbentzionalak erabiliz lortzeko zaila den informazio espezifikoa lortzea ahalbidetzen dute, beraz, mikrosistema berritzairen integratuak sortzeko bidean, implementatzeko errazak diren mikrofabrikazio protokoloen erabilerak monitorizazio plataforma miniarutizatuen erabilera bultzatuko lukete. Tesi honetan, materialen zientzia eta mikrofabrikazioa konbinatu dira monitorizazio kimiko eta zelularrako mikrosistemak garatzeko, sistema miniaturizatuetan material funtzionalen integrazioa oinarri izanik, sentsoretzat diharduten estrategia berriak sortuz.

Chapter 1: Aim and Outline of The Thesis	15
1.1 General Introduction	3
1.2 Aim and Chapter Overview	5
1.3 Chapter overview	8
1.4 References	11
Chapter 2: Current Challenges in the Development of Miniaturised Biosensors	15
2.1 Introduction	17
2.2 Miniaturisation and integration of the recognition element	19
2.2.1 Microfabrication techniques	20
2.2.1.1 Photolithography	20
2.2.1.2 Soft-lithography	23
2.2.1.3 Hot Embossing	24
2.2.1.4 Screen printing	25
2.2.1.5 Inkjet printing	27
2.2.1.6 3D printing	29
2.2.2 Material integration for biosensing applications	31
2.2.2.1 Metals	31
2.2.2.2 Polymers	33
2.2.2.3 Biomaterials	36
2.3 Integration of the signal transduction	38
2.3.1 Optical biosensors	38
2.3.2 Electrochemical biosensors	42
2.3.3 Piezoelectric biosensors	44
2.3.4 Magnetic biosensors	47
2.3.5 Thermometric sensors	48

2.4 Conclusions	49
2.5 References	52
Chapter 3: Precise Integration of Polymeric Functional Materials in 3D Printed Microfluidic Devices	69
3.1 Introduction	71
3.2 Results and Discussion	74
3.2.1 Device architecture	74
3.2.2 Microfluidic device fabrication	75
3.2.3 Integration of pH sensitive ionogels in a 3D printed microfluidic device	77
3.2.4 pH sensing with integrated hybrid microfluidic device	81
3.2.5 Verification of the pH sensing in the 3D microfluidic device	84
3.2.6 Sensing device reusability	87
3.3 Conclusions	90
3.4 Experimental	91
3.4.1 Materials	91
3.4.2 Device architecture and fabrication by 3D printing	92
3.4.3 Synthesis of the pH sensing polymers	93
3.4.4 Set-up and imaging	94
3.4.5 pH sensor ionogel characterisation	95
3.4.6 Acid/base reaction performance	96
3.5 References	98
Chapter 4: Micro Aperture Array for the Fabrication of High Density Microsensor Arrays	101
4.1 Introduction	103
4.2 Results and discussion	106

4.2.1 Micropillar array fabrication	106
4.2.2 Colorimetric pH sensing assay	115
4.3 Conclusions	121
4.4 Experimental	123
4.4.1 Materials	123
4.4.2 Synthesis of the prepolymer solutions	123
4.4.3 Fabrication of the micropillars	124
4.4.4 Fabrication of the microfluidic device	126
4.4.5 Colorimetric assay and imaging	127
4.5 References	129
Chapter 5: Polymeric Micropillar Arrays and Microfluidics for the Production and Monitoring of Lipid Membrane Nanotubes	133
5.1 Introduction	135
5.2 Results and discussion	139
5.2.1 Fabrication of the micropillar arrays	139
5.2.2 Generation of lipid NTs between micropillars	147
5.3 Conclusions	153
5.4 Experimental	155
5.4.1 Materials	155
5.4.2 Fabrication of the microfluidic devices	156
5.4.3 Lipid NT formation	158
5.4.4 Imaging and characterisation of the lipid NTs	160
5.5 References	161
Chapter 6: Optical Single Cell Resolution Cytotoxicity Biosensor Based on Single Cell Adhesion Dot Arrays	165
6.1 Introduction	167

6.2 Results and discussion	170
6.2.1 Monitoring cell adhesion and detachment to protein substrates with single cell resolution	170
6.2.2 Monitoring cytotoxicity of K ₂ CrO ₄ and DMSO measured by label-free SCADA viability test	174
6.2.3 Cytotoxicity colorimetric SCADA viability test	176
6.2.4 SCADA on Chip	178
6.2.5 General discussion	182
6.3 Conclusions	184
6.4 Experimental	185
6.4.1 Materials	185
6.4.2 Photolithography and soft lithography	186
6.4.3 Microcontact Printing	188
6.4.4 Quantification of cell adhesion and detachment	190
6.4.5 Flow cytometry	191
6.4.6 Microscopy images	191
6.4.7 SCADA on chip	191
6.5 References	193

Chapter 7: Smart Functional Electrodes for the Simultaneous Monitoring of Cell Capture and Release Processes	195
7.1 Introduction	197
7.2 Results and discussion	201
7.2.1 Characterisation of the electrodes by EIS	201
7.2.2 Characterisation of the thermo-responsiveness and conducting properties of the copolymer	204
7.2.3 Cell capture and release with PEDOT:PSS/pNIPAAm copolymer	209
7.2.4 Characterisation of protein capture and release by fluorescence microscopy	216

7.3 Conclusions	217
7.4 Experimental	218
7.4.1 Materials	218
7.4.2 Electrode fabrication	219
7.4.3 PEDOT:PSS and PEDOT:PSS/pNIPAAm layer formation	221
7.4.4 Electric Impedance Spectroscopy measurements	222
7.4.5 Swelling/shrinking capability of PEDOT:PSS and PEDOT:PSS/pNIPAAm	223
7.4.6 Characterisation of the PEDOT:PSS/pNIPAAm copolymer by Raman spectroscopy	223
7.4.7 Cell capture and release mechanisms	224
7.4.8 Protein capture and release by fluorescence microscopy	225
7.5 References	227
 Chapter 8: Final Remarks and Future Work	233
8.1 Final Remarks and Future Work	235
8.2 References	240
 Materialen Zientzia Eta Mikrofabrikazioa: Gako Tresnak Monitorizazio Kimiko Eta Zelularra Burutzeko Mikrosistemak Garatzeko	
I. Kapitulua: Gaur Egungo Erronkak Biosentsore Miniaturizatuen Garapenean	243
I.1 Sarrera	245
I.2 Elementu hartzalearen miniaturizazio eta integrazioa	248
I.2.1 Mikrofabrikazio teknikak	248
I.2.1.1 Fotolitografia	248
I.2.1.2 Litografia biguna	252

I.2.1.3 Estanpazio beroa	253
I.2.1.4 Serigrafia	254
I.2.1.5 Inkjet inprimaketa	256
I.2.1.6 3D inprimaketa	258
I.2.2 Materialen integrazioa biosentsore erabiltzeko	260
I.2.2.1 Metalak	260
I.2.2.2 Polimeroak	263
I.2.2.3 Biomaterialak	266
I.3 Seinalearen transdukzioaren integrazioa	268
I.3.1 Biosentsore optikoak	268
I.3.2 Biosentsore elektrokimikoak	272
I.3.3 Biosentsore piezoelektrikoak	274
I.3.4 Biosentsore magnetikoak	277
I.3.5 Biosentsore termometrikoak	278
I.4 Ondorioak	279
I.5 Erreferentziak	282
II. Kapitulua: Material Funtzional Polimerikoen Integrazioa 3D Inprimaketaz Fabrikatutako Gailu Mikrofluidikoetan	299
II.1 Eskema nagusia	301
II.2 Emaitzak	301
II.2.1 Gailu mikrofluidikoaren fabrikazioa	301
II.2.2 pH detekziorako ionogel sentsoreen integrazioa 3D inprimaketaz egindako gailu mikrofluidikoan	302
II.2.3 pH detekzioa gailu mikrofluidiko hibrido integratua erabiliz	303
II.2.4 3D gailu mikrofluidikoaren pH detekzio ahalmenaren egiaztapena	304
II.2.5 Sentsore mikrofluidikoaren berrerabilera	306

III. Kapitulua: Mikrosentsore Anitzeko Formakuntzak Gauzatzeko "Mikro Irekitedun Formakuntza" Substratua	309
III. 1 Eskema nagusia	311
III.2 Emaitzak	311
III.2.1 Mikrozutabe formakuntzaren fabrikazioa	311
III.2.2 pH detekzio kolorimetrikoa	316
III.3 Ondorioak	318
IV. Kapitulua: Mikrozutabe Polimerikoak eta Mikrofluidika Nanotubo Lipidikoen Sorkuntza eta Monitorizaziorako	321
IV.1 Eskema nagusia	323
IV.2 Emaitzak	323
IV.2.1 Mikrozutabe formakuntzen fabrikazioa	323
IV.2.2 Mikrozutabeen arteko lipidozko nanotuboen (NT) sorkuntza	327
IV.3 Ondorioak	329
V. Kapitulua: Toxizitate Zelularra Zelula Indibidual Erresoluzioarekin Antzemateko Biosentsore Optikoa	331
V.1 Eskema nagusia	333
V.2 Emaitzak	334
V.2.1 Fibronektina patroien produkzioa	334
V.2.2 Zelulen proteina substratuekiko atxikipen eta askapenaren monitorizazia zelula indibidual erresoluzioarekin	336
V.2.3 K ₂ CrO ₄ eta DMSO konposatuen toxizitate zelular testa etiketa gabeko SCADA erabiliz.	338
V.2.4 SCADA zelulen bideragarritasun test kolorimetrikoa	339

V.2.5 SCADA on Chip	340
V.3 Ondorioak	341
VI. Kapitulua: Elektrodo Inteligente eta Funtzionalak Zelulen Harrapaketa eta Askapenerako eta Aldibereko Monitorizaziorako	343
VI.1 Eskema nagusia	345
VI.2 Emaitzak	346
VI.2.1 Elektrodoen fabrikazioa	346
VI.2.2 Inpedantzia elektrokimiko espektroskopia (EIS) bidezko karakterizazioa	347
VI.2.3 Kopolimeroaren termo-erantzunaren eta propietate eroalearen karakterizazioa	349
VI.2.4 Zelulen harrapaketa eta askapena PEDOT:PSS/pNIPAAm kopolimeroa erabiliz	352
VI.2.5 Proteinen harrapatze eta askapenaren karakterizazioa fluoreszentzia mikroskopiaz	357
VI.3 Ondorioak	357
VII. Kapitulua: Harrak eta Etorkizuneko Lana	359
VII.1 Oharrak eta Etorkizuneko Lana	361
VII.2 Erreferentziak	367
Acknowledgements	369

1

Aim and Outline of the Thesis

1.1 General Introduction

During the last three decades, many efforts have been made on the development of miniaturised sensing microsystems, also known as micro total analysis systems (μ -TAS) or lab-on-a-chip (LOC). These microsystems integrate conventional laboratory operations and analysis at the microscale. Their reduced dimensions enable portability, point of care (POC) testing, the use of smaller volumes of samples and reagents, simpler operation, faster analysis times, higher sensitivity, and potential parallelisation and automation, which lead to an overall cost reduction of the analysis¹⁻⁴.

Monitoring is a systematic process that implies collecting information of target events and analysing it in order to track an ongoing target activity. Chemical and cellular monitoring is crucial to obtain information of the targeted events, such as identifying when objectives are reached, detect problems in order to take actions to solve them, and/or gain knowledge about a targeted activity or molecule. Chemical monitoring is crucial for fields such as environmental safety⁵, physical exercise⁶, health care^{7,8} and global public health⁹. Particularly, miniaturised systems enable the precise control of cellular microenvironments, so cellular monitoring at the micron scale permits to collect information that cannot be obtained with conventional techniques, due to the difficulties to mimic cell microenvironment *in vitro*¹⁰.

Although the current trend to miniaturise monitoring systems, together with the technological advances, have boosted the innovation towards the development of LOC platforms, their fabrication is still far from mass production and cost-effectiveness. Microfabrication enables the precise manufacturing of integrated miniaturised devices with micro- or nano-scale resolution, using techniques that

are well established, such as micromachining, photolithography or dry etching^{11,12}. However, an integrated LOC device often incorporates many different functional elements or modules, like the ones for sensing, transporting and mixing of fluids or signal transduction¹³. This commonly implies the use of multiple materials and microfabrication techniques to manufacture a single miniaturised device, which complicates and increases the cost of the manufacturing. The microsystems could be so complex for their use and manufacturing that, despite their enhanced capabilities in contrast with bench top analytical techniques, are difficult to commercialise and to extend their use to the general consumers^{14,15}. Therefore, easily implementable microfabrication protocols for the integration of components in LOC devices would contribute to position microsystems as enabling technologies for monitoring¹⁶. In order to achieve that, innovative monitoring devices, which provide specific information that may be difficult to obtain by other types of technology, can be obtained through the development of novel sensing strategies based on the integration of functional materials in miniaturised systems.

The sensing of the target molecule or event in such monitoring systems is carried out at the detection side of the device, and this information is then transformed into a physicochemical signal by a transducer, which converts it into a readable output, which can be optical¹⁷⁻²², electrochemical²³⁻²⁵ or piezoelectric²⁶ among others^{27,28}. In particular, optical sensors stand out because they are easy to implement in LOC devices. They offer a signal readout, using simple and available instrumentation²⁹, and have huge potential for the development of portable instrumentation³⁰⁻³².

1.2 Aim and Chapter Overview

The aim of this thesis is to demonstrate that the integration of functional materials into miniaturised platforms may be used for the development of simplified and compact microsystems for chemical and cellular monitoring. In particular, ionogel microstructures have been integrated into microfluidic platforms for pH sensing and for lipid nanotube formation and monitoring. In addition, 2D patterning of proteins has been used to develop a novel strategy to monitor cellular adhesion and cellular death. Finally, the combination of electroactive and stimuli-responsive polymers on microelectrodes has been used to develop a method for the selective capture of cells and their triggered release with simultaneous monitoring of the cell loading on the polymer electrodes.

All the sensing approaches reported in this thesis are highly versatile. The performance of each microsystem was demonstrated for an individual sensing assay or for a specific cell type, but their versatility could allow them to be used for other type of sensing assays or cells, after some modifications. Moreover, they have a common optical readout, with no need of sophisticated equipment. For instance, simple and easily available microscopes were used to interpret the colorimetric signal of pH sensing ionogels and to visualise the integrated polymeric micropillars for lipid nanotube production. Then, cells were analysed using an optical microscope available in most cell laboratories. Additionally, in the case of the cell capture and release system, the optical monitoring was complemented with a potentiostat for the simultaneous electrical monitoring of cell behaviour.

To reach the stated main goals, the following sub-objectives were established:

- Integration of pH sensitive ionogels into 3D microfluidic platforms.
- Generation of high density arrays of ionogel microstructures.
- Development of a microsystem for the controlled production and monitoring of lipid membrane nanotubes.
- Development of a digital assay to monitor cell adhesion and cytotoxicity.
- Development of a microsystem for the selective cell capture and triggered release with simultaneous monitoring of cell behaviour on a novel hybrid material, through the combination of conductive and stimuli-responsive polymers with microelectrodes.

Figure 1.1 shows the aim and objectives of this thesis: the convergence of materials science and microfabrication for the development of microsystems as enabling technologies for chemical and cellular monitoring.

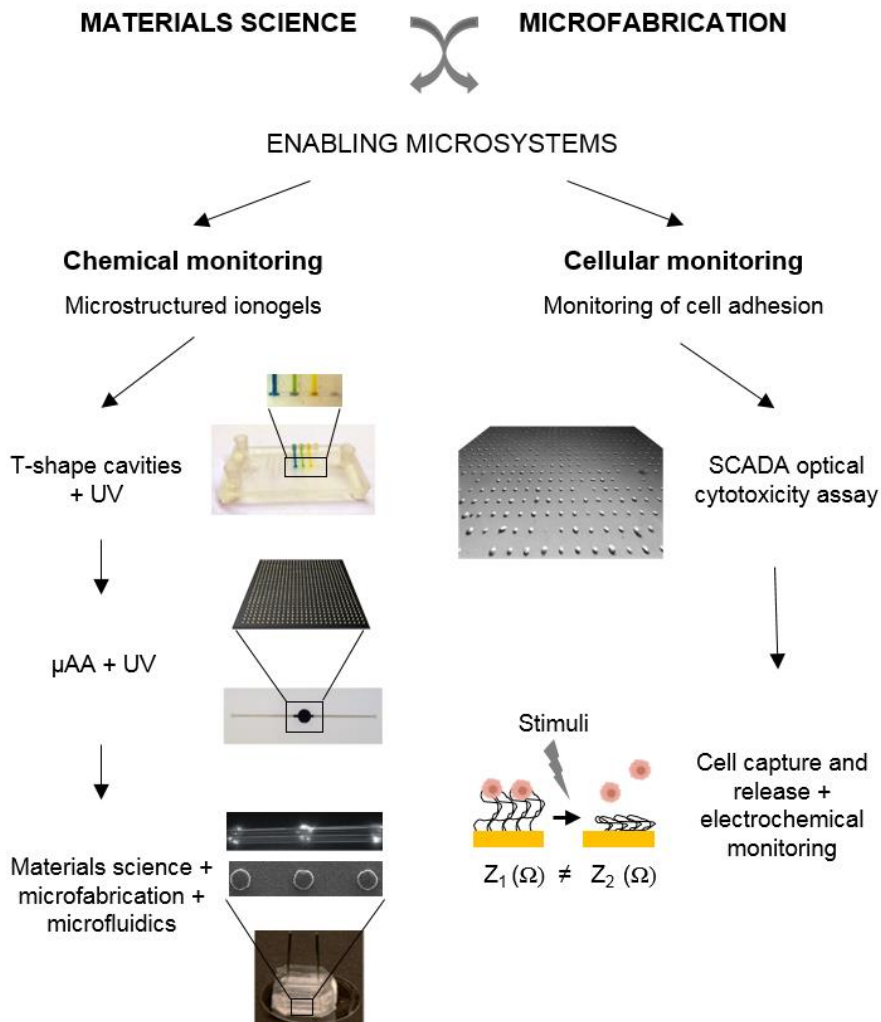


Figure 1.1. Scheme of the work described in this thesis: the development of microsystems for chemical and cellular monitoring through the combination of materials science and microfabrication.

1.3 Chapter overview

A detailed overview of each chapter, together with particular contributions from research collaborators (where applicable), are given below:

Chapter 2 provides a general overview on the miniaturisation and integration of sensors within analytical devices. The chapter defines the most common techniques for the manufacturing of miniaturised sensing devices, some of them used in this thesis. It also reviews the state of the art of the miniaturised biosensors, catalogued by their transduction mechanism. It summarises the state of the art of the microsystems developed for such application, and it highlights the new inputs provided in the field.

Chapter 3 reports a strategy for the integration of functional pH sensitive materials into a 3D printed microfluidic device. A smart architecture or microfluidic design was developed (T-shape cavities) for the easy and precise integration of functional materials with *in situ* UV polymerisation. As a proof of concept, colorimetric pH sensing was presented by barcode colour interpretation.

Chapter 4 describes the miniaturisation of the previous colorimetric pH sensor. A high-density microsensor array was developed by the fabrication of micropillars of pH sensitive ionogels. The microsensor array was directly fabricated on top of a Mylar® photomask applying UV light, which is referred as Micro Aperture Array (μ AA). This fabrication strategy provided two main advantages; first the exposure of UV light, applied through the substrate, created the microsensor array *in situ*, in a single step, on a substrate that may be used as the bottom plate of a microfluidic platform or as an integrable element. Second, the result of the fabrication was an array of microsensors where each sensing

micropillar was surrounded by a black background that enhanced the signal to noise ratio of the optical signal of each sensing micropillar.

Chapter 5 presents the fabrication of microsystems for the high throughput production and monitoring of lipid membrane nanotubes. The microsystems combined arrays of polymer micropillars with a microfluidic platform. It enabled both, *in situ* creation of free-standing lipid nanotubes, and precise observation and monitoring of the dynamic formation and scission of the nanotubes. It was used to explore the tunability of the length and radii of the nanotubes by changing the distance and chemical composition of the micropillars.

This work was done in collaboration with the group of Dr. Anna Shnyrova, from the Biofisika Institute (CSIC, UPV/EHU) and the Department of Biochemistry and Molecular Biology, University of the Basque Country, Spain.

Chapter 6 describes an optical cytotoxicity test with single cell resolution based on Single Cell Adhesion Dot Arrays (SCADA). 2D protein patterning was used to create an array of single cell-adhesion sites on a substrate. In this platform, the number of cells can be easily counted due to the digitalisation of the signal (individual cell counting) by assessing the number of empty or occupied adhesion sites. Cellular death was precisely and dynamically monitored at single cell resolution by measuring either stained cells with a viability staining or cell detachment along the time of the assay.

Chapter 7 shows a platform for the specific capture of cells and on demand release with simultaneous electrical monitoring of the cell behaviour. This platform was comprised of gold microelectrodes coated with a conductive and stimuli-responsive copolymer. Specifically, the functional copolymer was made of poly(3,4-ethylenedioxythiophene) polystyrene sulfonate (PEDOT:PSS) and

poly(*N*-isopropylacrylamide) (pNIPAAm). This copolymer acted simultaneously as an actuator, triggering cell release upon temperature increase, which induces the shrinking of pNIPAAm, and as a bioelectronic sensor due to the conductive properties of PEDOT:PSS.

This work was done in collaboration with the group of Dr. Róisín Owens, Bioelectronic Systems Technology group, at the Department of Chemical Engineering and Biotechnology, from the University of Cambridge, UK, during my three months research visit.

Finally, in Chapter 8 the final remarks and future work are presented.

1. 4 References

1. Lopez, G. A.; Estevez, M.; Soler, M.; Lechuga, L. M. Recent advances in nanoplasmonic biosensors: applications and lab-on-a-chip integration. *Nanophotonics* 2017, 6, 123-136.
2. Dahlin, A. B. Size matters: problems and advantages associated with highly miniaturized sensors. *Sensors* 2012, 12, 3018-3036.
3. Derkus, B. Applying the miniaturization technologies for biosensor design. *Biosens. Bioelectron.* 2016, 79, 901-913.
4. Soleymani, L.; Li, F. Mechanistic challenges and advantages of biosensor miniaturization into the nanoscale. *ACS sensors* 2017, 2, 458-467.
5. Pol, R.; Céspedes, F.; Gabriel, D.; Baeza, M. Microfluidic lab-on-a-chip platforms for environmental monitoring. *TrAC Trends Anal. Chem.* 2017, 95, 62-68.
6. Guo, X.; Liu, J.; Chen, Y. When your wearables become your fitness mate. *Smart Health* 2020, 16, 100114.
7. Sengupta, P.; Khanra, K.; Chowdhury, A. R.; Datta, P. Lab-on-a-chip sensing devices for biomedical applications. In *Bioelectronics and Medical Devices* Elsevier: 2019; pp 47-95.
8. Vashist, S. K.; Luppa, P. B.; Yeo, L. Y.; Ozcan, A.; Luong, J. H. Emerging technologies for next-generation point-of-care testing. *Trends Biotechnol.* 2015, 33, 692-705.
9. Yager, P.; Edwards, T.; Fu, E.; Helton, K.; Nelson, K.; Tam, M. R.; Weigl, B. H. Microfluidic diagnostic technologies for global public health. *Nature* 2006, 442, 412-418.
10. El-Ali, J.; Sorger, P. K.; Jensen, K. F. Cells on chips. *Nature* 2006, 442, 403-411.
11. Wise, K. D.; Najafi, K. Microfabrication techniques for integrated sensors and microsystems. *Science* 1991, 254, 1335-1342.
12. Madou, M. J. *Fundamentals of microfabrication: the science of miniaturization*; CRC press: 2018.
13. Haeberle, S.; Zengerle, R. Microfluidic platforms for lab-on-a-chip applications. *Lab Chip* 2007, 7, 1094-1110.
14. Mohammed, M. I.; Haswell, S.; Gibson, I. Lab-on-a-chip or Chip-in-a-lab: Challenges of Commercialization Lost in Translation. *Proc. Technol.* 2015, 20, 54-59.
15. Temiz, Y.; Lovchik, R. D.; Kaigala, G. V.; Delamarche, E. Lab-on-a-chip devices: How to close and plug the lab? *Microelectron. Eng.* 2015, 132, 156-175.
16. Ren, K.; Zhou, J.; Wu, H. Materials for microfluidic chip fabrication. *Acc. Chem. Res.* 2013, 46, 2396-2406.

17. Curto, V. F.; Fay, C.; Coyle, S.; Byrne, R.; O'Toole, C.; Barry, C.; Hughes, S.; Moyna, N.; Diamond, D.; Benito-Lopez, F. Real-time sweat pH monitoring based on a wearable chemical barcode micro-fluidic platform incorporating ionic liquids. *Sens. Actuator B Chem.* 2012, 171, 1327-1334.
18. Shin, J.; Liu, Z.; Bai, W.; Liu, Y.; Yan, Y.; Xue, Y.; Kandela, I.; Pezhouh, M.; MacEwan, M. R.; Huang, Y. Bioresorbable optical sensor systems for monitoring of intracranial pressure and temperature. *Sci. Adv.* 2019, 5, eaaw1899.
19. Zhu, Q.; Zhou, Q.; Zhang, H.; Zhang, W.; Lu, D.; Guo, M.; Yuan, Y.; Sun, F.; He, H. Design and construction of a metal-organic framework as an efficient luminescent sensor for detecting antibiotics. *Inorg. Chem.* 2020, 59, 1323-1331.
20. Stich, M. I.; Nagl, S.; Wolfbeis, O. S.; Henne, U.; Schaeferling, M. A dual luminescent sensor material for simultaneous imaging of pressure and temperature on surfaces. *Adv. Funct. Mater.* 2008, 18, 1399-1406.
21. Basabe-Desmonts, L.; Benito-López, F.; Gardeniers, H. J.; Duwel, R.; van den Berg, A.; Reinhoudt, D. N.; Crego-Calama, M. Fluorescent sensor array in a microfluidic chip. *Anal. Bioanal. Chem.* 2008, 390, 307-315.
22. Zhang, L.; Liu, X. A.; Gillis, K. D.; Glass, T. E. A High-Affinity Fluorescent Sensor for Catecholamine: Application to Monitoring Norepinephrine Exocytosis. *Angew. Chem. Int.* 2019, 58, 7611-7614.
23. Kang, X.; Wang, J.; Wu, H.; Liu, J.; Aksay, I. A.; Lin, Y. A graphene-based electrochemical sensor for sensitive detection of paracetamol. *Talanta* 2010, 81, 754-759.
24. Zhang, R.; Rejeeth, C.; Xu, W.; Zhu, C.; Liu, X.; Wan, J.; Jiang, M.; Qian, K. Label-free electrochemical sensor for cd44 by ligand-protein interaction. *Anal. Chem.* 2019, 91, 7078-7085.
25. Zhang, D.; Peng, Y.; Qi, H.; Gao, Q.; Zhang, C. Label-free electrochemical DNA biosensor array for simultaneous detection of the HIV-1 and HIV-2 oligonucleotides incorporating different hairpin-DNA probes and redox indicator. *Biosens. Bioelectron.* 2010, 25, 1088-1094.
26. El Kacimi, A.; Pauliac-Vaujour, E.; Eymery, J. Flexible capacitive piezoelectric sensor with vertically aligned ultralong GaN wires. *ACS Appl. Mater. Interfaces* 2018, 10, 4794-4800.
27. Wang, Z.; Wang, X.; Li, M.; Gao, Y.; Hu, Z.; Nan, T.; Liang, X.; Chen, H.; Yang, J.; Cash, S. Highly sensitive flexible magnetic sensor based on anisotropic magnetoresistance effect. *Adv Mater* 2016, 28, 9370-9377.
28. Varga, M.; Ladd, C.; Ma, S.; Holbery, J.; Tröster, G. On-skin liquid metal inertial sensor. *Lab Chip* 2017, 17, 3272-3278.
29. Pires, N. M. M.; Dong, T.; Hanke, U.; Hoivik, N. Recent developments in optical detection technologies in lab-on-a-chip devices for biosensing applications. *Sensors* 2014, 14, 15458-15479.

30. Wang, Y.; Zeinhom, M. M.; Yang, M.; Sun, R.; Wang, S.; Smith, J. N.; Timchalk, C.; Li, L.; Lin, Y.; Du, D. A 3D-printed, portable, optical-sensing platform for smartphones capable of detecting the herbicide 2, 4-dichlorophenoxyacetic acid. *Anal. Chem.* 2017, 89, 9339-9346.
31. Purohit, B.; Kumar, A.; Mahato, K.; Chandra, P. Smartphone-assisted personalized diagnostic devices and wearable sensors. *Curr. Opin. Biomed. Eng.* 2020, 13, 42-50.
32. Zhang, D.; Liu, Q. Biosensors and bioelectronics on smartphone for portable biochemical detection. *Biosens. Bioelectron.* 2016, 75, 273-284.

2

Current Challenges in the Development of Miniaturised Biosensors

The detection and monitoring of biological events is essential in research laboratories, pharmaceutical industry, environmental analysis or healthcare. The miniaturisation of these biosensing assays improves sensitivity, decreases analysis times and economic costs, reduces handling, and allows automation and parallelisation of simultaneous reactions. Due to these inputs, the scaling down of these assays enables the systematic collection of data, and thus, facilitates the monitoring of biologic events. Moreover, the miniaturisation of biosensing assays allows collecting information that could not be obtained with conventional biosensing assays. This chapter provides an overview of the most used microfabrication techniques for the manufacturing of miniaturised biosensing devices, and reviews some recently developed integrated miniaturised biosensors, sorting them out by the material used for sensing, and the transduction mechanism.

2.1 Introduction

Biosensing involves the detection of biological or chemical reactions or molecules, and it is essential in several fields such as drug development, food safety, environmental analysis or healthcare¹. Moreover, systematic biosensing measurements enable the monitoring of biological events, which provide crucial information such as pollution peaks in environmental safety, serve as guidance in the prognosis of a disease, or provide unknown information about a tracked biological activity. A biosensor is comprised of a receptor, and a transducer. The receptor is the element that interacts with the analyte and it incorporates a biomolecule for bio-recognition. The transducer is the component that takes the chemical information provided by the receptor and transforms it into a physicochemical signal (optical, piezoelectric, electrochemical...) ^{1,2}.

Conventional biosensing assays usually require expensive reagents, long analysis times and trained personnel for accurate performance. However, the integration of these assays within miniaturised systems, also called lab-on-a-chip (LOC), presents several benefits for the user in terms of portability, reduced analysis times and working space, small reagent and sample volumes, and user-friendly performance, reduced handling and waste generation, and possible multiplexing³⁻⁵ (Figure 2.1). Moreover, when body fluids are analysed, since small volumes are required, the discomfort of the patient during sampling is reduced. Due to these inputs, miniaturised biosensing facilitates systematic measurements and monitoring, enabling to do systematic measurements of a target analyte and/or tracking biological activities/events. Moreover, due to the control at the micro-scale obtained with these devices, the miniaturisation of biosensors provides with information that cannot be obtained with conventional assays, such as the production and monitoring of lipid membrane nanotubes (see

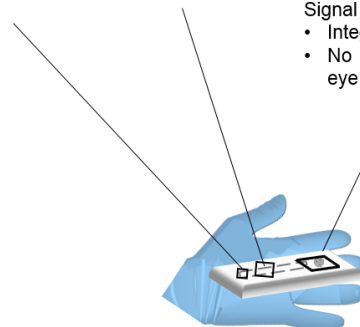
Chapter 5)⁶ or the quantification of cell adhesion (see chapter 6)^{7,8}.

Microtechnology enables the fabrication of features with high resolution at the micro-scale⁹, and many advances have been made so far towards the miniaturisation of biosensors thanks to the development of the microtechnology. For example, sensing strategies like DNA-arrays^{10,11}, protein-arrays^{7,12}, photonic crystal arrays^{13,14}, membrane protein sensing¹⁵, polymeric arrays^{16,17} and smart materials^{18,19} are being developed. Despite the advances in the miniaturisation of sensing assays, an integrated LOC device contains multiple functional elements such as the recognition part, components to control fluidics or a transducer. Therefore, different microfabrication techniques are required, hindering their manufacturing. In fact, some challenges remain unsolved, like the integration of elements for fluidic control²⁰ or to supply electrical power²¹, which ends up in sensing devices that are not fully miniaturised²². Moreover, data processing often requires complex external devices to transduce the information coming from the detector into readable and measurable information, such as microscopes for optical microsensors and electronic equipment for electrochemical sensors, among others². This means that the miniaturisation of the biosensing platform gets delayed by the reduction of the dimension of the sensing element and by the nature of the detection method (*e.g.* simple naked eye visualisation *versus* the use of a miniaturised transducer). Due to these technical challenges, LOC devices are still far from being well established methods in industry and in centralised laboratory facilities.

This chapter will review the recent advances towards miniaturised biosensing assays, using examples of developed technologies, classified by the type of sensor. It will present the most common microfabrication techniques used for their manufacturing and an overview of the materials used for the integration of

miniaturised biosensors.

	SAMPLE AND REAGENTS	INTERVENTION	OPERATION AND SIGNAL PROCESSING	OPERATION TIMES
Conventional biosensing assays	 Few milliliters	 Increased handling Large reagent volumes	 Expensive and big equipment	 Long
Miniaturised LOC	Few microliters	Reduced handling, user friendly	Scaled down sensing area Signal readout: <ul style="list-style-type: none"> • Integrated transducer • No transducer, naked eye readout 	Short



Reduced costs
\$
Parallelisation
Higher sensitivity

Figure 2.1. Comparison between traditional biosensing assays and miniaturised LOC biosensing platforms.

2.2 Miniaturisation and integration of the recognition element

The scaling down of the sensing unit provides with a controlled environment for the interaction of the receptor with the analyte, providing the following advantages over traditional sensors: the use of smaller sample and reagent

volumes, precise manipulation of the environment, accurate control of fluid flow and homogeneous distribution of molecules all along the sensor ⁴. Miniaturisation also leads to multiplexing, having several microsensors in a defined space to detect different species ^{23,24}.

The first step towards the miniaturisation of biosensors is the manufacturability of small features, which can be achieved by the use of microtechnology. There are many microfabrication techniques available, each of them favourable for some materials, but not recommended for others.

2.2.1 Microfabrication techniques

Microfabrication enables the miniaturisation and integration of functional components in microdevices, resulting in fully integrated platforms to perform analytical processes. The advances in microfabrication have enabled the development of successful biosensing platforms.

2.2.1.1 Photolithography

Photolithography offers to transfer a geometric pattern from a photomask to a substrate, using UV light. This technique can go down to 100 nm resolution, and as its efficiency highly depends on the wavelength of the employed light. For instance, the use of deep UV light allows to go down to features of 50 nm ²⁵. Due to its resolution and precision, this additive manufacturing technique has been the core of the mass production in the sensor industry for many decades, especially for integrated microelectronic circuits ²⁶.

Several recent works have reported miniaturised electrochemical biosensors fabricated by photolithography for targets such as body metabolites ^{27,28}, nucleic

acids^{29,30}, proteins^{31,32} and cells^{33,34}. Glucose is one of the most targeted molecules by miniaturised biosensing assays. As an example, micro-nano hybrid structures made by photolithography were reported by Hsu et al., who fabricated arrays of columns of 3 µm diameter covered by gold²⁸ (Figure 2.2A). These structures were then covered with gold nanoparticles, which enhanced the electrochemical detection of glucose to reach a limit of detection of 9 µM.

Silicon and glass are the most common substrate materials used for photolithography. The rigidity and mechanical stability of inorganic materials such as silicon have enabled huge advances in sensor miniaturisation. However, new trends in health monitoring of interstitial fluid, sweat, skin or internal tissue healing require the use of flexible and biocompatible materials. For instance, implantable sensing devices are in contact with the skin or other internal tissues, therefore they need to be flexible to reduce discomfort and to better mimic the biological environment of the analyte to be sensed^{35,36}. Wearable sensors are a growing trend and a valuable tool to monitor health through the measuring of biomarkers such as glucose^{37,38}, heavy metals³⁹, proteins³² and hormones⁴⁰. For instance, Kim et al. recently reported a flexible MoS₂-polyimide electrode for the electrochemical sensing of PTH, T3 and T4 hormones⁴⁰. The patterned gold electrode was modified using an electrochemical e-ELISA for the recognition of hormones through an antibody specific interaction (Figure 2.2B).

Although photolithography is the most used lithography technique, there are many others that have also been used for the fabrication of sensing microsystems, such as e-beam lithography^{41,42}, two photon lithography⁴³ and nanoimprint lithography^{44,45} among others⁴⁶. Nanoimprint lithography is a simple method for the fabrication of nanostructures, so it has been used to increase the surface area of working electrodes, aiming to increase their sensitivity. As an example,

nanostructured UV-curable and conductive pyrrole polymers on platinum electrodes were used to increase the sensitivity for glucose⁴⁴ (Figure 2.2C).

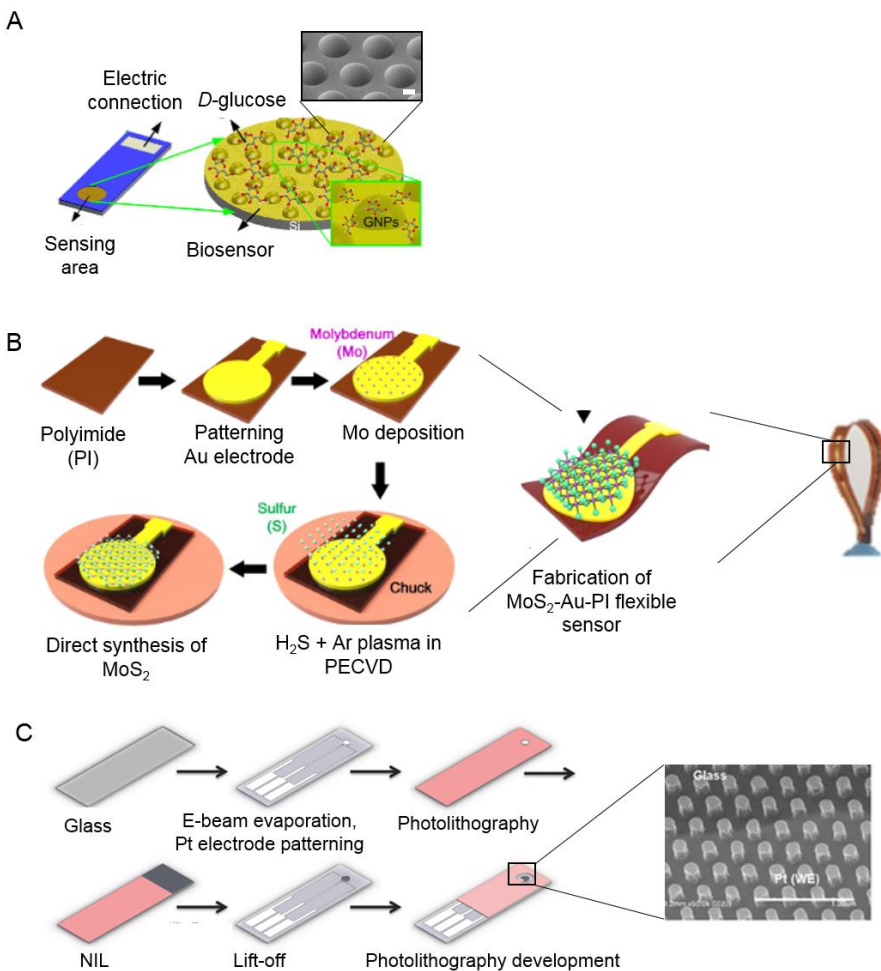


Figure 2.2. A) Schematic of a biosensor with micro/nano hybrid structured electrodes made by photolithography, and a scanning electron microscope image of the wafer after Au sputtering. Scale bar corresponds to 5 μm²⁸. B) Illustration of the synthesis of MoS₂ on a flexible Au–polyimide electrode patterned by photolithography⁴⁰. C) Fabrication of a polypyrrole electrode by nanoimprinting lithography: scheme of the fabrication (left) and SEM image (right) of the electrode. Scale bar corresponds to 1 μm⁴⁴.

2.2.1.2 Soft-lithography

Soft-lithography comes from traditional lithography, and involves the replica moulding of a rigid substrate (usually made by photolithography) on a flexible material⁴⁷. The emergence of soft lithography supposed a step forward in the manufacturing of miniaturised biosensing devices, due to the fast fabrication of high-resolution features on the flexible and biocompatible polydimethylsiloxane (PDMS)^{48,49}. The main advantage relies on the fast prototyping of microfluidic devices to perform bio-assays within them with a decreased volume of reagents and a remarkable reduction in economic costs due to the materials used^{3,4}.

This technique paved the way for the development of microcontact printing, which patterns molecules on a surface through stamping a microstructured PDMS. Biosensors manufactured by microcontact printing go from polymer⁵⁰, to protein^{7,8,51}, or even graphene⁵² based miniaturised biosensing assays. Actually, specific designs may allow new functionalities, for example, extracellular matrix protein arrays have been reported for cellular integrin profiling. In this work, arrays of protein dots designed for the positioning of single cells were printed on a polymeric surface, so the percentage of protein dots occupied by a single cell were quantified. Cell adhesion was monitored by quantifying the number of adhered cells for different biomaterial-dots, which enabled to obtain digital or quantitative data to calculate and characterise cell-biomaterial interactions⁸ (Figure 2.3).

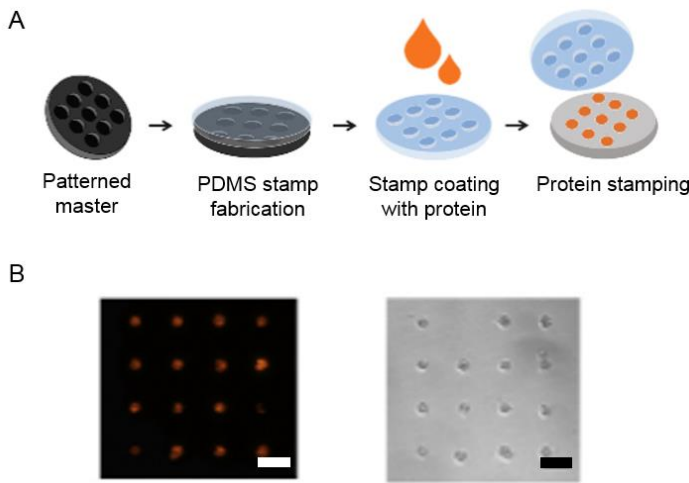


Figure 2.3. A) Graphic illustration of the fabrication of the extracellular matrix protein microarray platform. B) Fluorescence microscopy image of the protein pattern (left) and optical microscopy image of the single cell array on the protein pattern (right). Scale bars correspond to 50 μm ⁸.

2.2.1.3 Hot Embossing

Hot embossing is a low-cost fabrication method capable of reaching high aspect ratio microfeatures and nanoimprinted patterns of polymers. It relies on stamping a rigid pattern on a polymeric surface which has been previously softened with a temperature increase just above its glass transition temperature⁵³. The rigid pattern is usually manufactured by well established microfabrication techniques, that can reach to the sub-micron resolution, but using expensive material and equipment. Usually, the stamps that fix the microstructures on the polymeric substrate can be used once and again to produce the same pattern on a great extent of materials. The development of adequate hot embossing protocols led to nanostructured features with good resolution, avoiding lift-off steps^{54,55}. Hot embossing was used for the fabrication of electrodes for sensing.

Higher signal gain is obtained for smaller gaps between electrodes⁵⁶, so high resolution electronics fabricated by hot embossing brought electronics closer to rapid prototyping and mass production.

The combination of hot embossing with a metal deposition step was used by Lee *et al.* for the development of a bovine serum albumin (BSA) biosensor by surface plasmon resonance (SPR) in a polycarbonate flexible substrate⁵⁵. Partel *et al.* deposited gold to create an interdigitated electrode array with nanogaps on cycle-olefin polymer (COP)⁵⁴ (Figure 2.4) demonstrating that low cost and fast manufacturing of integrated sensors by hot embossing could be possible.

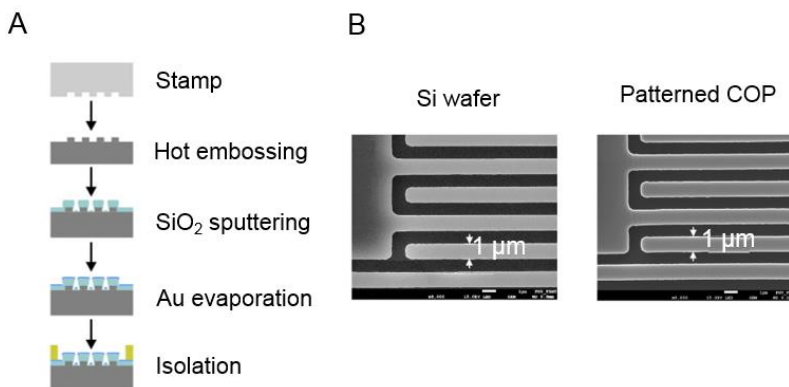


Figure 2.4. A) Fabrication of the disposable interdigitated electrode array based sensor, consisting on a silicon rigid stamp, hot embossing to COP, sputter deposition of SiO₂, deposition of Au, and addition of the insulating layer to passivate the wafer. B) Images of the silicon stamp (left) and the structure on COP substrate after hot embossing⁵⁴.

2.2.1.4 Screen printing

Screen printing relies on the deposition of organic or inorganic materials on a

substrate. A liquid paste is applied with a rubber squeegee through a mesh, with a mask containing the pattern to be transferred to the surface of the substrate⁵⁷. Although this technique was used for artistic means for a long time, it has been a valuable tool to fabricate biosensors for some decades⁵⁸. The resolution that can be obtained with screen printing is 100 µm, which is far worse than the one obtained by other microfabrication techniques, but this technology has a huge potential for prototyping and mass scale production, and it has been already applied to manufacture biosensors targeting physiological analytes⁵⁹⁻⁶¹.

Screen printing is very versatile when it comes to the range of materials that can be used as substrate, such as ceramics⁶², glass fibres⁶³ or flexible polyethylene terephthalate (PET)⁶⁴ and polycarbonate⁶⁵. Conductive inks are the most used materials for screen printed sensors, enabling easy fabrication of patterned electrochemical sensors on multiple substrates, offering easier manufacturing protocols than traditional lithographic techniques, although high resolution can be compromised⁶⁶.

For instance, Kim *et al.* developed an intra-mouth wearable screen printed biosensor for the monitoring of salivary uric acid⁵⁹. They used prussian blue graphite ink to make the working electrode of 3 mm diameter, modified with uricase enzyme, which was able to perform the electrochemical monitoring of uric acid in saliva with wireless data transmission (Figure 2.5). In a more recent work, the authors pursued the same saliva detection objective, developing screen printed carbon ink working electrodes that were modified with carbon nanotubes and uricase for the detection of uric acid⁶⁰.

Screen printing technology has been also used to develop tattoo-like flexible biosensors, for the simultaneous monitoring of sweat and interstitial fluid via screen-printed prussian blue electrodes⁶⁷. The biosensing platform consisted of

a glucose oxidase based electrochemical sensor at the cathode side, and an alcohol oxidase based electrochemical biosensor at the anode to measure glucose in interstitial fluid and alcohol in sweat, respectively. The system transmitted the sensing data to a smartphone, standing out as an option for cost-effective and easy to fabricate disposable biosensing devices.

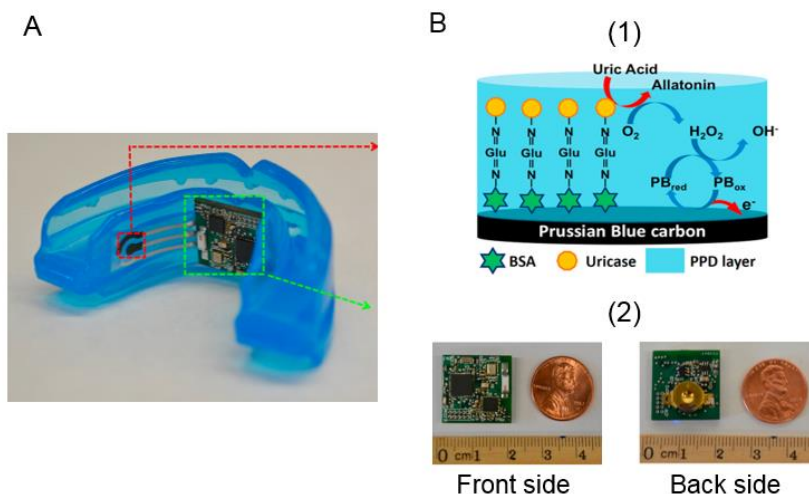


Figure 2.5. A) Photograph of the screen printed mouth guard biosensor. B) (1) Schematics of the reagent layers of the prussian blue carbon working electrode containing uricase and (2) a photograph of the wireless amperometric circuit board: front side (left) and back side (right) ⁵⁹.

2.2.1.5 Inkjet printing

Inkjet printing recreates a computer design by depositing droplets, usually on a porous substrate. It is a very interesting technique for the development of micro-biosensors, since the deposition of small volumes ($10 - 20 \text{ pL drop}^{-1}$) of material on a surface can be carried out at high speed and without contact, being compatible with flexible substrates ⁶⁸. Although the sub-micron resolution is not

possible, accurate deposition with micro-spatial resolution has been achieved⁶⁹. For instance, Beduk *et al.* developed a PEDOT:PSS/ZnO sol-gel hydrazine electrochemical sensor on paper, being able to reach 20 µm of resolution⁷⁰. Besides, inkjet printing is highly versatile, since a wide range of materials can be spotted to act as sensors⁷¹, such as sol-gel materials^{70,72}, conducting^{73,74} and smart polymers⁷⁵, light emitting diodes^{76,77}, nanoparticles^{78,79}, metals^{80,81} and biomolecules^{82,83}.

Microfabrication techniques like photolithography and hot embossing present high resolution and are well established, with great reproducibility and efficacy. However, when sub-micron resolution is not needed, inkjet printing is the solution, bringing the manufacturing of microsensors closer to mass production. For instance, Godoy *et al.* developed an inkjet printed SPR sensor for the detection of thiram fungicide, using a highly concentrated glycerol/ethanol dispersion of gold nanospeheres as ink on hydrophobic chromatography paper⁸⁴.

Bioinks are patterned using inkjet printing to develop biosensors based on biological recognition. As an example, an aptameric ink has been printed on a lateral-flow assay for the optical detection of *E. coli*⁸³. The colorimetric response was captured with a mobile phone camera (Figure 2.6).

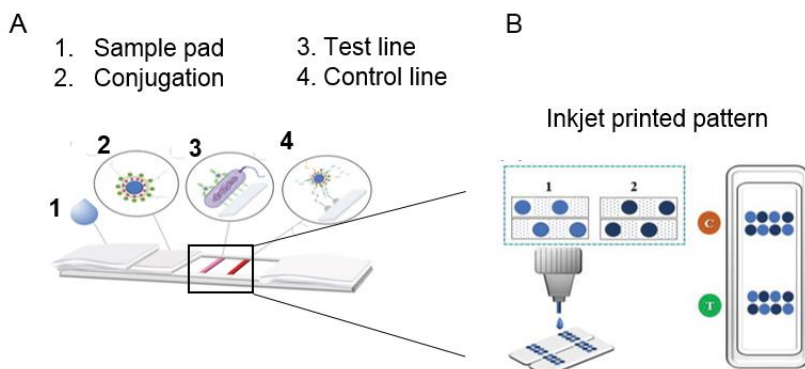


Figure 2.6. A) Scheme of the lateral flow assay for the detection of *E. coli* based on an inkjet printed aptamer ink sensor. B) Graphical illustration of the aptamer ink pattern used for sensing⁸³.

2.2.1.6 3D printing

3D printing enables the fabrication of a three-dimensional object from a computer-aided design draw. In the last years, the precision, resolution (down to 10 µm), repeatability and the range of available materials to be printed have increased, subsequently increasing the popularity of this technique for the fabrication of microsystems⁸⁵⁻⁸⁷. 3D printing enables the production of complex shapes, with internal hollow parts, and rapid prototyping due to the rapid design iterations that reduce prototype optimisation times. These are advantages over traditional microfabrication techniques such as photolithography, soft lithography, hot embossing, etc⁸⁵.

Unlike the previous microfabrication methods that are either structural or patterning techniques, 3D printing offers both approaches. An adequate design can generate an internal element of a microdevice such as, injection valves⁸⁸ or preconcentrating/sorting components^{89,90}. For instance, a 3D printed helical channel combined with antibody functionalised magnetic nanoparticles was

used for the detection and separation of pathogenic bacteria in milk samples by inertial focusing (Figure 2.7) ⁹⁰. Furthermore, the combination of 3D printed internal smart architectures with photopolymerisable functional materials provides an easy approach to *in situ* immobilise gel like materials within microfluidic structures, as presented in Chapter 3, which simplifies the integration of functional materials and reduces costs ⁹¹.

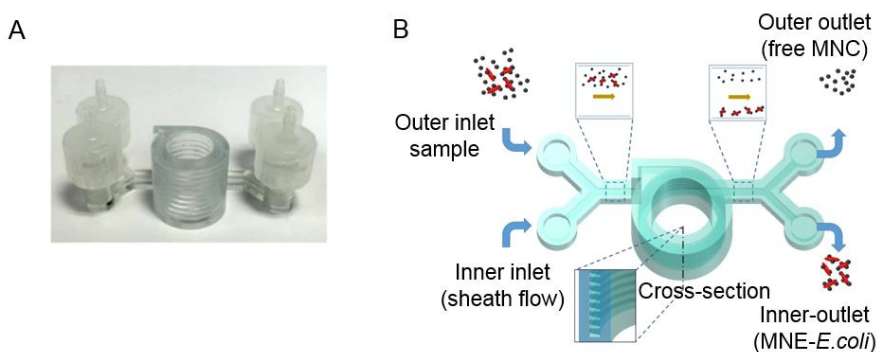


Figure 2.7. A) Photograph of the 3D printed device for the detection and separation of pathogens. B) Schematic illustration of the separation and capture of *E. coli* by inertial focusing ⁹⁰.

3D printing is also a valuable tool to directly print or pattern the sensor itself on a substrate, as it is for 3D printed electronics ^{92,93} or 3D printed optics ^{94,95}, two novel trends that are in its infancy, but whose popularity is increasing fast. 3D printed electronics is very attractive since it enables high resolution (in the order of 15 μm in some cases) electrode patterns without using a photomask, and possibilities to be used on flexible substrates ^{96,97}. For example, extrusion 3D printing has been reported useful for the manufacturing of a miniaturised and integrated potentiostat circuit prototype ⁹⁶. Using a highly viscous silver nanoparticle ink, a printed board circuit was fabricated on a flexible substrate, obtaining a linear detection range for lactate of 1 - 20 mM. This facilitates the

manufacturability of integrated electrochemical biosensors towards mass production.

On the other hand, 3D printing optics still suffers from major drawbacks due to the limitations of this additive manufacturing technique to create fully transparent and smooth surfaces, since deposited layers affect light reflection and transmission⁹⁸. Nevertheless, Hinman *et al.* developed a 3D-printed prism that after some polishing steps was functional for plasmonic sensing of bacterial toxins, reducing fabrication costs and facilitating the fabrication of optical components⁹⁵.

2.2.2 Material integration for biosensing applications

Materials are playing a key role as part of the recognition element, since they provide chemical information about the interaction of the analyte with the transducer. There is a wide range of materials that can be used as sensors, but generally, the material has to fulfil technical, metrological and economic criteria for each sensing application. The materials used as the recognition element can be classified in the following groups.

2.2.2.1 Metals

Metals, being the base of electrodes, are the main used material for sensing. They have great electricity and heat conducting properties, which makes them good choices as electronic sensors. Moreover, their physical properties like malleability and ductility facilitate their processability⁹⁹. Due to their conductivity, corrosion resistance, hardness and the downsizing capability, traditional metals such as copper¹⁰⁰, graphite¹⁰¹, titanium¹⁰² and silver¹⁰³, have been the most widely used for the fabrication of miniaturised electrodes. However, gold presents high

affinity to interact with biomolecules, high stability and high interface energy, which enable the manufacturing of highly sensitive biosensors¹⁰⁴, so most researchers use gold for biosensing electrodes.

Metals in electrochemical biosensing have been mostly used for the detection of metabolites^{28,105} and cells^{33,106} but they are good choices for challenging sensing reactions such as DNA detection. Sensitive, selective, rapid and label-free detection of DNA is a challenging task, but metallic materials such as nanoparticles¹⁰⁷, carbon nanotubes¹⁰⁸, silicon nanowires¹⁰⁹, graphene oxide¹¹⁰ and molybdenum disulphide (MoS_2)²⁹ are gaining popularity in the field. For instance, Mei *et al.* reported an ultrasensitive biosensor for DNA, using a MoS_2 based transistor²⁹. After fabricating the gold microelectrodes, the sensing channel was covered with MoS_2 and phosphorodiamidate morpholino oligos (PMO). PMO-DNA hybridisation was detected showing good selectivity, repeatability and a limit of detection of 6 fM.

Interestingly, biological samples sometimes show intrinsically negligible magnetic susceptibility that can be measured by nuclear magnetic resonance (NMR). Huber *et al.* reported a rapid biosensor to detect dengue fever and molecularly profile cancer cells in parallel, by coupling a hetero-nuclear resonance multichannel electronic system with NMR technique¹¹¹. In addition, some biosystems are electrically excitable, producing biomagnetic fields, allowing metal electrodes to detect those¹¹². For instance, using a pulse-driven magnetoimpedance sensor, the magnetic field of musculature from guinea-pigs was monitored and correlated with biological electric activity¹¹³.

Electrodes themselves are sensitive and effective, but coating them with other materials can improve their performance; these materials can be metals as well, or another material, forming a hybrid sensor. Metal organic frameworks (MOF),

for instance, are metal-polymer networks with high structural versatility, large surface area and adsorption capability¹¹⁴. They can respond to the interaction between the framework itself and a hosted guest molecule, enhancing the sensitivity of, for instance, gold electrodes^{115,116}. Carbon nanomaterial coatings are also used to enhance the sensitivity of electrodes¹¹⁷. Specifically, graphene is a transparent and flexible conducting material with interesting electrochemical properties, which serves to enhance electrode selectivity^{118,119}. Finally, metals also may present plasmonic properties. As a demonstration, Elbahri *et al.* used plasmonic metaparticles (plasmonic dipoles) to create specular reflection colours for the successful naked eye detection of human serum exosomes (Figure 2.8)¹²⁰.

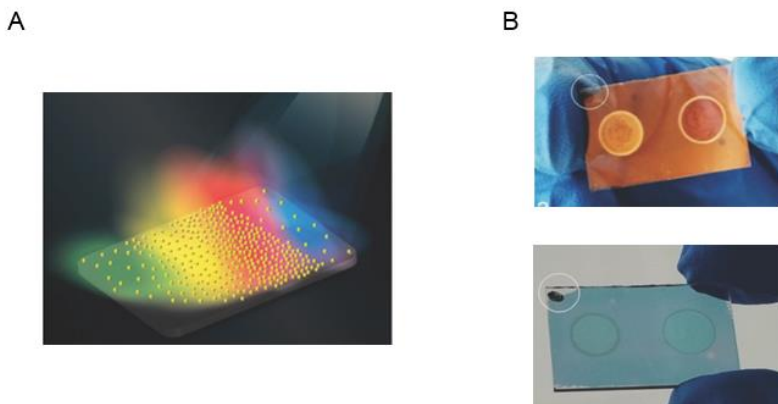


Figure 2.8. A) Schematic illustration of specular colours radiated from the plasmonic nanoparticles. B) Pictures of the sample containing Au nanoclusters exposed to the exosomes of a patient with inflammatory bowel disease (left circle) and to the exosomes of a healthy individual (right circle), in two modes: reflection (top) and transmission (bottom)¹²⁰.

2.2.2 Polymers

Biosensors may be based on polymeric materials. Polymers are highly versatile,

they have a wide range of chemical and physical properties, such as variable ability to interact with biological components at the molecular level, viscoelastic properties, capacity to incorporate biomolecules within their structure¹²¹, etc... Additionally, they can easily be patterned to create micro-sized structures where biochemical reactions can take place and can be *in situ* detected, as it was shown by Wang *et al.*, who achieved patterns of poly(acrylic acid) brushes in spots of 100 µm diameter by microcontact printing⁵⁰. In this work, Hepatitis-B-Virus - Hepatitis-B-Virus surface antibody interactions were monitored by fluorescence microscopy and SPR (Figure 2.9). Patterned poly(acrylic acid) brushes brought high signal amplification of the virus detection in comparison to non-patterned brushes, giving a wide linear range for detection.

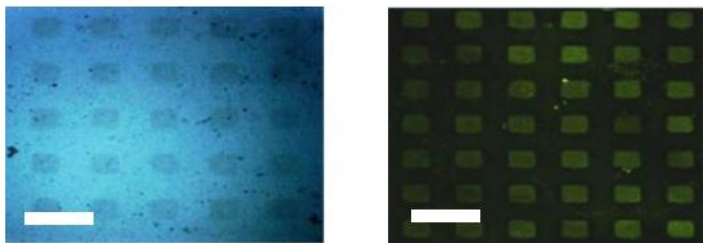


Figure 2.9. Optical microscopy image of poly(acrylic acid) brushes surface pattern with human-IgG (left), and fluorescence microscopy image of poly(acrylic acid) brushes pattern surface with human-IgG after incubation with FITC-goat-anti-H-IgG (right)⁵⁰. Scale bar corresponds to 100 µm.

Polymer sensors are also versatile in terms of signal output. Their structure allows them to be combined with other molecules, so they can work as colorimetric¹²², fluorescent¹²³ or chemiluminescent^{124,125} biosensors. They can also be used for organic bioelectronics, combining them with traditional metallic electrodes to improve biosensing^{126,127} or to use them as working electrodes, as

flexible electrochemical biosensing platforms¹²⁸. In particular, semiconductor polymers are useful for electrochemical biosensing^{32,129}, but current trends are moving towards more advanced –flexible and stretchable- monitoring microsystems, mimicking artificial skin and providing multisensing for pH, urea and lactic acid in sweat¹³⁰.

Specifically, functional materials or the also called “smart materials” are defined as materials that react to changes in their environment in a specific and reproducible way¹³¹. Within the polymer family, some are stimuli responsive polymers, which have gained the attention of the biosensor community, because their response to stimulus can be measured and correlated with a specific phenomenon. These polymers can be used alone¹³² or in combination with other sensing elements^{133,134}. For instance, coating optic fibres with an acrylamide hydrogel for pH sensing by SPR showed an increased functionality¹³³. The hydrogel swelled with increasing pH values, resulting in a higher absorption of water, and so, a decreased the refractive index, giving more sensitivity to the pH measurement. Moreover, polymers with different functionalities can be combined to obtain hybrid materials with multiple functionalities. In Chapter 7, a novel copolymer was developed from the combination of thermo-responsive pNIPAAm and conducting poly(3,4-ethylenedioxythiophene) polystyrene sulfonate. The copolymer, functionalised with fibronectin protein, acted as an actuator, performing the capture and temperature triggered release of cells and as a sensor, monitoring the process by electrochemical impedance spectroscopy. As mentioned before, polymers present great physical and chemical versatility. An example is the formation of photonic crystals (PC), which are periodic optical nanostructures with a band gap (photonic band gap)¹³⁵. PCs diffract incident light in the visible spectrum when they are sub-micrometer sized, generating excellent naked-eye colorimetric sensors¹³⁶. For instance, crystalline colloidal

arrays made of monodispersed polystyrene colloids (100 nm diameter) embedded in an acrylamide-*bis*acrylamide network were reported for glucose sensing¹³⁷. In another work, Endo *et al.* used nanoimprint lithography to create PCs on COP embedded in polyethylene glycol (PEG) for the reflectometric detection of influenza virus in human saliva, reaching a detection limit of 1 ng mL⁻¹¹³⁸.

Nanoscale polymers give some advantages in terms of processability, opening their use in microfabrication. For instance, polyaniline nanoparticle dispersions were processed by inkjet printing to control the size and thickness of polymer structures on electrodes^{139,140}. These electrochemical sensors were used for urea detection¹³⁹.

2.2.2.3 Biomaterials

Biomolecules –proteins, carbohydrates and nucleic acids- are polymeric chains or complex networks. They specifically interact between them with high affinity, even generating covalent bonds. Miniaturised biosensors usually incorporate one of these recognition biomolecules, with high affinity for the target, which provide sensitivity and selectivity¹⁴¹. These recognising biomolecules can be integrated within other sensing materials¹⁴²⁻¹⁴⁴ to form hybrid sensing biomaterials or be directly immobilised, adhered or micropatterned to a surface, to generate the recognition element^{7,8}. For example, the modification of electrodes with specific enzymes is a widely used technique that provides sensitivity and selectivity to the biosensor¹⁴⁵. In addition, the possibility to covalently bind enzymes on biopolymer coated electrodes guarantees the stability of the enzyme, for longer storage times, keeping great electrochemical performance. Martin *et al.* used polydopamine polymeric films to covalently bond cholesterol oxidase to

nanostructured platinum electrodes¹⁴². The biosensor showed high stability and great performance for cholesterol sensing, with a limit of detection of 10.5 µM. Moreover, modified nanoparticles were used for optical biosensing, for instance, by modifying gold nanoparticles with aptamers¹⁴⁶.

On the other hand, the direct patterning of biomolecules on surfaces is a straightforward technique that has been widely applied for biosensing. Very high resolutions were obtained, depending on the technique. For instance, surface protein micropatternings for individual cells, open new ways for biological data acquisition and interpretation based on the individualisation of the detection output⁷. Considering each cell as an individual output, the system collects quantitative data, like the optical detection of protein binding affinity^{8,147}, cytotoxicity testing (see Chapter 6)⁷, cell responses to extracellular matrix proteins¹⁴⁸, cell polarisation¹⁴⁹, secretion of biomolecules¹⁵⁰ and migration¹⁵¹. As an example, Van Dongen *et al.* used protein micropatterns as dynamic surface coatings for the control of cell adhesion, migration and shape change¹⁵², Figure 2.10.

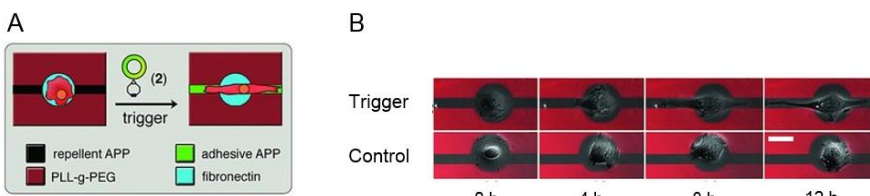


Figure 2.10. A) Scheme of the double pattern of poly-(L-lysine)-graft-PEG with thin lines of azido-[polylysine-g-PEG] (APP). Cells only migrated into a restricted area after triggering it with bicyclo[6.1.0]nonyne-Arg-Gly-Asp peptide (2), requiring shape change. B) The stretching of RPE1 cells occurred over time after addition of (2). 2 was not added to the control samples¹⁵². Scale bar corresponds to 25 µm.

Additionally, the patterning of single molecules has a great potential for biosensing, promising higher specificity and sensitivity, opening multiplexing capabilities¹⁵³. New techniques such as DNA-origami^{153,154}, electron beam lithography^{155,156} or hole mask colloidal lithography¹⁵⁷ already enabled the precise location of single biomolecules. Actually, hole mask lithography offers a benchtop method for the patterning of single molecules on any type of substrate materials (polymers, glass, metal surfaces, ...), with no specific temperature and humidity requirement, with high design versatility¹⁵⁷. As a scalable and rapid technique, is promising for single-molecule sensing in the near future.

2.3 Integration of the signal transduction

The transduction element is essential to get a readable output of the detection occurred on the sensing element. The requirement of transduction equipment limits the scaling down of the sensing device, and thus its portability. Often, although the miniaturisation of the recognition element part is achieved, the need for non-miniaturised external equipment for signal transduction increases the dimensions of the final system, and it also limits the usefulness of the device.

There are five main transduction mechanisms, used in literature, for sensing: optical, electrochemical, piezoelectric, magnetic and thermometric. They present very different sensing and transduction requirements as reviewed below.

2.3.1 Optical biosensors

Optical biosensors are commonly used for the development of microsystems. They require an optical transducer to interpret the output of the sensing element as a readable signal, such as a refractometer, spectrometer, interferometer, camera/microscope, angular displacement transducer, among others.

Nevertheless, some optical biosensors involve a reaction that produces a colorimetry^{146,158}, fluorescence¹⁵⁹, luminescence^{114,160} or plasmonics^{120,161} signal, detectable by naked eye, which does not require any external output reader. This greatly reduces the overall size of the biosensing system, reaching to the generation of microsystems. However, the miniaturisation of the receptor element carries a harder perception of the signal by eye, requiring the use of a magnifying device such as a microscope. Optical biosensors are divided in three groups, depending on their following transduction mechanism: absorption, luminescence and resonance.

Absorption-based sensors are selective, safe, and user friendly, but they present some drawbacks in terms of ambient light interfering during measurement, long-term stability and limited dynamic range¹⁶². In particular, colorimetric sensors are extensively used for rapid biosensing¹⁶³⁻¹⁶⁵. Colorimetry presents several advantages compared to other methods, such as low cost, qualitative or semi-quantitative identification by naked eye, and simple instrument requirements (no instruments for naked eye and potential adaptation to smartphone technology for data analysis). Compared to other absorption methods that require external equipment for the signal transduction, colorimetry facilitates autonomy, portability, remote sensing and miniaturisation of integrated monitoring microsystems. Besides, the manufacturing of miniaturised colorimetric sensors is compatible with simple fabrication methods (*e.g.* inkjet printing, screen printing...), and the performance of the sensor, the data collection and the analysis are commonly user friendly¹⁶⁶. For instance, Fraser *et al.* developed a microfluidic device for the colorimetric diagnosis of malaria disease via an aptamer-tethered enzyme capture assay on chip¹⁶⁴. The detection was monitored with a mobile phone (Figure 2.11A).

Luminescence relies on the emission of light by a material as a consequence of energy absorption from a source like a chemical reaction, UV light, electrical inputs, among others. Luminescent sensors emit light as the detection output. After the material is excited by the energy source, it goes back to the unexcited state, emitting light. These sensors are often more sensitive than absorption based sensors, allowing further miniaturisation of the devices. In particular, fluorescent sensors are traditionally used in miniaturised devices, because the signal is directly measured, relative to a dark background, enabling the detection of low levels of fluorescence ¹⁶⁶. Fluorescence is the most common technique in bioassays, being also a useful tool for point-of-care diagnostics. As an example, the work of Natajaran *et al.*, who developed a fluorescent point-of-care device for the diagnosis of acute myocardial infarction ¹⁶⁷. Nevertheless, fluorescent microsystems require external specific tools for data interpretation, which limits the overall size reduction of the platform, besides materials with self-fluorescence may condition the performance of the biosensor. When considering the background signal, within luminescent sensors, chemiluminescent sensors present excellent signal to noise ratios for low intensity samples ¹⁶⁸. Several efforts have been made towards the miniaturisation and integration of chemiluminescent assays in microfluidic systems ¹⁶⁹⁻¹⁷¹. It is worth mentioning the work reported by Hu *et al.* ¹⁷¹ about a portable microfluidic device to perform chemiluminescent immunoassays, which showed good reproducibility and high sensitivity for C-reactive protein and testosterone. Automated digital microfluidics have also been combined with chemiluminescence ¹⁷². In this case, the device was entirely controlled with a smartphone App, including an integrated image processing system to solve the non-uniformity luminescence problems on the pictures taken by the smartphone.

Finally, resonance-based sensors such as plasmonics, are becoming very popular

due to their label-free detection capabilities, high sensitivity, real-time monitoring possibilities and the sensing platform reusability¹⁷³. In SPR, when the electrons of a metal surface are excited by an incident light, a small change in reflective index happens, which can be measured with a spectrophotometer^{174,175} or by naked eye^{176,177}, offering great possibilities for miniaturisation and portability when integrated into a microfluidic device^{178,179}. For example, a Lab-on-a-disc device was developed for the quantitative detection of IgG by SPR, using a smartphone camera (Figure 2.11B)¹⁷⁸. The authors immobilised anti-IgG on a gold surface integrated in a lab-on-a-disc, and performed the detection of IgG, showing great potential to be used for biosensing through the immobilisation of other bioconjugates. In another interesting work, Dipalo *et al.*¹⁸⁰ presented a microsystem for the monitoring of extra- and intercellular events from hiPSC-derived cardiac cells under drug effects using plasmonic metaelectrodes. They developed a planar and porous electrode with double functionality: it worked as an electrode, and mimicked the optical and biological behaviour of three-dimensional plasmonic antennas, which enabled the simultaneous monitoring of thousands of cells applying a laser scan.

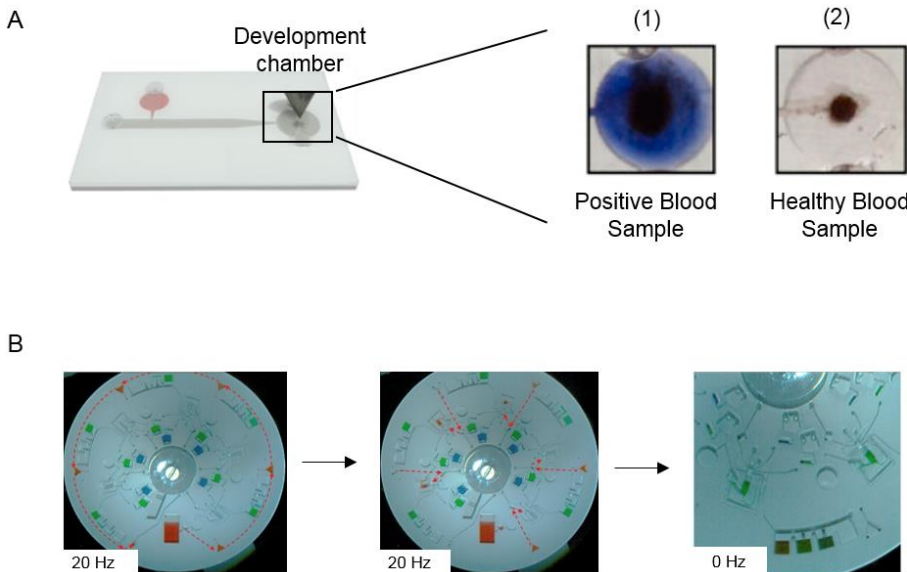


Figure 2.11. A) On the left, the performance of the microfluidic colorimetric biosensor for malaria diagnosis. The aptamer coated magnetic beads were magnetically moved to the development chamber, where the interaction between the aptamer and the parasite protein PfLDH resulted in the generation of diformazan purple dye. On the right, images of the colorimetric results of two tested blood samples: a *Plasmodium falciparum* malaria positive (1) and a negative result from a healthy patient (2)¹⁶⁴. B) Pictures of the lab-on-a-disc performance, where red, blue and green colours were used for sample, washing and SPR measuring buffers, respectively. Left, plasma aliquoting and metering; middle, centripetal pumping of sample to the reaction chamber and right, eventual measurement of the IgG detection¹⁷⁸.

2.3.2 Electrochemical biosensors

In electrochemical biosensors, the analyte reacts on the sensor generating an electrical signal, which is proportional to the analyte concentration, or characteristic for a specific analyte. Electrochemical biosensors are well-

established, and they stand out for their robustness, easy miniaturisation, high sensitivity and possible label-free detection ¹⁸¹. They usually measure the detection in terms of amperometry, potentiometry or impedometry.

Amperometry involves the measurement of current under a constant potential ¹⁴⁵. Amperometric biosensor are widely used for enzymatic biosensing, measuring the output of a redox reaction occurring on the working electrode ^{27,105}. Kaur *et al.* reported an amperometric microfluidic device for cholesterol monitoring using nickel oxide modified platinum working electrodes ²⁷. Moreover, challenging detection of molecules such as 16S ribosomal RNA, was reported by amperometry, with no need of any previous amplification ²³. In that work, authors identified pathogens via 16S ribosomal RNA with a compact and portable amperometric device (2.5 x 7.5 cm) consisting of 16 sensors.

In potentiometry, the electrical potential difference between two electrodes connected by an electrolyte is measured. Potentiometric biosensors are label-free, robust, easy to use and highly sensitive ¹⁸², and they have been used to detect the activity of immobilised microorganisms ^{183,184} or enzymes ^{185,186} that react with the target analyte. For example, a transducer composed of two layers was reported for the potentiometric quantitative detection of phenols in honey and propolis ¹⁸⁶. Particularly, in zero current potentiometry, instead of measuring the change in the redox potential, the technique detects the change in interfacial potential ¹⁸⁷. Zero current potentiometry has also enabled the challenging monitoring of DNA hybridisation with no previous label or modification of the target, based on its effect on the interfacial potential ¹⁸⁸.

Finally, impedimetry involves the measurement of the electric opposition or impedance of a system when an alternating current is applied. Impedimetric biosensors are usually compatible with biosystems due to the low voltages used

for impedance measurements and the label-free capability of the technique. They are widely used for the monitoring of biological events at the electrode/electrolyte interface^{189,190}, and have been applied from the quantitative monitoring of cellular processes^{191,192}, to the label-free detection of specific cells^{34,106} and proteins¹⁹³. Recently, Ghassemi *et al.* reported an impedance based biosensor for the detection and quantification of circulating tumour cells via deformability impedance cytometry³⁴ (Figure 2.12).

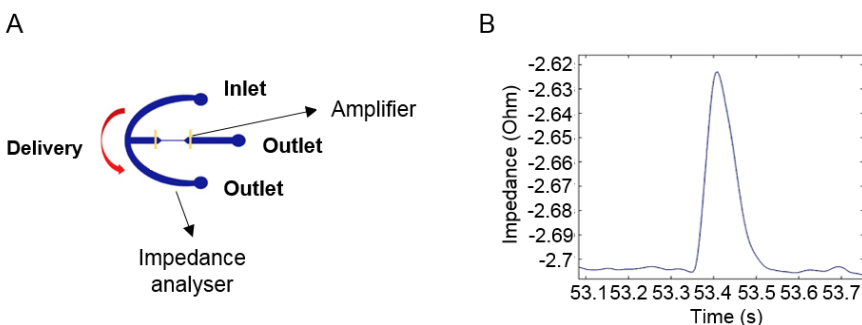


Figure 2.12. A) Design of the device for the analysis of circulating tumour cells by deformability impedance spectroscopy. B) Impedance *versus* time plot showing an example of the impedance value obtained for a single cancer cell³⁴.

2.3.3 Piezoelectric biosensors

Piezoelectric sensors are useful tools for label-free biosensing, and they are traditionally made of anisotropic crystals. Two electrodes apply an alternating voltage on the surface of the biosensor, causing oscillations on the crystal frequency. When an analyte attaches to the crystal surface, it results in a change in oscillation frequency, which is measured as the output of the detection¹⁹⁴.

The Quartz Crystal Microbalance (QCM) is the most common miniaturised piezoelectric biosensor, due to its well-established fabrication and label-free

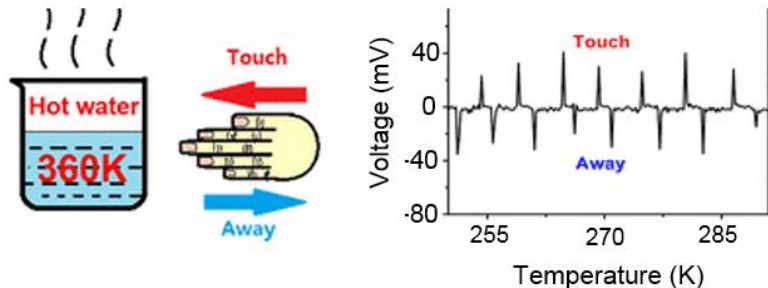
detection. QCM is a highly sensitive mass balance, which permits precise measurements at the micro- and nanogram level. It is comprised of a thin quartz disc with electrodes on the opposite side. An alternating electric field applied over the electrodes induces oscillation on the quartz crystal at a defined frequency. Addition or removal of mass on the quartz crystal makes the oscillation frequency change, so its monitoring provides information about the interactions occurring at the surface¹⁹⁵. QCM have been widely used for dynamic biosensing, such as cytotoxicity assessment of a vitamin E derivative, to monitor cell adhesion in presence of α -tocopherol amidomalonate¹⁹⁶. Dynamic molecular interactions can also be monitored as demonstrated by Jin *et al.*, who measured real-time molecular recognitions and interactions between damaged DNA and cellular responsive proteins¹⁹⁷.

QCM with dissipation increases sensitivity (more than 200 data points per second)¹⁹⁸, enabling reliable diagnosis of Systemic Lupus Erythematosus. For instance, Asai *et al.* used sputtering and etching techniques on a QCM to create an anodic aluminium oxide nanostructures (holes with diameters of 40, 60 and 80 nm) to increase the surface area of the sensing element, and thus, increase the frequency shift in response to mass-based detection¹⁹⁹.

Piezoelectric biosensors are used in wearables²⁰⁰ or artificial skin^{201,202}, both considered devices for the development of robotics, which can be tuned to measure physical and chemical parameters simultaneously. For instance, a self-powered wearable piezoelectric device was reported as an electronic skin for real-time blood analysis, in which the output obtained by the piezoelectric sensor was employed as a power source for the device and as a sensor to interpret this piezoelectric signal and detect C-reactive proteins via antibody-antigen recognition²⁰⁰. In another interesting publication, Wang *et al.* developed a bionic

single-electrode piezoelectric nano-generator for steady-state pressure sensing and simultaneous monitoring of heat/cold²⁰³ (Figure 2.13).

A



B

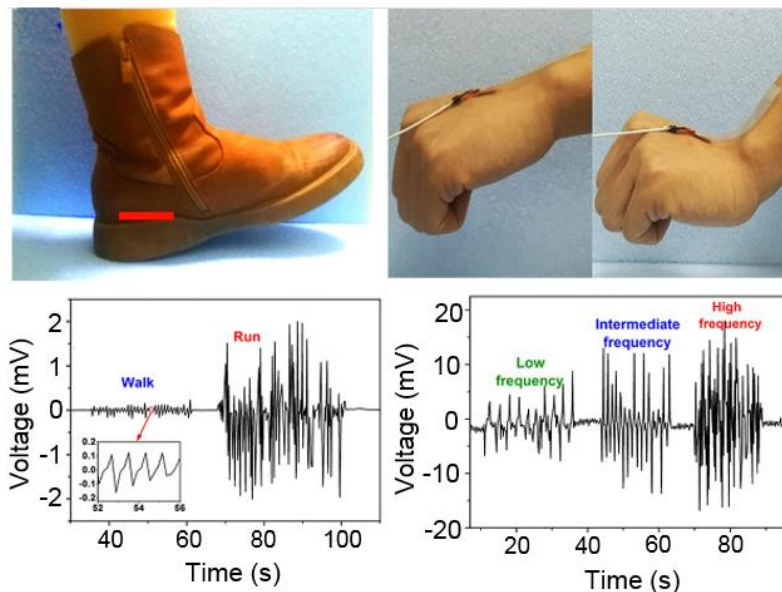


Figure 2.13. A) Scheme of a hand touching and moving away from hot water (87 °C) with an electronic skin and the corresponding output voltage. B) At the top, photographs of the electronic skin on a heel and joint imitating patting a table, walking, running (left) and on a wrist, imitating bending motion (right). At the bottom, graphs corresponding to the activity registered by the electronic skin devices from the top photographs²⁰³.

2.3.4 Magnetic biosensors

Magnetic biosensors present some advantages such as stability over time, lack of background noise, possible remote measurements for point of care applications and high sensitivity²⁰⁴. There are magnetic immunoassays based on a sandwich reaction, and giant magnetoresistance-based immunoassays must be highlighted, which are robust biosensors that detect analytes with high selectivity and sensitivity²⁰⁵. Ferrielectric core-shell magnetoelectric nanoparticles were used as nuclear NMR nanoprobes for cancer cell detection, being capable of distinguishing between different cancer cells²⁰⁶.

Another advantage of magnetism in biosensing microsystems, relies on the specificity of the detection and the ability to make particles move on a sensor towards a specific area, accelerating the interactions between the target molecule or analyte and the receptor element in presence of a magnetic field. In the last decades, the popularity of magnetic nanoparticles in research has exponentially grown for applications such as hyperthermia treatment^{207,208}, targeted drug delivery^{209,210} and as contrast agents in magnetic resonance imaging^{211,212}.

The term magnetoelectronics has emerged lately as a promising tool for miniaturised biosensing devices^{206,213}, and it relies on the incorporation of a ferromagnetic material into an integrated electronic device. This leads to devices with stable magnetisation states and with the possibility of manipulating the “spin” state with voltage or current²¹⁴. For instance, Xi *et al.* reported a magnetoelectric device for the detection and quantification of iron in the liver, based on a superconducting quantum interference device²¹³. Moreover, flexible magnetoelectronics is a recent trend that highlights the impact that magnetic sensing can have in touch-less human-machine interaction²¹⁵. Although it is still in its infancy, there are already several materials for flexible magnetoelectronic

devices such as artificial skins^{216,217}.

2.3.5 Thermometric sensors

Thermometric biosensors measure the temperature of any biological reaction that generates heat, usually using a sensitive thermistor²¹⁸. Enzyme thermistors have become the most popular thermometric biosensors, measuring the heat produced by the activity of immobilised enzymes with improved analytical performance^{219,220}. Although there are few reports of miniaturised thermometric biosensors, in the last five years some successful micro-sized calorimetric or thermometric biosensors have been described²²¹⁻²²⁴.

The encapsulation of enzymes within polymeric microcapsules is getting attention due to the efficiency of the catalytic performance and its detection by thermometry^{223,225}. For instance, Gaddes *et al.* reported an ultrasensitive thermometric sensor comprised of a Y-cut quartz resonator, to measure the activity of encapsulated creatinine deiminase enzyme for the quantification of creatinine²²³ (Figure 2.14). The lack of specificity is a drawback of thermometric sensors, because all enthalpy changes are measured, whether they are caused by the target reaction or not. To address this drawback, Wang *et al.*²²¹ fabricated a cantilever thermocouple structure for the detection of glucose by measuring the catalytic activity of glucose oxidase immobilised on a cantilever.

The measurement of enzymatic activity can also be used to develop sandwich-type thermal immunosensors²²². Bari *et al.* employed a glucose oxidase-conjugated detection antibody for the detection of tumour necrosis factor- α in a microfluidic device. When adding glucose to the media, the glucose oxidase conjugated to the recognition antibody oxidised glucose, releasing heat, which was measured by the thermal sensor.

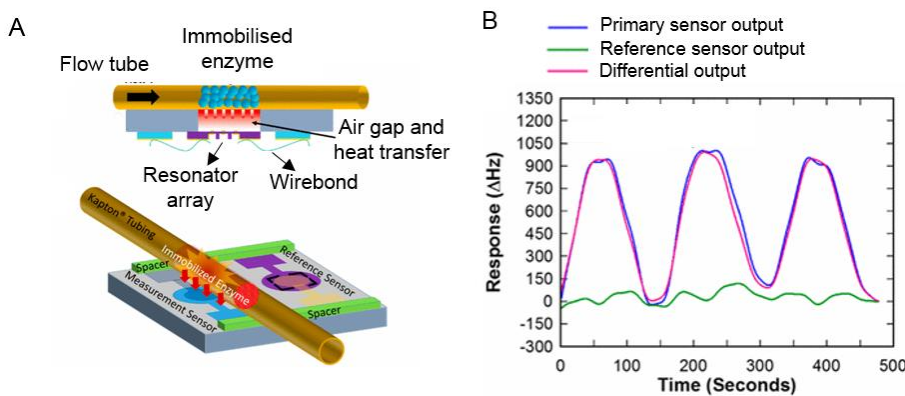


Figure 2.14. A) Schematics of a thermometric biosensor. B) Response of the primary and reference sensors to the binding of 25 mM creatinine solution, as well as the difference between the two sensors ²²³.

2.4 Conclusions

The advances in technology have boosted innovation of miniaturised biosensors, and their integration in LOC devices. The manufacturing and integration of miniaturised sensing elements was achieved decades ago by well established techniques such as lithography and hot embossing, but they require specialised and expensive equipment and trained personnel to be performed. Recent microfabrication trends point out screen printing, inkjet printing and 3D printing as easier microfabrication techniques for miniaturised biosensors. Nevertheless, microtechnology is continuously evolving, reaching higher resolutions, and extending the applicability of each technique to more materials to be used as substrates or as recognition elements.

The miniaturisation of the recognition element plays a key role in the information that can be obtained. For instance, the miniaturisation of metallic materials has led to the fabrication of smaller electrodes capable of detecting challenging

biomolecules like 16S RNA, and to the development of magnetoelectronics, allowing the detection of intrinsic biomagnetic fields of musculature or use negligible magnetic susceptibility of biological samples for biosensing. Regarding polymers, their patterning at the microscale has demonstrated to be more sensitive for sensing, and furthermore, their use for electronic biosensors has opened the door to flexible bioelectronics and organic bioelectronics.

The integration of biomaterials or biomolecules is capital for biosensing. Apart from the combination of biomolecules with other miniaturised sensing materials for the recognition of an analyte, the direct printing of biomolecules on a substrate is a straightforward method for the integration of bio-recognition elements. Suitable designs led to single cell (enabling the quantification of cellular events) or single molecule resolution, with high precision and sensitivity.

Moreover, an overall size decrease of biosensing platforms needs the recognition element and the transducer both, to be scaled down. The adequate selection of the type of sensor is crucial to develop a successful miniaturised biosensor, since each sensor has different requirements and capabilities.

Electrochemical sensors are the most popular, due to their versatility and sensitivity. Screen printing and inkjet printing techniques are lately being used to facilitate the fabrication of electrodes, particularly for flexible electronics. On the other hand, optical biosensors are becoming good alternatives since the signal output can be detected by naked eye, so no transducer element is needed. The sensitivity of optical sensors is higher for smaller recognition structures, but this size reduction compromises naked eye visualisation of the signal. Particularly, plasmonics is emerging as a sensitive tool for biosensing, enabling also naked eye visualisation. On the other hand, piezoelectric biosensors are very sensitive and efficient, but their fabrication is still expensive and time consuming. Although

the use of magnetic biosensors is not very extended, their popularity has grown during the last decade thanks to the technological advances that have facilitated their fabrication, the emergence of magnetic nanomaterials (for anticancer therapies, NMR...) and the possibility to be combined with electronics, leading to sensitive and compact magnetoelectronic biosensors. Finally, thermometric biosensors, although they may be interesting for very particular applications, *e.g.* bioreactions that release heat, they are not widely used for biosensing.

In summary, huge advances have been made in the miniaturisation of biosensing platforms, demonstrating higher sensitivities and easier to use operations. In the way to generate fully integrated LOC devices for biosensing, most of the miniaturised biosensing platforms developed so far require external elements such as flow controllers, transducers or power supplies, being miniaturisation of those elements still a challenge during their fabrication and operation. However, they are already valuable tools to obtain new scientific knowledge, as the ones presented in the following Chapters.

2.5 References

1. Banica, F. Chemical sensors and biosensors: fundamentals and applications; John Wiley & Sons: 2012.
2. Fraden, J. Handbook of modern sensors: physics, designs, and applications; Springer Science & Business Media: 2004.
3. Vyawahare, S.; Griffiths, A. D.; Merten, C. A. Miniaturization and parallelization of biological and chemical assays in microfluidic devices. *Chem. Biol.* 2010, 17, 1052-1065.
4. Derkus, B. Applying the miniaturization technologies for biosensor design. *Biosens. Bioelectron.* 2016, 79, 901-913.
5. Soleymani, L.; Li, F. Mechanistic challenges and advantages of biosensor miniaturization into the nanoscale. *ACS sensors* 2017, 2, 458-467.
6. Galvez, J. M. M.; Garcia-Hernando, M.; Benito-Lopez, F.; Basabe-Desmonts, L.; Shnyrova, A. V. Microfluidic chip with pillar arrays for controlled production and observation of lipid membrane nanotubes. *Lab Chip* 2020, 20, 2748-2755.
7. Garcia-Hernando, M.; Calatayud-Sanchez, A.; Etxebarria-Elezgarai, J.; de Pancorbo, M. M.; Benito-Lopez, F.; Basabe-Desmonts, L. Optical Single Cell Resolution Cytotoxicity Biosensor Based on Single Cell Adhesion Dot Arrays. *Anal. Chem.* 2020, 9658-9665.
8. Gonzalez-Pujana, A.; Santos-Vizcaino, E.; García-Hernando, M.; Hernaez-Estrada, B.; de Pancorbo, M. M.; Benito-Lopez, F.; Igartua, M.; Basabe-Desmonts, L.; Hernandez, R. M. Extracellular matrix protein microarray-based biosensor with single cell resolution: Integrin profiling and characterization of cell-biomaterial interactions. *Sens. Actuator B Chem.* 2019, 299, 126954.
9. Lee, S. J.; Sundararajan, N. Microfabrication for microfluidics; Artech house: 2010.
10. Nawattanapaiboon, K.; Kiatpathomchai, W.; Santanirand, P.; Vongsakulyanon, A.; Amarit, R.; Somboonkaew, A.; Sutapun, B.; Srikririn, T. SPR-DNA array for detection of methicillin-resistant *Staphylococcus aureus* (MRSA) in combination with loop-mediated isothermal amplification. *Biosens. Bioelectron.* 2015, 74, 335-340.
11. Abbott, J.; Ham, D.; Xu, G. All-Electrical Graphene DNA Sensor Array. In *Biosensors and Biodetection* Springer: 2017; pp 169-187.
12. Gogalic, S.; Sauer, U.; Doppler, S.; Preininger, C. Investigating Colorimetric Protein Array Assay Schemes for Detection of Recurrence of Bladder Cancer. *Biosensors* 2018, 8, 10.
13. Chakravarty, S.; Tang, N.; Yan, H.; Yang, C.; Zou, Y.; Shen, Q.; Chen, R. Photonic crystal microarray sensing of breast cancer cell line lysates 2014.
14. Zhang, Y.; Zhao, Y.; Zhou, T.; Wu, Q. Applications and developments of on-chip biochemical sensors based on optofluidic photonic crystal cavities. *Lab Chip* 2018, 18, 57-74.

15. Wittenberg, N. J.; Im, H.; Johnson, T. W.; Xu, X.; Warrington, A. E.; Rodriguez, M.; Oh, S. Facile assembly of micro-and nanoarrays for sensing with natural cell membranes. *ACS nano* 2011, 5, 7555-7564.
16. Peveler, W. J.; Landis, R. F.; Yazdani, M.; Day, J. W.; Modi, R.; Carmalt, C. J.; Rosenberg, W. M.; Rotello, V. M. A rapid and robust diagnostic for liver fibrosis using a multichannel polymer sensor array. *Adv Mater* 2018, 30, 1800634.
17. Ngernpimai, S.; Geng, Y.; Makabenta, J. M.; Landis, R. F.; Keshri, P.; Gupta, A.; Li, C.; Chompoosor, A.; Rotello, V. M. Rapid identification of biofilms using a robust multichannel polymer sensor array. *ACS Appl. Mater. Interfaces* 2019, 11, 11202-11208.
18. Wang, L.; Jackman, J. A.; Tan, E.; Park, J. H.; Potroz, M. G.; Hwang, E. T.; Cho, N. High-performance, flexible electronic skin sensor incorporating natural microcapsule actuators. *Nano Energy* 2017, 36, 38-45.
19. Shen, J.; Pang, J.; Xu, G.; Xin, X.; Yang, Y.; Luan, X.; Yuan, S. Smart stimuli-responsive fluorescent vesicular sensor based on inclusion complexation of cyclodextrins with Tyloxapol. *RSC Adv.* 2016, 6, 11683-11690.
20. Ter Schiphorst, J.; Saez, J.; Diamond, D.; Benito-Lopez, F.; Schenning, A. P. Light-responsive polymers for microfluidic applications. *Lab Chip* 2018, 18, 699-709.
21. Dinh, T.; Nguyen, T.; Phan, H.; Nguyen, T.; Dau, V. T.; Nguyen, N.; Dao, D. V. Advances in rational design and materials of high-performance stretchable electromechanical sensors. *Small* 2020, 16, 1905707.
22. Temiz, Y.; Lovchik, R. D.; Kaigala, G. V.; Delamarche, E. Lab-on-a-chip devices: How to close and plug the lab? *Microelectron. Eng.* 2015, 132, 156-175.
23. Gao, J.; Jeffries, L.; Mach, K. E.; Craft, D. W.; Thomas, N. J.; Gau, V.; Liao, J. C.; Wong, P. K. A multiplex electrochemical biosensor for bloodstream infection diagnosis. *SLAS Technol.* 2017, 22, 466-474.
24. Huertas, C. S.; Domínguez-Zotes, S.; Lechuga, L. M. Analysis of alternative splicing events for cancer diagnosis using a multiplexing nanophotonic biosensor. *Sci. Rep.* 2017, 7, 1-8.
25. Andrews, D.; Nann, T.; Lipson, R. H. Comprehensive nanoscience and nanotechnology; Academic press: 2019.
26. Panzarasa, G.; Soliveri, G. Photocatalytic Lithography. *Appl. Sci.* 2019, 9, 1266.
27. Kaur, G.; Tomar, M.; Gupta, V. Development of a microfluidic electrochemical biosensor: Prospect for point-of-care cholesterol monitoring. *Sens. Actuator B Chem.* 2018, 261, 460-466.
28. Hsu, C.; Su, F.; Peng, P.; Young, H.; Liao, S.; Wang, G. Highly sensitive non-enzymatic electrochemical glucose biosensor using a photolithography fabricated micro/nano hybrid structured electrode. *Sens. Actuator B Chem.* 2016, 230, 559-565.

29. Mei, J.; Li, Y.; Zhang, H.; Xiao, M.; Ning, Y.; Zhang, Z.; Zhang, G. Molybdenum disulfide field-effect transistor biosensor for ultrasensitive detection of DNA by employing morpholino as probe. *Biosens. Bioelectron.* 2018, 110, 71-77.
30. Xu, S.; Zhan, J.; Man, B.; Jiang, S.; Yue, W.; Gao, S.; Guo, C.; Liu, H.; Li, Z.; Wang, J. Real-time reliable determination of binding kinetics of DNA hybridization using a multi-channel graphene biosensor. *Nat. Commun.* 2017, 8, 14902.
31. Tran, T.; Clark, K.; Ma, W.; Mulchandani, A. Detection of a secreted protein biomarker for citrus Huanglongbing using a single-walled carbon nanotubes-based chemiresistive biosensor. *Biosens. Bioelectron.* 2020, 147, 111766.
32. Xu, M.; Yadavalli, V. K. Flexible biosensors for the impedimetric detection of protein targets using silk-conductive polymer biocomposites. *ACS sensors* 2019, 4, 1040-1047.
33. An, L.; Wang, G.; Han, Y.; Li, T.; Jin, P.; Liu, S. Electrochemical biosensor for cancer cell detection based on a surface 3D micro-array. *Lab Chip* 2018, 18, 335-342.
34. Ghassemi, P.; Ren, X.; Foster, B. M.; Kerr, B. A.; Agah, M. Post-enrichment circulating tumor cell detection and enumeration via deformability impedance cytometry. *Biosens. Bioelectron.* 2020, 150, 111868.
35. Someya, T.; Bao, Z.; Malliaras, G. G. The rise of plastic bioelectronics. *Nature* 2016, 540, 379-385.
36. Klauk, H. *Organic electronics II: more materials and applications*; John Wiley & Sons: 2012; Vol. 2.
37. Kudo, H.; Sawada, T.; Kazawa, E.; Yoshida, H.; Iwasaki, Y.; Mitsubayashi, K. A flexible and wearable glucose sensor based on functional polymers with Soft-MEMS techniques. *Biosens. Bioelectron.* 2006, 22, 558-562.
38. Xuan, X.; Yoon, H. S.; Park, J. Y. A wearable electrochemical glucose sensor based on simple and low-cost fabrication supported micro-patterned reduced graphene oxide nanocomposite electrode on flexible substrate. *Biosens. Bioelectron.* 2018, 109, 75-82.
39. Gao, W.; Nyein, H. Y.; Shahpar, Z.; Fahad, H. M.; Chen, K.; Emaminejad, S.; Gao, Y.; Tai, L.; Ota, H.; Wu, E. Wearable microsensor array for multiplexed heavy metal monitoring of body fluids. *Acs Sensors* 2016, 1, 866-874.
40. Kim, H.; Kim, H. Y.; Seok, H.; KANADE, V. K.; Yoo, H.; Park, K.; Lee, J.; Lee, M.; Kim, T. Flexible MoS₂-Polyimide Electrode for Electrochemical Biosensors and their Applications for the highly sensitive Quantification of Endocrine Hormones: PTH, T3, and T4. *Anal. Chem.* 2020.
41. Huang, H.; Ger, T.; Lin, Y.; Wei, Z. Single cell detection using a magnetic zigzag nanowire biosensor. *Lab Chip* 2013, 13, 3098-3104.
42. Presnova, G.; Presnov, D.; Krupenin, V.; Grigorenko, V.; Trifonov, A.; Andreeva, I.; Ignatenko, O.; Egorov, A.; Rubtsova, M. Biosensor based on a silicon nanowire field-effect transistor functionalized by gold nanoparticles for the highly sensitive determination of prostate specific antigen. *Biosens. Bioelectron.* 2017, 88, 283-289.

43. Bakhtina, N. A.; Loeffelmann, U.; MacKinnon, N.; Korvink, J. G. Two-Photon Nanolithography Enhances the Performance of an Ionic Liquid–Polymer Composite Sensor. *Adv. Funct. Mater.* 2015, 25, 1683–1693.
44. Ahn, J.; Kwon, S.; Jung, S.; Lee, W. S.; Jeong, J.; Lim, H.; Shin, Y.; Lee, J. Fabrication of Pyrrole-Based Electrochemical Biosensor Platform Using Nanoimprint Lithography. *Adv. Mater. Interfaces* 2018, 5, 1701593.
45. Mohapatra, S.; Kumari, S.; Moirangthem, R. S. Fabrication of a cost-effective polymer nanograting as a disposable plasmonic biosensor using nanoimprint lithography. *Mater. Res. Express* 2017, 4, 076202.
46. Vazquez-Mena, O.; Sannomiya, T.; Tosun, M.; Villanueva, L. G.; Savu, V.; Voros, J.; Brugger, J. High-resolution resistless nanopatterning on polymer and flexible substrates for plasmonic biosensing using stencil masks. *ACS nano* 2012, 6, 5474–5481.
47. Xia, Y.; Whitesides, G. M. Soft lithography. *Annu. Rev. Mater. Sci.* 1998, 28, 153–184.
48. Fischer, R.; Steinert, S.; Fröber, U.; Voges, D.; Stubenrauch, M.; Hofmann, G.; Witte, H. Cell cultures in microsystems: Biocompatibility aspects. *Biotechnol. Bioeng.* 2011, 108, 687–693.
49. Bélanger, M.; Marois, Y. Hemocompatibility, biocompatibility, inflammatory and in vivo studies of primary reference materials low-density polyethylene and polydimethylsiloxane: A review. *J. Biomed. Mater. Res.* 2001, 58, 467–477.
50. Wang, Y.; Cui, Y.; Cheng, Z.; Song, L.; Wang, Z.; Han, B.; Zhu, J. Poly (acrylic acid) brushes pattern as a 3D functional biosensor surface for microchips. *Appl. Surf. Sci.* 2013, 266, 313–318.
51. Hu, S.; Chen, T.; Zhao, Y.; Wang, Z.; Lam, R. H. Protein–substrate adhesion in microcontact printing regulates cell behavior. *Langmuir* 2018, 34, 1750–1759.
52. Tsai, S.; Goshia, T.; Chen, Y.; Kagiri, A.; Sibal, A.; Chiu, M.; Gadre, A.; Tung, V.; Chin, W. High-throughput label-free microcontact printing graphene-based biosensor for valley fever. *Colloids Surf. B Biointerfaces* 2018, 170, 219–223.
53. Worgull, M. Hot embossing: theory and technology of microreplication; William Andrew: 2009.
54. Partel, S.; Kasemann, S.; Matylitskaya, V.; Thanner, C.; Dincer, C.; Urban, G. A simple fabrication process for disposable interdigitated electrode arrays with nanogaps for lab-on-a-chip applications. *Microelectron. Eng.* 2017, 173, 27–32.
55. Lee, K.; Wu, T.; Hsu, H.; Yang, S.; Wei, P. Low-cost and rapid fabrication of metallic nanostructures for sensitive biosensors using hot-embossing and dielectric-heating nanoimprint methods. *Sensors* 2017, 17, 1548.
56. Partel, S.; Dincer, C.; Kasemann, S.; Kieninger, J.; Edlinger, J.; Urban, G. Lift-off free fabrication approach for periodic structures with tunable nano gaps for interdigitated electrode arrays. *ACS nano* 2016, 10, 1086–1092.

57. MacDougall, A. Screen printing today: The basics; ST Books, a division of Media Group International: 2008.
58. Tudorache, M.; Bala, C. Biosensors based on screen-printing technology, and their applications in environmental and food analysis. *Anal. Bioanal. Chem.* 2007, 388, 565-578.
59. Kim, J.; Imani, S.; de Araujo, W. R.; Warchall, J.; Valdés-Ramírez, G.; Paixão, T. R.; Mercier, P. P.; Wang, J. Wearable salivary uric acid mouthguard biosensor with integrated wireless electronics. *Biosens. Bioelectron.* 2015, 74, 1061-1068.
60. Shi, W.; Li, J.; Wu, J.; Wei, Q.; Chen, C.; Bao, N.; Yu, C.; Gu, H. An electrochemical biosensor based on multi-wall carbon nanotube-modified screen-printed electrode immobilized by uricase for the detection of salivary uric acid. *Anal. Bioanal. Chem.* 2020, 1-9.
61. Jiang, D.; Chu, Z.; Peng, J.; Jin, W. Screen-printed biosensor chips with Prussian blue nanocubes for the detection of physiological analytes. *Sens. Actuator. B Chem.* 2016, 228, 679-687.
62. Rantala, T.; Pirttiaho, L.; Lantto, V. Simulation studies of non-ohmic conductance behaviour in SnO₂ thick-film gas sensors. *Sens. Actuator B Chem.* 1993, 16, 323-327.
63. Galán-Vidal, C. A.; Muñoz, J.; Domínguez, C.; Alegret, S. Glucose biosensor based on a reagentless graphite-epoxy screen-printable biocomposite. *Sens. Actuator B Chem.* 1997, 45, 55-62.
64. Hu, F.; Liu, T.; Pang, J.; Chu, Z.; Jin, W. Facile preparation of porous Co₃O₄ nanocubes for directly screen-printing an ultrasensitive glutamate biosensor microchip. *Sens. Actuator B Chem.* 2020, 306, 127587.
65. Burrell, M. C.; Tilley, M. G. Surface chemistry of polycarbonate film and adhesion of ultraviolet-cured inks. *J. Vac. Sci. Technol.* 1994, 12, 2507-2514.
66. Gonzalez-Macia, L.; Killard, A. Screen printing and other scalable point of care (POC) biosensor processing technologies. In *Medical Biosensors for Point of Care (POC) Applications* Elsevier: 2017; pp 69-98.
67. Kim, J.; Sempionatto, J. R.; Imani, S.; Hartel, M. C.; Barfidokht, A.; Tang, G.; Campbell, A. S.; Mercier, P. P.; Wang, J. Simultaneous monitoring of sweat and interstitial fluid using a single wearable biosensor platform. *Adv. Sci.* 2018, 5, 1800880.
68. Wilson Jr, W. C.; Boland, T. Cell and organ printing 1: protein and cell printers. *Anat. Rec.* 2003, 272, 491-496.
69. Barron, J.; Wu, P.; Ladouceur, H.; Ringisen, B. Biological laser printing: a novel technique for creating heterogeneous 3-dimensional cell patterns. *Biomed. Microdevices* 2004, 6, 139-147.
70. Beduk, T.; Bihar, E.; Surya, S. G.; Castillo, A. N.; Inal, S.; Salama, K. N. A paper-based inkjet-printed PEDOT: PSS/ZnO sol-gel hydrazine sensor. *Sens. Actuator B Chem.* 2020, 306, 127539.

71. Calvert, P. Inkjet printing for materials and devices. *Chem. Mater.* 2001, 13, 3299-3305.
72. Hossain, S. Z.; Luckham, R. E.; Smith, A. M.; Lebert, J. M.; Davies, L. M.; Pelton, R. H.; Filipe, C. D.; Brennan, J. D. Development of a bioactive paper sensor for detection of neurotoxins using piezoelectric inkjet printing of sol-gel-derived bioinks. *Anal. Chem.* 2009, 81, 5474-5483.
73. Yoshioka, Y.; Jabbour, G. E. Inkjet printing of oxidants for patterning of nanometer-thick conducting polymer electrodes. *Adv Mater* 2006, 18, 1307-1312.
74. Pöldsalu, I.; Harjo, M.; Tamm, T.; Uibu, M.; Peikolainen, A.; Kiefer, R. Inkjet-printed hybrid conducting polymer-activated carbon aerogel linear actuators driven in an organic electrolyte. *Sens. Actuator B Chem.* 2017, 250, 44-51.
75. Tijero, M.; Díez-Ahedo, R.; Benito-Lopez, F.; Basabe-Desmonts, L.; Castro-López, V.; Valero, A. Biomolecule storage on non-modified thermoplastic microfluidic chip by ink-jet printing of ionogels. *Biomicrofluidics* 2015, 9, 044124.
76. Chang, S.; Liu, J.; Bharathan, J.; Yang, Y.; Onohara, J.; Kido, J. Multicolor organic light-emitting diodes processed by hybrid inkjet printing. *Adv Mater* 1999, 11, 734-737.
77. Liu, Y.; Li, F.; Xu, Z.; Zheng, C.; Guo, T.; Xie, X.; Qian, L.; Fu, D.; Yan, X. Efficient all-solution processed quantum dot light emitting diodes based on inkjet printing technique. *ACS Appl. Mater. Interfaces* 2017, 9, 25506-25512.
78. Jang, J.; Ha, J.; Cho, J. Fabrication of water-dispersible polyaniline-poly(4-styrenesulfonate) nanoparticles for inkjet-printed chemical-sensor applications. *Adv Mater* 2007, 19, 1772-1775.
79. Lee, H.; Harden-Chaters, W.; Han, S. D.; Zhan, S.; Li, B.; Bang, S. Y.; Choi, H. W.; Lee, S.; Hou, B.; Occhipinti, L. G. Nano-to-Microporous Networks via Inkjet Printing of ZnO Nanoparticles/Graphene Hybrid for Ultraviolet Photodetectors. *ACS Appl. Nano Mater.* 2020, 3, 4454-4464.
80. Trotter, M.; Juric, D.; Bagherian, Z.; Borst, N.; Gläser, K.; Meissner, T.; von Stetten, F. v.; Zimmermann, A. Inkjet-Printing of Nanoparticle Gold and Silver Ink on Cyclic Olefin Copolymer for DNA-Sensing Applications. *Sensors* 2020, 20, 1333.
81. Jensen, G. C.; Krause, C. E.; Sotzing, G. A.; Rusling, J. F. Inkjet-printed gold nanoparticle electrochemical arrays on plastic. Application to immunodetection of a cancer biomarker protein. *Phys. Chem. Chem. Phys.* 2011, 13, 4888-4894.
82. Creran, B.; Li, X.; Duncan, B.; Kim, C. S.; Moyano, D. F.; Rotello, V. M. Detection of bacteria using inkjet-printed enzymatic test strips. *ACS Appl. Mater. Interfaces* 2014, 6, 19525-19530.
83. Díaz-Amaya, S.; Zhao, M.; Lin, L.; Ostos, C.; Allebach, J. P.; Chiu, G. T.; Deering, A. J.; Stanciu, L. A. Inkjet Printed Nanopatterned Aptamer-Based Sensors for Improved Optical Detection of Foodborne Pathogens. *Small* 2019, 15, 1805342.

84. Godoy, N.; García-Lojo, D.; Sigoli, F.; Pérez-Juste, J.; Pastoriza-Santos, I.; Mazali, I. Ultrasensitive inkjet-printed based SERS sensor combining a high-performance gold nanosphere ink and hydrophobic paper. *Sens. Actuator B Chem.* 2020, 128412.
85. Amin, R.; Knowlton, S.; Hart, A.; Yenilmez, B.; Ghaderinezhad, F.; Katebifar, S.; Messina, M.; Khademhosseini, A.; Tasoglu, S. 3D-printed microfluidic devices. *Biofabrication* 2016, 8, 022001.
86. Bustillos, J.; Montero, D.; Nautiyal, P.; Loganathan, A.; Boesl, B.; Agarwal, A. Integration of graphene in poly (lactic) acid by 3D printing to develop creep and wear-resistant hierarchical nanocomposites. *Polym. Compos.* 2018, 39, 3877-3888.
87. Muralidharan, A.; Uzcategui, A. C.; McLeod, R. R.; Bryant, S. J. Stereolithographic 3D Printing for Deterministic Control over Integration in Dual-Material Composites. *Adv. Mater. Technol.* 2019, 4, 1900592.
88. Su, C.; Hsia, S.; Sun, Y. Three-dimensional printed sample load/inject valves enabling online monitoring of extracellular calcium and zinc ions in living rat brains. *Anal. Chim. Acta* 2014, 838, 58-63.
89. Su, C.; Peng, P.; Sun, Y. Fully 3D-printed preconcentrator for selective extraction of trace elements in seawater. *Anal. Chem.* 2015, 87, 6945-6950.
90. Lee, W.; Kwon, D.; Choi, W.; Jung, G. Y.; Au, A. K.; Folch, A.; Jeon, S. 3D-printed microfluidic device for the detection of pathogenic bacteria using size-based separation in helical channel with trapezoid cross-section. *Sci. Rep.* 2015, 5, 7717.
91. Etxebarria-Elezgarai, J.; García-Hernando, M.; Basabe-Desmonts, L.; Benito-Lopez, F. In In 3D printed high quality bechtop microfluidic devices integrating smart materials as sensors; 21st International Conference on Miniaturized Systems for Chemistry and Life Sciences, MicroTAS 2017; 2020, pp 305-306.
92. Park, J. S.; Kim, T.; Kim, W. S. Conductive cellulose composites with low percolation threshold for 3D printed electronics. *Sci. Rep.* 2017, 7, 1-10.
93. Yin, M.; Xiao, L.; Liu, Q.; Kwon, S.; Zhang, Y.; Sharma, P. R.; Jin, L.; Li, X.; Xu, B. 3D printed microheater sensor-integrated, Drug-Encapsulated microneedle patch system for pain management. *Adv. Healthc. Mater.* 2019, 8, 1901170.
94. Udoфia, E. N.; Zhou, W. 3D Printed optics with a soft and stretchable optical material. *Addit. Manuf.* 2020, 31, 100912.
95. Hinman, S. S.; McKeating, K. S.; Cheng, Q. Plasmonic sensing with 3D printed optics. *Anal. Chem.* 2017, 89, 12626-12630.
96. Dong, Y.; Min, X.; Kim, W. S. A 3-D-printed integrated PCB-based electrochemical sensor system. *IEEE Sens. J.* 2018, 18, 2959-2966.
97. Siebert, L.; Lupan, O.; Mirabelli, M.; Ababii, N.; Terasa, M.; Kaps, S.; Cretu, V.; Vahl, A.; Faupel, F.; Adelung, R. 3D-Printed chemiresistive sensor array on nanowire CuO/Cu₂O/Cu heterojunction nets. *ACS Appl. Mater. Interfaces* 2019, 11, 25508-25515.

98. Sharafeldin, M.; Jones, A.; Rusling, J. F. 3D-printed biosensor arrays for medical diagnostics. *Micromachines* 2018, 9, 394.
99. Mortimer Charles, E. Chemistry: A Conceptual Approach. 1975.
100. De Oliveira, I. M.; Pla-Roca, M.; Escriche, L.; Casabó, J.; Zine, N.; Bausells, J.; Teixidor, F.; Crespo, E.; Errachid, A.; Samitier, J. Novel all-solid-state copper (II) microelectrode based on a dithiomacrocycle as a neutral carrier. *Electrochim. Acta* 2006, 51, 5070-5074.
101. Luo, J.; Zhang, M.; Pang, D. Selective and sensitive determination of uric acid at DNA-modified graphite powder microelectrodes. *Sens. Actuator B Chem.* 2005, 106, 358-362.
102. McCarthy, P.; Rao, M.; Otto, K. Simultaneous recording of rat auditory cortex and thalamus via a titanium-based, microfabricated, microelectrode device. *J. Neural Eng.* 2011, 8, 046007.
103. Yang, H.; Rahman, M. T.; Du, D.; Panat, R.; Lin, Y. 3-D printed adjustable microelectrode arrays for electrochemical sensing and biosensing. *Sens. Actuator B Chem.* 2016, 230, 600-606.
104. Abdulbari, H. A.; Basheer, E. A. Electrochemical biosensors: electrode development, materials, design, and fabrication. *ChemBioEng Reviews* 2017, 4, 92-105.
105. Mi, S.; Xia, J.; Xu, Y.; Du, Z.; Sun, W. An integrated microchannel biosensor platform to analyse low density lactate metabolism in HepG2 cells in vitro. *RSC Adv.* 2019, 9, 9006-9013.
106. Abdolahad, M.; Taghinejad, M.; Taghinejad, H.; Janmaleki, M.; Mohajerzadeh, S. A vertically aligned carbon nanotube-based impedance sensing biosensor for rapid and high sensitive detection of cancer cells. *Lab Chip* 2012, 12, 1183-1190.
107. Cai, B.; Huang, L.; Zhang, H.; Sun, Z.; Zhang, Z.; Zhang, G. Gold nanoparticles-decorated graphene field-effect transistor biosensor for femtomolar MicroRNA detection. *Biosens. Bioelectron.* 2015, 74, 329-334.
108. Li, J.; Lee, E. Functionalized multi-wall carbon nanotubes as an efficient additive for electrochemical DNA sensor. *Sens. Actuator B Chem.* 2017, 239, 652-659.
109. Hameed, M. F. O.; Saadeldin, A. S.; Elkaramany, E. M.; Obayya, S. Silicon Nanowires for DNA Sensing. In Computational Photonic Sensors Springer: 2019; pp 321-342.
110. Lu, C.; Huang, P. J.; Liu, B.; Ying, Y.; Liu, J. Comparison of graphene oxide and reduced graphene oxide for DNA adsorption and sensing. *Langmuir* 2016, 32, 10776-10783.
111. Huber, S.; Min, C.; Staat, C.; Oh, J.; Castro, C. M.; Haase, A.; Weissleder, R.; Gleich, B.; Lee, H. Multichannel digital heteronuclear magnetic resonance biosensor. *Biosens. Bioelectron.* 2019, 126, 240-248.
112. Wang, T.; Zhou, Y.; Lei, C.; Luo, J.; Xie, S.; Pu, H. Magnetic impedance biosensor: A review. *Biosens. Bioelectron.* 2017, 90, 418-435.

113. Nakayama, S.; Atsuta, S.; Shinmi, T.; Uchiyama, T. Pulse-driven magnetoimpedance sensor detection of biomagnetic fields in musculatures with spontaneous electric activity. *Biosens. Bioelectron.* 2011, 27, 34-39.
114. Zhang, Q.; Wang, C.; Lv, Y. Luminescent switch sensors for the detection of biomolecules based on metal-organic frameworks. *Analyst* 2018, 143, 4221-4229.
115. Venkatasubramanian, A.; Lee, J.; Stavila, V.; Robinson, A.; Allendorf, M. D.; Hesketh, P. J. MOF@ MEMS: Design optimization for high sensitivity chemical detection. *Sens. Actuator B Chem.* 2012, 168, 256-262.
116. Chen, Q.; Li, X.; Min, X.; Cheng, D.; Zhou, J.; Li, Y.; Xie, Z.; Liu, P.; Cai, W.; Zhang, C. Determination of catechol and hydroquinone with high sensitivity using MOF-graphene composites modified electrode. *J Electroanal Chem* 2017, 789, 114-122.
117. Yang, C.; Denno, M. E.; Pyakurel, P.; Venton, B. J. Recent trends in carbon nanomaterial-based electrochemical sensors for biomolecules: A review. *Anal. Chim. Acta* 2015, 887, 17-37.
118. Kudr, J.; Zhao, L.; Nguyen, E. P.; Arola, H.; Nevanen, T. K.; Adam, V.; Zitka, O.; Merkoçi, A. Inkjet-printed electrochemically reduced graphene oxide microelectrode as a platform for HT-2 mycotoxin immunoenzymatic biosensing. *Biosensors and Bioelectronics* 2020, 156, 112109.
119. Chang, Y.; Venton, B. J. Optimization of graphene oxide-modified carbon-fiber microelectrode for dopamine detection. *Anal. Methods* 2020.
120. Elbahri, M.; Abdelaziz, M.; Homaeigohar, S.; Elsharawy, A.; Keshavarz Hedayati, M.; Röder, C.; El Haj Assad, M.; Abdelaziz, R. Plasmonic Metaparticles on a Blackbody Create Vivid Reflective Colors for Naked-Eye Environmental and Clinical Biodetection. *Adv Mater* 2018, 30, 1704442.
121. Cichosz, S.; Masek, A.; Zaborski, M. Polymer-based sensors: A review. *Polym. Test.* 2018, 67, 342-348.
122. Huang, J.; Li, M.; Zhang, P.; Zhang, P.; Ding, L. Temperature controlling fiber optic glucose sensor based on hydrogel-immobilized GOD complex. *Sens. Actuator B: Chem.* 2016, 237, 24-29.
123. Dong, S.; Ji, W.; Ma, Z.; Zhu, Z.; Ding, N.; Nie, J.; Du, B. Thermosensitive Fluorescent Microgels for Selective and Sensitive Detection of Fe³⁺ and Mn²⁺ in Aqueous Solutions. *ACS Appl. Polym. Mater.* 2020.
124. Shen, H.; Liu, B.; Liu, D.; Zhu, X.; Wei, X.; Yu, L.; Shen, Q.; Qu, P.; Xu, M. Lanthanide coordination polymer-based biosensor for citrate detection in urine. *Anal. Methods* 2019, 11, 1405-1409.
125. Wang, Z.; Qian, Y.; Wei, X.; Zhang, Y.; Wu, G.; Lu, X. An “on-off” electrochemiluminescence biosensor based on molecularly imprinted polymer and recycling amplifications for determination of dopamine. *Electrochim. Acta* 2017, 250, 309-319.

126. Liu, W.; Li, H.; Yu, S.; Zhang, J.; Zheng, W.; Niu, L.; Li, G. Poly (3, 6-diamino-9-ethylcarbazole) based molecularly imprinted polymer sensor for ultra-sensitive and selective detection of 17- β -estradiol in biological fluids. *Biosens. Bioelectron.* 2018, 104, 79-86.
127. Inal, S.; Rivnay, J.; Suiu, A.; Malliaras, G. G.; McCulloch, I. Conjugated polymers in bioelectronics. *Acc. Chem. Res.* 2018, 51, 1368-1376.
128. Pal, R. K.; Farghaly, A. A.; Wang, C.; Collinson, M. M.; Kundu, S. C.; Yadavalli, V. K. Conducting polymer-silk biocomposites for flexible and biodegradable electrochemical sensors. *Biosens. Bioelectron.* 2016, 81, 294-302.
129. Antensteiner, M.; Khorrami, M.; Fallahianbijan, F.; Borhan, A.; Abidian, M. R. Conducting polymer microcups for organic bioelectronics and drug delivery applications. *Adv Mater* 2017, 29, 1702576.
130. Gao, B.; Wang, X.; Li, T.; Feng, Z.; Wang, C.; Gu, Z. Gecko-Inspired Paper Artificial Skin for Intimate Skin Contact and Multisensing. *Adv. Mater. Technol.* 2019, 4, 1800392.
131. Bogue, R. Smart materials: a review of recent developments. *Assem. Autom.* 2012.
132. Lee, M. E.; Armani, A. M. Flexible UV exposure sensor based on UV responsive polymer. *ACS Sensors* 2016, 1, 1251-1255.
133. Zhao, Y.; Lei, M.; Liu, S.; Zhao, Q. Smart hydrogel-based optical fiber SPR sensor for pH measurements. *Sens. Actuator B Chem.* 2018, 261, 226-232.
134. Wang, T.; Liu, J.; Nie, F. Non-dye cell viability monitoring by using pH-responsive inverse opal hydrogels. *J. Mater. Chem. B* 2018, 6, 1055-1065.
135. Yablonovitch, E. Photonic band-gap crystals. *J. Phys. Condens. Matter* 1993, 5, 2443.
136. Endo, T.; Ozawa, S.; Okuda, N.; Yanagida, Y.; Tanaka, S.; Hatsuzawa, T. Reflectometric detection of influenza virus in human saliva using nanoimprint lithography-based flexible two-dimensional photonic crystal biosensor. *Sens. Actuator B Chem.* 2010, 148, 269-276.
137. Ben-Moshe, M.; Alexeev, V. L.; Asher, S. A. Fast responsive crystalline colloidal array photonic crystal glucose sensors. *Anal. Chem.* 2006, 78, 5149-5157.
138. Endo, T.; Ozawa, S.; Okuda, N.; Yanagida, Y.; Tanaka, S.; Hatsuzawa, T. Reflectometric detection of influenza virus in human saliva using nanoimprint lithography-based flexible two-dimensional photonic crystal biosensor. *Sens. Actuator B Chem.* 2010, 148, 269-276.
139. O'Reilly, E.; Kelly, M.; Morrin, A.; Smyth, M. R.; Killard, A. J. Chronocoulometric determination of urea in human serum using an inkjet printed biosensor. *Anal. Chim. Acta* 2011, 697, 98-102.
140. Hibbard, T.; Crowley, K.; Killard, A. J. Direct measurement of ammonia in simulated human breath using an inkjet-printed polyaniline nanoparticle sensor. *Anal. Chim. Acta* 2013, 779, 56-63.

141. Zang, F.; Fan, X. Z.; Gerasopoulos, K. D.; Ben-Yoav, H.; Brown, A. D.; Culver, J. N.; Ghodssi, R. In In Scale-down effects: Towards miniaturization of an electrochemical sensor using biomolecules; *SENSORS*, 2013 IEEE; IEEE: 2013, pp 1-4.
142. Martín, M.; Salazar, P.; Álvarez, R.; Palmero, A.; López-Santos, C.; González-Mora, J. L.; González-Elipe, A. R. Cholesterol biosensing with a polydopamine-modified nanostructured platinum electrode prepared by oblique angle physical vacuum deposition. *Sens. Actuator B Chem.* 2017, 240, 37-45.
143. Moreira, F. T.; Dutra, R. A.; Noronha, J. P.; Sales, M. G. F. Electrochemical biosensor based on biomimetic material for myoglobin detection. *Electrochim. Acta* 2013, 107, 481-487.
144. Draghici, C.; Mikhalevich, V.; Gunkel-Grabole, G.; Kowal, J.; Meier, W.; Palivan, C. G. Biomimetic planar polymer membranes decorated with enzymes as functional surfaces. *Langmuir* 2018, 34, 9015-9024.
145. Dzyadevych, S.; Arkhypova, V.; Soldatkin, A.; El'Skaya, A.; Martelet, C.; Jaffrezic-Renault, N. Amperometric enzyme biosensors: Past, present and future. *Irbm* 2008, 29, 171-180.
146. Jiang, Y.; Shi, M.; Liu, Y.; Wan, S.; Cui, C.; Zhang, L.; Tan, W. Aptamer/AuNP biosensor for colorimetric profiling of exosomal proteins. *Angew. Chem. Int.* 2017, 56, 11916-11920.
147. Jose, B.; McCluskey, P.; Gilmartin, N.; Somers, M.; Kenny, D.; Ricco, A. J.; Kent, N. J.; Basabe-Desmonts, L. Self-powered microfluidic device for rapid assay of antiplatelet drugs. *Langmuir* 2016, 32, 2820-2828.
148. Melero, C.; Kolmogorova, A.; Atherton, P.; Derby, B.; Reid, A.; Jansen, K.; Ballestrem, C. Light-Induced Molecular Adsorption of Proteins Using the PRIMO System for Micro-Patterning to Study Cell Responses to Extracellular Matrix Proteins. *JoVE* 2019, e60092.
149. Zhang, Y.; De Mets, R.; Monzel, C.; Acharya, V.; Toh, P.; Chin, J. F. L.; Van Hul, N.; Ng, I. C.; Yu, H.; Ng, S. S. Biomimetic niches reveal the minimal cues to trigger apical lumen formation in single hepatocytes. *Nat. Mater.* 2020, 1-10.
150. Khan, E. S.; Sankaran, S.; Paez, J. I.; Muth, C.; Han, M. K.; del Campo, A. Photoactivatable Hsp47: a tool to regulate collagen secretion and assembly. *Adv. Sci.* 2019, 6, 1801982.
151. Pavlou, G.; Touquet, B.; Vigetti, L.; Renesto, P.; Bougdour, A.; Debarre, D.; Balland, M.; Tardieu, I. Coupling Polar Adhesion with Traction, Spring and Torque Forces Allows High Speed Helical Migration of the Protozoan Parasite Toxoplasma. *ACS Nano* 2020.
152. van Dongen, S. F.; Maiuri, P.; Marie, E.; Tribet, C.; Piel, M. Triggering cell adhesion, migration or shape change with a dynamic surface coating. *Adv Mater* 2013, 25, 1687-1691.

153. Koirala, D.; Shrestha, P.; Emura, T.; Hidaka, K.; Mandal, S.; Endo, M.; Sugiyama, H.; Mao, H. Single-Molecule Mechanochemical Sensing Using DNA Origami Nanostructures. *Angew. Chem.* 2014, 126, 8275-8279.
154. Sajfutdinow, M.; Uhlig, K.; Prager, A.; Schneider, C.; Abel, B.; Smith, D. Nanoscale patterning of self-assembled monolayer (SAM)-functionalised substrates with single molecule contact printing. *Nanoscale* 2017, 9, 15098-15106.
155. Spitzberg, J. D.; Zrehen, A.; van Kooten, X. F.; Meller, A. Plasmonic-Nanopore Biosensors for Superior Single-Molecule Detection. *Adv Mater* 2019, 31, 1900422.
156. Sun, H.; Jiang, Z.; Xin, N.; Guo, X.; Hou, S.; Liao, J. Efficient Fabrication of Stable Graphene-Molecule-Graphene Single-Molecule Junctions at Room Temperature. *ChemPhysChem* 2018, 19, 2258-2265.
157. Lum, W.; Gautam, D.; Chen, J.; Sagle, L. B. Single molecule protein patterning using hole mask colloidal lithography. *Nanoscale* 2019, 11, 16228-16234.
158. Chen, Z.; Lin, Y.; Ma, X.; Guo, L.; Qiu, B.; Chen, G.; Lin, Z. Multicolor biosensor for fish freshness assessment with the naked eye. *Sens. Actuator B Chem.* 2017, 252, 201-208.
159. Hou, L.; Qin, Y.; Li, J.; Qin, S.; Huang, Y.; Lin, T.; Guo, L.; Ye, F.; Zhao, S. A ratiometric multicolor fluorescence biosensor for visual detection of alkaline phosphatase activity via a smartphone. *Biosens. Bioelectron.* 2019, 143, 111605.
160. Peng, T.; Wang, J.; Zhao, S.; Zeng, Y.; Zheng, P.; Liang, D.; Mari, G. M.; Jiang, H. Highly luminescent green-emitting Au nanocluster-based multiplex lateral flow immunoassay for ultrasensitive detection of clenbuterol and ractopamine. *Anal. Chim. Acta* 2018, 1040, 143-149.
161. Karami, C.; Mehr, S. Y.; Deymehkar, E.; Taher, M. A. Naked eye detection of Cr 3 and Co 2 ions by Gold nanoparticle modified with azomethine. *Plasmonics* 2018, 13, 537-544.
162. Lobnik, A.; Turel, M.; Urek, Š Optical chemical sensors: design and applications; InTech Rijeka, Croatia: 2012.
163. Nam, J.; Jung, I.; Kim, B.; Lee, S.; Kim, S.; Lee, K.; Shin, D. A colorimetric hydrogel biosensor for rapid detection of nitrite ions. *Sens. Actuator B Chem.* 2018, 270, 112-118.
164. Fraser, L. A.; Kinghorn, A. B.; Dirkzwager, R. M.; Liang, S.; Cheung, Y.; Lim, B.; Shiu, S. C.; Tang, M. S.; Andrew, D.; Manitta, J. A portable microfluidic Aptamer-Tethered Enzyme Capture (APTEC) biosensor for malaria diagnosis. *Biosens. Bioelectron.* 2018, 100, 591-596.
165. Liu, X.; Huang, D.; Lai, C.; Qin, L.; Zeng, G.; Xu, P.; Li, B.; Yi, H.; Zhang, M. Peroxidase-Like Activity of Smart Nanomaterials and Their Advanced Application in Colorimetric Glucose Biosensors. *Small* 2019, 15, 1900133.

166. Kangas, M. J.; Burks, R. M.; Atwater, J.; Lukowicz, R. M.; Williams, P.; Holmes, A. E. Colorimetric sensor arrays for the detection and identification of chemical weapons and explosives. *Crit. Rev. Anal. Chem.* 2017, 47, 138-153.
167. Natarajan, S.; Su, F.; Jayaraj, J.; Shah, M. I. I.; Huang, Y. A paper microfluidics-based fluorescent lateral flow immunoassay for point-of-care diagnostics of non-communicable diseases. *Analyst* 2019, 144, 6291-6303.
168. Dodeigne, C.; Thunus, L.; Lejeune, R. Chemiluminescence as diagnostic tool. A review. *Talanta* 2000, 51, 415-439.
169. Inpota, P.; Nacapricha, D.; Sunintaboon, P.; Sripumkhai, W.; Jeamsaksiri, W.; Wilairat, P.; Chantiwas, R. Chemiluminescence detection with microfluidics for innovative in situ measurement of unbound cobalt ions in dynamic equilibrium with bound ions in binding study with polyethyleneimine and its functionalized nanoparticles. *Talanta* 2018, 188, 606-613.
170. Al Mughairey, B.; Al-Lawati, H. A.; Suliman, F. O. Characterization and application of nanocolloidal Mn (IV) in a chemiluminescence system for estimating the total phenolic content in pomegranate juices using a nanodroplet microfluidics platform. *Sens. Actuator B Chem.* 2018, 277, 517-525.
171. Hu, B.; Li, J.; Mou, L.; Liu, Y.; Deng, J.; Qian, W.; Sun, J.; Cha, R.; Jiang, X. An automated and portable microfluidic chemiluminescence immunoassay for quantitative detection of biomarkers. *Lab Chip* 2017, 17, 2225-2234.
172. Zeng, Z.; Zhang, K.; Wang, W.; Xu, W.; Zhou, J. Portable electrowetting digital microfluidics analysis platform for chemiluminescence sensing. *IEEE Sens. J.* 2016, 16, 4531-4536.
173. Li, M.; Cushing, S. K.; Wu, N. Plasmon-enhanced optical sensors: a review. *Analyst* 2015, 140, 386-406.
174. Fu, C.; Hu, C.; Liu, Y.; Xu, S.; Xu, W. Bioidentification of biotin/avidin using surface plasmon resonance and surface-enhanced Raman scattering (SPR-SERS) spectroscopy. *Anal. Methods* 2012, 4, 3107-3110.
175. Barroso, J.; Ortega-Gomez, A.; Calatayud-Sanchez, A.; Zubia, J.; Benito-Lopez, F.; Villatoro, J.; Basabe-Desmonts, L. Selective ultrasensitive optical fiber nanosensors based on plasmon resonance energy transfer. *ACS sensors* 2020.
176. Moitra, P.; Alafeef, M.; Dighe, K.; Frieman, M.; Pan, D. Selective Naked-Eye Detection of SARS-CoV-2 Mediated by N Gene Targeted Antisense Oligonucleotide Capped Plasmonic Nanoparticles. *ACS nano* 2020.
177. Ismail, M.; Khan, M.; Akhtar, K.; Seo, J.; Khan, M. A.; Asiri, A. M.; Khan, S. B. Phytosynthesis of silver nanoparticles; naked eye cellulose filter paper dual mechanism sensor for mercury ions and ammonia in aqueous solution. *J. Mater. Sci. Mater. Electron.* 2019, 30, 7367-7383.
178. Miyazaki, C. M.; Kinahan, D. J.; Mishra, R.; Mangwanya, F.; Kilcawley, N.; Ferreira, M.; Ducrée, J. Label-free, spatially multiplexed SPR detection of immunoassays on a

- highly integrated centrifugal Lab-on-a-Disc platform. *Biosens. Bioelectron.* 2018, 119, 86-93.
179. Špringer, T.; Piliarik, M.; Homola, J. Surface plasmon resonance sensor with dispersionless microfluidics for direct detection of nucleic acids at the low femtomole level. *Sens. Actuator B Chem.* 2010, 145, 588-591.
180. Dipalo, M.; Melle, G.; Lovato, L.; Jacassi, A.; Santoro, F.; Caprettini, V.; Schirato, A.; Alabastri, A.; Garoli, D.; Bruno, G. Plasmonic meta-electrodes allow intracellular recordings at network level on high-density CMOS-multi-electrode arrays. *Nat. Nanotechnol.* 2018, 13, 965-971.
181. Wilson, M. S. Electrochemical immunosensors for the simultaneous detection of two tumor markers. *Anal. Chem.* 2005, 77, 1496-1502.
182. Ding, J.; Qin, W. Recent advances in potentiometric biosensors. *TrAC Trends in Anal. Chem.* 2020, 124, 115803.
183. Ebrahimi, E.; Yazdian, F.; Amoabediny, G.; Shariati, M. R.; Janfada, B.; Saber, M. A microbial biosensor for hydrogen sulfide monitoring based on potentiometry. *Process Biochemistry* 2014, 49, 1393-1401.
184. Rotariu, L.; Bala, C.; Magearu, V. New potentiometric microbial biosensor for ethanol determination in alcoholic beverages. *Anal. Chim. Acta* 2004, 513, 119-123.
185. Yang, Z.; Zhang, C.; Zhang, J.; Bai, W. Potentiometric glucose biosensor based on core-shell Fe₃O₄-enzyme-polypyrrole nanoparticles. *Biosens. Bioelectron.* 2014, 51, 268-273.
186. Draghi, P. F.; Fernandes, J. C. B. Label-free potentiometric biosensor based on solid-contact for determination of total phenols in honey and propolis. *Talanta* 2017, 164, 413-417.
187. Gao, W.; Song, J. Towards surface acid-base property of the carboxylic multi-walled carbon nanotubes by zero current potentiometry. *Electrochim. Commun.* 2009, 11, 1285-1288.
188. Wu, N.; Gao, W.; He, X.; Chang, Z.; Xu, M. Direct electrochemical sensor for label-free DNA detection based on zero current potentiometry. *Biosens. Bioelectron.* 2013, 39, 210-214.
189. Rivnay, J.; Ramuz, M.; Leleux, P.; Hama, A.; Huerta, M.; Owens, R. M. Organic electrochemical transistors for cell-based impedance sensing. *Appl. Phys. Lett.* 2015, 106, 8_1.
190. Steinem, C.; Janshoff, A.; Galla, H.; Sieber, M. Impedance analysis of ion transport through gramicidin channels incorporated in solid supported lipid bilayers. *Bioelectrochem. Bioenerget.* 1997, 42, 213-220.
191. Bird, C.; Kirstein, S. Real-time, label-free monitoring of cellular invasion and migration with the xCELLigence system. *Nat. Methods* 2009, 6, v-vi.

192. Stolwijk, J. A.; Wegener, J. STOLWIJK, Judith A.; WEGENER, Joachim. Impedance-Based Assays Along the Life Span of Adherent Mammalian Cells In Vitro: From Initial Adhesion to Cell Death. En Label-Free Monitoring of Cells in vitro. Springer, Cham, 2019. p. 1-75.
193. Lee, J. A.; Hwang, S.; Kwak, J.; Park, S. I.; Lee, S. S.; Lee, K. An electrochemical impedance biosensor with aptamer-modified pyrolyzed carbon electrode for label-free protein detection. *Sens. Actuator B: Chem.* 2008, 129, 372-379.
194. Pohanka, M. Overview of piezoelectric biosensors, immunosensors and DNA sensors and their applications. *Materials* 2018, 11, 448.
195. Skládal, P. Piezoelectric biosensors. *TrAC Trends Anal. Chem.* 2016, 79, 127-133.
196. Fohlerová, Z.; Turánek, J.; Skládal, P. The cell adhesion and cytotoxicity effects of the derivate of vitamin E compared for two cell lines using a piezoelectric biosensor. *Sens. Actuator B Chem.* 2012, 174, 153-157.
197. Jin, Y.; Xie, Y.; Wu, K.; Huang, Y.; Wang, F.; Zhao, R. Probing the dynamic interaction between damaged DNA and a cellular responsive protein using a piezoelectric mass biosensor. *ACS Appl. Mater. Interfaces* 2017, 9, 8490-8497.
198. Hussain, M.; Northoff, H.; Gehring, F. K. QCM-D providing new horizon in the domain of sensitivity range and information for haemostasis of human plasma. *Biosens. Bioelectron.* 2015, 66, 579-584.
199. Asai, N.; Shimizu, T.; Shingubara, S.; Ito, T. Fabrication of highly sensitive QCM sensor using AAO nanoholes and its application in biosensing. *Sens. Actuator B Chem.* 2018, 276, 534-539.
200. Lei, Y.; Zhao, T.; He, H.; Zhong, T.; Guan, H.; Xing, L.; Liu, B.; Xue, X. A self-powered electronic-skin for detecting CRP level in body fluid based on the piezoelectric-biosensing coupling effect of GaN nanowire. *Smart Mater. Struct.* 2019, 28, 105001.
201. Gogurla, N.; Roy, B.; Kim, S. Self-powered artificial skin made of engineered silk protein hydrogel. *Nano Energy* 2020, 105242.
202. Chung, S. Y.; Lee, H.; Lee, T. I.; Kim, Y. S. A wearable piezoelectric bending motion sensor for simultaneous detection of bending curvature and speed. *Rsc Adv.* 2017, 7, 2520-2526.
203. Wang, X.; Song, W.; You, M.; Zhang, J.; Yu, M.; Fan, Z.; Ramakrishna, S.; Long, Y. Bionic single-electrode electronic skin unit based on piezoelectric nanogenerator. *Acs Nano* 2018, 12, 8588-8596.
204. Nabaei, V.; Chandrawati, R.; Heidari, H. Magnetic biosensors: Modelling and simulation. *Biosens. and Bioelectron.* 2018, 103, 69-86.
205. Krishna, V. D.; Wu, K.; Perez, A. M.; Wang, J. Giant magnetoresistance-based biosensor for detection of influenza A virus. *Front. Microbiol.* 2016, 7, 400.
206. Nagesetti, A.; Rodzinski, A.; Stimpson, E.; Stewart, T.; Khanal, C.; Wang, P.; Guduru, R.; Liang, P.; Agoulnik, I.; Horstmyer, J. Multiferroic coreshell magnetoelectric

- nanoparticles as NMR sensitive nanoprobes for cancer cell detection. *Sci. Rep.* 2017, 7, 1-9.
207. Jordan, A.; Scholz, R.; Wust, P.; Fähling, H.; Felix, R. Magnetic fluid hyperthermia (MFH): Cancer treatment with AC magnetic field induced excitation of biocompatible superparamagnetic nanoparticles. *J Magn Magn Mater* 1999, 201, 413-419.
208. Das, P.; Colombo, M.; Prosperi, D. Recent advances in magnetic fluid hyperthermia for cancer therapy. *Colloid Surf. B* 2019, 174, 42-55.
209. Arruebo, M.; Fernández-Pacheco, R.; Ibarra, M. R.; Santamaría, J. Magnetic nanoparticles for drug delivery. *Nano today* 2007, 2, 22-32.
210. Gao, X.; Zhai, M.; Guan, W.; Liu, J.; Liu, Z.; Damirin, A. Controllable synthesis of a smart multifunctional nanoscale metal-organic framework for magnetic resonance/optical imaging and targeted drug delivery. *ACS Appl. Mater. Interfaces* 2017, 9, 3455-3462.
211. Rohrer, M.; Bauer, H.; Mintorovitch, J.; Requardt, M.; Weinmann, H. Comparison of magnetic properties of MRI contrast media solutions at different magnetic field strengths. *Invest. Radiol.* 2005, 40, 715-724.
212. Du, Y.; Liu, X.; Liang, Q.; Liang, X.; Tian, J. Optimization and design of magnetic ferrite nanoparticles with uniform tumor distribution for highly sensitive MRI/MPI performance and improved magnetic hyperthermia therapy. *Nano letters* 2019, 19, 3618-3626.
213. Xi, H.; Qian, X.; Lu, M.; Mei, L.; Rupprecht, S.; Yang, Q. X.; Zhang, Q. A room temperature ultrasensitive magnetoelectric susceptometer for quantitative tissue iron detection. *Sci. Rep.* 2016, 6, 29740.
214. Johnson, M. Introduction to magnetoelectronics. In *Magnetoelectronics* Elsevier: 2004; pp 1-65.
215. Melzer, M.; Kaltenbrunner, M.; Makarov, D.; Karnaushenko, D.; Karnaushenko, D.; Sekitani, T.; Someya, T.; Schmidt, O. G. Imperceptible magnetoelectronics. *Nat. Commun.* 2015, 6, 1-8.
216. Makarov, D.; Melzer, M.; Karnaushenko, D.; Schmidt, O. G. Shapeable magnetoelectronics. *Appl. Phys. Rev.* 2016, 3, 011101.
217. Sagar, R. U. R.; Galluzzi, M.; García-Peña, A.; Bhat, M. A.; Zhang, M.; Stadler, F. J. Large unsaturated room temperature negative magnetoresistance in graphene foam composite for wearable and flexible magnetoelectronics. *Nano Research* 2019, 12, 101-107.
218. Ramanathan, K.; Danielsson, B. Principles and applications of thermal biosensors. *Biosens. Bioelectron.* 2001, 16, 417-423.
219. Xu, N.; Bai, J.; Peng, Y.; Qie, Z.; Liu, Z.; Tang, H.; Liu, C.; Gao, Z.; Ning, B. Pretreatment-free detection of diazepam in beverages based on a thermometric biosensor. *Sens. Actuator B Chem.* 2017, 241, 504-512.

Chapter 2

220. Yakovleva, M.; Buzas, O.; Matsumura, H.; Samejima, M.; Igarashi, K.; Larsson, P.; Gorton, L.; Danielsson, B. A novel combined thermometric and amperometric biosensor for lactose determination based on immobilised cellobiose dehydrogenase. *Biosens. Bioelectron.* 2012, 31, 251-256.
221. Wang, Z.; Kimura, M.; Ono, T. Manufacturing and characterization of simple cantilever thermal biosensor with Si-Metal thermocouple structure for enzymatic reaction detection. *Thermochim. Acta* 2018, 668, 110-115.
222. Bari, S. M. I.; Reis, L. G.; Nestorova, G. G. Calorimetric sandwich-type immunosensor for quantification of TNF- α . *Biosens. Bioelectron.* 2019, 126, 82-87.
223. Gaddes, D.; Reeves, W. B.; Tadigadapa, S. Calorimetric biosensing system for quantification of urinary creatinine. *ACS sensors* 2017, 2, 796-802.
224. Kazura, E.; Mernaugh, R.; Baudenbacher, F. A Capillary-Perfused, Nanocalorimeter Platform for Thermometric Enzyme-Linked Immunosorbent Assay with Femtomole Sensitivity. *Biosensors* 2020, 10, 71.
225. Wang, Z.; Kimura, M.; Inomata, N.; Ono, T. In In A freestanding microfluidic-based thermocouple biosensor for enzyme-catalyzed reaction analysis; 2016 IEEE 11th Annual International Conference on Nano/Micro Engineered and Molecular Systems (NEMS); IEEE: 2016, pp 58-61.

3

Precise Integration of Polymeric Functional Materials in 3D Printed Microfluidic Devices

This chapter presents a new architecture concept for microfluidic devices, which combines the conventional 3D printing integrating specific architectures with *in situ* polymerisation. The approach leads to the stable and precise integration of polymeric functional materials in small footprints within microchannels, solving the assembly errors that normally occur during their integration. The method was demonstrated embedding four pH sensing ionogel microstructures along the main channel of a complex 3D printed microfluidic device, for a colour barcode pH detection, which highly enhanced the adhesion force of the microstructures of diverse chemical composition to the 3D printed microfluidic channel. The performance of this sensor was investigated using image analysis of the colour variations obtained from photographs taken with a conventional camera.

*Parts of this Chapter have been published in: Etxebarria-Elezgarai, J., Garcia-Hernando, M., Basabe-Desmonts, L., & Benito-Lopez, F. 3D printed high quality benchtop microfluidic devices integrating smart materials as sensors, paper presented at the 21th International Conference on Miniaturized Systems for Chemistry and Life Sciences, Micro-TAS 2017, 2020, pp. 305 – 306.

3.1 Introduction

During the last two decades, many efforts have been done in order to reduce the size of analytical components, in order to further miniaturise microfluidic devices. In this scaling down process, the size of the sensing element of an analytical device is critical. Miniaturisation of the sensing elements within microfluidic devices increases the ratio between the surface-area and the volume of the sensors, resulting in improved diffusion and enhanced mass transfer through the sensing materials, accelerating response times¹. This size reduction requires smaller sample volume, provides accurate control of fluid flow and ensures a homogeneous distribution of species all along the sensor², guaranteeing a highly controllable environment for analysis, chemically speaking, when compared to traditional sensors. Miniaturisation also allows multiplexing by having a number of micro-sensors in a controlled area, for the simultaneous sensing of different species, or to perform the same reaction in parallel with many sensors^{3,4}. Multiplexing can also lead to barcode sensing, in which the final result of the analysis comes from the combination of all the sensing outputs⁵.

As explained in the previous chapter, micromachining enables the integration of miniaturised sensors through fabrication, which often imply the use of expensive and specialised equipment, as well as tedious and long fabrication protocols. Therefore, there is still a lack of truly integrative strategies that are simple to implement and that enable functional materials to be adequately coupled within hybrid polymeric LOC devices⁶. 3D printing technology is gaining attraction over similar techniques used for the integration of materials or reagents within microfluidic devices, such as inkjet printing⁷ or non-contact microarrays⁸. 3D printing technology enables rapid design iterations and fast optimisation during

the development of the technology, offering great advantages over traditional microfabrication techniques such as photolithography, soft lithography, xurography, hot embossing, *etc.*⁹

The versatility of 3D printing extends its use in very different fields, from assembly-free fluidic valves and pumps within 3D printed microfluidic devices⁹, to the printing of materials for 3D cell culture with customised cell distribution, heterogeneity or tissue-specific functions¹⁰. Such approaches are successful for the printing of multiple materials, but they require modifications of the printers or the chemical composition of the material to be printed, to adapt them to the specific fabrication needs, which complicate and increase fabrication costs. Actually, the majority of the integration techniques require long and expensive fabrication procedures, and/or chemical or physical surface treatments to enable successful integration when plastic devices are used, or when the adhesion of hydrophilic materials on polymers is not optimal^{11..}.

Recent developments in portable and disposable analytical instrumentation reveal an increasing interest in the integration of sensing smart materials¹³⁻¹⁵ and functional materials¹⁶⁻¹⁸ in microfluidic systems. These materials provide new functionalities for *in situ* operations, and fulfil the needs of more autonomous and easy-to-use devices, which may allow lower energy consumptions, and thus, improved operability over traditional benchtop and microfluidic systems^{2,19}. Ionogels (IOs) are polymeric hybrid materials, which are attractive for sensing applications²⁰. They incorporate an ionic liquid (IL), which gives a polymeric network that combines the properties of both, the three-dimensional solid structure of the hydrogel and the immobilised IL. ILs present interesting properties such as negligible vapour pressure, and often, high solvation power, being able to dissolve substances that are difficult to dissolve in conventional

solvents (monomers, cross-linkers...) ²⁰. IL family is composed by ILs of variable nature, depending on the anion and the cation of the IL molecule, so they can strongly change the chemical and physical properties of the ionogel ²¹. This 3D network enables the integration of other molecules within it, which can provide with new functionalities to the polymers ^{19,22}. In this chapter, a pH dye is added to the ionogel to acquire a functional poly(*N*-isopropylacrylamide) (pNIPAAm) polymer for colorimetric pH sensing.

Colorimetric sensors allow to interpret the output either by naked eye or by using optical instruments, so their simplicity and versatility facilitate their implementation in microfluidic and portable devices. While other common signal outputs require specific instrumentation for the readout, colorimetry offers a more affordable and user-friendly approach with adequate data collection and digital imaging analysis ²³. Data analysis systems based in three basic colours such as the RGB system, are the most popular, but they may result in loss of information and diminishment of the robustness of the signal. HSV colorimetry system is a transformation of RGB, where the hue component (*H*) defines the colour, and it is represented with a number from 0 to 360 that corresponds to a position on a colour space coordinate diagram, defining a unique and precise colour. The other two coordinates of the system correspond to intensity (*S*) and darkness (*V*). Hue is stable and easy to calculate, which makes it promising for colorimetry sensing applications such as microfluidic analytical devices ²⁴.

Considering the technological limitations during the integration of functional materials within microfluidic devices, I present an especially designed microfluidic architecture. It allows the easy integration of multiple materials in discrete zones with controlled dimensions within 3D printed microfluidic

devices, avoiding assembly errors. The fabrication combines a smart design strategy as T-shape cavities for the easy integration of the material and photopolymerisation, leading to the *in situ* and precise integration of functional materials, with no need of surface functionalisation. The T-shaped cavities solve the issue of the complicated and tedious integration of functional materials – hydrophilic and hydrophobic- into 3D printed microchannels without any surface functionalisation, simplifying the manufacturability of analytical hybrid microfluidic devices. As a proof of principle, the proposed system was used to embed four pH sensing ionogels of different chemical compositions, in order to provide pH measurements over a wide range of pH values and within the microchannels of hybrid microfluidic devices.

3.2 Results and Discussion

3.2.1 Device architecture

A scheme of the design and a real picture of the microfluidic device is depicted in Figure 3.1A and Figure 3.1B. The device featured internal microfluidic channels directly connected to external connectors. The adjacent integration channels and the main microfluidic channel were connected using three-dimensional T-shaped cavities that allowed the pipetted material to be embedded and anchored on the walls of the reservoirs fabricated on the bottom side of the main microchannel, Figure 3.1C. A Y-shaped channel and a serpentine were included at the inlet to enable simultaneous injection and mixing of two reagents, so that chemical reactions could be performed inside the meandering channel section, located before the sensing zones of the device. A Pressure Sensitive Adhesive (PSA) layer was added on the top to seal the device.

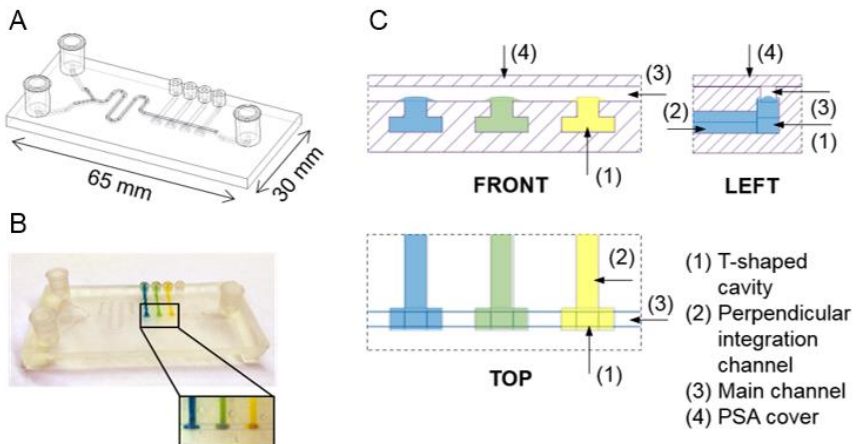


Figure 3.1. A) 3D model design of the microfluidic device. B) Picture of the 3D printed device with integrated pH sensing. C) Illustration of the integration system, showing the main microfluidic channel, the T-shaped cavities and the perpendicular integration channel connecting both of them, as well as the PSA layer to close the main channel.

3.2.2 Microfluidic device fabrication

The printing process was optimised to enable internal and superficial channels and internal T-shaped features, by means of a conventional stereolithography 3D printing method, Figure 3.2. As shown in a previous work²⁵, the model orientation and the supporting structures are of utmost importance to generate successful printings of complex features containing internal cavities. Supporting structures were found to be important to give physical support to the desired 3D printed features and to avoid shrinkage and compression of bottom layers in case of models that contain a flat surface. Therefore, an incorrect orientation of any of the parts led to internal microchannel clogging, thus a proper orientation was necessary to enable the draining of the uncured resin trapped inside the microstructures. Figure 3.3 shows an adequate orientation and supporting

structures for a model that resulted in satisfactory 3D printed device features. In this case, the most critical features -with the deepest cavities- were placed in the uppermost plane, so they were printed at the last moment, to avoid the clogging of cavities. The printing time and removal of the uncured resin before bringing the printed part to ambient light was also considered, to avoid clogging of the internal structures.

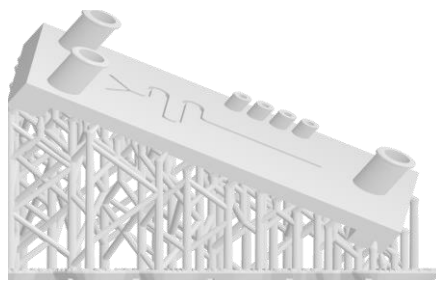


Figure 3.2. Image of a printing model including a supporting structure and proper model orientation. Supports avoid compression tension at the bottom layers closest to the built platform. The model was oriented placing the most critical structures and longest internal micro-channels in the uppermost location, allowing the uncured resin to drain.

The microfluidic structures could also be fabricated by other microfabrication techniques such as lamination or the popular soft lithography, but these are more laborious and require precise alignment and bonding of more than one part to construct the device. In addition, due to the high hydrophobicity of PDMS, in our experience, ionogels strongly interact with this elastomer, repelling it and thus, avoiding attachment to it, which would complicate filling the integration channels. 3D printing is based on loading the CAD design and waiting for the result, which facilitates any possible change needed in the design, while for techniques like soft lithography a design change means the addition of long fabrication steps after the modification of the CAD design. The lack of alignment

steps to seal the device is also a major advantage of 3D printing, which in this case just required a polishing step to smoothen the material's surface and the adhesion of a PSA layer to close the channel.

The use of an open channel aimed to increase the transparency of the device in the positions where colorimetric measurements need to be carried out. This type of resin is highly transparent after fabrication, but it suffers from aging over time, developing a yellowish colour ²⁶. This reduces considerably the transparency of the material, so the colour measurements would not be accurate over time. Although several 3D printable resins are catalogued as optically clear, such as the FLGP CL02 resist, which is the one used in this chapter, their transparency depends on the roughness of the surface of the device and of the internal channel walls, making these materials translucent at the best, but not transparent ²⁷. Therefore, in order to avoid the mentioned transparency issues, the open microfluidic channel was fabricated and subsequently sealed using PSA to enhance optical transparency. PSA is a transparent film that is not supposed to lose transparency, and in case it is damaged, it can be easily replaced by another PSA layer for the same device.

3.2.3 Integration of pH sensitive ionogels in a 3D printed microfluidic device

The strategy to integrate functional materials in 3D printed microfluidic relies on the combination of T-shape cavities with the UV curable functional materials. This method facilitates the precise positioning of the sensing materials inside the microfluidic channel without the need of using complex 3D printing processes or multiple materials' addition or spotters.

To evaluate the efficacy of the proposed strategy, the shape and adhesion

strength of ionogels loaded and polymerised within T-shaped anchoring structures or directly on the surface of a rectangular microfluidic channel (Figure 3.3A) were compared. Four different ionogels were tested, each of them with a pH indicator: bromocresol green (BG), bromocresol purple (BP), phenol red (PR) and phenolphthalein (Ph). BG, PR and Ph polymerised in the presence of 1-ethyl-3-methylimidazolium ethyl sulphate (EMIES) IL, and BP with trihexyltetradecylphosphonium dicyanamide (DCA) IL. The same volume of the four pH sensitive ionogels was added in both, the conventional rectangular channel and in the T-shape cavities. After UV-polymerisation of the ionogels, the microfluidic channels were closed with a PSA layer, and the device was connected to a pump for flow control. Well defined and regular ionogel shapes with the T-shape cavities were obtained, however, inhomogeneous sensing sections with different shapes, areas and heights, in the rectangular microchannel were observed (without the T-shape cavities) after ionogel polymerisation.

To test the adhesion of the gels within the microfluidic channel, an increasing flow from 100 to 600 $\mu\text{L}\cdot\text{min}^{-1}$ was applied. All the ionogels immobilised within the T-shape structures remained attached. On the other hand, in the rectangular channels, the pH sensor containing BP, -which had a hydrophobic ionic liquid (DCA)- easily detached from the microchannel during the rinsing step with distilled water (Figure 3.3B). The other three pH sensors, with the hydrophilic ionic liquid (EMIES), remained attached to the channel surface even after flowing water with increasing flows (Figure 3.3C).

These results demonstrated that the integrated T-shape cavities increased the anchoring capacity of the materials, avoiding surface functionalisation and enabling the integration of sensing zones with a well-defined shape. The T-shaped configuration provided a precise positioning of the pH sensors, with

reproducible sensing areas, previously defined during the microfluidic designing step.

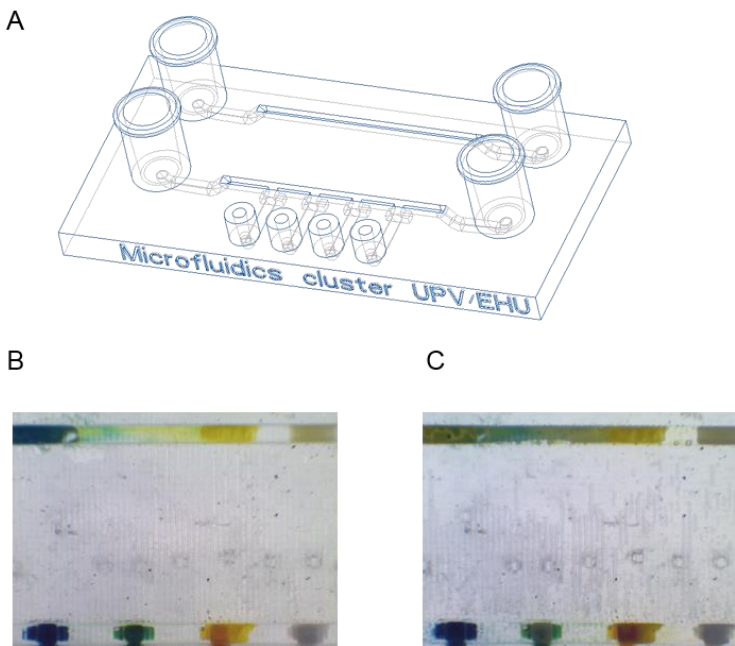


Figure 3.3. Comparison between single rectangular channel architecture (top channel) and T-shaped architecture for sensing array fabrication (bottom channel). A) 3D model representation of the microfluidic device, in which two different 3D printed structures were compared: a simple rectangular channel and the proposed T-shaped well architecture. B) Image showing the integration of the materials right after polymerisation and rinsing with distilled water. C) Image showing the integration of the materials after 2 min flow at $600 \mu\text{L}\cdot\text{min}^{-1}$, $\text{pH} = 6$.

This strategy has important implications, the inhomogeneity of the sensing area impacts on the sensor performance and on the obtained results. This is even more important for colorimetric sensors where the colour distribution on the sensing surface should be homogeneous. Obviously, the sensors generated on the

conventional channels were not able to provide good responses over time and from device to device, leading to a high pH value deviations over equal sensors.

In the case of the pH sensors, the diffusion of protons through the sensing matrix is important to control the response time of the sensor. Therefore, in the nonhomogeneous sensor moieties, their response to pH variations was randomly distributed. On the contrary, the shapes of those pH ionogel sensors generated within the T-shape configuration were homogeneous and repetitive in all the sensing areas, no matter their chemical composition and type of device. Therefore, the results evidence that the fabrication protocol presented in this chapter ensures the reproducibility in shape for the manufacturing of polymeric sensing areas within 3D printed microfluidic networks.

It is important to note that the chemistry of the ionogel influences the integration process, *e.g* DCA *versus* EMIES IL, evidencing the need of a functionalisation step when using ionogels in conventional microfluidic channels. The adhesion results presented in Figure 3.3 demonstrated that a surface functionalisation treatment is necessary in order to generate a stable ionogel microstructure, with defined dimensions and shapes, as previously reported by the Microfluidics Cluster UPV/EHU in conventional channels¹. The functionalisation of the surface of a microfluidic device in a specific location of the channel, is already very complicated and becomes more complicated for microfluidic devices fabricated by 3D printing, due to the nature (chemistry) of the printing materials and the device fabrication protocols, making this type of sensing capabilities impractical. However, when the T-shape feature is combined with UV curable functional materials, acting as physical anchorages for the sensors, the previously mentioned limitations are overtaken.

In addition, T-shape cavities are suitable for loading viscous solutions, as shown

in this chapter, where viscous ionogel solutions were easily introduced through the perpendicular channels to reach the T-shaped cavities. Then, they were photopolymerised and solidified *in situ*, being trapped within the wells at the bottom of the main channel, in precise locations.

3.2.4 pH sensing with integrated hybrid microfluidic device

The performance of the device at different pHs is depicted in Figure 3.4A. Each picture shows four sensing areas, one per sensor, at different pH values. An immediate colour change was observed, mainly in the middle of the sensor (< 0.5 s), and the colour spread to cover the entire exposed sensor surface in 2 min. The overall Hue signal of the 1×1 cm did not significantly varied during these 2 min, but the measurements were done after this time in order to ensure a homogeneous colour all over the 1×1 cm area. However, the 2 minutes are not a limitation, a systematic measurement of a smaller ROI in the middle of this area enables an immediate analysis without waiting 2 minutes to homogenise the whole $1 \text{ cm} \times 1 \text{ cm}$ area set by design.

According to the results presented in Figure 3.4B, each sensor had a characteristic sensing performance, showing a colour change at a specific pH value. The characterisation of the sensor was carried out with three different devices, which were fabricated at different times, using fresh ionogel solutions.

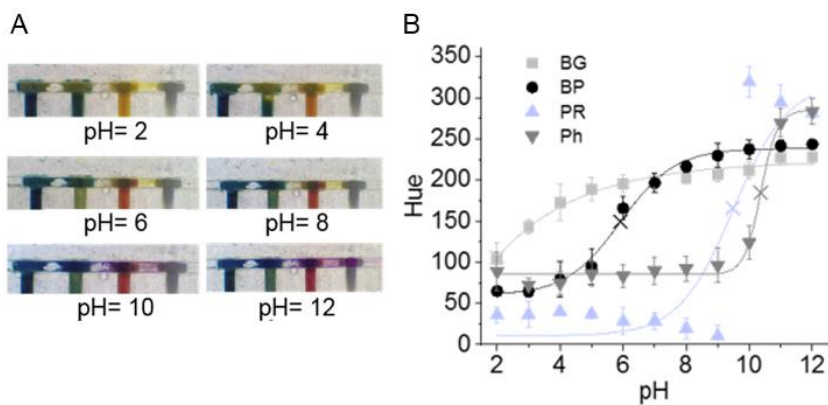


Figure 3.4. A) Images acquired for the microfluidic sensor device for six pH conditions, ranging from 2 to 12. B) Hue (H) values for each ionogel pH sensor, when varying the pH from 2 to 12. Error bars correspond to the standard deviation from the mean for $n = 3$. (X) shows the pK_a values for each ionogel, see section 3.2.5.

This chapter of my thesis does not intend to elucidate the complex mechanism that occurs during the pH analysis of the different ionogels/pH indicators, where other considerations such as hydrophobicity and ion extraction capability of the IL^{28,29} and the effect of the continuous flow regime -enabling dynamic interactions within the sensors among others- could have an effect in the behaviour of ionogels. Ion co-extraction capability of ILs plays an essential role in sensing when the IL takes active part in the sensing reaction, for example when the pH dye is part of the IL^{28,30}; however in these polymeric sensors, the pH responsive dye is independent from the IL, and it is the one giving the colour response to pH changes. In this chapter, the IL does not take active part in sensing, but it provides chemical stability to the polymeric sensors. Moreover, this study does not consider possible colour interferences coming from the matrix when using real samples; for that, modifications to lightning conditions should be considered.

Taken the previous considerations into account, the performance of the pH indicators inside the ionogel matrix can be described with the Equation (1), where the coefficient A , B , C and D can be derived by fitting the calibration curves, to sigmoidal equations, as shown in Figure 3.5B. The pK_a value of each pH indicator was obtained by calculating the inflexion point of the sigmoidal fittings in MATLAB.

$$Hue = A + \frac{(B-A)}{(1+10^{(C-pH)/D})} \quad (1)$$

The BG ionogel showed an evident colour switch from pH 2 to 4 (pK_a of 2.0, Table 3.1), with a less pronounced variation of the Hue value, 200 ± 25 , from pH 6, which can be considered as the Hue plateau of this particular sensor. The BP ionogel displayed a colour switch from pH 4 to 9 (pK_a of 5.9) with pseudo-plateau Hue values of 75 ± 25 and 225 ± 25 , before and after the colour of the sensor switched. On the other hand, the colour switch of the PR and the Ph ionogels undergo a drastic change to purple, at pH 9 - 10 (pK_a of 9.5) and at pH 10 - 11 (pK_a of 10.4) respectively. For acidic pH values, the colour did not change for both sensors, which corresponds with the behaviour of these types of indicators in solution. For instance, PR has low solubility in acidic and neutral media, being soluble in alkaline solutions with a 6.8-8.2 gradual transition, from yellow to purple. Therefore, the prepolymer solution containing PR was slightly alkalinised before polymerisation, in order to improve the solubility of PR, which also helped getting a functional pH sensing ionogel for alkaline pHs.

The transition ranges reported in literature for the pH indicators in solution used in this chapter are 3.8 - 5.4 for BG, 5.2 - 6.8 for BP, 6.8 - 8.2 for PR and 8.2 - 10 for Ph³¹. These values are slightly different from the ones found by me. The group has previously observed the deviation in the response range of the pH indicators

in ionogels, from their expected values in solution, which can be attributed to the immobilisation of the indicators in a gel-like structure⁵. Besides, the EMIES ionic liquid is particularly slightly acid³², which acidifies the environment of the polymeric network hosting the pH indicator, explaining that the sensor needs a higher pH to change colour. This may induce the shift in the acid–base equilibrium of the ionogel sensor matrix and thus the pH responses.

It is worth mentioning that for the four ionogels, the biggest deviations in Hue values occur at pH values that are close to the switching point of each indicator. At those points, local variations on the colour, brightness and shadowing, at different areas of the ionogel surface are observed, due to the inhomogeneity of the ionogel surface. This leads to a less homogeneous colour, and so to an increased error on the Hue value determination. Other types of image analysis techniques could be used in order to reduce these errors.

3.2.5 Verification of the pH sensing in the 3D microfluidic device

In order to validate the pH sensing device, a simple acid-base reaction, with a known pH value to the final solution, was carried out in the device. The pH value of the solution resulting from the acid/base reaction was estimated from the calibrated Hue values of each sensor. This was done by fitting the calibration curves to sigmoidal equations and resolving the pH values with Solver for each Hue obtained from the ionogels (Table 3.1).

An acidic solution, 0.1 M HCl was introduced in one of the inlets and a basic solution, 0.1 M NaOH, was passed through the other inlet at a flow rate of 150 $\mu\text{L min}^{-1}$. These two solutions mixed in the serpentine, where the acid-base reaction took place. The pH of the mixture was expected to be 7, since equimolar solutions of acid and base from both inlets were introduced. Pictures of the

sensors were taken after hydrating the sensors with DI water (Figure 3.5A) and after the reaction took place (Figure 3.5B). Then, their Hue values were calculated.

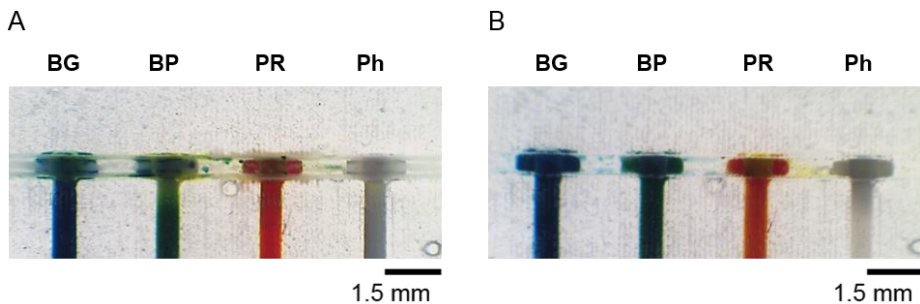


Figure 3.5. A) Picture of the pH ionogel sensors after hydrating it in DI water for 15 min. B) Picture of the pH ionogel sensors after the reaction of an equimolar mixture of HCl and NaOH was performed inside the meandering channel and passed through the sensing areas.

Hue values of the sensing areas after getting in contact with the reaction were calculated to be 207 for BG, 201 for BP and 32 for PR and 121 for Ph, and were compared with the Hue values given by those sensing areas during the characterisation process, Figure 3.5B.

The pH of the solution was obtained from a sigmoid function, given the usual sigmoidal response of pH dyes, $HI \rightleftharpoons H^+ + I^-$ with a given pK_a .

$$pH = pK_a + \log \left(\frac{[I^-]}{[HI]} \right) \quad (2)$$

According to the results obtained from the fitted equations, the Hue signal given by the different sensing areas were 7.5 for BG, 7.2 for BP, 6.9 for PR and 6.8 for Ph. The average pH value for the acid/base reaction performed in the microfluidic device of the four sensors was 7.1 according to the MATLAB fittings,

which also fits with the experimental values summarised in Table 3.1. The product of the equimolar reaction was measured with a commercial pHmeter in order to identify the accuracy of the pH detection. The pH detected by the microfluidic pH device as a result of the sensor barcode was 7.1 and the commercial pHmeter determined a pH value of 7.0, so the device detected the pH of the solution with an accuracy of 0.1.

Table 3.1. Fitting data for the calibration curves of BG, BP and PR.

Fitting coefficient	BG	BP	PR	pH
A	-303402.4	59.9	10.7	86.99
B	222.6	238.5	319.0	284.7
C	-19.3	5.9	9.5	10.4
D	0.16	0.50	0.50	1.66
R²	0.9615	0.9902	-	0.9887
p _{k_a}	2	5.9	9.5	10.4
Hue (acid/base reaction)	211	206	25	87
pH (solver)	7.5	7.2	6.9	6.8

Some recent studies reported the development of microsystems for pH sensing with the sensors in suspension ^{33,34} or with surface sensors ³⁵. They show short response times and good sensitivity, but they require expensive and specialised equipment such as fluorescence or optical spectrometer, photodiodes and a laser. Surface enhanced Raman spectroscopy measurements of smart-nano-in-micro particles show a sensitivity of 0.2 in pH variation, but, it requires sample handling to collect the particles and measure their response under a specialised equipment³³. Although they seem to respond rapidly to pH changes, there is a lack of real-time measurement due to the time gap due to handling. Moradi *et al.*

reported a fluorescence based microfluidic pH sensor, which is sensitive and performs real-time measurements, but it requires specialised equipment to induce and measure fluorescence³⁴. Lu *et al.* suggest a colorimetric surface sensing approach for pH monitoring for $\text{pH} < 3$ and $\text{pH} > 6$ ³⁵. Similar to our work, they combined a colorimetric pH dye with a polymeric membrane, but they collected the data and transformed it to voltage, in a complex process that requires specialised equipment. Besides, this surface sensor relied on trapping the membrane between the bottom and the upper part of the device, which complicated device fabrication. Therefore, this chapter offers a colorimetric pH measurement tool with dynamic fabrication features that does not require expensive or specialised equipment for the data analysis, demonstrating its unique sport within previously existing technology.

Furthermore, barcode sensing ensures four simultaneous measurements in a simple way. The combination of the response of the four sensors should match with one of the combinations obtained in the calibration. Therefore, if one of the sensors does not properly work, it could be easily detected due to a mismatch with the other three measurements.

3.2.6 Sensing device reusability

The performance of the device was investigated by measuring the Hue of the four sensing areas at two different pH values over time for fourteen times, using a strong acid solution (pH 2) followed by a strong basic solution (pH 12). A solution of pH 2 was introduced through the inlet, and after 2 min, Hue values were measured. Then the basic solution was introduced, measuring the colorimetric response after 2 min Figure 3.6.

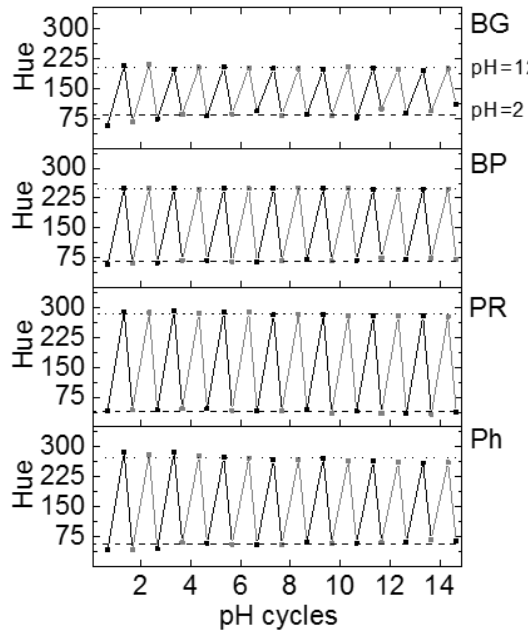


Figure 3.6. Hue values at pH 2 and pH 12 for 14 cycles of passing, through the sensing areas, an acidic solution followed by a basic solution. The Hue values were obtained after 2 min stabilisation time for the BG, BP, PR and Ph dyes in the ionogels. The dashed and dotted lines indicate the average of the Hue values from all the cycles for each sensor at pH 2 and 12, respectively.

According to the results displayed in Figure 3.7, BP and PR show the best repetitiveness, showing little deviation from the average value for all the cycles. BP displays good repetitiveness values during the 14 cycles, with Hue values of 68 ± 5 for pH 2 and 249 ± 1 for pH 12. For PR, the Hue values were also stable, 40 ± 5 for pH 2 and 284 ± 5 for pH 12, Figure 3.8. When it comes to BG and Ph, both sensors display lower stability after several cycles. BG keeps giving a stable signal for pH 12 during all the cycles, showing a Hue signal of 201 ± 4 , while at pH 2, the signal starts to decrease from cycle 12 on, showing a Hue of 85 ± 16 . On the other hand, Ph ionogel seems to have a less repetitive performance. Indeed, the

Hue values at both pHs do not recover the original values after the third cycle (Figure 3.6). As a demonstration of that, the observed Hue is 57 ± 8 for pH 2 and 271 ± 9 for pH 12 (Figure 3.7).

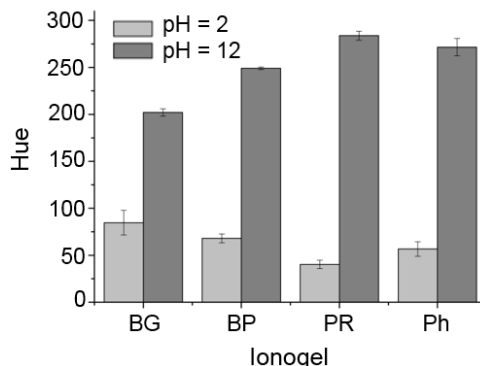


Figure 3.7. Reproducibility tests for the sensors over 14 cycles of pH change between 2 and 12. The bars indicate the average Hue values and the error bars represent the repetitiveness for each sensor at the two pH values.

It must be highlighted that the dyes that do not fully recover the initial Hue values are BG (responding in a pH range of 1-3) and Ph (responding in a range of pH 10-12). In contrast, BP (responding to pH 5-9) and PR (responding to pH 9-11) recover well the colours during 14 cycles (pH 2 to 12). In order to explain this, it is possible to speculate about an accumulative effect of protons from the solution at pH 2 that is not fully neutralised with the base of the solution at pH 12, varying the BG and the Ph colours at those extreme pHs. On the other hand, BP and PR responded well to those two pH changes during the 14 cycles in a reversible way, with low deviation in the Hue values, showing great recovery and performance, since the colour switch is far from the two extreme pH values investigated. Additionally, the fast and homogenous colorimetric response from the dyes in the ionogels demonstrated an adequate diffusion of protons thought the entire ionogel polymeric matrix ($\sim 0.01 \text{ cm}^2 \text{ s}^{-1}$).

3.3 Conclusions

The proposed strategy aims to simplify the task of integrating functional materials within 3D printed microfluidic devices. It combines a smart architecture and UV curable functional materials to embed a functional material -usually a polymeric matrix-, within a device fabricated by conventional 3D printing, followed by *in situ* photopolymerisation. The main advantages include the simplicity of the integration procedure, making the process user-friendly and accessible to many end users from different scientific fields.

The enhanced adhesion obtained due to the anchoring characteristics of the architecture avoids the needs of any chemical functionalisation on the surface for the generation of precise and stable sensing zones. The reproducible dimensions of the sensing zone minimises assembly errors and enhances sensing performance. Moreover, this strategy combines 3D printing and UV curable functional materials, so it does not require any modification of conventional printers, or materials to be integrated, in order to fulfil the requirements for a successful integration of materials within 3D printed microfluidic devices.

The integration procedure was satisfactorily demonstrated for a miniaturised pH sensor array, composed of four optical pH sensors of different chemical compositions, where each sensor aimed to provide high performance resolution in a specific pH range, and all the sensors together covered the whole pH range.

The possibility of producing multiple sensing zones along the main microchannel opens multiplexing capabilities, by embedding different kind of sensors in each sensing area. The dimensions and design used in this chapter enabled easy data collection and colorimetric analysis with no specialised equipment, but we would like to highlight the versatility of the technique. The system could be used

in diverse designs and purposes, integrating many functional materials -that could be used either as sensors or actuators, and miniaturisation would be limited by the printer and the sensor itself, since each sensor type permits a maximum miniaturisation that guarantees a good performance.

Furthermore, this fabrication method uses conventional bench-top 3D printing, offering the advantage of rapid fabrication cycles, which leads to cost reduction and enhanced efficiency, allowing agile production of complex geometries to bridge the gap between the new ideas and the generation of prototypes for design optimisation. This, combined with the aforementioned advantages provided by the integration method, enables to achieve optimised and accelerated transitions from prototype to product, in a way that is lean, cost-effective and reduces the risks associated with manufacturing.

3.4 Experimental

3.4.1 Materials

3D printing: Clear resin FLGP CL02 was purchased from Formlabs, U.S., Isopropyl alcohol was from Scharlab, Spain and) was used to rinse the printed devices, and the Pressure Sensitive Adhesive (PSA) sheets were obtained from Adhesive Research, Ireland.

pH sensing ionogels: bromocresol green (BG) (Scharlab, Spain), bromocresol purple (BP) (Acros Organics, Spain), phenol red (PR) and phenolphthalein (Ph) pH indicators were purchased from Sigma Aldrich, Spain. For the synthesis of the polymeric precursor cocktail, *N*-isopropylacrylamide (NIPAAm) monomer, dimethoxy-2-phenylacetophenone (DMPA) photoinitiator, *N*, *N'*-methylenebisacrylamide (mBAA) crosslinker and 1-ethyl-3-methylimidazolium

ethyl sulphate (EMIES) and trihexyltetradecylphosphonium dicyanamide (DCA) ILs were purchased from Sigma Aldrich, Spain.

Microfluidic connections: The luers were obtained from Microfluidics ChipShop, Germany and the tubing from Altmann Analytik GmbH & Co., Germany.

3.4.2 Device architecture and fabrication by 3D printing

A picture of the devices is shown in Figure 3.1A. The three female-luer connectors, two at the inlet and one at the outlet, allowed the connection of the main microfluidic channel with external fluidic sources, being compatible with P-675 male luer to 1/4-28 female connector and with Barb to Slip-Type male luer adapters (Fisher Scientific, USA). The main channel featured an open channel section 32 mm long, 700 μm wide and 700 μm high, located on the top side of the device, which was closed with a pressure sensitive adhesive layer (PSA) when in operation. The other four small connectors, with internal cone shape of $D_1 = 1.3$ mm, $D_2 = 1$ mm, and $H = 3$ mm, were specially designed to allow precise coupling of pipette tips for leak-free pipetting of viscous materials. These connectors, together with adjacent internal channels, were arranged perpendicularly to the main channel, aiming to facilitate the integration of the material of interest.

T-shaped cavities shown in Figure 3.1.C consisted of an internal channel, 11.2 mm long and 1 mm diameter, and a T-shaped cavity of 2.2 μL . The total volume to be integrated in this structure was 12.4 μL . The four pH-sensing ionogels were integrated within the T-shaped anchorage structure, leading to strategically positioned sensing zones, of 1 mm^2 surface area, at the bottom of the main channel.

The Y-shaped channels and serpentine were 15.8 mm long, 500 µm wide and 600 µm high, and the meandering channel was 44 mm long, 700 µm wide and 700 µm high.

3D printing technology was used to manufacture the microfluidic device. Using a stereolithography (SLA) 3D printer (Formlab 1+, Formlabs, U.S.), it consists in a light-based stereolithography process that builds individual layers of a model with liquid polymer, by hardening it with a laser beam. Creo Parametrics 2.0 CAD software was used to design 3D models of the microfluidic device, Figure 3.1A, and PreForm software to build the supporting structures that allow for a satisfactory printing of the devices. The device was 3D printed as a single piece, in acrylic material, using a 50 µm printing resolution. After printing, the obtained structure was rinsed in isopropyl alcohol for 4 min in order to eliminate the uncured resin from the cavities, and subsequently post-cured under 365 nm UV light (Spectroline™, Hampshire, United Kingdom) for 15 min. Then, the holders were removed from the microfluidic devices with a snip and the final devices were wet sand-polished to enhance transparency.

3.4.3 Synthesis of the pH sensing polymers

The prepolymer solution of each pH sensor was comprised of NIPAAm monomer, DMPA, mBAAm crosslinker, IL and a pH indicator (BG, BP, PR or Ph). The molar relation for the polymer matrix is the same in all the sensors: 40:0.4:0.1 (NIPAAm:DMPA:mBAAm), but the ratio varies for the pH indicators and the ILs. The polymeric precursor reaction was synthesised as follows for BG sensor: 452.0 mg NIPAAm, 30.9 mg mBAAm, 30.0 mg DMPA and 5.0 mg BG dissolved in 2.0 mL of EMIES ionic liquid at 80 °C under stirring conditions. Following the same procedure, the rest of the precursor solutions were carried out, with slightly

different recipes. For the BP: 452.0 mg NIPAAm, 30.9 mg mBAAm, 30.0 mg DMPA 5.0 mg BP and 1.5 mL DCA IL were mixed together. For the Ph: 452.0 mg NIPAAm, 30.9 mg mBAAm, 30.0 mg DMPA, 7.0 mg Ph and 2.0 mL EMIES were used. Finally, for the PR: first 452.0 mg NIPAAm, 30.9 mg mBAAm, 30.0 mg DMPA, 5.0 mg PR and 1.0 mL EMIES IL were mixed together. Then, to that mixture, 60.0 μ L of NaOH 0.01 M and 20.0 μ L NaOH 1M were added at continuous stirring.

The integration of the sensing materials was carried out by loading 13.0 μ L of the different ionogel precursor cocktails from the four pipette-tip connectors to the T-shaped structures, and the cocktails were subsequently photopolymerised under UV light at 365 nm (EF-180C hand-held UV lamp) for 45 min. Once polymerised, the ionogels were rinsed with isopropanol and distilled water in order to eliminate any non-polymerised material. After polymerisation, the ionogel containing BP was soaked in a saturated solution of BP in ethanol, 1.0 μ L of the solution, for 15 min. To prepare BP concentrated solution, 10.0 mg of BP powder were dissolved in 10.0 mL of ethanol. Finally, the device was sealed with a PSA layer to close the main channel and generate a fully functional microfluidic device for pH sensing.

3.4.4 Set-up and imaging

The device was characterised using the set-up shown in the Figure 3.8. It consisted of a Standard Infuse/Withdraw Pump 11 Elite Programmable Syringe Pump (Harvard apparatus, Spain) to drive the liquid through the device, a microscope with an integrated camera and a software application for image acquisition. The samples were reproducibly illuminated, using a light source composed of a LED lamp and a LED ring-light. The captured images were saved

in TIF format with a resolution of 2584 x 1936 pixels, and the white balance settings of the microscope camera were kept constant during the experiments. Free Fiji software was used to determine the RGB colorimetric parameters of each pH sensor ionogel, and from those, Hue (from HSV) was then calculated using Wolfram Alpha, an on line answer engine, in order to obtain the exact colour of the ionogel.

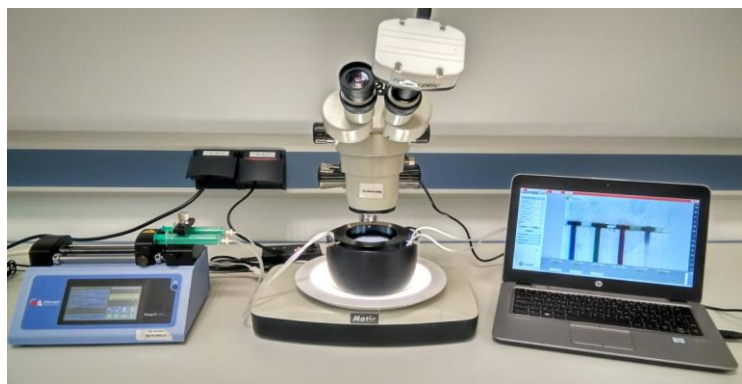


Figure 3.8. Set-up used for the characterisation of the sensor.

A microscope with an integrated camera (ISH500 Tucsen Photonics, China) and a software application (TCapture, Tucsen Photonics, China) were used for image acquisition. The samples were reproducibly illuminated, using a light source composed of a LED lamp (MKM012405WH1, 25W, ADEO) and a LED ring-light.

3.4.5 pH sensor ionogel characterisation

The pH sensing performance of the ionogels was characterised by flowing solutions at different pHs, from 2 to 12, at $150 \mu\text{L min}^{-1}$ through the 3D printed microfluidic device. A picture was taken after 2 min in contact with each pH solution and analysed as explained above.

The pH solutions were prepared using HCl for the acidic ones (from 1 to 7) and

NaOH for the alkaline ones (from 8 to 14). For the acidic series, pH 1 stock solution was first prepared making a 0.1 M HCl solution in distilled water, and subsequent pH solutions were made with a 1:10 dilution of the stock pH solution. Milwaukee pH-51 pH-meter (error ± 0.1) was used to measure the pH of each solution. To prepare the pH solutions of the basic series, the same procedure was followed, first NaOH 1 M (pH 14) was made, and sequential 1:10 dilutions were done until pH 8 solution was reached. After passing a pH solution through the channel, the acquired images for each pH value and each sensing zone were analysed as explained before, and the operation ranges were defined for the four pH sensor ionogels.

Ionogel adhesion tests were performed with distilled water and flow rates ranging from 25 to 600 $\mu\text{L min}^{-1}$ for both, the proposed microfluidic structure, see above, and using simple rectangular channels with integrated ionogels on the surface. In order to do that, 2.0 μL of the four pH sensing ionogels were immobilised directly on precise zones along the main rectangular channel. The ionogel volumes, pipetted in this way, generated sensing areas on the main microfluidic channel, similar to those ionogels embedded within T-shaped cavities. No surface functionalisation treatment was employed on the acrylic substrates to enhance the wettability or adhesion properties of the ionogels to the substrate.

3.4.6 Acid/base reaction performance

As a proof of concept, an acid/base reaction was performed inside the microchannel by introducing HCl 0.1 M and NaOH 0.1 M solutions from both inlets, using the same flow than for the characterisation of the pH sensing ($150 \mu\text{L min}^{-1}$). Pictures of the sensing areas were taken, and the colorimetric response

of the sensors was measured and compared to those values from the calibration in order to determine the pH value after the reaction. The pH value of the reaction was also measured using a commercial benchtop pH sensor.

3.5 References

1. Czugala, M.; O'Connell, C.; Blin, C.; Fischer, P.; Fraser, K. J.; Benito-Lopez, F.; Diamond, D. Swelling and shrinking behaviour of photoresponsive phosphonium-based ionogel microstructures. *Sensor Actuat. B-Chem.* 2014, 194, 105-113.
2. Derkus, B. Applying the miniaturization technologies for biosensor design. *Biosensor Bioelectron.* 2016, 79, 901-913.
3. Herranz, S.; Marciello, M.; Marco, M.; Garcia-Fierro, J. L.; Guisan, J. M.; Moreno-Bondi, M. C. Multiplex environmental pollutant analysis using an array biosensor coated with chimeric haptens-dextran-lipase constructs. *Sensor Actuat. B-Chem.* 2018, 257, 256-262.
4. Lee, J.; Haddon, D. J.; Wand, H. E.; Price, J. V.; Diep, V. K.; Hall, D. A.; Petri, M.; Baechler, E. C.; Balboni, I. M.; Utz, P. J. Multiplex giant magnetoresistive biosensor microarrays identify interferon-associated autoantibodies in systemic lupus erythematosus. *Sci Rep.* 2016, 6, 27623.
5. Curto, V. F.; Fay, C.; Coyle, S.; Byrne, R.; O'Toole, C.; Barry, C.; Hughes, S.; Moyna, N.; Diamond, D.; Benito-Lopez, F. Real-time sweat pH monitoring based on a wearable chemical barcode microfluidic platform incorporating ionic liquids. *Sensor Actuat. B-Chem.* 2012, 171, 1327-1334.
6. Ren, K.; Zhou, J.; Wu, H. Materials for microfluidic chip fabrication. *Acc. Chem. Res.* 2013, 46, 2396-2406.
7. Tijero, M.; Díez-Ahedo, R.; Benito-Lopez, F.; Basabe-Desmonts, L.; Castro-López, V.; Valero, A. Biomolecule storage on non-modified thermoplastic microfluidic chip by ink-jet printing of ionogels. *Biomicrofluidics* 2015, 9, 044124.
8. Rendl, M.; Böniisch, A.; Mader, A.; Schuh, K.; Prucker, O.; Brandstetter, T.; Ruhe, J. Simple one-step process for immobilization of biomolecules on polymer substrates based on surface-attached polymer networks. *Langmuir* 2011, 27, 6116-6123.
9. Amin, R.; Knowlton, S.; Hart, A.; Yenilmez, B.; Ghaderinezhad, F.; Katebifar, S.; Messina, M.; Khademhosseini, A.; Tasoglu, S. 3D-printed microfluidic devices. *Biofabrication* 2016, 8, 022001.
10. Capel, A. J.; Rimington, R. P.; Lewis, M. P.; Christie, S. D. 3D printing for chemical, pharmaceutical and biological applications. *Nat. Rev. Chem.* 2018, 2, 422-436.
11. Cui, L.; Ranade, A. N.; Matos, M. A.; Dubois, G.; Dauskardt, R. H. Improved adhesion of dense silica coatings on polymers by atmospheric plasma pretreatment. *ACS Appl. Mater. Interfaces* 2013, 5, 8495-8504.
12. Zhang, X.; Li, L.; Luo, C. Gel integration for microfluidic applications. *Lab Chip* 2016, 16, 1757-1776.
13. Czugala, M.; Gorkin III, R.; Phelan, T.; Gaughran, J.; Curto, V. F.; Ducrée, J.; Diamond, D.; Benito-Lopez, F. Optical sensing system based on wireless paired emitter detector

- diode device and ionogels for lab-on-a-disc water quality analysis. *Lab Chip* 2012, 12, 5069-5078.
- 14. Mendes-Felipe, C.; Oliveira, J.; Etxebarria, I.; Vilas-Vilela, J. L.; Lanceros-Mendez, S. State-of-the-Art and Future Challenges of UV Curable Polymer-Based Smart Materials for Printing Technologies. *Adv. Mater. Technol.* 2019, 4, 1800618.
 - 15. Oliveira, J.; Correia, V.; Castro, H.; Martins, P.; Lanceros-Mendez, S. Polymer-based smart materials by printing technologies: Improving application and integration. *Addit. Manuf.* 2018, 21, 269-283.
 - 16. Deng, W.; Jie, J.; Xu, X.; Xiao, Y.; Lu, B.; Zhang, X.; Zhang, X. A Microchannel-Confining Crystallization Strategy Enables Blade Coating of Perovskite Single Crystal Arrays for Device Integration. *Adv Mater* 2020, 32, 1908340.
 - 17. Seo, J.; Wang, C.; Chang, S.; Park, J.; Kim, W. A hydrogel-driven microfluidic suction pump with a high flow rate. *Lab Chip* 2019, 19, 1790-1796.
 - 18. Mugherli, L.; Lety-Stefanska, A.; Landreau, N.; Tomasi, R. F.; Baroud, C. N. Quantifying the sol-gel process and detecting toxic gas in an array of anchored microfluidic droplets. *Lab Chip* 2020.
 - 19. Saez, J.; Glennon, T.; Czugala, M.; Tudor, A.; Ducreé, J.; Diamond, D.; Florea, L.; Benito-Lopez, F. Reusable ionogel-based photo-actuators in a lab-on-a-disc. *Sensor Actuat. B-Chem.* 2018, 257, 963-970.
 - 20. Kavanagh, A.; Byrne, R.; Diamond, D.; Fraser, K. J. Stimuli responsive ionogels for sensing applications—an overview. *Membranes* 2012, 2, 16-39.
 - 21. Gil-Gonzalez, N.; Akyazi, T.; Castaño, E.; Benito-Lopez, F.; Morant-Minana, M. C. Elucidating the role of the ionic liquid in the actuation behavior of thermo-responsive ionogels. *Sensor Actuat. B-Chem.* 2018, 260, 380-387.
 - 22. Lee, H. Y.; Cai, Y.; Velioglu, S.; Mu, C.; Chang, C. J.; Chen, Y. L.; Song, Y.; Chew, J. W.; Hu, X. M. Thermochromic ionogel: A new class of stimuli responsive materials with super cyclic stability for solar modulation. *Chem. Mater.* 2017, 29, 6947-6955.
 - 23. Kangas, M. J.; Burks, R. M.; Atwater, J.; Lukowicz, R. M.; Williams, P.; Holmes, A. E. Colorimetric sensor arrays for the detection and identification of chemical weapons and explosives. *Crit. Rev. Anal. Chem.* 2017, 47, 138-153.
 - 24. Cantrell, K.; Erenas, M.; de Orbe-Payá, I.; Capitán-Vallvey, L. Use of the hue parameter of the hue, saturation, value color space as a quantitative analytical parameter for bitonal optical sensors. *Anal. Chem.* 2010, 82, 531-542.
 - 25. Etxebarria-Elezgarai, J.; García-Hernando, M.; Basabe-Desmonts, L.; Benito-Lopez, F. In In 3D printed high quality benchtop microfluidic devices integrating smart materials as sensors; 21st International Conference on Miniaturized Systems for Chemistry and Life Sciences, MicroTAS 2017; 2020, pp 305-306.
 - 26. Kazmer, D. "Three Dimensional Printing of Plastics" in *Applied Plastics Engineering Handbook*, Elsevier, Second Edition, 2017, 617-634.

27. Bhattacharjee, N.; Urrios, A.; Kang, S.; Folch, A. The upcoming 3D-printing revolution in microfluidics. *Lab Chip* 2016, 16, 1720-1742.
28. Mizuta, T.; Sueyoshi, K.; Endo, T.; Hisamoto, H. Ionic liquid-based dye: A “Dyed plasticizer” for rapid and highly sensitive anion optodes based on a plasticized PVC membrane. *Sensor Actuat. B-Chem.* 2018, 258, 1125-1130.
29. Gourishetty, R.; Crabtree, A. M.; Sanderson, W. M.; Johnson, R. D. Anion-selective electrodes based on ionic liquid membranes: effect of ionic liquid anion on observed response. *Anal. Bioanal. Chem.* 2011, 400, 3025-3033.
30. Gao, L.; Lin, X.; Zheng, A.; Shuang, E.; Wang, J.; Chen, X. Real-time monitoring of intracellular pH in live cells with fluorescent ionic liquid. *Anal. Chim. Acta* 2020.
31. Sabnis, R. W. *Handbook of acid-base indicators*, CRC Press, San Francisco, U.S.A, First Edition, 2007
32. Hajipour, A.; Rafiee, F. Basic ionic liquids. A short review. *J. Iran. Chem. Soc.* 2009, 6, 647-678.
33. Liu, Y.; Yue, S.; Wang, Y.; Wang, Y.; Xu, Z. A multicolor-SERS dual-mode pH sensor based on smart nano-in-micro particles. *Sensor Actuat. B-Chem.* 2020, 310, 127889.
34. Moradi, V.; Akbari, M.; Wild, P. A fluorescence-based pH sensor with microfluidic mixing and fiber optic detection for wide range pH measurements. *Sensor Actuat. A-Phys.* 2019, 297, 111507.
35. Lu, Y.; Feng, Q.; Zhang, R.; Lu, H.; Su, J.; Cui, Y.; Zhu, L. An online pH detection system based on a microfluidic chip. *Anal. Chim. Acta* 2020.

4

Micro Aperture Array for the Fabrication of High Density Microsensor Arrays

The development of Lab-on-a-chip devices often involves the integration of sensors into microfluidic architectures. Therefore, the development of suitable sensors and sensor architectures is important. In particular, polymers are promising materials for the development of sensors, since they provide rapid and cheap fabrication protocols and they have high potential for integration into microfluidic devices. This chapter describes a cost-effective methodology to create high-density arrays of tuneable microsensors using photo-patternable polymeric materials. A Mylar® photomask, composed of an array of light micro-apertures, is used as a support for the fabrication of the array, called micro aperture array. This novel approach has the potential to produce integrable chemical sensors into Lab-on-a-chip devices.

4.1 Introduction

As mentioned in Chapter 3, the use of polymers as matrices, during the development of sensors is a highly versatile alternative that could be performed at low cost^{1,2}. Due to their tuneable physico-chemical properties, they can be combined with other molecules and be tailored to fulfill particular tasks, such as the detection of a specific target^{3,4}. Moreover, in contrast to the direct immobilisation of sensing molecules on a substrate, the synthesis of polymeric three dimensional (3D) matrixes hosting functional molecules, offers some advantages such as high functional group density, which improves the immobilisation of functional molecules and their reaction capacity⁵⁻¹⁰. In addition, miniaturisation improves the signal/noise ratio of sensors¹¹, thus polymers can be miniaturised in microsized stable dimensions¹² and can be integrated on a substrate¹².

Within polymers, hydrogels are widely used to easily fabricate three-dimensional polymeric networks consisting of crosslinked hydrophilic chains in an aqueous microenvironment. They are tuneable and suitable for the entrapment of molecules with functionalities, however, they show limited mechanical strength when they are not immersed in an aqueous solution¹³. To address this drawback, ionogels are emerging polymers that combine a polymeric network and an IL instead of an aqueous solution, as it was introduced in Chapter 3. ILs have lower symmetry than common salts thus, the charges of the cations and the anions are distributed over the volume of the large molecules by resonance¹⁴. The high-thermal stability and negligible vapour pressure of the ILs^{15,16}, when entrapped in a polymeric network, favours the maintenance of the ionogel shape when dry. Moreover, ILs have been reported to enhance the

stability of enzymes^{17,18}, europium (II)¹⁹, nanoparticles²⁰, proteins²¹⁻²³, antibodies²⁴ and nucleic acids²⁵⁻²⁷. Besides, ionogels can be designed to be photopatternable, increasing their suitability for miniaturisation with up to 15 µm of resolution through photolithography, see Chapter 5¹².

Chemical sensors detect a chemical analyte or an event, such as the presence or concentration of an analyte, and convert it into a readable signal. As explained in Chapter 2, a sensor is consisted of two elements: the recognition element, where the interaction with the analyte takes place and the transducer, which converts the previous chemical information into a readable output^{28,29}. In particular, optical sensors are cost-effective and have a great potential when integrated in LOC devices by the use of multiplexing and minaturisation techniques³⁰. As shown in Chapter 3, polymeric matrices can be used to host colorimetric reactions within their networks, acting as colorimetric sensors^{1,31}. The miniaturisation of the sensing features improves the distribution of the species on the sensor^{11,32} and thus its performance. Miniaturisation also increases the surface area/volume ratio, which improves diffusion and enhances mass transfer through the sensing materials, accelerating response times³³. Cho and Bright reported arrays of xerogel microsensors of 100 µm done by pin printing on rigid surfaces, with a fabrication rate of a sensor per second³⁴. Photopatterning, combined with photopatternable materials, can lead to the rapid fabrication of high-density arrays of stable and well-defined microstructures¹². Therefore, the use of photopatternable sensors has the potential to create thousands of microsensors in a matter of minutes.

In this chapter, the Micro Aperture Array (μ AA) is proposed to create precisely positioned, high-density polymeric microsensor arrays directly on the substrate in a single step. For that, Mylar® photomasks, 200 µm thick polymeric sheets

made of polyethylene terephthalate (PET), are used as substrates to create high density arrays of independent polymeric microsensors *in situ* by UV exposure (Figure 4.1A). For that, Mylar® substrates consisted of transparent and black (inked) areas have been designed to create arrays of individual polymeric microsensors surrounded by black areas. Based on Chapter 3, but aiming for further miniaturisation, the polymeric microsensors were doped with a pH responsive colorimetric dye to function as pH microsensors. This transparent/black configuration would help limiting the regions of interest (ROIs) for colorimetric measurements, due to the surrounding black areas, which could increase the signal to noise ratio, and therefore improve colorimetric measurements. The μAA is a step forward in the development of easy-to-fabricate and cheap sensing elements, with high integration potential for chemical monitoring in LOC devices (Figure 4.1B).

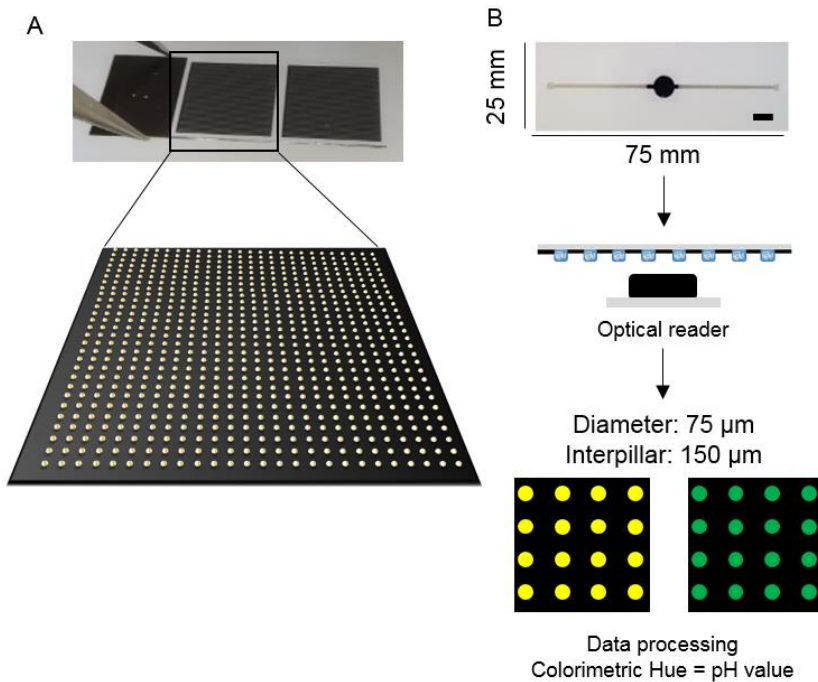


Figure 4.1. A) Picture of the Mylar® substrate and illustration of the zoomed μ AA high density array of microsensors created *in situ* by photopolymerisation. B) At the top, picture of the microsensor array integrated in a microfluidic device; circle: 1 cm diameter and channel width: 1 mm. Ruler corresponds to 1 cm. In the middle, an illustration showing the integration of a μ AA substrate in a microfluidic device and the optical readout at the bottom, for pH colorimetric sensing, and at the bottom, a scheme of the array at two different pH values (acidic yellow; basic green).

4.2 Results and discussion

4.2.1 Micropillar array fabrication

In order to decide for the best polymer to be used as sensing micropillars, five

different polymers were investigated. These polymers had different chemical compositions and mass ratio between their components, which were optimised to obtain polymer sensors with stable and reproducible shape and with smooth surfaces, in order to improve colorimetric measurements.

All of the polymeric sensors investigated in this Chapter had in common the monomer poly(N-isopropylacrylamide) (NIPAAm), the crosslinker N,N'-Methylenebisacrylamide (mBAAm) and Dimethoxy-2-phenylacetophenone photoinitiator (DMPA) (Figure 4.2A). This polymeric mixture was considered suitable for the fabrication of microsensors due to the high-water uptake of pNIPAAm, which may accelerate the integration of the aqueous solution, sensing moieties, within the gels, and therefore, speed up the response of the analyte detection. In order to explore the micropatterning capabilities of different materials on Mylar® photomasks, two hydrogels and three ionogels were used, see experimental sections 4.4.2 and 4.4.3.

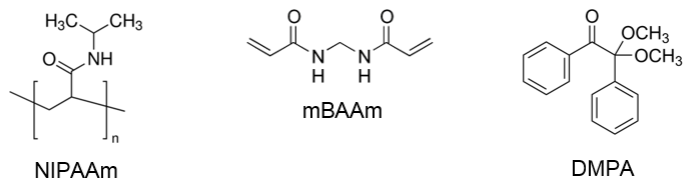
For the synthesis of the hydrogel, dimethyl sulfoxide (DMSO) and acetic acid (AA) were used as solvents. The two solvents affect the performance of the generated pH sensors in different ways due to their distinct acidities, pK_a 35 for DMSO and 4.74 for AA. For the ionogel micropillars, trihexyltetradecylphosphonium dicyanamide (DCA), tetrabutylphosphonium p-toluenesulfonate (P-TOS) and choline acetate (ChA) ILs were used as solvents.

The DCA ionogel was used in Chapter 3 for the bromocresol purple (BP) sensor, obtaining a gradual colorimetric response over the whole pH range. Therefore, I firstly decided to investigate its miniaturisation and array performance. Then, the P-TOS ionogel was chosen because of the low acidity of the cation and the neutrality of the anion, so it was assumed to not modify the acidity of the media surrounding the indicator³⁵. Finally, the ChA ionogel was investigated because

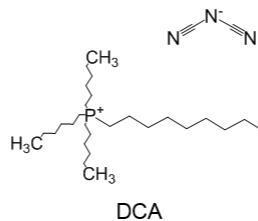
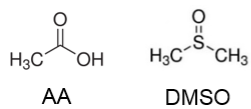
of its biocompatibility³⁶, in order to open this sensing array for future bio-applications. A graphical illustration of the composition of an ionogel is depicted in Figure 4.2B.

The prepolymers were made as explained in experimental section 4.4.2, mixing the monomer, the crosslinker and the photoinitiator with one of the solvents, following the compositions summarised in Table 4.1. First of all, in order to get an idea about the polymerisation rates of the five prepolymer mixtures and observe their physical stability, 100 µL of each of the prepolymer solutions were added in the wells of a 96 microtiter plate, and photopolymerised using UV light at 365 nm. It took 10 min to polymerise the three ionogels and the DMSO hydrogel, while the AA hydrogel needed 40 min. Although the AA hydrogel polymerised, the consistency and shape of the generated structure was poor, with a rough surface. Moreover, the generated structure was very brittle when dried.

A

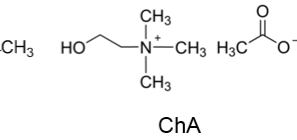


Conventional solvents

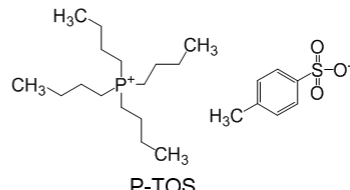


DCA

ILs



ChA



P-TOS

B

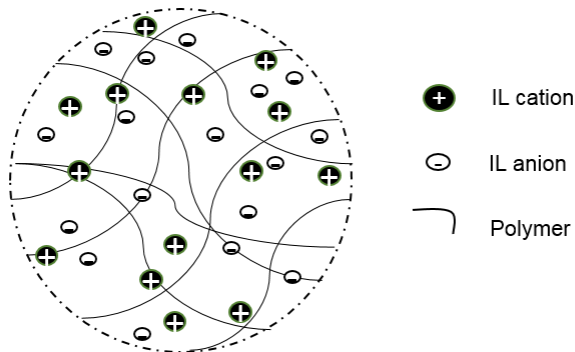


Figure 4.2. A) Scheme with the chemical formulas of the different molecules used for the polymer matrix and the solvents. B) Illustration of the network of an ionogel.

Once the polymerisation time was defined, the prepolymer solutions were coated and subsequently patterned on the inked side of the Mylar® photomask. Mylar® is an acetate photomask with a hydrophobic ink on one side. The ink is used to generate the desired pattern by black areas, to block the light, and transparent areas or light apertures that allow the light to pass through the μ AA (Figure 4.3A). Therefore, a specific design was made for the creation of miniaturised microsensor arrays by μ AA. The array consisted of transparent dots with a diameter of 75 μ m separated to each other by 150 μ m. This configuration allows a clear visualisation of the dots with a simple microscope, increasing the number of microsensors that can be interrogated in a defined area.

Then, the fabrication of the micropillars was systematically investigated. As explained in section 4.4.3, in order to fabricate homogeneous and stable micropillars, 50 μ L of the prepolymer solutions were added on the substrate and the film applicator, set for 400 μ m height, was applied in order to spread them over the inked side of the Mylar®. Then, UV light (365 nm) was applied from the non-inked side, polymerising only the prepolymer solutions on the transparent dots of the photomask (Figure 4.3B).

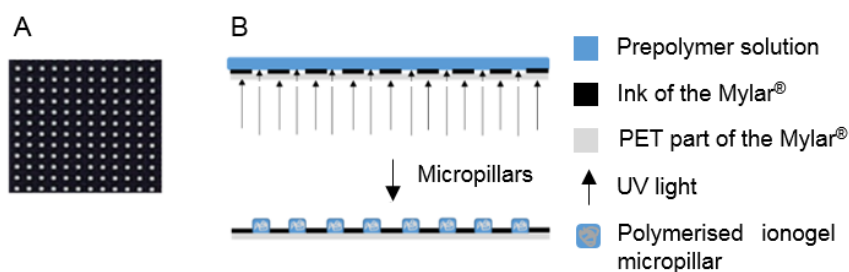


Figure 4.3. A) Image of the Mylar®. B) Representation of the photopolymerisation process using the μ AA and the creation of the polymeric micropillars on the inked side of the mask.

Several UV light power cycles were applied to investigate the patterning quality of the polymer solutions, using the photomask as a substrate, evaluating the coverage and homogeneity of the pattern all over the 1 cm x 1 cm substrate. Table 4.2 from the experimental section summarises the optimised parameters and the results obtained on the photopatterning of the different polymers.

Ionogels provided better μ AA microsensors, since they led to larger micropatterned areas over the Mylar[®] substrate compared to the hydrogels polymers. For instance, AA hydrogels hardly created polymer micropillars. The reason for that can be explained considering the different hydrophilicities of the prepolymer solution (hydrophilic) and the photomask (hydrophobic), which combination did not promote the formation of a homogeneous layer of prepolymer solution over the Mylar[®] substrate. Despite the longer lightning times applied to the AA hydrogel, 14 pulses of 20 s at $9.2 \text{ mJ cm}^{-2}\text{s}^{-1}$ (Table 4.2 in experimental section 4.4.3), just random micropillars could be obtained, with a significant surface roughness and heights ranging from 5 to 52 μm for different patterned areas in the same sample (Figure 4.4A). Therefore, the AA hydrogel was discarded for further development of the sensing micropillars.

On the other hand, the DMSO hydrogel led to a very compact, homogeneous and well defined micropillars on the photomask (Figure 4.4B). Although, large areas comprised of micropillars were obtained, their density over the whole Mylar[®] substrate was low. Moreover the height of the micropillars was not reproducible, obtaining heights from 24 to 65 μm (Figure 4.4B). Therefore, as in the case of the AA hydrogel, the DMSO hydrogel was discarded for the development of the sensing micropillars.

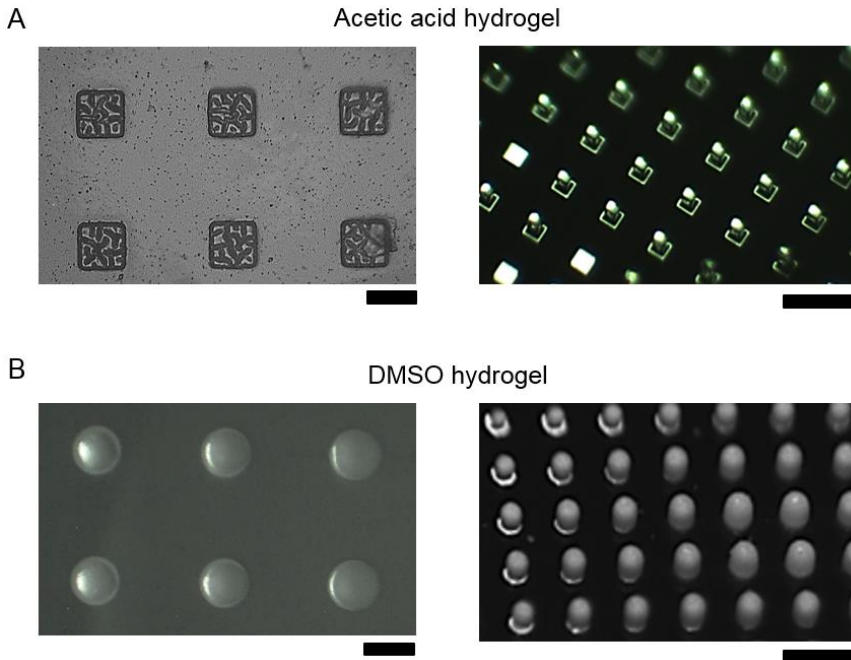


Figure 4.4. A) Images of the acetic AA hydrogel micropillars with a magnifying lens (left) and with an optical microscope (right). B) Images of the DMSO hydrogel micropillars with a magnifying lens (left) and with an optical microscope (right). Scale bar 100 μ m. All micropillars were generated over the μ AA.

In general, ionogels presented faster polymerisation times than hydrogels. Moreover, the DCA ionogel was not used for further experiments because of its stickiness to the photomask, which precluded the fabrication of homogeneous micropillars. The prepolymer spread well over the substrate, creating a homogeneous layer, but after photopolymerisation, the black areas of the substrate appeared with DCA ionogel residues that were impossible to wash out. Regarding the P-TOS and the ChA ionogels, high density of patterned areas were obtained, especially with the ChA ionogel, which led to the full coverage of the Mylar® substrate with micropillars. Although P-TOS ionogel created large

micropillar arrays, the individual micropillars did not seem to fill all the transparent dots, according to the optical microscopy images (Figure 4.5A, left). In contrast, the ChA ionogel micropillars completely filled all the transparent dots (Figure 4.5A, right). Both P-TOS and ChA were analysed by SEM. The P-TOS micropillars formed in a pyramid shape (Figure 4.5B, left) while the ChA micropillars presented a cylindrical and symmetric shape, with a flatter top surface. This flat configuration could improve the colorimetric analysis, due to the better focusing on the sensing surface, obtaining the whole ROI delimited by the Mylar® design focused (Figure 4.5B, right).

The height of P-TOS and ChA ionogel micropillars was measured by contact profilometer, obtaining height values of $79 \pm 8 \mu\text{m}$ ($n = 12$) for P-TOS ionogel (Figure 4.5C left) and $55 \pm 3 \mu\text{m}$ ($n = 12$) for ChA (Figure 4.5C right).

Although some micropillars were obtained with AA and DMSO hydrogels, P-TOS and ChA ionogels were the materials creating the largest micropatterned areas on the μAA . This difference can be explained due to the viscosity of the prepolymers and their capability to create a viscous and homogeneous layer on the photomask, which was harder to get with hydrogel prepolymers than with ionogels. The low viscosity of the hydrogels, specially AA, was a problem when placing the prepolymer solution on the Mylar® substrate. Moreover, the stability given by the ionic liquid to the prepolymer solution instead of the common solvents to the hydrogels (*e.g.* lack of evaporation) is also the responsible of the homogeneous shapes and the reproducibility in height values of the ionogel when compared to the hydrogel micropillars.

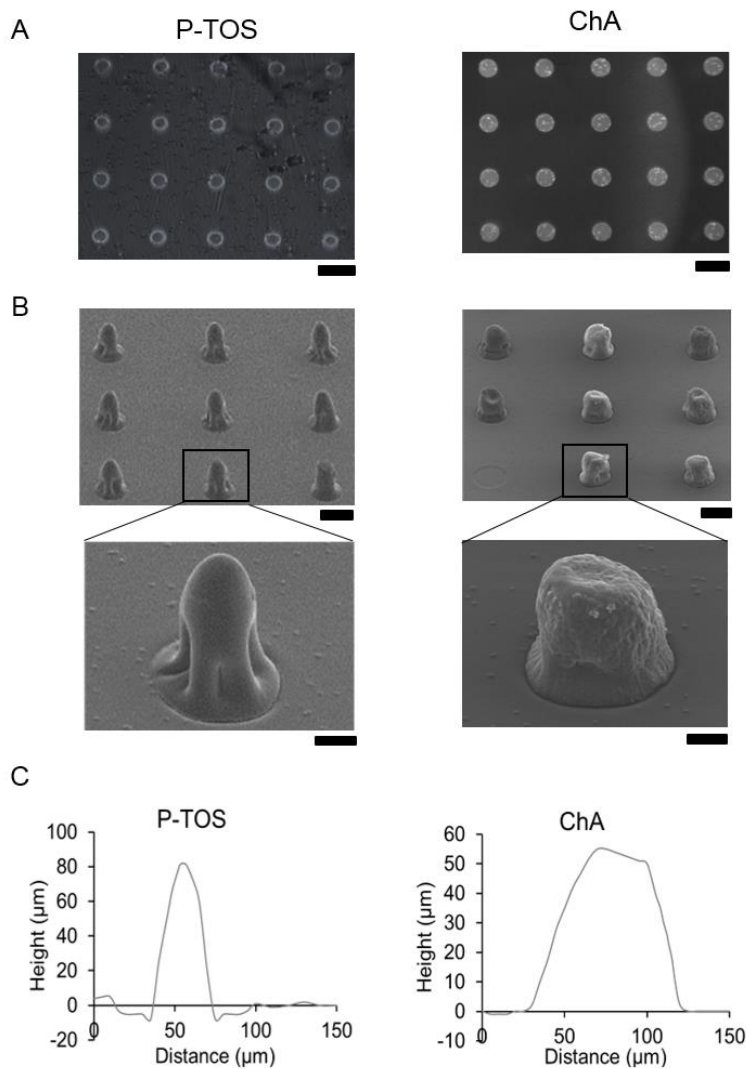


Figure 4.5. A) Optical microscopy images of P-TOS (left) and ChA (right) ionogel micropillars on the μ AA. Scale bars correspond to 150 μ m. B) SEM images of P-TOS (left) and ChA (right) micropillar arrays and the image of a single micropillar in a magnification (1000X) on the μ AA. Scale bars correspond to 75 μ m for the arrays and 20 μ m for the zoomed images. C) Graphic representation of the contact profilometer measurements of a P-TOS (left) and ChA (right) micropillar.

Interestingly, DMSO hydrogel, P-TOS ionogel and ChA ionogel micropillars attached very strongly to the surface of the Mylar® substrate, without the need of any surface functionalisation. UV light, used for photopolymerisation, was the only activation source applied that could be responsible for the micropillars-substrate bond. They remained attached to the substrate of the Mylar® even after rinsing them several times with IPA and DI H₂O. It is well known that UV light enhances the adhesion of polymer matrices on polymeric substrates using UV photografting ³⁷. This is explained because UV radiation initiates the polymerisation by activating not only the initiators and monomers but also the polymer chains on the surface of the polymeric substrate, grafting both materials together. Wang *et al.*³⁷ reported that UV (365 nm) improved the adhesion of acrylamide to polyethylene.

To the best of our knowledge, this is the first time that micrometer size ionogel pillar arrays have been fabricated on a plastic substrate with dimensions as small as 75 µm diameter using just a photomask. This is a considerable achievement on the microstructuration of ionogels. Ionogels have been microfabricated using soft imprinting lithography ³⁸, inkjet printing with photopolymerisation ^{39,40} and two-photon polymerisation ^{41,42}, achieving micron sized features. Particularly, two photon polymerisation of ionogels, using light pulses of femtoseconds, leads to 1 µm resolution, creating well-defined and reproducible ionogel microstructures. However, this technique is hardly available in any laboratory due to the elevated cost of the equipment. The use of the combination of a photomask as µAA, and UV exposure is an efficient methodology to create well-defined and positioned microstructures, in a fast and cost-effective way in a large scale format.

4.2.2 Colorimetric pH sensing assay

According to the previous section, ChA ionogel micropillars showed the most

symmetric shape and the larger micropatterned areas. Therefore, this ionogel was used to develop a pH responsive polymer micropillar array. ChA ionogel micropillars were doped with the BP pH indicator, as presented in Chapter 3, since the BP changes colour from yellow to green at the 4-9 pH range, in the ionogel. The flat top surface of the micropillar would enable a better focusing and a more reliable colour measurement due to their reproducible shape, with the ionogel covering the whole area of the transparent dots, facilitating imaging.

The ionogel prepolymer solution was made, as explained in the section 4.4.2, by adding 5 mg of BP to the prepolymer mixture containing NIPAAm monomer, mBAAm crosslinker, DMPA photoinitiator and ChA IL.

For the colorimetric tests, Mylar® with the micropillar arrays (μ AA substrate) was integrated in a microfluidic device made of poly(methyl methacrylate) (PMMA), pressure sensitive adhesive (PSA) and cyclic olefin polymer (COP). The microfluidic device contained a chamber on the bottom to place the μ AA substrate. For the fabrication protocol and dimensions are presented in the experimental section 4.4.4, (Figure 4.6). At the same time, the same colorimetric pH test was performed using the same microfluidic design, but with a photopolymerised layer of the BP ChA ionogel in the chamber instead of the integrated μ AA.

In order to monitor the pH of the solution passing through the microchannel under continuous flow, the μ AA was positioned focusing the surface of the array. The different pH solutions were added from the inlet, at a flow rate of 150 μ L min⁻¹, and pictures were taken after 4 min, following a similar protocol than in Chapter 3. Once the images were taken, they were processed with a programmed Raspberry Pi for the microsensor arrays and with ImageJ for the polymer layer (experimental section 4.4.5), and the Hue values from the HSV colorimetric

system were obtained. Hue was used for colorimetric measurements, which is calculated from RGB, since it provides an interpretation of the signal closer to the human vision colour perception. For the microsensors, the software detected the measurement frames (each micropillar) and the Hue value was calculated for every single circle. For the colorimetric measurements of the ionogel layer, the RGB values of 20 random circular areas with a diameter of 75 μm were analysed and the Hue value was calculated introducing these RGB values with the Wolfram alpha online calculator ⁴³.

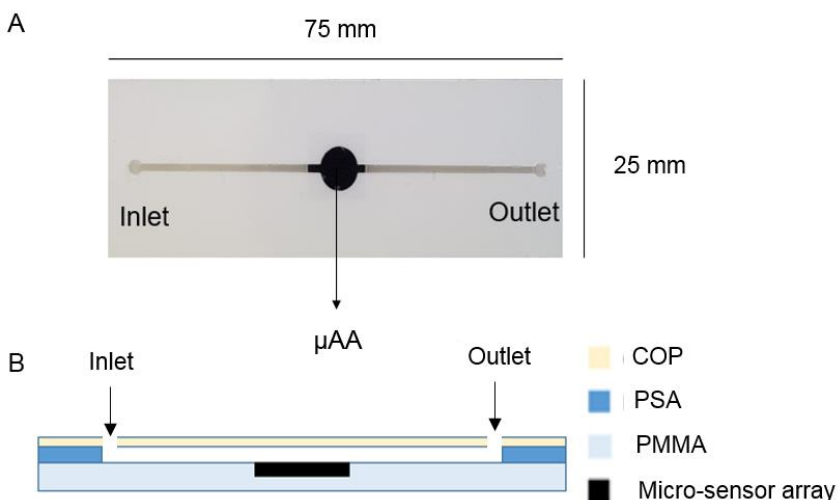


Figure 4.6. A) Picture of the microfluidic device used for the colorimetric characterisation of the μAA under continuous flow. B) Graphical image of the side view of the microfluidic device, composed of three polymeric layers and the integrated μAA substrate.

The image analysis of the surface of the ionogel layer and the ionogel micropillar array showed that, although the BP ionogel layer and micropillar sensor arrays have the same composition, they responded differently to pH, demonstrating that the size of the sensor affected the response. First, the colour change was more

visible for the ionogel layer (Figure 4.7A, top) than for the microsensor arrays (Figure 4.7A, bottom). This result was confirmed by the image analysis of the pictures taken in presence of solutions of different pHs. Two colour changes were observed on the ionogel layer due to variations on the pH of the solution, while just a single colour change was detected when using the micropillar array (Figure 4.7B). Moreover, the colours detected were slightly different. Figure 4.7C shows the Hue colour diagram, where the values obtained represent the green colour but with different tonalities or Hue. In chapter 3, the BP sensor changed gradually over the pH range 4 to 9, as corresponds to BP indicator⁴⁴, going from yellow to purple showing the intermediate colours in its way. In the case of the ionogel layer in this chapter, this gradual colour change from yellow to purple was observed in two stages. A Hue value of 86.0 ± 0.8 was obtained at pH 2, increasing to 114 ± 4 at pH 4 (from yellow to green). Then a second colour change was observed at pH 9, where the Hue value gradually varies from 109.0 ± 0.8 to 147 ± 3 when reaching pH 12, representing the switch from green to blue. On the other hand, the microsensor arrays showed green values closer to yellow, with lower Hue values than the layer, and just a colour change in response to pH at pH 12 from 69 ± 3 to 89 ± 3 when reaching pH 12. At this point, the colour of the micropillars changed from yellow to dark green. In both cases, the homogeneity within samples was excellent, as it is evidenced by the tiny error bars corresponding to the standard deviation of 20 micropillar sensors or random areas in the case of the ionogel layer.

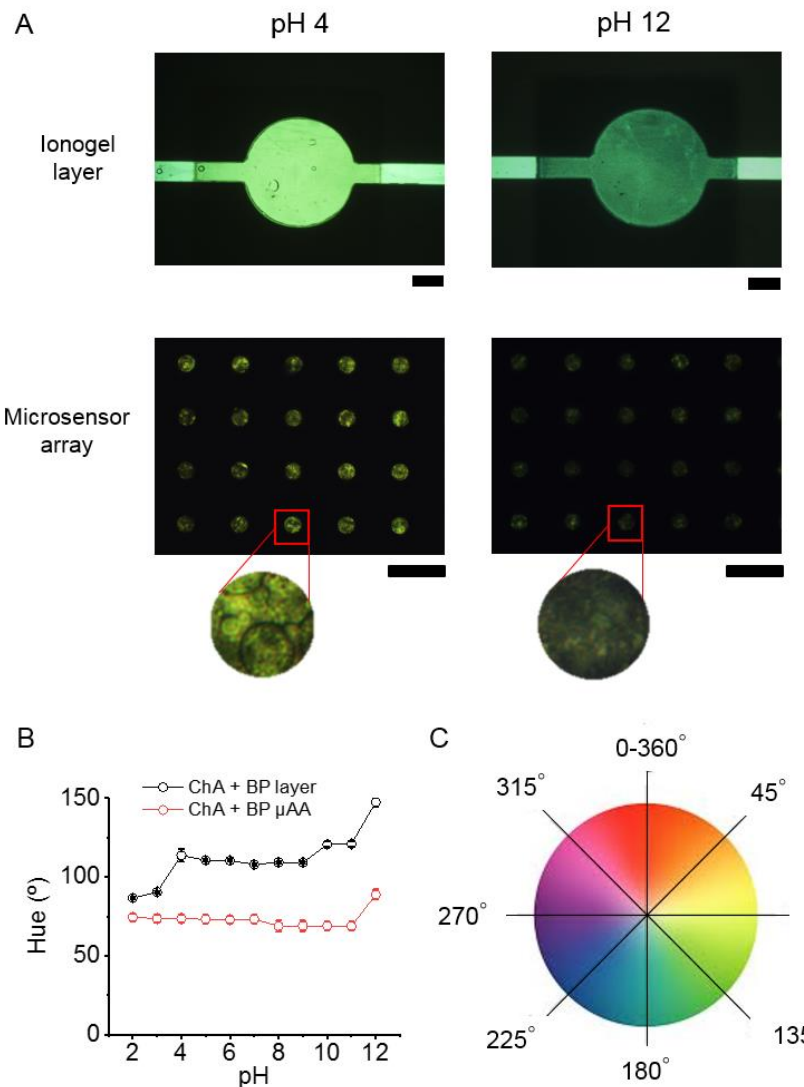


Figure 4.7. A) Optical microscopy images of the BP ionogel sensors at pH 4 and pH 12 for both surfaces, the ionogel layer (top, ruler 2 mm) and the μ AA sensor substrate with a zoomed micropillar (bottom, ruler 200 μ m). B) Plot displaying the colorimetric behaviour of the sensors over the 2 – 12 pH range. Error bars correspond to the standard deviation from the mean for $n = 20$. C) Hue diagram from the HSV colour measurement system.

The main hypothesis of this work was that the miniaturisation of the ionogel sensing materials on μ AA substrates, producing multiple size decreased sensors in an array format, would lead to improved colorimetric analysis. Nevertheless, a similar behaviour was observed for the μ AA sensor substrate compared to an ionogel layer with comparable experimental errors. Nevertheless, this is just a preliminary study of the possibilities of the μ AA sensor substrate thus, further experiments with different configurations and materials need to be performed in order to validate our hypothesis. As a positive remark on the use of the μ AA sensor substrate, in the current configuration, is its fast response time. The ionogel layer sensor needed 4 min to have a homogeneous response all over the sensor surface, while the μ AA sensor substrate immediately changed colour when in contact with the pH 12 solution, < 0.5 s. This indicates that the miniaturisation of sensors improves the mobility and diffusion of analytes within the ionogel matrix, an advantage previously reported for miniaturised sensors¹¹. In addition, a distinctive property of miniaturisation is the increased surface area/volume ratio, which also enhances diffusion within sensing materials, and thus, speeds up sensing times³³.

The results of this chapter suggest that when using the same ionogel composition, the detection of a colour change is less sensitive in the miniaturised polymer structure than in the layer. In the two BP ionogel sensor configurations presented here, layer and μ AA sensor substrate, the only variable is the dimension of the sensor. Actually, the miniaturisation of the ionogel to a μ AA sensor substrate format creates arrays of sensors, where each sensing micropillar, with a volume of 2×10^{-4} mm³, could work independently from each other, while the ionogel layer has total volume of 15.7 mm³. Actually, the ionogel sensors reported in Chapter 3 (volume 1 mm³), seem to have an adequate miniaturisation range that guarantees the sensing performance of the ionogel sensors in comparison with

the two configurations reported in this chapter, and present good response times as long as they have a good pH detection performance for the pH range 2 to 12. Due to the high mobility in and out of the ionogel, which is increased with the miniaturisation of the sensor, the release of the BP pH indicator could be higher for the μ AA substrate than for the layer thus, decreasing its sensitivity.

Nevertheless, this μ AA sensor substrate could be used with other approaches, such as specific enzymatic assays that could prove the functionality of the micropillars as optical sensitive sensors with lower risk of reagents releasing from the matrix due to the bigger size of the enzymes. Another option would be to use a more sensitive signal transduction mechanism, such as luminescence for the detection of the analyte.

4.3 Conclusions

This chapter presents a novel microfabrication technique for the high throughput generation of well positioned microsensor arrays in a flexible substrate, μ AA, with an easy integration in LOC devices. A flexible photomask (Mylar[®]), composed of specially designed transparent and black areas was used as substrate. Then, photopolymerisable materials, which can be used as sensors, were UV light polymerised in the Mylar[®] to generate a high density of microsensor arrays in a single step.

Different polymeric photopolymerisable materials, hydrogels and ionogels, were tested in order to investigate their suitability for the fabrication of a high density μ AA of micropillars. P-TOS and ChA ionogels showed the best performance, with high reproducibility in micropillar density, shape and size. The micropillars made of ChA were cylindrical and more symmetric than the P-TOS micropillars, enabling a better focusing on the surface during imaging and colorimetric

analysis for the assay.

Besides, the use of the photomasks and UV-light for polymerisation enabled the strong attachment of the ionogel micropillars to the substrate without the need of any surface modification. At the same time, the photomask facilitated the automated imaging analysis of colorimetric reactions thanks to the well-defined sensing areas, which are limited by design. In addition, the black substrate of the background enabled better optics, avoiding any background noise signal that usually comes during colorimetric measurements.

The ionogel material was modified with a pH indicator to add as a sensor material. According to the results of the colorimetric assay, differences were observed when using the same material as an ionogel layer or as a μ AA sensor substrate. In the array, the small dimensions of the sensor could promote a higher diffusion and mobility of molecules in and out of the ionogel, enhancing the release of the BP pH indicator and thus, decreasing the sensitivity of the array. On the other hand, the response of the ionogels to pH took 4 min for the ionogel layer, whereas the μ AA sensor substrate responded faster (< 0.5 s).

This chapter presents the first step towards an easy and low-cost fabrication of microsensors arrays on photomasks, elucidating the advantages of ionogels to be used as patternable microsensors. The development of the μ AA sensor substrate is still in its infancy. Nevertheless, I believe that has a great potential to produce high density microsensor arrays in a fast and reproducible way, and with some optimisations, it will be useful as easy integrable flexible sensing element for LOC devices.

4.4 Experimental

4.4.1 Materials

Ionogel: N-isopropylacrylamide (NIPAAm) monomer, dimethoxy-2-phenylacetophenone (DMPA) photoinitiator, N,N'-Methylenebisacrylamide (mBAA) crosslinker, acetic acid, dimethyl sulfoxide (DMSO), 1-ethyl-3-methylimidazolium ethyl sulfate (EMIES), 1-tetrabutylphosphonium p-toluenesulfonate (P-TOS) and Choline Acetate (ChA) were purchased from Sigma Aldrich, Spain.

Microfluidic device: PMMA (Microplanet Laboratorios, Spain), PSA (Adhesive research, Ireland) and COP (Chipshop microfluidics, Germany) polymers were used. COP and PSA were cut with a cutting plotter C6000-40 (Graphtec, Spain) and PMAA with a laser platform (Universal Laser Systems). The luers and the tubing were purchased from Chipshop microfluidics, Germany.

4.4.2 Synthesis of the prepolymer solutions

Two different hydrogels and three ionogels were synthesised, the optimised composition of each polymer for the better physical stability are summarised in Table 4.1:

Table 4.1. Summary of the different polymers tested and their compositions.

Polymer type	Solvent	NIPAAm:mBAAm:DMPA
Hydrogel	Acetic acid (1.5 mL)	452:20:20 (mg)
Hydrogel	DMSO (1 mL)	452:10:10 (mg)
Ionogel	DCA (1.5 mL)	452:30:30 (mg)
Ionogel	p-TOS (1.2 mL)	452:20:20 (mg)
Ionogel	ChA (1 g)	452:30:30 (mg)

For P-TOS and ChA IOs, the ILs were first melted at 120 °C, and then the rest of the reagents were mixed and kept stirring at 100 °C for 30 min until they were completely dissolved. For the rest of the prepolymer solutions, the reagents were directly mixed at 45 °C until dissolved.

For the μAA sensor substrate, the ionogel was doped with BP as follows: 226 mg of NIPAAm, 15 mg of MBAAm, 15 mg of DMPA, 500 mg of Choline Acetate and 5 mg of BP mixed until dissolved. The IL was first melted at 120 °C, and then the rest of the reagents were mixed and kept stirring at 120 °C for 30 min until complete solution.

4.4.3 Fabrication of the micropillars

An array of micrometer size ionogel pillars was created on the inked side of a Mylar® photomask (JD Photo Data, UK) by photopolymerisation. This photomask is a layer of PET with black ink on one side, creating a specific pattern -designed with AUTOCAD program (Student Edition)- of transparent and black areas composed by an array of individual circular transparent dots. The

dimensions of the photomask were 1 cm x 1 cm, and each circular shape sensor had a diameter of 75 μm separated from each other by 150 μm .

To create the ionogel pillars, Figure 4.5, the prepolymer solution was heated at 80 °C, and the mask at 45 °C. Then, 50 μL of the prepolymer solution were drop casted on top of the inked side of the photomask, and the film applicator ZUA 2000 (Zehntner Testing Instruments) was滑ed to create a layer of 400 μm of ionogel. The photomask was then placed upside down in the UV-KUB 2 lamp (KLOÉ) equipment, and UV light (365 nm) was applied through the photomask. The ionogel pillars were created on the transparent dots of the mask.

The parameters used were different depending on the prepolymer solution and the fabrication method. The optimised parameters for the fabrication of micropillar arrays are summarised in Table 4.2.

The coverage of the photomask with photopolymerised micropillars and their shape was characterised with a metallographic microscope, and their height was measured with a DektakXT (Bruker) profilometer. For the observation of the pillars a scanning electron microscope (SEM) Hitachi S-4800 was used.

Table 4.2. Summary of the photopolymerisation parameters and results.

Polymer type	Solvent	Photopolymerisation parameters	Patterning results
Hydrogel	Acetic acid (1.5 mL)	14 pulses 20 s ON + 30 s OFF ($9.2 \text{ mJ cm}^{-2} \text{ s}^{-1}$)	Few micropillars. Edges: block polymerisation
Hydrogel	DMSO (1.0 mL)	10 pulses 20 s ON + 30 s OFF ($9.2 \text{ mJ cm}^{-2} \text{ s}^{-1}$)	Low coverage, no reproducible heights
Ionogel	DCA (1.5 mL)	9 pulses 20 s ON + 30 s OFF ($9.2 \text{ mJ cm}^{-2} \text{ s}^{-1}$)	High coverage with hardly removable residues on the black areas
Ionogel	P-TOS (1.2 mL)	9 pulses 20 s ON + 30 s OFF ($9.2 \text{ mJ cm}^{-2} \text{ s}^{-1}$)	High coverage, reproducible heights
Ionogel	ChA (1.0 g)	7 pulses 20 s ON + 30 s OFF ($9.2 \text{ mJ cm}^{-2} \text{ s}^{-1}$)	High coverage, reproducible heights

4.4.4 Fabrication of the microfluidic device

The colorimetric characterisation of the sensing performance was carried out in a microfluidic device, under continuous flow conditions. For that, a simple system was AutoCAD designed, and then fabricated by cut and lamination techniques using the cutting plotter and the laser platform. The device is comprised of three layers: cyclic olefin polymer (COP) of 100 μm thickness on the top, pressure sensitive adhesive (PSA) layer of 127 μm in the middle and a polymethyl methacrylate (PMMA) layer with a thickness of 1.1 mm at the bottom (Figure 4.6). The device dimensions are 75 x 25 mm, with an inlet and an outlet of 2 mm diameter, with a circular chamber of 6 mm diameter in the center of the channel (1 mm wide, 63 mm long) for the imaging of the microsensor array that would be placed below. PSA and COP were cut with the cutting plotter, and

PMMA was cut with the CO₂ laser. To place the μAA substrate or for the macro scale experiment, to place the BP ionogel layer, a 10 x 10 x 0.2 mm chamber was made by laser ablation in the middle of the PMMA layer cut by CO₂ laser. For the colorimetric experiments with the ionogel layer, 15 μL of BP doped prepolymer was added in the chamber of the PMMA substrate and photopolymerised for 10 min with UV 365 nm. Then, once the μAA or the ionogel layer were placed in the chamber, the three polymeric layers were aligned and the connections (luers and tubing) were set.

4.4.5 Colorimetric assay and imaging

In order to perform the colorimetric measurements under continuous flow, aqueous solutions of different pH values were passed through the microfluidic channel with a flow rate of 150 μL min⁻¹, using a Standard Infuse/Withdraw Pump 11 Elite Programmable Syringe Pump (Harvard apparatus, Spain). The aqueous solutions were prepared using HCl for pH 1 to 7 and NaOH for pH 8 to 14). For the acidic series, pH 1 stock solution was prepared as 0.1 M HCl solution in DI water, and the subsequent pH solutions were by diluting this one. For the basic series, the same procedure was followed, from NaOH 1 M (pH 14) diluting for pH 12, 11, 10, 9 and 8.

With the microfluidic device placed upside down with the micropillars facing the objective of the inverted microscope with a CMOS camera (Beortek), the 20x objective was used for a more detailed view of the colorimetric response. A picture of the sensing area was taken after 4 min in contact with the flowing pH solution with the software application (TCapture, Tucsen Photonics). For the controlled lighting, a light source composed of a LED ring-light in a completely dark room.

For the imaging of the ionogel layer the pictures were analysed with ImageJ. Circular ROIs of 75 μm diameter were selected and the RGB values obtained. This RGB values were then converted to Hue from the HSV system using Wolfram Alpha Computational Intelligence.

For the microsensor arrays, the colours of the sensing micropillars were measured using a Raspberry Pi with a Raspbian operative system. The program detected the ROIs or the individual microsensors from the array, and converted the image to a binary black and white model. Then, the Hue values from each of the micropillar were extracted and the Hue values of the background (noise) were removed, normalising them to 0. Finally the program made an average value with all the Hue values of each sensor.

4.5 References

1. Adhikari, B.; Majumdar, S. Polymers in sensor applications. *Progress in polymer science* 2004, 29, 699-766.
2. Spychalska, K.; Zajac, D.; Baluta, S.; Halicka, K.; Cabaj, J. Functional Polymers Structures for (Bio) Sensing Application—A Review. *Polymers* 2020, 12, 1154.
3. Huang, J.; Li, M.; Zhang, P.; Ding, L. Temperature controlling fiber optic glucose sensor based on hydrogel-immobilized GOD complex. *Sensors Actuators B: Chem.* 2016, 237, 24-29.
4. Saez, J.; Benito-Lopez, F.; Arana, G.; Fernandez-Cuadrado, L. A. In *In Ionogel-based nitrate sensor device*; 2016 IEEE SENSORS; IEEE: 2016;, pp 1-3.
5. Seo, J.; Lee, T. J.; Lim, C.; Lee, S.; Rui, C.; Ann, D.; Lee, S.; Lee, H. A highly sensitive and reliable strain sensor using a hierarchical 3D and ordered network of carbon nanotubes. *Small* 2015, 11, 2990-2994.
6. Yin, M.; Yao, M.; Gao, S.; Zhang, A. P.; Tam, H.; Wai, P. A. Rapid 3D patterning of poly (acrylic acid) ionic hydrogel for miniature pH sensors. *Adv Mater* 2016, 28, 1394-1399.
7. Yin, M.; Zhao, Q.; Wu, J.; Seefeldt, K.; Yuan, J. Precise micropatterning of a porous poly (ionic liquid) via maskless photolithography for high-performance nonenzymatic H₂O₂ sensing. *ACS nano* 2018, 12, 12551-12557.
8. Sangsuwan, A.; Narupai, B.; Sae-ung, P.; Rodtamai, S.; Rodthongkum, N.; Hoven, V. P. Patterned poly (acrylic acid) brushes containing gold nanoparticles for peptide detection by surface-assisted laser desorption/ionization mass spectrometry. *Anal. Chem.* 2015, 87, 10738-10746.
9. Hsu, C.; Su, F.; Peng, P.; Young, H.; Liao, S.; Wang, G. Highly sensitive non-enzymatic electrochemical glucose biosensor using a photolithography fabricated micro/nano hybrid structured electrode. *Sensors Actuators B: Chem.* 2016, 230, 559-565.
10. Wang, Y.; Cui, Y.; Cheng, Z.; Song, L.; Wang, Z.; Han, B.; Zhu, J. Poly (acrylic acid) brushes pattern as a 3D functional biosensor surface for microchips. *Appl. Surf. Sci.* 2013, 266, 313-318.
11. Dahlin, A. B. Size matters: problems and advantages associated with highly miniaturized sensors. *Sensors* 2012, 12, 3018-3036.
12. Galvez, J. M. M.; Garcia-Hernando, M.; Benito-Lopez, F.; Basabe-Desmonts, L.; Shnyrova, A. V. Microfluidic chip with pillar arrays for controlled production and observation of lipid membrane nanotubes. *Lab on a Chip* 2020, 20, 2748-2755.
13. Zhang, Y. S.; Khademhosseini, A. Advances in engineering hydrogels. *Science* 2017, 356, 10.1126/science.aaf3627.
14. Krossing, I.; Slattery, J. M.; Daguenet, C.; Dyson, P. J.; Oleinikova, A.; Weingärtner, H. Why are ionic liquids liquid? A simple explanation based on lattice and solvation energies. *J. Am. Chem. Soc.* 2006, 128, 13427-13434.

15. Lodge, T. P. Materials science. A unique platform for materials design. *Science* 2008, 321, 50-51.
16. Le Bideau, J.; Viau, L.; Vioux, A. Ionogels, ionic liquid based hybrid materials. *Chem. Soc. Rev.* 2011, 40, 907-925.
17. Naushad, M.; ALOthman, Z. A.; Khan, A. B.; Ali, M. Effect of ionic liquid on activity, stability, and structure of enzymes: a review. *Int. J. Biol. Macromol.* 2012, 51, 555-560.
18. Ha, S. H.; Lan, M. N.; Lee, S. H.; Hwang, S. M.; Koo, Y. Lipase-catalyzed biodiesel production from soybean oil in ionic liquids. *Enzyme Microb. Technol.* 2007, 41, 480-483.
19. Billard, I.; Moutiers, G.; Labet, A.; El Azzi, A.; Gaillard, C.; Mariet, C.; Lützenkirchen, K. Stability of divalent europium in an ionic liquid: Spectroscopic investigations in 1-methyl-3-butylimidazolium hexafluorophosphate. *Inorg. Chem.* 2003, 42, 1726-1733.
20. Gao, J.; Ndong, R. S.; Shiflett, M. B.; Wagner, N. J. Creating nanoparticle stability in ionic liquid [C₄mim][BF₄] by inducing solvation layering. *ACS nano* 2015, 9, 3243-3253.
21. Fujita, K.; Ohno, H. Enzymatic activity and thermal stability of metallo proteins in hydrated ionic liquids. *Biopolymers* 2010, 93, 1093-1099.
22. Fujita, K.; MacFarlane, D. R.; Forsyth, M.; Yoshizawa-Fujita, M.; Murata, K.; Nakamura, N.; Ohno, H. Solubility and stability of cytochrome c in hydrated ionic liquids: effect of oxo acid residues and kosmotropicity. *Biomacromolecules* 2007, 8, 2080-2086.
23. Quental, M. V.; Passos, H.; Kurnia, K. A.; Coutinho, J. A.; Freire, M. G. Aqueous biphasic systems composed of ionic liquids and acetate-based salts: phase diagrams, densities, and viscosities. *Journal of Chemical & Engineering Data* 2015, 60, 1674-1682.
24. Mondal, D.; Sharma, M.; Quental, M. V.; Tavares, A. P.; Prasad, K.; Freire, M. G. Suitability of bio-based ionic liquids for the extraction and purification of IgG antibodies. *Green Chem.* 2016, 18, 6071-6081.
25. Tateishi-Karimata, H.; Sugimoto, N. Structure, stability and behaviour of nucleic acids in ionic liquids. *Nucleic Acids Res.* 2014, 42, 8831-8844.
26. Nishimura, N.; Nomura, Y.; Nakamura, N.; Ohno, H. DNA strands robed with ionic liquid moiety. *Biomaterials* 2005, 26, 5558-5563.
27. Sharma, M.; Mondal, D.; Singh, N.; Trivedi, N.; Bhatt, J.; Prasad, K. High concentration DNA solubility in bio-ionic liquids with long-lasting chemical and structural stability at room temperature. *RSC Advances* 2015, 5, 40546-40551.
28. Kalantar-Zadeh, K. *Sensors: an introductory course*; Springer Science & Business Media: 2013; .
29. Fraden, J. *Handbook of modern sensors: physics, designs, and applications*; Springer Science & Business Media: 2004; .
30. Chen, C.; Wang, J. Optical biosensors: an exhaustive and comprehensive review. *Analyst* 2020, 145, 1605-1628.

31. Cichosz, S.; Masek, A.; Zaborski, M. Polymer-based sensors: A review. *Polym. Test.* 2018, 67, 342-348.
32. Derkus, B. Applying the miniaturization technologies for biosensor design. *Biosensors and Bioelectronics* 2016, 79, 901-913.
33. Czugala, M.; O'Connell, C.; Blin, C.; Fischer, P.; Fraser, K. J.; Benito-Lopez, F.; Diamond, D. Swelling and shrinking behaviour of photoresponsive phosphonium-based ionogel microstructures. *Sensors Actuators B: Chem.* 2014, 194, 105-113.
34. Cho, E. J.; Bright, F. V. Pin-printed chemical sensor arrays for simultaneous multianalyte quantification. *Anal. Chem.* 2002, 74, 1462-1466.
35. Hajipour, A.; Rafiee, F. Basic ionic liquids. A short review. *Journal of the Iranian Chemical Society* 2009, 6, 647-678.
36. Lopes, J. M.; Paninho, A. B.; Môlho, M. F.; Nunes, A. V.; Rocha, A.; Lourenço, N. M.; Najdanovic-Visak, V. Biocompatible choline based ionic salts: Solubility in short-chain alcohols. *The Journal of Chemical Thermodynamics* 2013, 67, 99-105.
37. Wang, J.; Liang, G.; Zhao, W.; Lü, S.; Zhang, Z. Studies on surface modification of UHMWPE fibers via UV initiated grafting. *Appl. Surf. Sci.* 2006, 253, 668-673.
38. Zhong, Y.; Nguyen, G. T.; Plesse, C.; Vidal, F.; Jager, E. W. Tailorable, 3D structured and micro-patternable ionogels for flexible and stretchable electrochemical devices. *Journal of Materials Chemistry C* 2019, 7, 256-266.
39. Tijero, M.; Díez-Ahedo, R.; Benito-Lopez, F.; Basabe-Desmonts, L.; Castro-López, V.; Valero, A. Biomolecule storage on non-modified thermoplastic microfluidic chip by ink-jet printing of ionogels. *Biomicrofluidics* 2015, 9, 044124.
40. Loeffelmann, U.; Wang, N.; Mager, D.; Smith, P. J.; Korvink, J. G. Solvent-free inkjet printing process for the fabrication of conductive, transparent, and flexible ionic liquid-polymer gel structures. *Journal of Polymer Science Part B: Polymer Physics* 2012, 50, 38-46.
41. Oubaha, M.; Kavanagh, A.; Gorin, A.; Bickauskaite, G.; Byrne, R.; Farsari, M.; Winfield, R.; Diamond, D.; McDonagh, C.; Copperwhite, R. Graphene-doped photo-patternable ionogels: tuning of conductivity and mechanical stability of 3D microstructures. *Journal of Materials Chemistry* 2012, 22, 10552-10559.
42. Kavanagh, A.; Copperwhite, R.; Oubaha, M.; Owens, J.; McDonagh, C.; Diamond, D.; Byrne, R. Photo-patternable hybrid ionogels for electrochromic applications. *J. Mater. Chem.* 2011, 21, 8687-8693.
43. Wolfram Alpha Computational Intelligence. <https://www.wolframalpha.com/> (accessed 16/02, 2021).
44. Sabnis, R. W. *Handbook of acid-base indicators*; CRC Press: 2007.

5

Polymeric Micropillar Arrays and Microfluidics for the Production and Monitoring of Lipid Membrane Nanotubes

Lipid membrane nanotubes are widely used templates for *in vitro* studies of cellular processes. Commonly, they are individually made using tedious and sophisticated techniques thus, methods to control, high throughput produce and monitor lipid membrane nanotubes are on demand. In this chapter a microfluidic lab-on-a-chip approach using an integrated micropillars array of different materials is presented. The combination of microfluidics and materials science enables the simultaneous formation of multiple well positioned, free-standing lipid membrane nanotubes and to control their length and radius.

*The work described in this chapter has been done in collaboration with the group of Anna Shnyrova from the Biofisika institute (CSIC,UPV/EHU). Parts of this Chapter have been published in: Galvez, J. M. M., Garcia-Hernando, M., Benito-Lopez, F., Basabe-Desmonts, L. & Shnyrova, A. V. Microfluidic chip with pillar arrays for controlled production and observation of lipid membrane nanotubes. *Lab Chip*. 2020, 2748-2755.

5.1 Introduction

Lipid nanotubes (NTs), 1D hollow membrane cylinders made of biologically important lipids, are a versatile and adequate template for quantitative reconstitution and *in vitro* analysis of membrane properties and related events. Particularly, lipid NTs have been extensively used to study protein and lipid sorting^{1,2}, mechanisms of membrane fission^{3,4}, and membrane remodelling by specialised proteins⁵.

Traditionally, the lipid NTs are formed by applying a local pulling force to a parent reservoir membrane⁶, which can be a planar bilayer lipid membrane or a giant unilamellar vesicle (GUV), a membrane sphere of several microns in diameter. The pulling is usually done using a micro-sized object, such as a microsphere, a tip of a glass pipette controlled with a precise manipulator system or optical tweezers^{6,7}. The lipid NT radius goes from a few to hundreds of nanometres, and the ratio between the bending rigidity of the previously mentioned parent membrane and the lateral tension define it⁶. The length of the lipid NT is more variable, and is conditioned by the manual operation.

Pucadyil and co-authors proposed a simplification for the production of lipid NTs^{8,9}, with a method based on rolling silica beads of 20 µm diameter covered with lipids over a passivated glass substrate. This enabled the fast and high throughput production of lipid NTs of several microns in length. Further development of this system was reported by Dar and co-authors, who achieved the formation of multiple lipid NTs applying a liquid flow to prehydrated lipid multilamellas^{4,10}. In this approach, the interaction of the lipids with the defects of the glass substrate stabilised the lipid NT position and geometry. Although this system has been posteriorly used for *in vitro* studies of lipid NTs^{4,11}, the

length and radius of the lipid NTs were random and could not be controlled, and the proximity between the positioned lipid NTs and the glass substrate may affect the interaction of the lipid NTs with target species of the ongoing *in vitro* assay.

Producing the lipid NTs in suspension sorts out the inconvenience of the proximity between the lipid NTs and the substrate; however, if they are not positioned, their monitoring would not be possible. Giving them partial support, like binding the ends with an adequate material and leaving the rest of the NT in suspension enables the positioning to free-standing lipid NTs, using the height of the micropillars to avoid proximity between the NTs and the substrate. SU-8 is a widely known patternable material with excellent mechanical stability that enables the creation of microstructures with precisely controlled height, size and shape via photolithography¹². Hurtig and co-authors showed for the first time that the lipid NTs pulled from a GUV membrane could be weaved around SU-8 photoresist micropatterns^{13,14}, demonstrating that SU-8 is a suitable material to give support to the lipid NTs and their reservoirs. This approach allowed the precise control on the length and geometry of the lipid NTs, but it required tedious micromanipulation, specific and expensive equipment, long operation times and trained personnel to perform it. Moreover, the lipid NTs could only be analysed individually, complicating the collection of enough data for statistical analysis.

Microfluidics enables precise control of very small volumes of fluids, μL to nL , guaranteeing an adequate environment for the performance of sample preparation, detection and monitoring of events in the same device¹⁵. Moreover, combining microfluidics with micropatterning, or in other words, combining the contributions of Pucadyil^{8,9}, Dar^{4,10} and Hurtig^{13,14}, the formation of partially

supported NTs with controlled length, using rolling beads within a microfluidic device could become a reality. However, in order to be able to modulate the radii of the lipid NTs as well, the interaction between the supportive material and the lipid should be modified. Therefore, a change on the chemistry of the supportive material should be also considered.

The interaction of Ionic Liquids (ILs) with lipid bilayers is becoming an interesting area of research due to the expansion of the use of ILs in biology, pharma and food industry¹⁶. ILs are ionic salts with a melting point below 100 °C and with interesting chemical properties such as high conductivity, negligible vapour pressure and high electrochemical and thermal stability^{17,18}. When ILs are incorporated in a solid-like polymeric matrix, ionogels are generated, and their physical and chemical properties can be easily modified and tuned by just changing the IL¹⁹. Jing *et al.* for instance, reported that when lipids are immersed in ILs, the cation of the IL tends to get inserted in the membrane, causing strong hydrophobic interactions and damaging the lipid bilayer, which could explain the toxicity of ILs²⁰. This behaviour was confirmed as well by Sharma and Mukhopadhyay²¹. This effect depends on the structure of the cation, which influences the interaction, reporting stronger bonding for those with a long hydrocarbon side chain. To avoid this potential harmful effect of the ILs, their entrapment within polymeric networks avoids the release of the IL to the solution, as previously reported by the Microfluidics Cluster UPV/EHU for 1-ethyl-3-methylimidazolium ethyl sulphate (EMIES) and trihexyltetradecylphosphonium dicyanamide (DCA) ILs¹⁹. Therefore, these types of ionogels can be used in direct contact with lipid bilayers without perturbing their structure. Ionogels are a novel type of patternable hybrid materials, as demonstrated in Chapter 3 and 4, which are emerging in the device fabrication sector, due to their interesting properties; they embrace the physical

properties of the polymer and the chemical stability of the IL. All of the above, make ionogels interesting and tuneable materials for the fabrication of micropillars as supporting materials for lipid NTs.

Here, we propose a simple and user-friendly hybrid microfluidic device for the fast formation of many free-standing lipid NTs with controlled geometry. Our system consists of polymeric micropillar arrays standing at set distances over a cover glass bottom of a microfluidic chip. The lipid NTs are produced by rolling silica microspheres covered with membrane lamellas over the micropillar arrays in a microfluidic channel (Figure 5.1). The resulting lipid NTs are attached to the top of the micropillars, being their length set by the interpillar distance. The relatively small height of the micropillars allows for real-time observation of the lipid NTs' behaviour with high-resolution objectives of an inverted fluorescence microscope, as well as it avoids the artefacts resulting from the proximity with the substrate. Moreover, the radius of the lipid NTs can be controlled by changing the chemistry of the micropillars and thus, the extension of the lipid reservoir on the pillars, making the system tuneable by design.

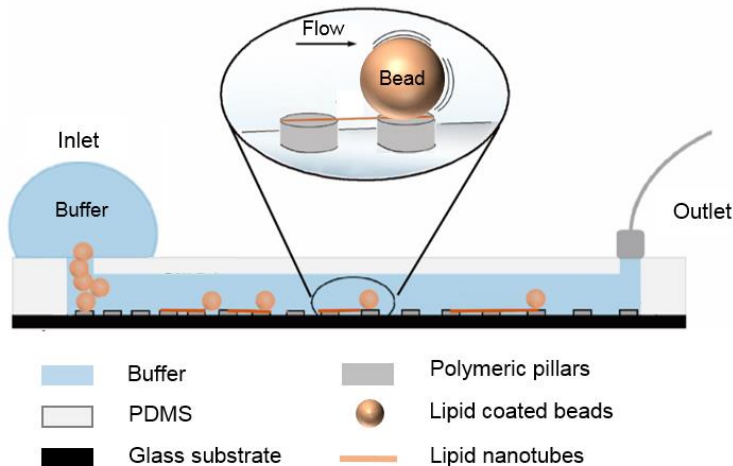


Figure 5.1. Illustration of the microfluidic device for the formation of lipid NTs.

5.2 Results and discussion

5.2.1 Fabrication of the micropillar arrays

Micropillar arrays were obtained with conventional SU-8 photoresist and three ionogels: IO-1 with EMIES IL, IO-2 with DCA IL and IO-3 with choline acetate (ChAc) IL, using the same photomask. The ionogels consisted of one of the ILs, and the polymeric matrix, comprised of poly-N-isopropylacrylamide (pNIPAAm). pNIPAAm was chosen because of its biocompatibility when polymerised 22,23. Moreover, the polymer is photopatternable, as presented and optimised in Chapter 4, allowing the generation of micropillar arrays. In addition, three different ionic liquids were used for the fabrication of the micropillar arrays considering the physico-chemical properties of the ionogels. IO-1 and IO-2 have been previously characterised 19, and their properties differ greatly from each other 19,24, while ChAc (for IO-3) was chosen due to its biocompatibility 25 and hygroscopic nature 26.

When it comes to the patterning of SU-8, a conventional photolithography process was carried out on glass covers, (Figure 5.2A), but for ionogels, a chemical surface functionalisation was necessary for the covalent attachment of the ionogel micropillars to the glass (Figure 5.2B) (experimental section 5.4.2). Previously in my group, glass surfaces were functionalised for the adhesion of ionogels, but for structures much bigger (500 µm), with a bigger contact area with the surface 27. In this chapter, three independent patterned areas of 2 x 8 mm were made on the substrate (Figure 5.2C). Each of them comprises four micropatterned zones with arrays of micropillars of 15 µm diameter separated by 10, 20, 30 and 40 µm (Figure 5.2D). This micropillar configuration was made by design, for beads of 40 µm diameter. For smaller beads, the array

configuration can be easily redesigned to shorten the distance between micropillars, so the beads do not fall to the substrate when rolling. At least three washing steps with 2-isopropanol and DI water were applied to the ionogel micropillar arrays without losing any of the features, regardless of the IL employed for fabrication.

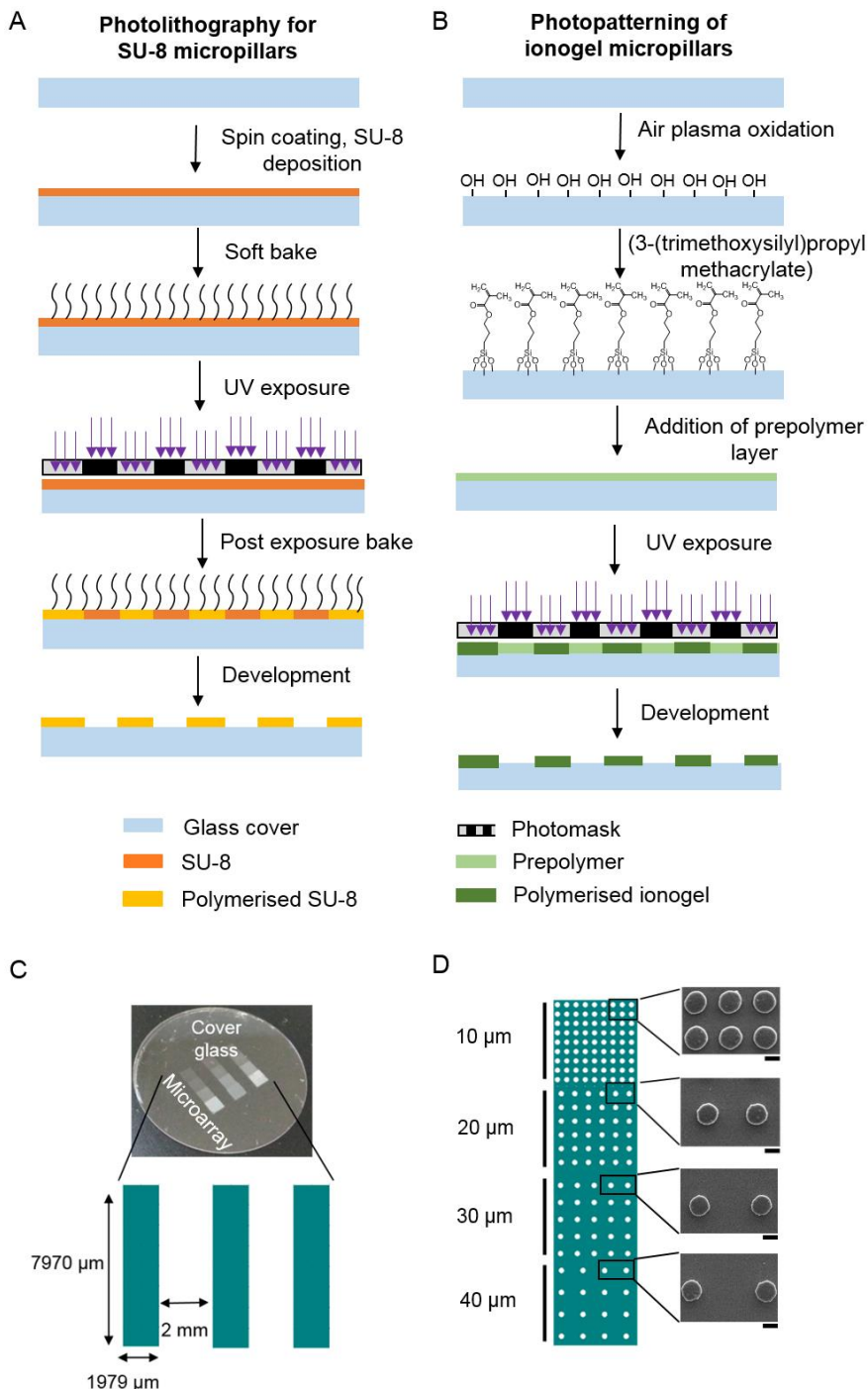


Figure 5.2. A) Scheme of the photolithography process for the fabrication of SU-

8 micropillar arrays. B) Scheme of the microfabrication process for the formation of ionogel micropillar arrays. C) The glass substrate of the microfluidic device with the micropillar arrays patterned on the surface, comprised of three rectangular areas, each of them for a microfluidic channel. The zoomed illustration represents the overall dimensions of the arrays. D) A zoom on one of the rectangular independent areas of micropillar arrays showing the micropillars with the SEM images showing the array zones with 10, 20, 30 and 40 μm separation between pillars. Scale bars are 10 μm .

SU-8 generated very well defined micropillars of 15 μm diameter separated by 10, 20, 30 and 40 μm (Figure 5.3). The obtained height value of the SU-8 micropillars was $4.2 \pm 0.3 \mu\text{m}$ ($n = 10$). For ionogels, although the settings were used to create the same prepolymer layer thicknesses, different micropillar heights were obtained for each ionogel. The measured heights were $2 \pm 1 \mu\text{m}$ for the IO-1, $1.3 \pm 0.4 \mu\text{m}$ for the IO-2 and $3 \pm 1 \mu\text{m}$ for the IO-3 ($n = 10$). The photopolymerisation parameters were optimised for each ionogel, considering the results obtained in Chapter 4, being the UV-light exposure time critical for the fabrication of homogeneous micropillars. For the three ionogels, the photomask and the prepolymer solutions were in direct contact with each other during the polymerisation, to improve resolution. The power of the lamp was set at 20 %, since lower or higher values presented poor resolutions and excess of polymerisation, respectively. Moreover, by using light pulses the resolution of the pattern for the three ionogels was improved.

The obtained micropillars were found to be robust and their surface functionalisation adequate, since the micropillars did not disengage even after experiencing thoroughly washing steps with water and isopropanol. Moreover, the devices used for the creation of the nanotubes were reused a minimum of 10

times, observing no evident damage of the micropillar arrays, demonstrating the stability of the materials and their bonding to the surface.

The three ionogels showed different polymerisation times, being IO-2 < IO-1 < IO-3 (experimental section 5.4.2). Monomer diffusion modulates polymerisation times during the synthesis of the polymer; the higher the diffusion, the faster is the polymerisation time ²⁸. The IL, which acts as a fluid matrix within the polymeric network and improves diffusion within the gels, is the only variable in the ionogel composition in this work, and thus it is responsible for the different polymerisation times. Therefore, it could be hypothesised that choline acetate (IL-3) is the one with a higher diffusion rate, as it was mentioned in Chapter 4.

Although ionogel micropillar arrays were obtained, they presented lower resolution when compared to the SU-8 micropillar arrays (Figure 5.3). 10 µm distance between micropillars was hardly achievable with the ionogels, while higher distances generated well defined micropillars all over the photopolymerised surface. For the best of my knowledge, this is the first time that such resolution has been obtained with photopolymerised ionogels using a polymeric photomask and a conventional UV lamp. As explained in Chapter 4, inkjet printing ^{29,30} and two photon polymerisation ^{31,32} have been used to create micron sized ionogels, with the inconveniences of longer fabrication times for inkjet printing, and the high cost and availability of the equipment for two photon polymerisation.

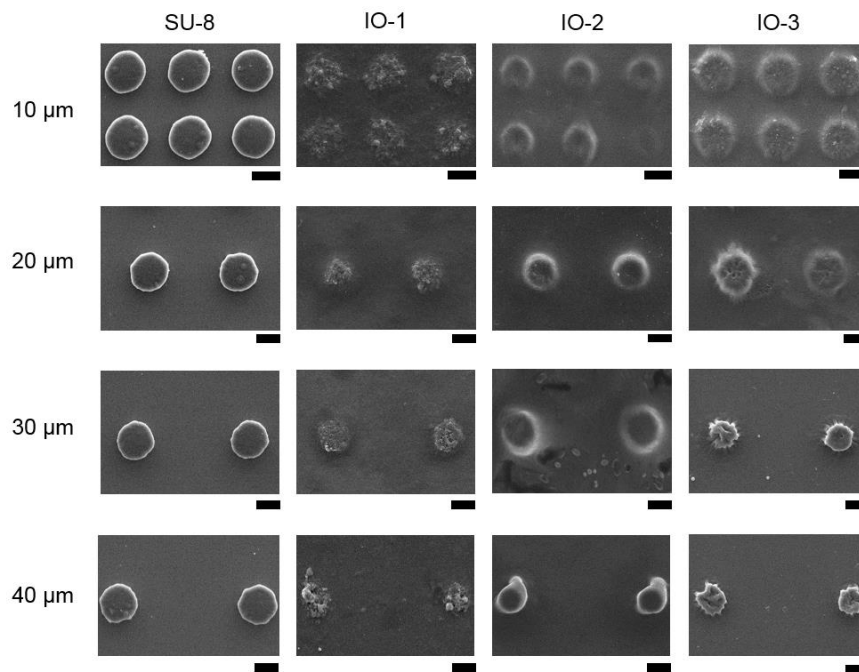


Figure 5.3. SEM images of the 15 μm diameter micropillars made of SU-8, IO-1, IO-2 and IO-3 for four the separations between micropillars: 10, 20, 30 and 40 μm . Scale bar corresponds to 15 μm .

This lower resolution could be explained considering the diffusion and mobility of monomers in the dynamic environment of the prepolymer solution, during the polymerisation process ³³, which is especially tricky to avoid in such small features. Moreover, considering that the solvent percentage affects photopolymerisation ³⁴, evidenced by the influence of the solvent in the resolution of SU-8 features ¹², it can be expected that the percentage of IL in each ionogel prepolymer solution is decisive too. In this case, the IL ratios used were adequate for the formation of a homogeneously spread prepolymer solutions over the substrate, finding a compromise between the quality of the prepolymer layer and the final resolution. Nevertheless, the interaction of the prepolymer

layer with the glass substrate needs to be also considered during the fabrication of the micropillar array, see Chapter 4. For instance, the IO-1 presented poorer shapes for every interpillar space investigated, compared to the other two ionogels. That could be explained considering the hydrophilic nature of IO-1 prepolymer solution and the hydrophobic nature of the functionalised surface (showing acrylate functional groups). The prepolymer solution hardly spread on the surface, demanding a fast manipulation of the samples to create the arrays, generating inhomogeneous features after polymerisation.

The ionogels were formed by the combination of an IL and the pNIPAAm polymer by UV polymerisation. The pNIPAAm is a porous and hydrophilic material with a high water uptake capability. When combined with an IL to generate an ionogel, the properties of the pNIPAAm ionogel such as the porosity and hydrophilicity, vary compared to the bare polymer. Moreover, the physicochemical properties of the ionogels vary when changing the IL. In order to study the physicochemical properties of the four materials, Atomic Force Microscopy (AFM) measurements were performed. For SU-8 micropillars, the surface was found to be similar before and after hydration (Figure 5.4A). On the other hand, the IO-1 has a “sponge” like structure, made of several pores of different sizes, in its dried state¹⁹ (Figure 5.4B, left). This, combined with the hydrophilicity of the EMIES IL, provides to the IO-1 with a high potential for water uptake, resulting in numerous swollen areas in its hydrated state (Figure 5.4B, right). In the case of the IO-2, it displayed some pores in its dried state (Figure 5.4C, left) and although the ionogel swells according to the AFM height scale, they remained well-defined, see AFM picture in Figure 5.4C, right. Nevertheless, due to the hydrophobic nature of the DCA IL, a lower water uptake was reported¹⁹. Finally, in the IO-3 many pores were observed in its dried state (Figure 5.4D, left), while after hydration, the ionogel presented almost no visible

pores, which seemed to be covered by a sponge like swelled state of the ionogel (Figure 5.4D, right). The high swelling observed in IO-3 could be expected because of the highly hygroscopic nature of ChA IL, assuming a bigger water uptake capacity.

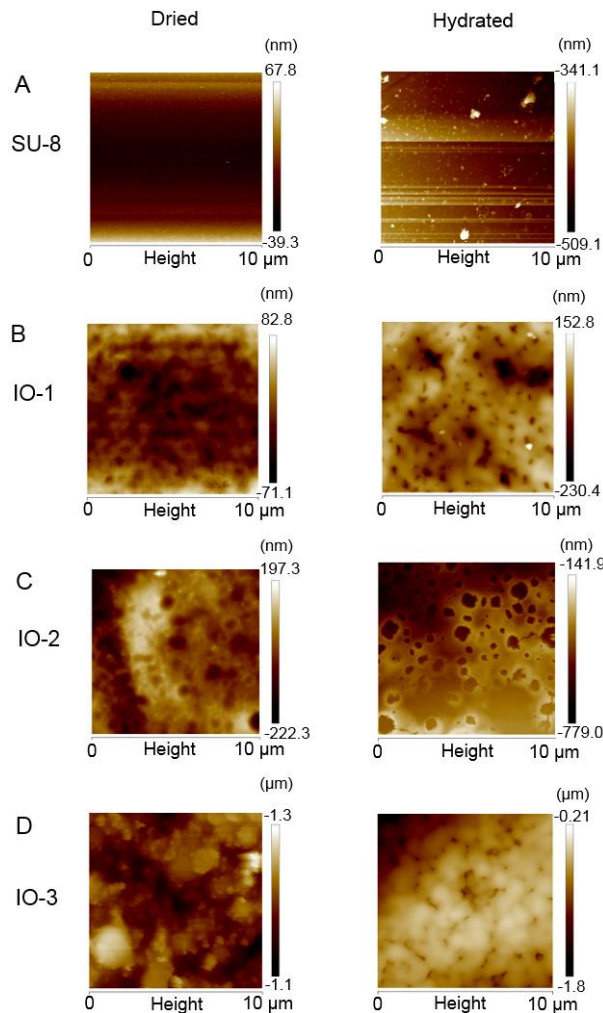


Figure 5.4. AFM images of the surface of the four materials used as micropillars. A) SU-8, B) IO-1, C) IO-2 and D) IO-3, surfaces dry (left) and hydrated (right).

5.2.2 Generation of lipid NTs between micropillars

To induce the formation of lipid NTs between the SU-8 and ionogel micropillars, lipid-coated silica beads were deposited into the inlet of the microfluidic chamber, which was previously filled with the working buffer, see experimental section 5.4.3. First, SU-8 micropillars were used for the optimisation of the production of lipid NTs since previous studies demonstrated their suitability^{13,14}. Two methods were used to make the silica beads to roll over the micropillars: tilting the device and use a laminar flow. For the tilting method, once the silica beads were in the inlet, they were rolled over the SU-8 micropillar arrays by gently tilting the chamber, which caused random movements of the microbeads over the micropillar array, resulting in the formation of a lipid NT net between the micropillar tops (Figure 5.5A).

In order to control the movement of the beads in the microfluidic device and produce lipid NTs with parallel alignments, the silica beads were deposited in the inlet containing the buffer, and a negative flow was induced by pulling the solution from the outlet with a syringe pump, making the beads to roll over the micropillar array in the microfluidic channel. The use of negative pumping instead of infusion reduced the formation of bubbles in the microfluidic channel, improving the formation of NTs. When 20 and 100 $\mu\text{L min}^{-1}$ flows were applied with the syringe pump, individual beads travelled at 21 ± 10 and $397 \pm 81 \mu\text{m s}^{-1}$ in the 40 μm separation region, respectively. In both cases, the beads moved linearly in the direction of the flow while touching the micropillars. As expected, the interaction of the beads with the micropillars resulted in the formation of parallel lipid NTs stretched between the micropillar tops (Figure 5.5B). Negative flows below 20 $\mu\text{L min}^{-1}$ were not sufficient to induce the movement of the beads through the microchannel. The configuration of the micropillar array, the

dimensions of the beads, their density in the solution and the negative flow value need to be optimised for a particular microchannel configuration to obtain well defined parallel lipids NTs.

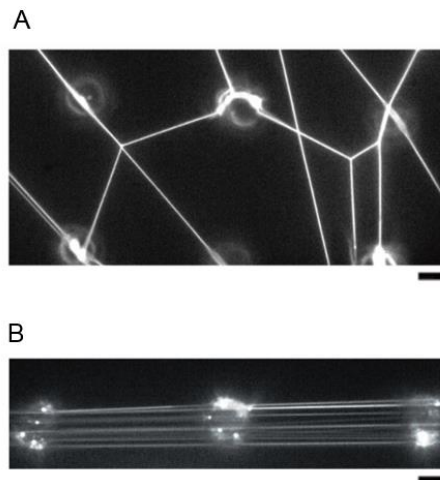


Figure 5.5. A) Fluorescence microscopy image of the lipid NTs created by the tilting method, rendering to a NT net connecting the micropillars. B) Fluorescence microscopy image of the parallel lipid NTs under the negative flow method. Scale bars correspond to 10 μm .

The lamellarity studies performed by our collaborators using the laminar flow method revealed two lipid NT populations for 20 $\mu\text{L min}^{-1}$, presumably corresponding to uni- and bilamellar NTs⁴. In contrast, more populations, including multilamellar ones, were identified for tilting method and for the 100 $\mu\text{L min}^{-1}$ flow rate. Moreover, the tilting method and the used 100 $\mu\text{L min}^{-1}$ flow resulted in broken lipid NTs in solution. Therefore, the laminar flow method at 20 $\mu\text{L min}^{-1}$ flow was used for further characterisation of the system.

The lipid NTs were obtained for all the interpillary distances (10, 20, 30 and 40 μm) with length values established by the interpillary distance (Figure 5.6), a parameter

tunable by the micropillar array design as depicted in Figure 5.2.

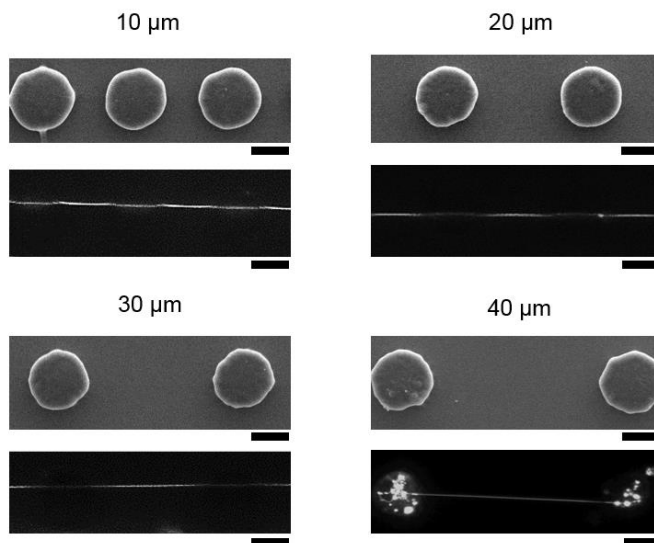


Figure 5.6. Images of a lipid NT attached to two adjacent micropillars of SU-8 at different interpillar distances. Scale bars correspond to 10 μm .

The lipid NT membrane-micropillar surface interaction is known to be responsible for the variation of the dimensions, including the radius, of the formed lipid NT for a given lipid composition^{35,36}. Therefore, the formation of the lipid NTs was investigated for the three ionogel micropillar arrays, producing the NTs as explained in experimental section 5.4.3.

The IO-3 was not suitable for the formation of lipid NTs, since they rapidly detached from the micropillars, leaving fluorescent lipid residues all over the microfluidic device. These residues inhibited the visualisation of the process, and so the characterisation of the formation of the lipid NTs. On the other hand, the fabrication of the micropillar array on the IO-1 was very difficult, obtaining undefined shapes, as observed in the SEM images presented in Figure 5.3.

Therefore, the formation of the lipid NTs was not possible. Finally, the IO-2, which has a different physicochemical interaction with lipids than SU-8, resulted efficient for the formation of lipid NTs between adjacent micropillars (Figure 5.7A). The higher affinity of the lipids to the IO-2 micropillars compared to SU-8 was demonstrated by observing the coverage of the whole micropillar with the lipid membrane (Figure 5.7A). The SU-8 micropillars were only sparingly covered (Figure 5.7B) or even, not visualised (Figure 5.6), with the membrane reservoir forming only at discrete points. This high coverage with lipid reservoir on IO-2 micropillars could be explained by the high porosity of the IO micropillars in contrast with the non-porous SU-8 (Figure 5.4), having higher reservoir capacity for the lipids, although both of them are hydrophobic.

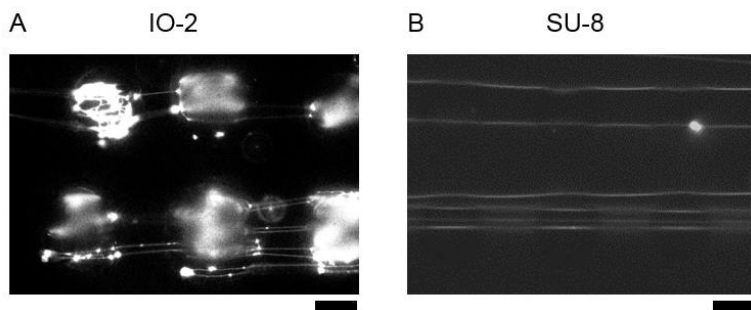


Figure 5.7. A) Fluorescent microscopy images of parallel lipid NTs on IO-2 micropillars, B) Fluorescent microscopy image of parallel lipid NTs on SU-8 micropillars. Scale bars correspond to 10 μm .

IO-2 (with DCA IL) is a porous material with high hydrophobicity, promoted by the IL, which gets hydrated due to the water uptake capability of the pNIPAAm (Figure 5.8A)¹⁹. The porosity of the material, whose pores are filled with water, could enhance the deposition of the lipid reservoirs surrounding the micropillar. Due to its hydrophobicity, lipids would have higher affinity than water to

accommodate within the pores, and water could be released, at the same time that the lipid gets inside, generating a local “dehydration of the ionogel” at the pore level, and increasing the pore dimension, thus reinforcing the absorption of more lipids (Figure 5.8B).

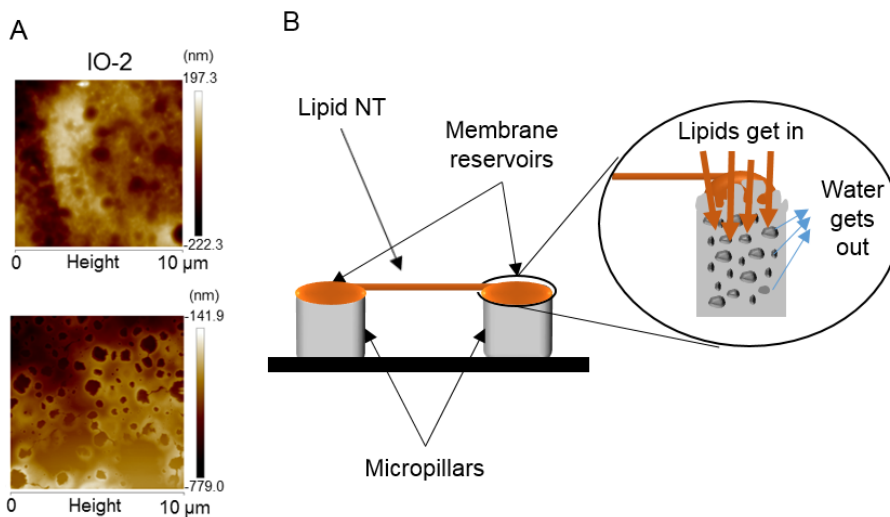


Figure 5.8. A) AFM images of the IO-2 surface in its dry (top) and hydrated (bottom) state. B) Scheme of the interface: lipid membrane/IO-2 micropillar.

The radius of the lipid NTs (r_{NT}) was investigated in both micropillar configuration using two type of lipid compositions (neutral 1,2-dioleoyl-sn-glycero-3-phosphocholine (DOPC) and charged 1,2-dioleoyl-sn-glycero-3-phosphocholine (DOPC): 1,2-dioleoyl-sn-glycero-3-phospho-L-serine (DOPS) (DOPC:DOPS)). The results showed that the radius increased on SU-8 micropillars and decreased when the lipid NTs were formed on the IO-2 as compared (Figure 5.9A). The smaller radius indicated higher lateral membrane tension due to the lipid affinity to the IO-2 micropillar. As presented before, the higher affinity of the lipids to the IO-2 micropillars was already observed in the lipid coverage on the micropillars (Figure 5.7B). Although both micropillar

materials are hydrophobic, the high porosity of the IO-2 makes the difference for an increased lipid reservoir capacity.

As mentioned in the introduction, ionic liquids interact with the lipid membranes, damaging them and generating disruption²⁰. Therefore, in order to confirm that the ionic liquid was not leaching from the micropillar and thus, was not the reason for the radius variations, the micropillars were put in contact with GUVs, and the morphologies of lipid GUVs when added to IO-2 and SU-8 substrates were compared. The GUVs are very sensitive to small variations on their membrane composition thus, the presence of IL on the surrounding will affect its shape. GUVs adhered well to the micropillars made from both materials and it was observed that the GUVs in contact with the IO-2 micropillars remained stable, with no apparent ionic liquid effect (Figure 5.9B). Therefore, this pointed out that by just changing the affinity between the membrane reservoir of the lipid NTs and the material of the micropillar, the geometry of the lipid NTs can be tuned through changes in its lateral tension.

Importantly, the radius of the lipid NTs pulled directly from the lipid reservoir on the silica beads (77 ± 2 nm)³⁷ was significantly higher than the NT radii measured in this chapter. The radii values were 14 ± 6 nm (DOPC, n = 81) and 19 ± 5 nm (DOPC:DOPS, n = 46) for SU-8 and 7 ± 2 nm (DOPC, n = 63) and 7 ± 3 nm (DOPC:DOPS, n = 45) for IO-2 (Figure 5.9A). A statistically significant decrease of the radii values was observed with IO-2 micropillars, explaining the lipid transfer from the beads to both SU-8 and IO-2 micropillars. Finally, the radii change was not significant when charged lipid species (DOPC:DOPS) were added to the lipid NTs formed on IO-2.

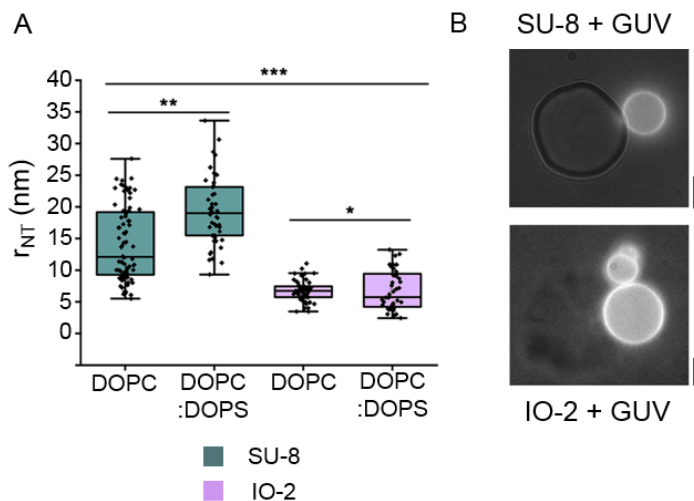


Figure 5.9. A) Graph depicting the changes in lipid NTs radii as a function of the membrane composition and membrane interaction with the material on the micropillars. Error bars correspond to the standard deviation from the mean of $n = 81$ for DOPC/SU-8, $n = 46$ for DOPC:DOPS/SU-8, $n = 63$ for DOPC/IO-2 and $n = 45$ for DOPC:DOPS/IO-2. Statistical significance: *** Significantly different at 0.05 level (Two-way ANOVA (substrate and lipid within-subjects), $p = 1.88 \cdot 10^{-18}$); ** Significantly different at 0.05 level (One-way ANOVA, $p = 3.2 \cdot 10^{-6}$); * Not significantly different at 0.05 level (One-way ANOVA, $p = 0.71$). B) Adhesion of GUVs to SU-8 (top) and IO-2 (bottom) micropillars. Scale bars correspond to 5 μm .

5.3 Conclusions

In contrast to current methods for lipid NT formation and monitoring, this microfluidic device, integrating functional materials as micropillar arrays, enables the easy, rapid and high throughput creation and monitoring of lipid NTs. Contrary to the conventional membrane micromanipulation procedures

used for the creation of lipid NTs, the methodology presented in this chapter does not require any sophisticated micromanipulations to qualitatively control the lipid NT length, enabling the control of the lipid NT radius. The combination of bead rolling, functional materials as micropillar arrays and microfluidics ensures a versatile and user-friendly methodology to create multiple lipid NTs in a short time in a controlled area.

The integration of a micropillar array into the bottom plate of the microfluidic device enables control over the flow regime and eases the automation of the fabrication and analysis process. Besides, the whole system remains contained within a microchannel, minimising the use of reagents, such as proteins or markers.

The lipid NTs obtained over the pillars are free-standing, reducing the possible artifacts coming from the interaction of the NT membrane and the support, seen in other high throughput systems^{4,11}. The low height of the micropillars, grown directly on a thin glass coverslip, allows fluorescence microscopy monitoring of the lipid NTs with high power objectives.

Ionogels can be excellent materials for photopatterning; this chapter proves that high resolution features (15 µm size) can be obtained and that they remain stable for months even after multiple uses. The high variability within the ionogel family and their suitability for photopatterning, combined with surface chemistry procedures, provides with a great versatility to the system. It enables to control the strength of the lipid NT interaction with the polymer support, and thus, the lipid NT radius. This user-friendly miniaturised approach to lipid NT formation will be a valuable addition to the toolkit of *in vitro* reconstitution assays of processes happening at high membrane curvature.

5.4 Experimental

5.4.1 Materials

Creation of the micropillars: 25 mm round cover glasses of 0.13-0.16 mm thickness were purchased from Hecht Assistant, Germany, the polymeric photomask was obtained from J.D. Photodata, UK and ethanol, 2-isopropanol, methanol and acetone for cleaning were from Scharlabs, Spain. For SU-8 micropillars, SU-8 2005 photoresist and its developer were purchased from Atis S.A. For the ionogel micropillars, *N*-isopropylacrylamide (NIPAAm) monomer, the crosslinker *N,N'*-methylene-bis(acrylamide) (mBAAm), the photoinitiator 2,2-dimethoxy-2-phenylacetophenone (DMPA), the silanising agent 3-(trimethoxysilyl)propyl methacrylate, and EMIES, DCA and ChAc ILs were from Sigma Aldrich, Spain.

Microfluidic device: PSA of 127 μm thickness (ARcare 8939) was obtained from Adhesive Research Inc., Ireland and Polydimethylsiloxane (PDMS) (SYLGARDTM 184 Silicone elastomer) from Farnell, Spain. For the fluidic connections, teflon Tubing 1 /16" OD, and 23 G stainless steel connectors were from Elveflow.

Lipid membrane NTs: 1,2-dioleoyl-sn-glycero-3-phosphoethanolamine (DOPE), 1,2-dioleoyl-sn-glycero-3-phosphocholine (DOPC), 1,2-dioleoyl-sn-glycero-3-phospho-L-serine (DOPS), Cholesterol, L- α -phosphatidylinositol-4,5-bisphosphate (PI(4,5)P₂), 1,2-dioleoyl-sn-glycero-3-phosphoethanolamine-*N*-(lissamine rhodamine B sulfonyl) (ammonium salt) (RhPE) were purchased from Avanti Lipids. 40 μm plain silica beads were from Microspheres-Nanospheres Co, USA; bovine serum albumin (BSA), KCl, (4-(2-hydroxyethyl)-1-piperazine

ethanesulfonic acid) (HEPES), and ethylenediaminetetraacetic acid (EDTA were from Fisher Scientific, Spain.

5.4.2 Fabrication of the microfluidic devices

Pattern of SU-8 micropillars on glass substrates:

Arrays of SU-8 micropillars were produced directly on a 25 mm round cover glass by photolithography (Figure 5.2A). A photomask was designed to create three arrays of cylindrical pillars of 15 µm in diameter, each array composed of 4 discrete zones with 10, 20, 30, and 40 µm separation between the pillars (Figure 5.2C and D). A mould fabrication station from BlackHole lab, France was used to perform photolithography.

For the production of SU-8 micropillars, first the cover glasses were rinsed with isopropanol, acetone, ethanol and methanol, and dehydrated at 220 °C for 2 h. Then, a 5 µm thick layer of SU-8 2005 photoresist was spin-coated directly onto a cover glass, at a maximum speed of 2000 rpm s⁻¹. It was then soft-baked (65 °C for 8 min and at 95 °C for 14 min), aligned with a high-resolution film photomask in physical contact and exposed to UV using the UV-KUB 2 lamp to (Kloé, France) (365 nm), in 4 pulses of 20 s of 5 mJ s⁻¹. After a post exposure bake (3 min at 65 °C and 6 min at 95 °C), the non-polymerised photoresist was removed by developer immersion, followed by an isopropanol wash and a hard bake (30 min at 150 °C) of the cover glass. The height and the structures of the micropillars of the imprinted SU-8 pattern were confirmed by optical profilometry with a DektakXT (Bruker) profilometer, and SEM with a Hitachi S-4800 Scanning Electronic Microscopy, respectively.

Pattern of ionogel micropillars on glass substrates:

For the fabrication of ionogel micropillars, first the prepolymer was made, following a protocol slightly modified from reference ²⁴. Prepolymers are comprised of monomer (NIPAAm), a photoinitiator (DMPA), a crosslinker (mBAAm) and a tuneable IL. The molar relation for the first three components was kept the same for all the them: 40:1:2 (NIPAAm:DMPA:mBAAm), while the volume of the IL was different in each solution. Three different prepolymer solutions were fabricated, with the following ILs: EMIES (IO-1), DCA (IO-2) and ChA (IO-3). For the IO-1, 452 mg NIPAAm, 30.9 mg mBAAm, 30 mg DMPA and 1 mL of EMIES ionic liquid were mixed. For the IO-2, 452 mg NIPAAm, 30.9 mg mBAAm, 30 mg DMPA and 1.5 mL of DCA were mixed. Finally, to get the IO-3 prepolymer solution, 1 g of choline acetate IL was melted at 120 °C for 1 h and subsequently 452 mg NIPAAm, 30.9 mg mBAAm and 30 mg DMPA were then added to it. The solution was kept stirring at 100 °C until all the solid compounds were dissolved.

Following the steps from Figure 5.2B, for the fabrication of ionogel microstructures, cover glasses required a chemical functionalisation step in order to keep the polymerised micropillars covalently attached to the surface. The glass covers were oxidised with air plasma (Harrick PDC-32G-2) for 30 min, followed by vapour deposition of (3-(trimethoxysilyl)propyl methacrylate) for 2 h. Then, a 10 µm high layer of prepolymer solution was spread over the functionalised cover glass with a ZUA 2000.60 film applicator (Zehntner). For the photopatterning of the IOs, the samples were exposed to UV light (365 nm) (UV-KUB 2 lamp (Kloé, France) for 4 cycles of 5 s (460 mJ) for IO-1, 5 cycles of 5 s (585 mJ) for IO-2 and 3 cycles of 5 s (351 mJ) for IO-3, every 30 s.

Finally, the obtained micropillar arrays were thoroughly washed with isopropanol and water. To further assure the absence of the ionic liquid in the final product, the pillars were heated to 45 °C to induce material shrinkage, generating a “sponge” like actuation effect and provoking unbound IL to get released from the polymer network.

The height and the structures of the ionogel micropillars were confirmed by optical profilometry with a DektakXT (Bruker) profilometer, and SEM with a Hitachi S-4800 Scanning Electronic Microscopy, respectively.

Fabrication of the microfluidic channels:

To complete the microfluidic device, three parallel channels were designed, with a 2 mm width per 8 mm length, which were transferred to a PSA film (127 µm thickness), cut with a Graphtec 6000-40 cutter plotter, and attached to the bottom of a 55 mm PyrexTM borosilicate glass Petri dish. PDMS at 10:1 ratio, was poured on top of the PSA mould at the bottom of the Petri dish, degassed and cured at 60 °C for 40 min. The polymerised PDMS was then peeled off from the dish, and baked at 60 °C for 2 h. After punching a 0.5 mm inlet and outlet orifices for fluidic connections, the PDMS section was attached to the previously micropatterned cover glass, so that the three channels were aligned with the three arrays of micropillars on the cover glass.

5.4.3 Lipid NT formation

First the lipid covered beads were prepared as reported previously for the giant supported bilayers template ³⁸. Briefly, the desired lipid mixtures (DOPC:RhPE 99:1 mol %, DOPC:DOPS:RhPE 49:50:1 mol % or DOPC:DOPE:DOPS:Chol:PI(4,5)P₂:RhPE 46:30:10:10:3:1 mol %) were prepared

from lipid stocks in chloroform to 0.1 mg of total lipid. The lipid mixtures were vacuum dried for 30 min, rendering uniform lipid films at the bottom of the vials. The films were then rehydrated in 100 µL of 1 mM HEPES, pH 7.0, and subjected to light vortexing, resulting in the formation of multilamellar vesicles (MLVs). The MLV solution can be stored at 4 °C for up to three days, depending on the lipid composition.

A small aliquot of 40 µm plain silica beads was washed three times with ultrapure water. A 0.2 µL aliquot of the beads solution in water was transferred into a 10 µL aliquot of MLVs. The bead-MLV mixture was then divided into five even drops on a clean Parafilm surface. The drops were dried in vacuum for 15-30 min or until the water evaporated completely. The resulting multi-layered lipid films on the surface of the microspheres were used to produce the lipid NTs. In order to achieve reproducibility in the next steps of the procedure, it is recommended to characterise the lipid coverage of the bead surface each time by measuring the lipid to bead ratio as described previously^{8,38}.

Lipid NT formation in the microfluidic device:

The *microfluidic device* was flashed with BSA solution at 0.1 g L⁻¹ in Mili-Q ultrapure water to prevent lipid adhesion to the coverslip and PDMS walls. The chamber was then washed and filled with the working buffer (150 mM KCl, 20 mM HEPES, 1 mM EDTA). 40 µm silica beads containing the lipid film multilayers were picked up with a fire-closed tip of a glass micropipette, and introduced into the cell through the input port of the PDMS section. The lipid NTs were formed by rolling the beads over the micropillar arrays. Such rolling was performed by applying negative pressure on the outlet port of the PDMS section with a Standard Infuse/Withdraw Pump 11 Elite Programmable Syringe Pump (Harvard apparatus, Spain) or by gently tilting the whole device. To avoid

undesirable background signals, the beads were purged away from the pillar array area of the chamber at the end of the lipid NT formation. If vesicles or membrane aggregates were detected in the bulk upon the removal of the beads, additional perfusion of the chamber was performed to ensure low fluorescence background.

5.4.4 Imaging and characterisation of the lipid NTs

The fluorescently labelled lipid NTs were imaged with a widefield fluorescence inverted microscope using the same intensity and camera settings each time. μ Manager software ³⁹ was used for image acquisition. Images were further analysed using Fiji ⁴⁰ and Origin 8.0 software.

The number of lipid NTs observed in a field of view depended upon the objective used, number of beads introduced, and the separation between the pillars. For the analysis of the lipid NT radii, NT micrographs with uniform and low background signals located near the focal plane were selected, allowing for quantification of the lipid NTs radii as described elsewhere ^{4,37}. The fluorescently labelled lipid NTs were imaged with a widefield fluorescence inverted microscope (Nikon Eclipse Ti-E motorised inverted microscope equipped with CoolLed pE-4000 light source and Andor Zyla sCMOS camera) using the same intensity and camera settings each time. The objectives used were TIRF oil immersion 100x/1.49 or 40x/0.75 air objectives.

5.5 References

1. Singh, P.; Mahata, P.; Baumgart, T.; Das, S. L. Curvature sorting of proteins on a cylindrical lipid membrane tether connected to a reservoir. *Phys. Rev. E* 2012, **85**, 051906.
2. Zhu, C.; Das, S. L.; Baumgart, T. Nonlinear sorting, curvature generation, and crowding of endophilin N-BAR on tubular membranes. *Biophys. J.* 2012, **102**, 1837-1845.
3. Shnyrova, A. V.; Bashkirov, P. V.; Akimov, S. A.; Pucadyil, T. J.; Zimmerberg, J.; Schmid, S. L.; Frolov, V. A. Geometric catalysis of membrane fission driven by flexible dynamin rings. *Science* 2013, **339**, 1433-1436.
4. Dar, S.; Kamerkar, S. C.; Pucadyil, T. J. A high-throughput platform for real-time analysis of membrane fission reactions reveals dynamin function. *Nat. Cell Biol.* 2015, **17**, 1588.
5. Simunovic, M.; Evergren, E.; Golushko, I.; Prevost, C.; Renard, H. F.; Johannes, L.; McMahon, H. T.; Lorman, V.; Voth, G. A.; Bassereau, P. How curvature-generating proteins build scaffolds on membrane nanotubes. *Proc. Natl. Acad. Sci. U. S. A.* 2016, **113**, 11226-11231.
6. Roux, A. The physics of membrane tubes: soft templates for studying cellular membranes. *Soft Matter* 2013, **9**, 6726-6736.
7. Frolov, V. A.; Lizunov, V. A.; Dunina-Barkovskaya, A. Y.; Samsonov, A. V.; Zimmerberg, J. Shape bistability of a membrane neck: a toggle switch to control vesicle content release. *PNAS* 2003, **100**, 8698-8703.
8. Neumann, S.; Pucadyil, T. J.; Schmid, S. L. Analyzing membrane remodeling and fission using supported bilayers with excess membrane reservoir. *Nat. Protoc.* 2013, **8**, 213-222.
9. Pucadyil, T. J.; Schmid, S. L. Real-time visualization of dynamin-catalyzed membrane fission and vesicle release. *Cell* 2008, **135**, 1263-1275.
10. Dar, S.; Kamerkar, S. C.; Pucadyil, T. J. Use of the supported membrane tube assay system for real-time analysis of membrane fission reactions. *Nat. Protoc.* 2017, **12**, 390-400.
11. Kamerkar, S. C.; Kraus, F.; Sharpe, A. J.; Pucadyil, T. J.; Ryan, M. T. Dynamin-related protein 1 has membrane constricting and severing abilities sufficient for mitochondrial and peroxisomal fission. *Nat. Commun.* 2018, **9**, 1-15.
12. Levinson, H. J. *Principles of lithography*; SPIE press: 2005; Vol. 146.
13. Hurtig, J.; Karlsson, M.; Orwar, O. Topographic SU-8 Substrates for Immobilization of Three-Dimensional Nanotube- Vesicle Networks. *Langmuir* 2004, **20**, 5637-5641.
14. Hurtig, J.; Gustafsson, B.; Tokarz, M.; Orwar, O. Electrophoretic transport in surfactant nanotube networks wired on microfabricated substrates. *Anal. Chem.* 2006, **78**, 5281-5288.
15. Herold, K.E. *Biosensors and biodetection*. Totowa, NJ: Humana Press, 2009.

16. Toledo Hijo, A. A.; Maximo, G. J.; Costa, M. C.; Batista, E. A.; Meirelles, A. J. Applications of ionic liquids in the food and bioproducts industries. *ACS Sustain. Chem. Eng.* 2016, *4*, 5347-5369.
17. Zhong, Y.; Nguyen, G. T.; Plesse, C.; Vidal, F.; Jager, E. W. Highly conductive, photolithographically patternable ionogels for flexible and stretchable electrochemical devices. *ACS Appl. Mater. Interfaces* 2018, *10*, 21601-21611.
18. Khodagholy, D.; Curto, V. F.; Fraser, K. J.; Gurfinkel, M.; Byrne, R.; Diamond, D.; Malliaras, G. G.; Benito-Lopez, F.; Owens, R. M. Organic electrochemical transistor incorporating an ionogel as a solid state electrolyte for lactate sensing. *J. Mater. Chem.* 2012, *22*, 4440-4443.
19. Gil-Gonzalez, N.; Akyazi, T.; Castaño, E.; Benito-Lopez, F.; Morant-Minana, M. C. Elucidating the role of the ionic liquid in the actuation behavior of thermo-responsive ionogels. *Sens. Actuator B Chem.* 2018, *260*, 380-387.
20. Jing, B.; Lan, N.; Qiu, J.; Zhu, Y. Interaction of ionic liquids with a lipid bilayer: a biophysical study of ionic liquid cytotoxicity. *J. Phys. Chem. B* 2016, *120*, 2781-2789.
21. Sharma, V.; Mukhopadhyay, R. Deciphering interactions of ionic liquids with biomembrane. *Biophys. Rev.* 2018, *10*, 721-734.
22. Saghebasl, S.; Davaran, S.; Rahbarghazi, R.; Montaseri, A.; Salehi, R.; Ramazani, A. Synthesis and in vitro evaluation of thermosensitive hydrogel scaffolds based on (PNIPAAm-PCL-PEG-PCL-PNIPAAm)/Gelatin and (PCL-PEG-PCL)/Gelatin for use in cartilage tissue engineering. *J. Biomater. Sci. Polym. Ed.* 2018, *29*, 1185-1206.
23. Ren, Z.; Wang, Y.; Ma, S.; Duan, S.; Yang, X.; Gao, P.; Zhang, X.; Cai, Q. Effective bone regeneration using thermosensitive poly (N-isopropylacrylamide) grafted gelatin as injectable carrier for bone mesenchymal stem cells. *ACS Appl. Mater. Interfaces* 2015, *7*, 19006-19015.
24. Gil-González, N.; Chen, C.; Akyazi, T.; Zuzuarregui, A.; Rodriguez, A.; Knez, M.; Castaño, E.; Benito-Lopez, F.; Morant-Miñana, M. C. AZO Embedded Interdigitated Electrodes for Monitoring Stimuli Responsive Materials. *Adv. Funct. Mater.* 2018, *28*, 1803127.
25. Lopes, J. M.; Paninho, A. B.; Môlho, M. F.; Nunes, A. V.; Rocha, A.; Lourenço, N. M.; Najdanovic-Visak, V. Biocompatible choline based ionic salts: Solubility in short-chain alcohols. *J. Chem. Thermodyn.* 2013, *67*, 99-105.
26. De Vreese, P.; Skoczyłas, A.; Matthijs, E.; Fransaer, J.; Binnemans, K. Electrodeposition of copper-zinc alloys from an ionic liquid-like choline acetate electrolyte. *Electrochim. Acta* 2013, *108*, 788-794.
27. Czugala, M.; O'Connell, C.; Blin, C.; Fischer, P.; Fraser, K. J.; Benito-Lopez, F.; Diamond, D. Swelling and shrinking behaviour of photoresponsive phosphonium-based ionogel microstructures. *Sens. Actuator. B Chem.* 2014, *194*, 105-113.
28. Krongauz, V.; Yohannan, R. Photopolymerization kinetics and monomer diffusion in polymer matrix. *Polymer* 1990, *31*, 1130-1136.

29. Tijero, M.; Díez-Abedo, R.; Benito-Lopez, F.; Basabe-Desmonts, L.; Castro-López, V.; Valero, A. Biomolecule storage on non-modified thermoplastic microfluidic chip by ink-jet printing of ionogels. *Biomicrofluidics* 2015, 9, 044124.
30. Loeffelmann, U.; Wang, N.; Mager, D.; Smith, P. J.; Korvink, J. G. Solvent-free inkjet printing process for the fabrication of conductive, transparent, and flexible ionic liquid-polymer gel structures. *J Polym. Sci. Part B: Polym. Phys.* 2012, 50, 38-46.
31. Oubaha, M.; Kavanagh, A.; Gorin, A.; Bickauskaite, G.; Byrne, R.; Farsari, M.; Winfield, R.; Diamond, D.; McDonagh, C.; Copperwhite, R. Graphene-doped photo-patternable ionogels: tuning of conductivity and mechanical stability of 3D microstructures. *J. Mater. Chem.* 2012, 22, 10552-10559.
32. Kavanagh, A.; Copperwhite, R.; Oubaha, M.; Owens, J.; McDonagh, C.; Diamond, D.; Byrne, R. Photo-patternable hybrid ionogels for electrochromic applications. *J. Mater. Chem.* 2011, 21, 8687-8693.
33. Ravve, A. *Principles of polymer chemistry*; Springer Science & Business Media: 2013.
34. Braun, D.; Cherdron, H.; Rehahn, M.; Ritter, H.; Voit, B. *Polymer synthesis: theory and practice: fundamentals, methods, experiments*; Springer Science & Business Media: 2012.
35. Evans, E.; Yeung, A. Hidden dynamics in rapid changes of bilayer shape. *Chem. Phys. Lipids* 1994, 73, 39-56.
36. Heinrich, V.; Waugh, R. E. A piconewton force transducer and its application to measurement of the bending stiffness of phospholipid membranes. *Ann. Biomed. Eng.* 1996, 24, 595-605.
37. Espadas, J.; Pendin, D.; Bocanegra, R.; Escalada, A.; Misticoni, G.; Trevisan, T.; Del Olmo, A. V.; Montagna, A.; Bova, S.; Ibarra, B. Dynamic constriction and fission of endoplasmic reticulum membranes by reticulon. *Nat. Commun.* 2019, 10, 1-11.
38. Velasco-Olmo, A.; Gisasola, J. O.; Galvez, J. M. M.; Lillo, J. V.; Shnyrova, A. V. Combining patch-clamping and fluorescence microscopy for quantitative reconstitution of cellular membrane processes with Giant Suspended Bilayers. *Sci. Rep.* 2019, 9, 1-12.
39. Edelstein, A.; Amodaj, N.; Hoover, K.; Vale, R.; Stuurman, N. Computer control of microscopes using μ Manager. *Curr. Protoc. Mol. Biol.* 2010, 92, 14.20. 1-14.20. 17.
40. Schindelin, J.; Arganda-Carreras, I.; Frise, E.; Kaynig, V.; Longair, M.; Pietzsch, T.; Preibisch, S.; Rueden, C.; Saalfeld, S.; Schmid, B. Fiji: an open-source platform for biological-image analysis. *Nat. Methods* 2012, 9, 676-682.

6

Optical Single Cell Resolution Cytotoxicity Biosensor Based on Single Cell Adhesion Dot Arrays

A high-resolution methodology to track cell death is presented. It is based on the dynamic digital quantification of cell viability by optical imaging, using “single cell adhesion dot arrays”, which are fibronectin dot arrays designed to accommodate a single cell on each fibronectin dot. It enables the quantitative and dynamic monitoring of cellular death through cell detachment, and it also allows the quantitative monitoring of cell viability in presence of lethal toxic compounds that inhibit cell detachment as a consequence of cellular death.

*Parts of this Chapter have been published in: Garcia-Hernando, M., Calatayud-Sanchez, A., Etxebarria-Elezgarai, J., de Pancorbo, M. M., Benito-Lopez, F., Basabe-Desmonts, L. Optical single cell resolution cytotoxicity biosensor based on single cell adhesion dot arrays. *Anal. Chem.* 2020, 92, 9658-9665.

6.1 Introduction

Cytotoxicity assays are mostly used for drug screening and testing of chemical induced cellular death. These tests are essential in basic research, in the pharmaceutical industry and in the elaboration of environmental regulation. There are several cytotoxicity tests available, a number of them are based on detecting specific metabolic processes through colorimetric or fluorometric assays, such as crystal violet, MTT, Annexin V, or Trypan Blue among others¹. Another well-established method for cytotoxicity testing is the Colony Formation Assay (CFA), which implies the quantification of the ability of cells to form colonies, counting by eye or by microscopy the number of cell colonies created during several days or weeks^{1,2}. On the other hand, flow cytometry provides accurate quantitative measurements of cellular death with single cell resolution, and offers the possibility of performing high throughput (HTP) analysis. However, flow cytometry analyses cells in suspension, it cannot be performed on surface, and cellular staining is required, preventing the possibility of real-time monitoring³.

Real-time cytotoxicity monitoring tests, such as Scalable Time-lapse Analysis of Cell death Kinetics (STACK) technology are also capable of performing HTP analysis of death dynamics similarly to flow cytometry. In these cases, fluorescence is used to identify alive and dead cell populations using fluorescence microscopy and careful optimisation of image analysis routines⁴. In addition, a system comprised of a high-density array of micro-cavities for single cells has been reported as a fluorescent-based single cell cytotoxicity assay. In that work, the array of individually entrapped cells enabled the precise quantification of dead cells that had been previously labelled with a fluorescent live/dead staining⁵.

In order to develop a simple to use and low-cost test to facilitate the screening of cytotoxicity at the point of need, it would be of interest to have a simple test that could provide cellular death kinetics with minimal intervention of the user or the need of specialised equipment for read out.

Upon exposure to toxic compounds, cells can lose their adhesion capability, resulting in cell detachment from a surface. A technology called xCELLigence Real-Time Cell Analysis (RTCA) monitors the effect of a toxic compound on a cell culture by monitoring cellular adhesion with a microelectrode-patterned surface. The electrochemical impedance of the electrode-based substrate changes in relation to the number of cells adhered to their surface, providing a label-free, real-time cell analysis platform for cell growth and detachment. Even though it is a very sensitive technique to monitor cellular responses to toxics, it is a non-specific technique, because morphological changes in cells also cause alterations in the impedance values. Therefore, it is not possible to distinguish between cellular detachment and a change in morphology without external labels ⁶⁻⁹. Additionally, impedance based techniques would not provide the means to distinguish between a living cell and a dead cell that remains attached to the surface because in both cases the impedance signal would be similar.

A methodology that enables both dynamic detachment monitoring but also rapid detection of toxic effects of compounds that promote cell adhesion would constitute a step forward towards high throughput cytotoxicity measurements. Protein patterning techniques enable the creation of cell arrays adhered to surfaces which have been used for many studies in cell biology, morphogenesis, cell polarity, cell division axis ¹⁰, whole blood platelet isolation and characterisation ¹¹⁻¹³ and HTP analysis ¹⁴. Recently, the Microfluidics Cluster UPV/EHU introduced the use of Single Cell Adhesion Dot Array (SCADA)

substrates as an optical biosensing platform for accurate quantification of cell affinity for protein substrates with single cell resolution¹⁵.

Herein, in this chapter I present an optical method to monitor cell death with single cell resolution using SCADA substrates, by accurate quantification of cell detachment and/or trypan blue staining (Figure 6.1).

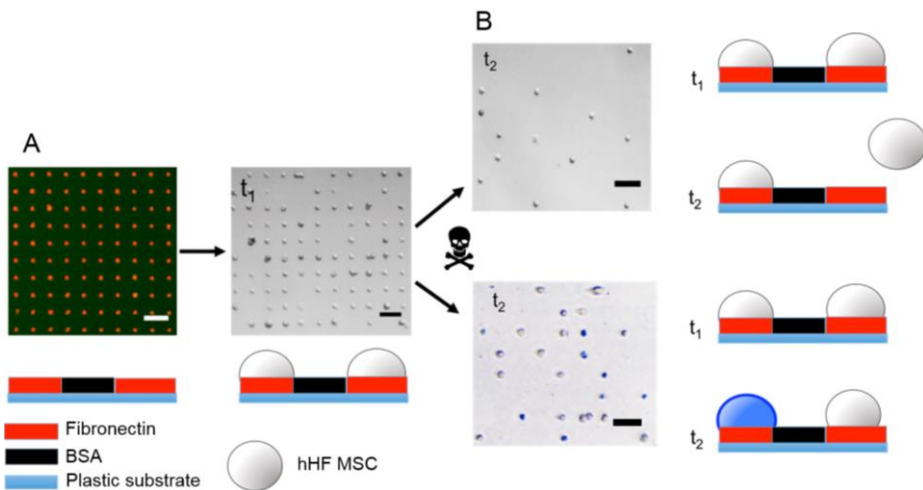


Figure 6.1. Scheme of cytotoxicity assay using SCADA substrates. A) Fluorescence microscopy image of a fluorescent labelled FN-SCADA substrate, comprised of an array of fibronectin (FN) dots (left); bright field microscopy image of the FN-SCADA substrate after incubation with a cellular suspension, showing single cell adhesion of human hair follicle Mesenchymal Stem Cells (hHF-MSCs) to the FN dots of the SCADA substrate (right). B) Bright field microscopy images of the cell-saturated SCADA substrates after incubation with two types of toxic compounds that caused cell death and triggered either cell detachment (top) or colour stain (bottom). Scale bar corresponds to 100 μm .

This is an application of SCADA substrates that to the best of my knowledge has not been explored before. The ordered distribution of individually adhered cells on the protein dot array, combined with optical detection, enables digital and dynamic monitoring of cell detachment or individual staining triggered by cell death without the need of a fluorescence read out.

6.2 Results and discussion

6.2.1 Monitoring cell adhesion and detachment to protein substrates with single cell resolution

Fibronectin is a protein of high molecular weight from the Extracellular Matrix (ECM), which plays a crucial role in cell adhesion, as it binds to integrins located in the cell membrane. On the other hand, hHf-MSCs, are adherent cells that express a number of integrin molecules like $\alpha 1$, $\alpha 2$, $\alpha 3$, $\alpha 4$, $\alpha 5$, αv , $\beta 1$, $\beta 3$ and $\beta 4$, some of which have been previously reported to be involved in MSC adhesion¹⁶.

In order to demonstrate the suitability of micro-patterned SCADA substrates to monitor cellular death, first the adhesion and detachment kinetics of hHf-MSCs to a FN-SCADA substrates were monitored as explained in experimental section 6.4.3. Arrays of 20 μm FN dots with inter dot space of 50 μm were created on polystyrene (PS) cellular culture dishes by micro-contact printing, and the remaining surface of the dish was blocked with Bovine Serum Albumin (BSA) to avoid non-specific cellular adhesion. To evaluate the homogeneity of the composition of the protein dot array, the fluorescence intensity and the diameter of 3300 dots were analysed within a single substrate. The coefficient of variation (CV) for fluorescence intensity and dot diameter values were of 6 % and 14 % respectively, confirming the homogeneity of the dot composition and their shape

along the substrate (Figure 6.2.).

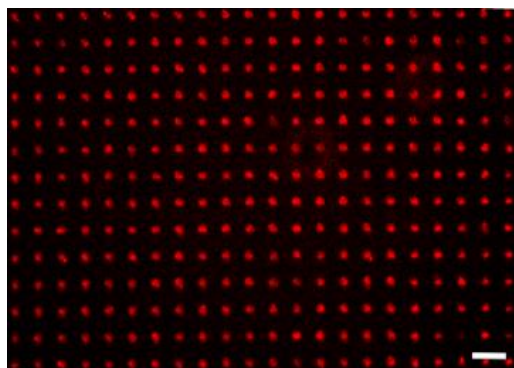


Figure 6.2. Fluorescent microscopy picture of a uniform protein pattern for single cell adhesion. Scale bar corresponds to 100 μm .

1 mL of 100000 cell mL^{-1} suspension was added to each patterned well, and kept incubating at 5 cycles per min (steep angle rocking). To determine adhesion kinetics, the Dot Array Occupancy (DAO) was measured after 15', 30', 45', 1 h, 1.5 h, 2 h, 2.5 h, 3 h and 3.5 h, taking optical microscopy images of the substrates at each time point and calculating the ratio of occupied binding dots. As shown in Figure 6.3, cells started to attach to FN dots soon after addition, and just after 30 min of incubation, there was more than 50 % of occupancy of the protein dot array. After 2 h of incubation, hHF-MSCs reached the adhesion plateau with a DAO of 97 %.

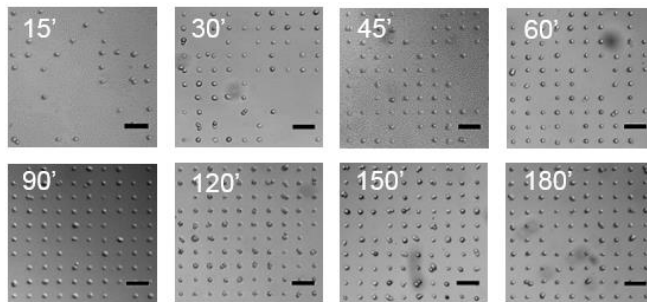
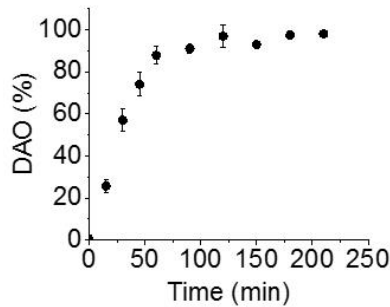
A**B**

Figure 6.3. Dynamic cell attachment on SCADA. A) Optical microscopy, bright field, images of single cell adhesion to the dot array at different time points: 15, 30, 45, 60, 90, 120, 180 and 210 min. B) DAO *versus* time. Scale bar corresponds to 100 μ m. Error bars correspond to the standard deviation from the mean for $n = 3$.

The homogeneity of the adhesion/detachment was evaluated along the whole substrate, containing 20000 dots. The average DAO calculated along the whole substrate using 3 random images containing 1728 spots was 75 %, with a CV of 4.7 % (Figure 6.4).

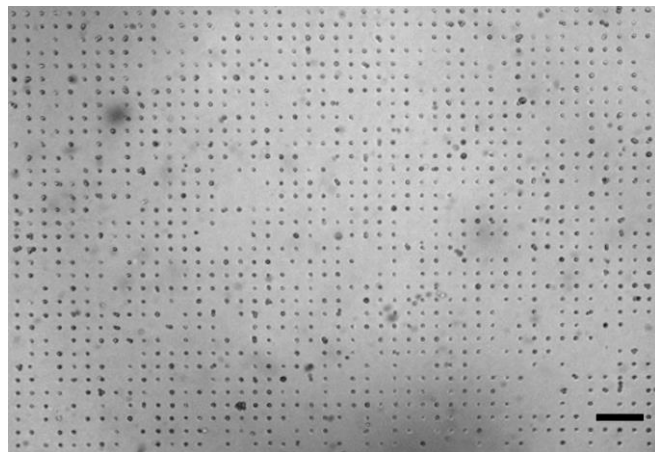


Figure 6.4. Bright field microscopy image of a SCADA substrate after incubation with hHF-MSCs, containing 1758 protein dots and 1298 cells. Scale bar corresponds to 250 μ m.

Controlled cellular detachment was induced by exposing the cell-saturated substrates to a solution of Phosphate Buffer Saline (PBS) lacking Ca^{2+} and Mg^{2+} . Integrins have 3 to 5 binding sites for divalent cations in each heterodimer. Different cations play different roles; they may act as adhesion promoters inducing ligand binding, but also as antagonists inhibiting adhesion¹⁷. It is known that the absence of Ca^{2+} and Mg^{2+} in the media affects the equilibrium between the active and the inactive forms of integrins, and promotes cellular detachment without damaging the cells¹⁸. hHF-MSCs detached from FN dots slowly in the first 40 min, whereas from that time on, their detachment kinetics increased significantly. After 2 h in PBS, cellular release from the surface became slower, until every adhered cell was detached, after 4 h (Figure 6.5).

Flow cytometry showed that more than 60 % of detached cells remained alive, confirming the controlled detachment triggered by the lack of Ca^{2+} and Mg^{2+} . This experiment proved the capability of this technique to perform a label-free,

quantitative and dynamic monitoring of cellular detachment with single cell resolution by using optical microscopy.

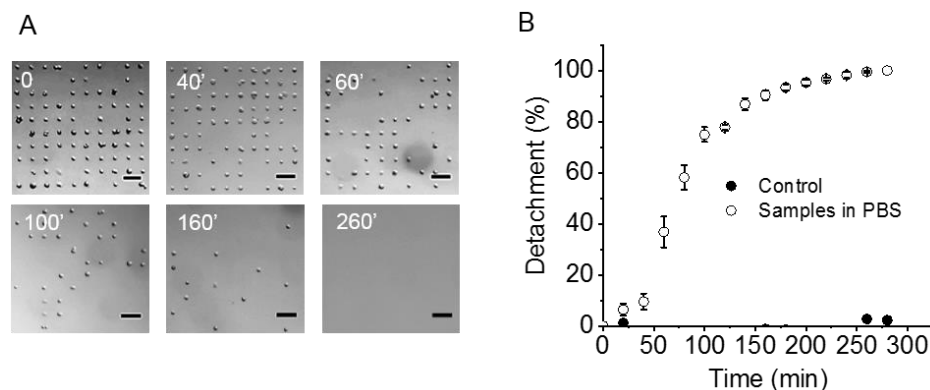


Figure 6.5. Dynamic cell detachment on SCADA. A) Optical microscopy images of single cell arrays at different times in presence of PBS: at time 0, 40, 60, 100, 160 and 260 min. Scale bar corresponds to 100 μ m. B) Detachment of hHF-MSCs *versus* time of exposure to PBS. Error bars correspond to the standard deviation from the mean for $n = 3$.

6.2.2 Monitoring cytotoxicity of K_2CrO_4 and DMSO measured by label-free SCADA viability test

Potassium chromate, K_2CrO_4 , is a strong oxidant agent, which is considered to be highly toxic, while DMSO is an organosulfur compound widely used for biological applications. DMSO induces membrane permeabilisation in living cells that ends up compromising membrane integrity for higher concentrations than 10 % (v/v), for this reason it is usually used at lower concentrations for cell culture¹⁹.

To monitor K_2CrO_4 induced cytotoxicity, cell saturated SCADA substrates were

incubated with solutions of 50 μM and 100 μM aqueous solutions of K_2CrO_4 for 30 h. The data obtained showed increasing cellular detachment with the exposure time and the concentration of the toxic, after 6 h of incubation (Figure 6.6A). After 30 h in presence of 50 and 100 μM of K_2CrO_4 , there was a 74 % and 87 % of cellular detachment in contrast with the control samples, which had only a 30 % of detachment. Cr (VI) has been previously reported to cause replication stress²⁰, which can lead to apoptosis or programmed cellular death^{21,22}. This agrees with the results shown in this chapter, where significant detachment could only be observed after 6 h of incubation with the toxic.

To evaluate the cytotoxicity of DMSO, the effect of 1, 2, 6, 8 and 10 % (v/v) DMSO was measured for 24 h on cells adhered to FN-SCADA substrates. The measurements showed an increasing detachment of cells with time of exposure to DMSO, reaching up to 40 % of detachment after 5 h for the highest concentration of DMSO in contrast with the control samples, which were not exposed to DMSO, and exhibited only a 4 % detachment at the same time. When cells were treated with 8 % and 10 % of DMSO (v/v), after 21 h, 100 % of the cells were detached from the substrate, while in the control samples only a 16 % of detachment was observed. In general, faster detachment kinetics were observed for higher concentrations of DMSO (Figure 6.6B). To the best of my knowledge, the effect of DMSO concentrations below 10 % for hHF-MSCs has not been precisely quantified before in terms of cellular death.

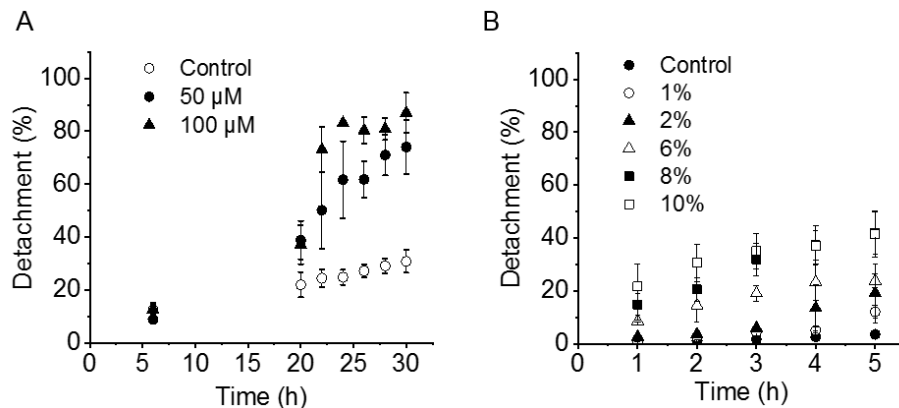


Figure 6.6. A) Cellular detachment kinetics in presence of 50 and 100 μM K_2CrO_4 for 30 h. Error bars correspond to the standard deviation from the mean for $n = 3$. B) Cellular detachment kinetics in presence of 1, 2, 4, 6, 8 and 10 % of DMSO for 5 h. Error bars correspond to the standard deviation from the mean for $n = 3$.

When the cytotoxicity of K_2CrO_4 and DMSO were evaluated, trypan blue viability test showed that the cells that remained adhered to the substrate were alive, while the cells detached were dead. These tests revealed a good correlation between cellular death and cell detachment from the SCADA substrates.

6.2.3 Cytotoxicity colorimetric SCADA viability test

In contrast to impedance-based techniques, the SCADA substrates could also be used to detect the toxic effect of compounds that promote stable cell adhesion after cell death. This is thanks to the fact that the SCADA methodology uses an optical readout. Hg^{2+} is a divalent cation which induces cellular death but inhibits the detachment of hHF-MSCs from FN. In this chapter, this model was used to monitor cell death by a colorimetric assay using the binary counting board. Cell containing SCADA substrates were exposed to HgSO_4 solutions of 5, 25 and 50 μM for 30 h. In the presence of HgSO_4 cells did not detach from the fibronectin

surface, and the DAO values were similar to the DAO values of the control samples (Figure 6.7A). To monitor cell death in this case, trypan blue was used, a life/death marker that penetrates the cellular membrane of dead cells, staining them in blue. As it cannot enter through healthy cellular membranes, living cells remain uncoloured (Figure 6.7B). Subsequently, cell saturated FN-SCADA substrates were exposed to 50 µM of HgSO₄ for 48 h, and trypan blue was added at different time points to measure cell viability. The quantification of blue and non-coloured cells on the substrate at each time point showed an increasing number of dead cells with the time of exposure to HgSO₄ (Figure 6.7C).

In a different experiment, cells adhered to FN-SCADA substrates were exposed to solutions of 5 µM, 25 µM and 50 µM of HgSO₄ for 48 h, and the trypan blue assay also showed an increasing rate of cell death with the concentration of HgSO₄, confirming its cytotoxicity (Figure 6.7D).

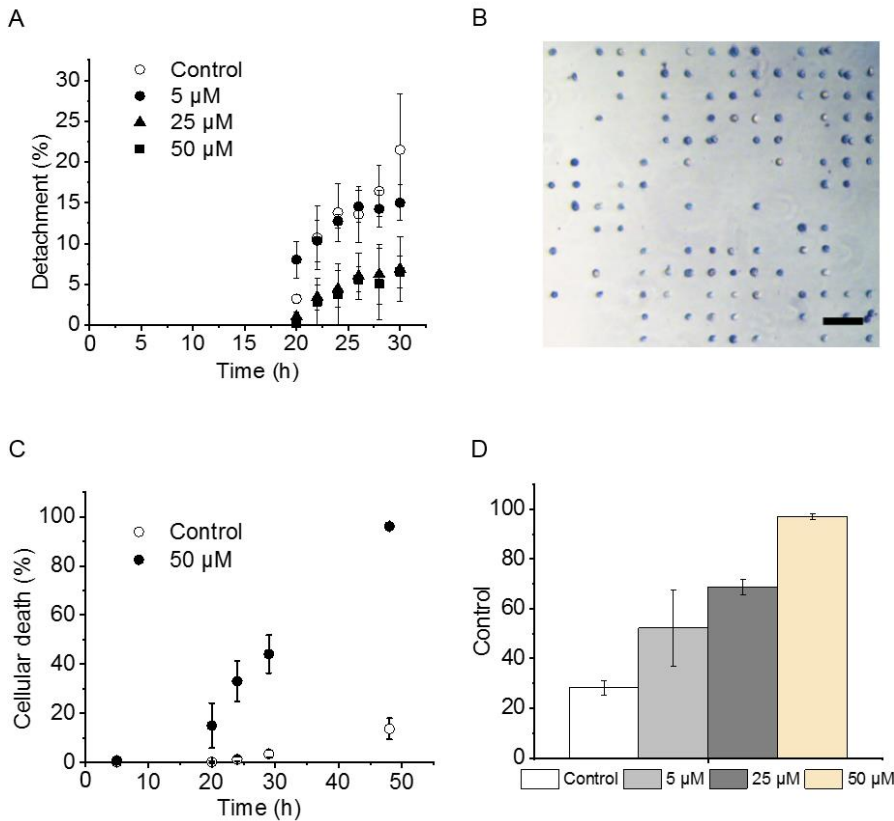


Figure 6.7. Cellular death after incubation with HgSO₄. A) Cellular detachment kinetics of hHF-MSCs in presence of 5, 25 and 50 µM of HgSO₄. B) Optical microscopy image (10x objective) of FN-SCADA substrates with hHF-MSCs 48 h after incubation with 25 µM of HgSO₄. Scale bar corresponds to 100 µm. C) Graphical representation of cellular death during 48 h in presence of 50 µM of HgSO₄. D) Plot of cell death after 48 h in the presence of 5, 25 and 50 µM of HgSO₄. Error bars correspond to the standard deviation from the mean for n = 3.

6.2.4 SCADA on Chip

The previous results demonstrated that the SCADA substrates were suitable to monitor cytotoxicity by optical imaging of a small substrate area. The integration

of FN-SCADA substrate into a flow cell would enable the continuous monitoring of cell adhesion and detachment by imaging a fixed area, while flowing a cell suspension or compounds that could alter viability or adhesion of the adhered cells. Preliminary experiments were performed as explained in experimental section 6.4.6, to integrate the SCADA assay into a microfluidic device (Figure 6.8A). The dimensions of the device were 24 mm x 60 mm (Figure 6.8B), and it consisted of three layers. A first layer of poly (methyl methacrylate) (PMMA) as the substrate, containing the FN dot array pattern, a 127 μm thick Pressure Sensitive Adhesive (PSA) layer defining the boundaries of the flow cell, and a top layer made of Cyclic Olefin Polymer (COP), with inlet and outlet openings (Figure 6.8C).

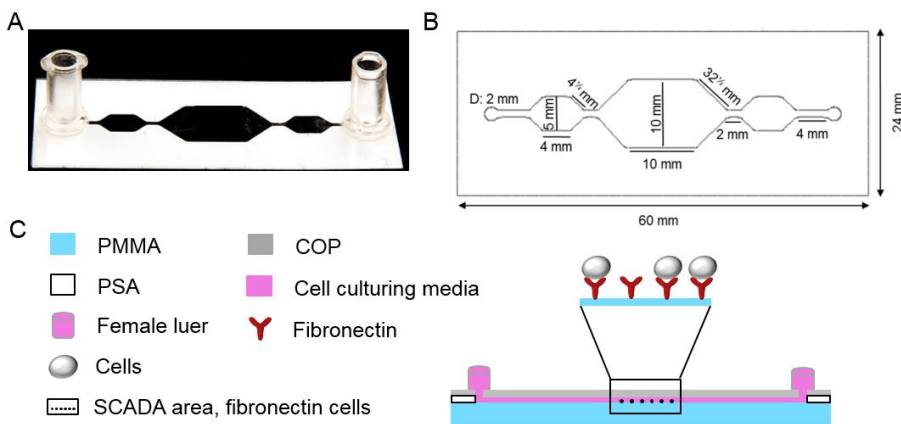


Figure 6.8. A) Picture of the microfluidic device mounted with the connections set. B) Top view of the designed microfluidic device with its corresponding dimensions and C) Side view representation of the hybrid microfluidic device composed of 3 polymeric layers: PMMA, PSA for the channel height and design and COP to seal it, not in scale. The zoom corresponds to the SCADA area.

Preliminary single cell adhesion experiments were carried out using 100000 cells mL⁻¹ under a continuous flow of 50 µL min⁻¹, but a very low adhesion of single-cells was obtained. Nevertheless, at these conditions and under a microscope, the cells could be seen rolling slowly on the surface, following a straight path and making contact with the surface, so the flow rate seemed adequate to obtain cellular adhesion. However, due to the precipitation of cells by gravity in the reservoir before entering the microfluidic channel, the concentration of cells within the device at different locations was different, so the adhesion results and required times would not be reliable. Also, due to the static period, cells aggregated, forming big clusters that complicated single cell adhesion.

Considering this, the pump was programmed to do infusion-withdrawal cycles with a flow rate of 50 µL min⁻¹, which enabled the use of lower volumes of cell suspension. Moreover, instead of having a new suspension passing through the channel in a continuous flow, the same suspension volume was recirculated several times. Therefore, considering the low adhesion values obtained with 100000 cells mL⁻¹ and the lower amount of cells in suspension required with the new flow conditions, 300000 cells mL⁻¹ were used in the next on-chip experiments to promote cell adhesion. As it is shown in Figure 6.9, cells specifically attached to the FN dots, obtaining a DAO of 84 % after 15 min of incubation (under recirculating conditions). The kinetics observed using microfluidics seemed to be faster, since this 84 % of adhesion was obtained in conventional wells after 1 h of incubation (Figure 6.3). However, the adhesion kinetics of both experiments cannot be straightly compared since the initial concentration of cells was different. For that, the Microfluidics Cluster UPV/EHU is currently working on the optimisation of this system.

Besides, due to the specific adhesion of cells to the protein dots Figure 6.9, PMMA

appears to be a good substrate for micropatterning by microcontact printing. It just needs an air plasma treatment before doing the micro-contact printing of FN. Nevertheless, on some FN spots two cells were observed, which might be due to the time that cells are static in the inlet reservoir, before entering the microfluidic channel. In this short period, cells could start aggregating, clustering between them.

The cell adhesion is specific in the microfluidic device, but keeping cells as single cells at every point is still challenging, and it is a future task to be investigated in order to obtain a portable and efficient SCADA microfluidic test device.

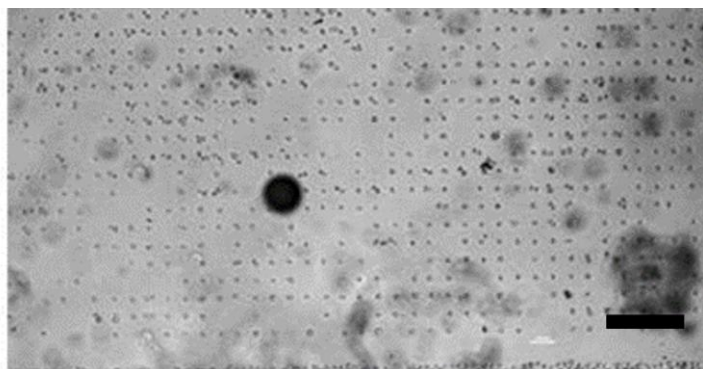


Figure 6.9. Optical microscopy image of the single cell adhesion on chip, after 15 min of incubation of cells. Scale bar corresponds to 300 μm .

Although the results shown in this section are preliminary, they seem promising for the future development of a user-friendly and portable SCADA devices for cytotoxicity testing. In order to do that, the microfluidic device and the flow conditions are being optimised to avoid cell clusters and guarantee that the shear forces are not an inconvenience for cells to create the single cell arrays. Moreover, the miniaturisation and simplification of the optical set-up is an ongoing task as well, which ambitions to provide a more cost-effective and user-friendly

approach of SCADA cytotoxicity test devices.

6.2.5 General discussion

SCADA substrates enabled, for the first time, to measure the toxic effect of DMSO and K₂CrO₄ on hHF-MSCs by monitoring cell detachment rate in a label-free mode by optical imaging. The precision of the SCADA system is based on a binary counting mode, which uses an array of adhesive dots occupied by individual cells for the quantification of cellular detachment with single cell resolution. The number of positive dots can be easily counted, and its percentage from the total number of adhesion dots calculated, being that the DAO or the cellular adhesion percentage. Each adhesion site is independent from each other, having each dot the same probability to be occupied by a single cell, emptied or labelled, constituting a binary digital code: occupied/vacant, stained/not stained, positive/negative or what is the same, 0/1.

There are a number of cytotoxicity tests currently available in the market, each of them with different characteristics, and each one providing different type of data. What cytotoxicity test to use may depend on the type of cell and the type of data required by the user.

Herein, I include a decision tree to help the user decide whether a SCADA test could provide the information needed for their specific system (Figure 6.10). SCADA cytotoxicity test is a non-invasive, specific technique useful to obtain cellular death kinetics with single cell resolution, using simply optical instrumentation. SCADA is a highly sensitive technique, designed to monitor cell death. Toxic effects that do not result in cell death cannot be detected with this platform. This methodology enables both, dynamic detachment monitoring, and rapid detection of toxic effects of compounds that promote cell adhesion.

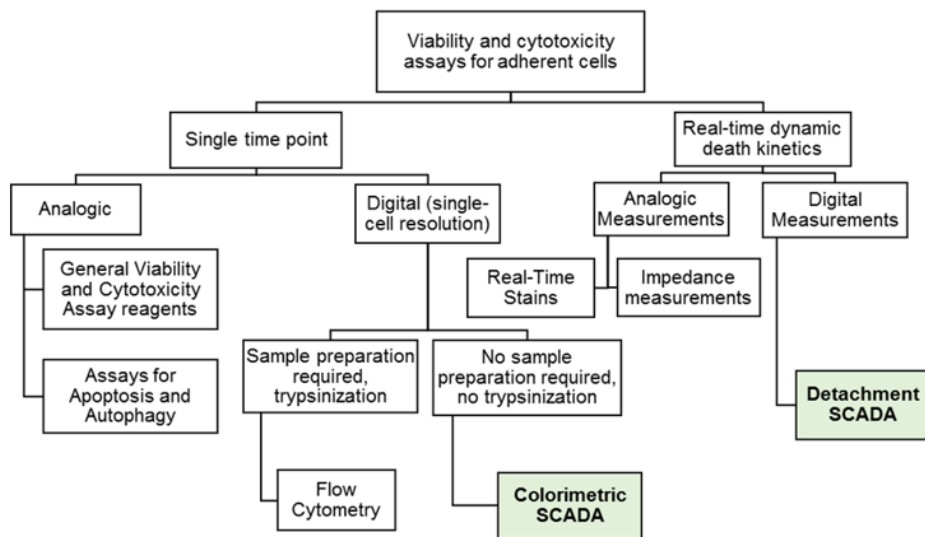


Figure 6.10. Classification of viability and cytotoxicity assays already available for adherent cells as a function of the type of data that may be obtained. SCADA provides digital measurements of cellular death without the need of sample preparation after exposure to the toxic.

PBS induced cellular detachment through integrin deactivation, lowering down the capability of cells to attach to fibronectin, which resulted in a 100 % detachment rate in 5 h. Cr (VI) induced cellular detachment by triggering the apoptosis of cells, which is a much slower process and DMSO triggered cell detachment faster, inducing cellular death. Contrarily, Hg^{2+} killed the cells as confirmed by Trypan Blue test, but kept them strongly adhered to FN dots. This divalent cation could be modulating cellular adhesion, activating or inactivating integrins through specific divalent cation-binding sites.

In contrast with current available cytotoxicity tests based on analogical signals like fluorescence, light or electrochemical impedance, SCADA is based on digital counting, providing the highest resolution, up to single cell resolution. Besides,

compared to flow cytometry, SCADA methodology allows dynamic and real time measurements, because it avoids the time gap between the target time when the toxic is added and the time in which the cellular death measurements are performed.

SCADA assays require only a patterned substrate area of less than 1 cm², and a reduced number of cells, ranging from hundreds to thousands of cells, while other techniques normally use more than 10000 cells per measurement. Nonetheless, the number of cells analysed in SCADA could be increased to a million cells if needed, by using larger patterned areas of the substrate and automated microscopy scanning. For this proof of concept, the patterned substrates were created by micro-contact printing, but other methods such as light directed chemical patterning could be used by any laboratory with commercially available equipment.

A combination of assays such as colorimetric or flow cytometry may be necessary to correlate cellular viability and cellular adhesion in the presence of a specific compound to test. Once determined that correlation, the system can provide extra information such as toxicity kinetics or cell population heterogeneity.

The readout of this assay requires only optical components to be carried out, avoiding the need of high sensitivity detectors like in the case of fluorescence measurements, or the complex fabrication process of microelectrode arrays used in the xCELLigence RTCA.

6.3 Conclusions

SCADA forms the bases for a high-resolution methodology to track cell death. It is based on dynamic digital quantification of cell viability by optical imaging,

enabling both, dynamic cell detachment monitoring but also rapid detection of toxic effects of compounds that promote cell adhesion. The applicability of SCADA cytotoxicity methodology could be extended to many different types of cells and assays, by customising the protein dot array, changing the shape of the dots, their number and their composition. I believe that the impact of this methodology for accurate measurement of cytotoxicity will extend to fundamental research and commercial applications through the integration of SCADA substrates into microfluidic devices with low cost portable optical components, enabling high throughput cytotoxicity measurements at the point of need.

6.4 Experimental

6.4.1 Materials

Photolithography and soft lithography: Dow Corning Sylgard 184 was purchased from Ellsworth Adhesive, trimethoxy (octadecyl) silane was purchased from Sigma Aldrich, silicon wafers (500 µm thick) were purchased from University Wafer Inc. (U.S.A.), and SU-8 2025 photoresist and SU-8 developer were obtained from ATIS S.A. (Spain). Microcontact printing: Bovine Plasma Fibronectin and Tetramethylrhodamine conjugated Albumin from Bovine Serum (BSA-TAMRA) were purchased from Fisher Scientific (Life Technologies, Spain). PBS (0.01 M phosphate buffer, 0.0027 M potassium chloride and 0.137 M sodium chloride, pH = 7.4 at 25 °C) and BSA powder were purchased from Sigma Aldrich, Spain, and polystyrene (PS) P12 culture dishes Vari-Mix steep angle rocker were obtained from Fisher Scientific Spain.

SCADA on chip: PMMA 4 mm thick was obtained from Microplanet

Laboratorios S.L., Spain, double side PSA from Adhesive Research (Ireland), 100 µm thick COP and the luers from Microfluidics ChipShop (Germany). The tubing was from Altman Analytik GmbH & Co., (Germany).

Cell culture: Human adult Mesenchymal Stem Cells were obtained from human hair follicles, provided from Ercilla Medical Clinic Bilbao (Spain). Growth Medium (GM) consisted of Dulbecco's Modified Eagle's Medium (DMEM) supplemented with 30 % Fetal Bovine Serum (FBS) and 10 % Penicillin/Streptomycin (P/S). These reagents and Gibco Trypan Blue Solution (0.4 %) were purchased from Fisher Scientific (Spain). Paraformaldehyde 4 % for fixation was purchased from Panreac Química (Spain). For the cytotoxicity tests, Potassium Chromate (K_2CrO_4) and Mercury Sulfate ($HgSO_4$) were purchased from Merck and from Panreac Química (Spain), respectively, and DMSO from Fisher Scientific (Spain).

6.4.2 Photolithography and soft lithography

SU-8 mould fabrication station (BlackHole-Lab, France) was used for the manufacturing of the SU-8 master on silicon wafers, following the steps from Figure 6.11A. The silicon wafer was first dehydrated at 220 °C, and then SU-8 2025 was dynamically spun on top of the wafer, reaching a maximum of 5500 rpm. The wafer was soft baked for 2 min at 65 °C and 4 min at 95 °C. To achieve the adequate resolution of the design of the photo mask, the rigid surface was exposed to UV light during 4 pulses of 5 s each, and then it was baked on the hot plate for 1 min at 65 °C and 3 min at 95 °C. Finally, the features were developed dipping the master in the developer in 2 cycles of 1 min to obtain the developed wafer (Figure 6.11B).

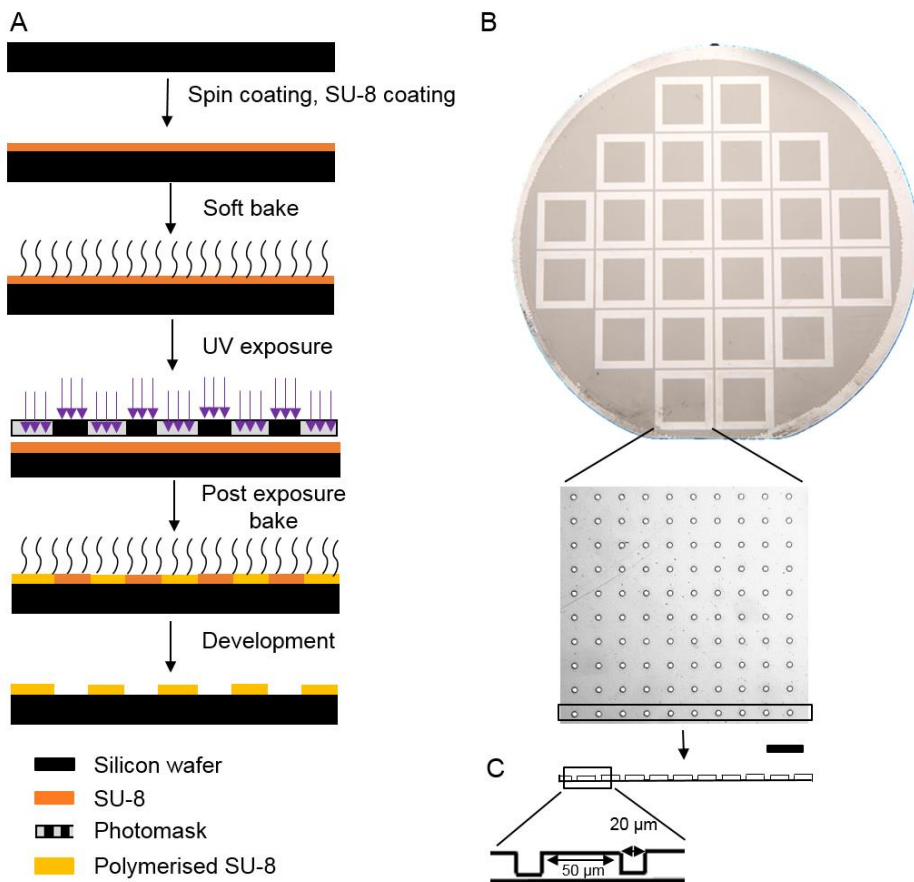


Figure 6.11. A) Graphic representation of photolithography technique. B) picture of the manufactured silicon wafer with optical microscopy picture of the micropattern amplified. Scale bar corresponds to 100 μm . C) Side view and profile of the manufactured silicon wafer comprised of holes of 20 μm diameter separated by 50 μm .

After the fabrication of the master, it was silanised, adding a layer of trimethoxy(octadecyl)silane by vapour deposition for 1 h, to avoid damages to the master when releasing the PDMS. PMDS stamps were made by pouring a mixture of Sylgard 184 elastomer and curing agent (10:1 v/v) over the fabricated

silicon master. It was degassed and cured at 60 °C for 1 h, then the PDMS was detached from the wafer and it was kept at 60°C for 16 h more to make sure the crosslinking was completed.

To get the stamps, the PDMS mould obtained was cut in pieces of (1 x 1) cm. Each stamp was comprised of 20000 pillars of 20 µm diameter with a separation of 50 µm between dots.

6.4.3 Microcontact Printing

The wells of PS P12 culture dishes were used as substrates for protein patterning and the process was performed as explained elsewhere²³ (Figure 6.12A). Briefly, first the PDMS stamps were inked with a solution of 115 nM of fibronectin and 100 nM of BSA-TAMRA in PBS for 30 min. During that incubation time, the polymeric surfaces of the culture dishes were oxidised with air plasma for 40 s, to make the surface more hydrophilic and to enhance the protein transfer from the PDMS stamp to the substrate.

The excess of protein ink solution was removed with the micropipette, the PDMS stamps were rinsed with distilled water, and they were then carefully dried with compressed air to eliminate humidity. The patterned area of the stamps was then put in contact with the substrate for 30 min, and then the stamps were removed, creating a protein pattern on the surface, comprised of 20000 dots of 20 µm diameter and separated from each other by 50 µm. Finally, 1 mL of 1 % BSA solution in PBS was added to each patterned well to block any surface area that had not been in contact with proteins. The blocking solution was kept overnight at 4 °C. For every experiment, the surface patterning for cell adhesion was carried out the day before the addition of the cells was performed.

All the substrates were characterised by fluorescence microscopy to evaluate the quality of the FN dot array (Figure 6.12B). The fluorescence intensity and the diameter of 3300 dots within a single substrate was first analysed. A substrate was considered as adequate if the CVs in their fluorescence intensity and their shape were lower than 20 %.

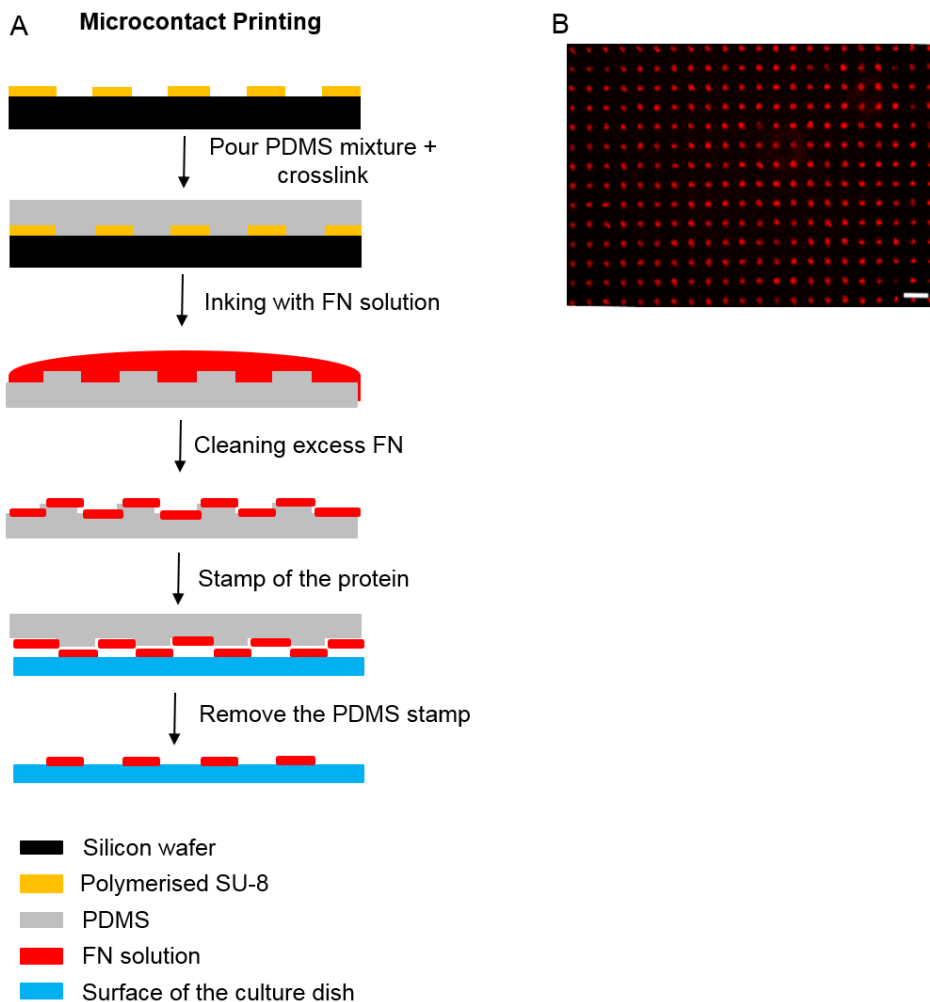


Figure 6.11. A) Graphic representation of microcontact printing technique. B) Fluorescent microscopy picture of a uniform protein pattern for single cell adhesion. Scale bar corresponds to 100 μm .

6.4.4 Quantification of cell adhesion and detachment

hHF-MSCs cultured in T75 PS flasks were trypsinised, and after centrifugation cells were quantified to obtain an adequate number of cells. Then, they were resuspended in pattern medium, comprised by DMEM and P/S (9:1 v/v) in a concentration of 100000 cell·mL⁻¹. 1 mL of cell suspension was added to each patterned well, which was previously washed 3 times with PBS, and incubated at 37 °C and 5 % CO₂ on a rocker (steep angle rocking), at a speed of 5 cycles per min for at least 90 min, in order to achieve a DAO over 90 %. After that, the wells were washed twice with PBS, and subsequently PBS or a solution of a toxic compound was added to the medium. Cellular adhesion was monitored for several hours, keeping cells at 37 °C and 5 % of CO₂.

To quantify the number of cells adhered on a patterned surface, bright field microscopy images were taken. DAO was calculated as the percentage of binding sites (fluorescent dots) occupied by cells. Cellular detachment was calculated by subtracting the DAO value at a certain time from the initial DAO normalised to 100 %.

Each data point in this chapter corresponds to the arithmetic average of DAO among 3 different replicas of the same sample type. For each replica, 1 random image was taken, with a field of view of 13.5 mm², each replica comprised of 1728 protein dots.

Trypan-Blue-test was performed in other samples to confirm that the adhered cells were alive, cell media was removed, the samples were washed twice with PBS, and 50 % (v/v) of Trypan Blue in DMEM was added to immediately track their viability. Optical microscopy pictures were taken and cellular viability was measured by counting the number of blue stained cells and divided by the total

number of cells.

6.4.5 Flow cytometry

To calibrate the system, 1200 µL of trypsinised cells were collected from a standard culture flask. 250 µL of ethanol (70 %) and 10 µL of ethidium bromide were added to cause and detect cell death, respectively. Subsequently, cell loaded SCADA substrates were exposed to PBS lacking Ca²⁺ and Mg²⁺. Cell adhesion data was collected at different time points and the cell media was collected to determine the rate of live and dead cells on the detached cells. 10 µL of ethidium bromide was added per 1200 µL of detached cells containing media. Those samples were introduced in the cytometer with the previously determined settings for those cells, and the percentage of dead cells was calculated. Ratios alive/dead cells of 63/37, 72/28, 60/40 were obtained after 1, 2 and 3 h incubation of the SCADA substrate with PBS.

6.4.6 Microscopy images

A Nikon Eclipse TE2000-S inverted microscope coupled with ANDOR ZYLA sCMOS camera and C-LHG1 100W Mercury lamp was used to obtain images of the fluorescent protein patterns and bright field images of adherent cells arrays. An Olympus IMT-2 inverted microscope, coupled with a TUCSON BCA 5.0 colour camera was used to perform the trypan blue viability assay on the SCADA substrates.

6.4.7 SCADA on chip

The microfluidic device was designed using AUTOCAD 2.0 and fabricated by lamination of three layers, PMMA, double side PSA and COP. PMMA was cut

using a CO₂ laser system and PSA and COP polymeric sheets were cut with a cutter plotter system. Figure 6.8. shows the design of the fluidic cell, which had a final total volume of 26.3 µL. PSA and COP were cut with Graphtec CE6000-40 and PMMA was cut using a CO₂ laser system. A Standard Infuse/Withdraw Pump 11 Elite Programmable Syringe Pump (Harvard apparatus) was used to drive the cell suspension through the device.

For the protein pattern, the PMMA substrate was consciously rinsed with distilled water and ethanol, dried with compressed air and subsequently oxidised with air plasma for 20 min. After oxidation, the PSA with the microchannel was adhered on one side to this slide and micro-contact printing was performed as explained in section 6.3.2.2, patterning single-cell fibronectin dot arrays on the central part of the substrate. Once the protein pattern was created, the upper protective cover layer of PSA was removed and the COP layer was attached to close the microfluidic device. Two female luers were positioned in the inlet and the outlet of the flow chamber. The barrel of a 1 mL syringe was connected to the inlet luer to act as a reservoir. 1 mL BSA 1 % was added in the barrel and introduced in the flow chamber, withdrawing from the other side carefully to avoid the formation of bubbles. After 1 h of incubation at RT with BSA, the BSA was replaced with cell media without FBS. Then, cells were added in a concentration of 300000 cells·mL⁻¹ in DMEM/PS medium, with a flow of 50 µL min⁻¹, doing withdrawal/infusion cycles for 15 min.

6.5 References

1. Stoddart, M. J. Cell viability assays: introduction. In *Mammalian Cell Viability: Methods and Protocols*; Stoddart, M.J., Ed.; Humana Press: Totowa, NJ, USA, 2011; pp 1-6.
2. Ngo, L. P.; Chan, T. K.; Ge, J.; Samson, L. D.; Engelward, B. P. Microcolony Size Distribution Assay Enables High-Throughput Cell Survival Quantitation. *Cell Rep.* 2019, 26, 1668-1678. e4.
3. Gelles, J. D.; Chipuk, J. E. Robust high-throughput kinetic analysis of apoptosis with real-time high-content live-cell imaging. *Cell Death Dis* 2016, 7, e2493.
4. Forcina, G. C.; Conlon, M.; Wells, A.; Cao, J. Y.; Dixon, S. J. Systematic quantification of population cell death kinetics in mammalian cells. *Cell Syst.* 2017, 4, 600-610. e6.
5. Hosokawa, M.; Hayashi, T.; Mori, T.; Yoshino, T.; Nakasono, S.; Matsunaga, T. Microfluidic device with chemical gradient for single-cell cytotoxicity assays. *Anal. Chem.* 2011, 83, 3648-3654.
6. Atienza, J. M.; Zhu, J.; Wang, X.; Xu, X.; Abassi, Y. Dynamic monitoring of cell adhesion and spreading on microelectronic sensor arrays. *J Biomol. Screen.* 2005, 10, 795-805.
7. Xing, J. Z.; Zhu, L.; Jackson, J. A.; Gabos, S.; Sun, X.; Wang, X.; Xu, X. Dynamic monitoring of cytotoxicity on microelectronic sensors. *Chem. Res. Toxicol.* 2005, 18, 154-161.
8. Susloparova, A. Electrical cell-substrate impedance sensing with field-effect transistors is able to unravel cellular adhesion and detachment processes on a single cell level. *Lab Chip* 2015, 15, 668-679.
9. Abassi, Y. A.; Xi, B.; Zhang, W.; Ye, P.; Kirstein, S. L.; Gaylord, M. R.; Feinstein, S. C.; Wang, X.; Xu, X. Kinetic cell-based morphological screening: prediction of mechanism of compound action and off-target effects. *Chem. Biol.* 2009, 16, 712-723.
10. Azioune, A.; Storch, M.; Bornens, M.; Théry, M.; Piel, M. Simple and rapid process for single cell micro-patterning. *Lab Chip* 2009, 9, 1640-1642.
11. Basabe-Desmonts, L.; Ramstrom, S.; Meade, G.; O'neill, S.; Riaz, A.; Lee, L.; Ricco, A.; Kenny, D. Single-step separation of platelets from whole blood coupled with digital quantification by interfacial platelet cytometry (iPC). *Langmuir* 2010, 26, 14700-14706.
12. Lopez-Alonso, A.; Jose, B.; Somers, M.; Egan, K.; Foley, D. P.; Ricco, A. J.; Ramström, S.; Basabe-Desmonts, L.; Kenny, D. Individual platelet adhesion assay: measuring platelet function and antiplatelet therapies in whole blood via digital quantification of cell adhesion. *Anal. Chem.* 2013, 85, 6497-6504.
13. Jose, B.; McCluskey, P.; Gilmartin, N.; Somers, M.; Kenny, D.; Ricco, A. J.; Kent, N. J.; Basabe-Desmonts, L. Self-powered microfluidic device for rapid assay of antiplatelet drugs. *Langmuir* 2016, 32, 2820-2828.

14. Li, Q.; Ma, L.; Su, M. Single identical cell toxicity assay on coordinately ordered patterns. *Anal. Chim. Acta* 2019, 1065, 56-63.
15. Gonzalez-Pujana, A.; Santos-Vizcaino, E.; García-Hernando, M.; Hernaez-Estrada, B.; de Pancorbo, M. M.; Benito-Lopez, F.; Igartua, M.; Basabe-Desmonts, L.; Hernandez, R. M. Extracellular matrix protein microarray-based biosensor with single cell resolution: Integrin profiling and characterization of cell-biomaterial interactions. *Sensor Actuat. B-Chem.* 2019, 299, 126954.
16. Ruster, B.; Gottig, S.; Ludwig, R. J.; Bistrian, R.; Muller, S.; Seifried, E.; Gille, J.; Henschler, R. Mesenchymal stem cells display coordinated rolling and adhesion behavior on endothelial cells. *Blood* 2006, 108, 3938-3944.
17. Plow, E. F.; Haas, T. A.; Zhang, L.; Loftus, J.; Smith, J. W. Ligand binding to integrins. *J. Biol. Chem.* 2000, 275, 21785-21788.
18. Tiwari, S.; Askari, J. A.; Humphries, M. J.; Bulleid, N. J. Divalent cations regulate the folding and activation status of integrins during their intracellular trafficking. *J. Cell. Sci.* 2011, 124, 1672-1680.
19. de Ménorval, M.; Mir, L. M.; Fernández, M. L.; Reigada, R. Effects of dimethyl sulfoxide in cholesterol-containing lipid membranes: a comparative study of experiments in silico and with cells. *PloS one* 2012, 7, e41733.
20. Liu, F.; Barchowsky, A.; Opresko, P. L. The Werner syndrome protein suppresses telomeric instability caused by chromium (VI) induced DNA replication stress. *PLoS One* 2010, 5, e11152.
21. De Zio, D.; Cianfanelli, V.; Cecconi, F. New insights into the link between DNA damage and apoptosis. *Antioxid Redox Signal.* 2013, 19, 559-571.
22. Bagchi, D.; Bagchi, M.; Stohs, S. J. Chromium (VI)-induced oxidative stress, apoptotic cell death and modulation of p53 tumor suppressor gene. *Mol. Cell. Biochem.* 2001, 222, 149-158.
23. Hamon, C.; Henriksen-Lacey, M.; La Porta, A.; Rosique, M.; Langer, J.; Scarabelli, L.; Montes, A. B. S.; González-Rubio, G.; de Pancorbo, M. M.; Liz-Marzáñ, L. M. Tunable nanoparticle and cell assembly using combined self-powered microfluidics and microcontact Printing. *Adv. Funct. Mater.* 2016, 26, 8053-8061.

7

Smart Functional Electrodes for the Simultaneous Monitoring of Cell Capture and Release Processes

This chapter presents a microsystem configuration that combines functional materials, for the non-invasive capture and release of cells, and simultaneous cell monitoring. For that the thermo-responsive poly(*N*-isopropylacrylamide) has been combined with the electroactive material, poly(3,4-ethylenedioxythiophene) polystyrene sulfonate, to create a smart and conductive copolymer. The copolymer is casted on gold electrodes and functionalised with fibronectin to capture cells. The copolymer undergoes a conformational change in response to temperature, acting as an actuator, and therefore causing the release of the cells. Simultaneously, the copolymer acts as a sensor, enabling the monitoring of the whole cell capture and release process by electrochemical impedance spectroscopy.

* Saez, J., Garcia-Hernando, M., Savva, A., Basabe-Desmonts, L., Owens R., Benito-Lopez, F. PEDOT:PSS/pNIPAAm hydrogel-based electrodes for the monitoring of the capture and release of label-free biomarkers. *2020 MRS Spring/Fall Meeting & Exhibit, 27 November-4 December, 2020.*

7.1 Introduction

Non-invasive collection of flowing cells such as Circulating Tumour Cells (CTCs)¹⁻⁴, bacteria^{5,6}, viruses⁷ or exosomes⁸⁻¹⁰ is fundamental for cell biology, diagnosis and prognosis of diseases, cancer research, drug development and regenerative medicine. In these research fields, cells usually need to be analysed after their collection, so guaranteeing their viability during the process is essential. The most popular and conventional approaches for the collection of target cells include density-gradient centrifugation^{11,12}, flow cytometry^{13,14} and immunomagnetism¹⁵, which are complex and laborious, and require size-dependent sorting^{16,17}.

Immunocapture based biosensors bring selectivity for the target cells^{18,19}, using specific cell-ligand interactions, which are valuable for specific capture, taking advantage of biochemically modified particles. Specific aptamer²⁰⁻²² and DNA^{23,24} ligands are also useful for the capture and release of cells, due to specific cell binding nucleic acid sequences. In these cases, cell release is enzymatically triggered, cutting the ligand at a restriction point. However, a system with no enzymatic release would ensure the non-invasiveness for the cells during their capture and release, by using specific ligand-cell bonding based systems.

The popularity of hybrid functional materials is rising for non-invasive cell capture and release. Within functional materials, poly(*N*-isopropylacrylamide) (pNIPAAm) has been used for pH sensing in Chapters 3 and 4, and its versatility has been proven in Chapter 5 as supporting material for the controlled and high throughput formation and monitoring of lipid nanotubes. Nevertheless, pNIPAAm is a thermo-responsive polymer with a lower critical solution temperature (LCST) at 32 °C. Below the LCST, the polymer is hydrophilic, and

swells due to hydrogen bond interactions between chains. When the temperature is above the LCST, conformational changes cause the disruption of the hydrogen bonding interactions, causing the material to shrink ²⁶. Due to this stimuli-responsive behaviour and the compatibility of its LCST with cellular viability, pNIPAAm is useful as an actuator to modulate cellular adhesion/detachment ²⁷.

The use of functionalised pNIPAAm networks for the capture and release of cells, triggered by a change in temperature, has been reported before ^{3,28-30}. The working principle consisted in the capture of CTCs at 37 °C, on pNIPAAm functionalised with cell adhesion moieties. The release was triggered by cooling the material below 32 °C, changing the conformation and topography of pNIPAAm. pNIPAAm is a versatile polymer whose combination with other materials can generate new hybrid functional materials with improved physicochemical properties. As an example, Hao *et al.* combined temperature-responsive pNIPAAm with light-responsive spiropyran molecules to generate polymeric brushes capable of capture and release cells ⁴. Although these systems allow non-invasive and specific capture and release of target cells, often external labels – usually fluorescent- are required for the monitoring of the system.

Bioelectronics devices enable the monitoring of cellular processes, providing information on cell processes such as growth and differentiation ^{31,32}. They have already been used to monitor cell capture and release ^{22,33}. For instance, Gao *et al.* ³³ designed a capture and release system based on ferrocene (Fc) and β-cyclodextrin (β-CD). By applying a reduction voltage, the uncharged Fc could bind to the β-CD, which was immobilised on the electrode surface. Cells were released because of the electrochemical oxidation. Later, Cao *et al.* ²² presented a nanochannel-ion channel, functionalised with an aptamer, for the capture and enzymatic release of cells continuously measuring the ion flow through the

nanochannel. They reported a decrease of the ion flow due to cell adhesion, which was recovered after the release. Therefore, the combination of electroactive materials with pNIPAAm could allow the monitoring of cell capture and release, providing real-time information without disturbing the cellular wellbeing.

Electrochemical impedance spectroscopy (EIS) is a technique that applies an alternating current (AC) across a system, and measures the output current over a frequency range. Due to the low voltages required, and the AC operation, EIS is compatible with biological systems, providing mid-throughput and label-free biosensing at the electrode/biology/electrolyte interface³⁴⁻³⁶. EIS has been applied for the automatic, sensitive and quantitative monitoring of many cellular processes³⁷⁻⁴¹. Poly(3,4-ethylenedioxythiophene) polystyrene sulfonate (PEDOT:PSS) is a widely used conducting polymer in the bioelectronics field, due to its mixed ionic and electronic conduction properties, stable operation in aqueous electrolytes, and easy processing^{42,43}. Conducting polymer based electrodes have been previously used for monitoring cell attachment and proliferation by EIS, measuring the change in impedance caused by cell adhesion on PEDOT:PSS^{44,45}.

In this Chapter, an electroactive functional copolymer (PEDOT:PSS/pNIPAAm) created by the combination of PEDOT:PSS and pNIPAAm is presented, which combines the conducting properties of the first and the thermo-actuation capabilities of the second. This material enables the non-invasive capture and release of cells with simultaneous EIS monitoring of the process (Figure 7.1). The presence of PEDOT:PSS in the copolymer enables the monitoring of cell loading during the capture and release process. In contrast to the SCADA approach presented in Chapter 6 for monitoring cell adhesion by optical readout, here we introduce an electrical monitoring approach enabled by organic bioelectronics.

To validate the capture and release performance of the system, the well-known SW480 cell line from a primary colon adenocarcinoma was used⁴⁶⁻⁴⁸. SW480s are considered responsible for tumour initiation, development and metastasis, and have been previously used as model samples to evaluate capture and release systems^{49,50}. Our approach relies on the addition of fibronectin (FN) protein to the PEDOT:PSS/pNIPAAm, to induce cell adhesion at room temperature, followed by an increase of the temperature to 37 °C to induce the polymer shrinking and subsequent cell release. FN is an extracellular matrix protein that adheres to the integrins of the cellular membrane, which are crucial in the metastasis led by SW480 cells^{51,52}, since they contribute to chemo-resistance of cells to certain anticancer drugs⁵³ and promote epithelial-to mesenchymal transition^{54,55}.

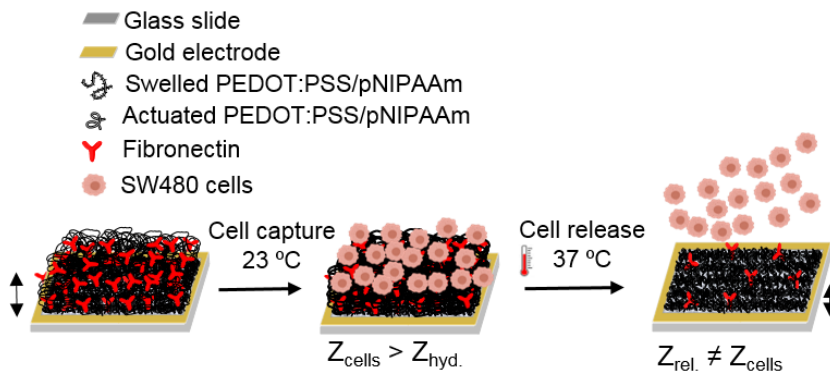


Figure 7.1. Schematics of the mechanism of cell capture and release and electrical monitoring based on the hybrid functional PEDOT:PSS/pNIPAAm copolymer. The arrows at the left and right corners indicate the correspondent height for the swelled PEDOT:PSS/pNIPAAm (left) and actuated PEDOT:PSS/pNIPAAm (right).

7.2 Results and discussion

7.2.1 Characterisation of the electrodes by EIS

PEDOT:PSS/pNIPAAm covered gold-electrodes were fabricated by photolithography as described in experimental section 7.4.2. A copolymer layer was synthesised over the electrodes by blending two polymer precursors (experimental section 7.4.3); one photoactive, consisting of NIPAAm monomer, the cross-linker N,N'-Methylenebisacrylamide (mBAAm) and the photoinitiator 2,2-Dimethoxy-2-phenylacetophenone (DMPA); and a second PEDOT:PSS with the temperature polymerisation initiator 3-glycidyloxypropyltrimethoxysilane (GOPS) (Figure 7.2). After spin-casting on the electrodes, they were soft-baked at 70 °C, to trigger the polymerisation of PEDOT:PSS. The samples were then exposed to UV light to polymerise the pNIPAAm/mBAAm, followed by a hard-bake at 120 °C to fully crosslink the copolymer.

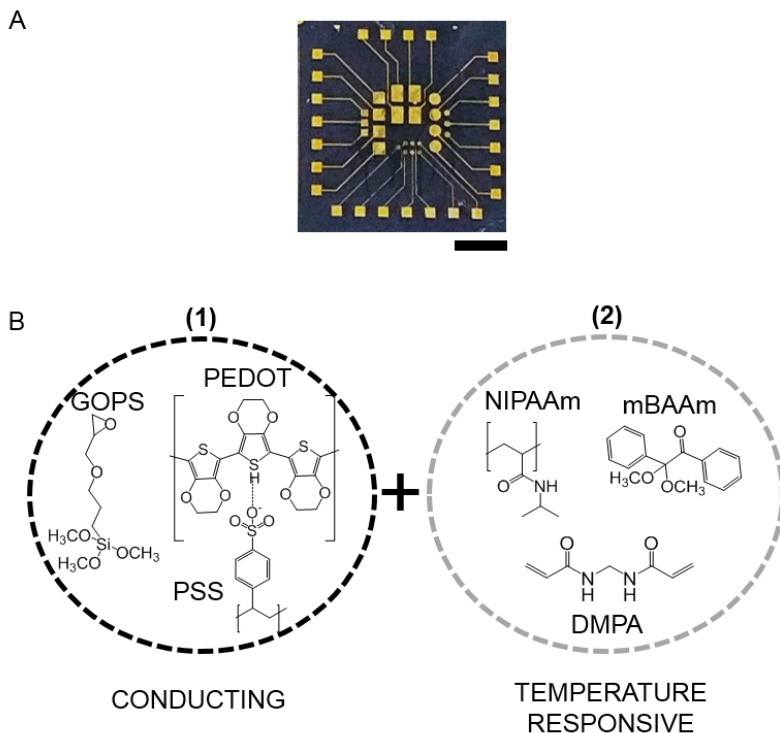


Figure 7.2. A) Photograph showing the photolithographically patterned device consisting of a 24 gold-electrode array on glass. Ruler corresponds to 5 mm. B) Chemical structure of the components of (1) the conducting polymer: PEDOT and PSS with GOPS crosslinker and (2) the thermo-responsive polymer consisting of NIPAAm monomer, mBAAm crosslinker and DMPA photoinitiator.

First, EIS measurements were performed on all the micro-fabricated electrodes covered with PEDOT:PSS/pNIPAAm (Figure 7.3A), as explained in experimental section 7.4.4, and the impedance data showed different impedance profiles for each electrode size (Figure 7.3B). From this impedance data, the electrode resistance (R_{el}) and capacitance (C_{el}) were obtained by fitting a R(RC) Randles circuit, which evidenced a decreasing resistance and increasing capacitance for bigger electrodes (Figure 7.3C). Considering the results obtained during

characterisation, subsequent experiments were carried out with the larger electrodes (rectangular electrodes $L = 1.7 \text{ mm} \times W = 1.2 \text{ mm}$) due to the low R_{el} ($967 \pm 217 \text{ k}\Omega$) and high C_{el} ($5 \pm 2 \mu\text{F}$).

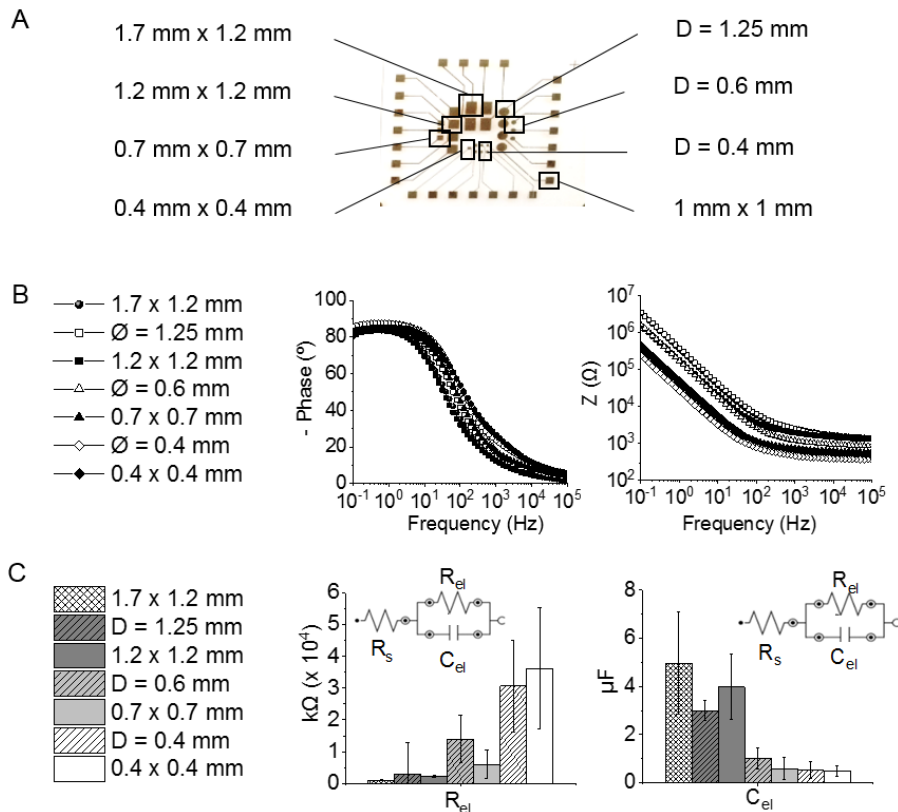


Figure 7.3. A) Picture of the electrode with the 7 designs, circles or squares of different dimensions. B) Impedance *versus* Frequency (middle) and Phase *versus* Frequency (right) plots of the experimental EIS data for PEDOT:PSS/pNIPAAm electrodes of different dimensions. C) R_{el} and C_{el} electric parameters obtained for the experimental data collected from EIS measurements of PEDOT:PSS/pNIPAAm electrodes for all the dimensions and shapes. Error bars correspond to the standard deviation from the mean for $n = 3$. The inset of the plots correspond to a R(RC) circuit, which correlates with the EIS experimental data of PEDOT:PSS/pNIPAAm copolymer.

7.2.2 Characterisation of the thermo-responsiveness and conducting properties of the copolymer

To explore thermo-responsive properties of the copolymer, the thickness of the film, at different temperatures, was measured with a contact profilometer, as explained in experimental section 7.4.5. The thickness-change triggered by temperature was investigated for the copolymer and compared to PEDOT:PSS polymer.

The thickness of the swelled and shrunk PEDOT:PSS/pNIPAAm and PEDOT:PSS films was measured just after polymerisation, after hydration in DI water for 10 min and after heating the material for 20 min at 37 °C. It is well known that PEDOT:PSS can present high swelling ratios in electrolyte solution⁵⁶, but this capacity deeply decreases for higher ratios of GOPS⁵⁷. Likewise, low swelling capacity of PEDOT:PSS has previously been reported⁵⁸. The PEDOT:PSS films here, with GOPS 3 wt %, showed only a 5 % of swelling in cell culture media. The PEDOT:PSS/pNIPAAm copolymer showed a thickness increase of 26 % after hydrating, which decreased back to initial values after the thermal treatment. It showed consistent and repetitive changes, demonstrating their predictable thermo-responsive behaviour (Figure 7.4A). The behaviour of the copolymer films correlated well with the previously described performance of pNIPAAm⁵⁹. Higher errors were found just after polymerisation and washing, due to the differences in hydration of the copolymer after the rinsing of the layers.

PEDOT:PSS/pNIPAAAM was also characterised in terms of its electrochemical properties, measuring EIS as explained in experimental section 7.4.4. The volumetric capacitance of the copolymer was found to be similar to PEDOT:PSS capacitance behaviour described by Proctor *et al.*⁶⁰, showing that the capacitance

of PEDOT:PSS/pNIPAAm scales with the volume of the film as a linear function ($y = 2.4x + 3.6 \cdot 10^{-7}$; $R^2 = 0.90$) (Figure 7.4B). The linearity between capacitance and volume indicates that the ionic charge injected from the electrolyte is uniformly distributed within the dynamic copolymer thus, suggesting that PEDOT:PSS/pNIPAAm films behave as ideal volumetric capacitors.

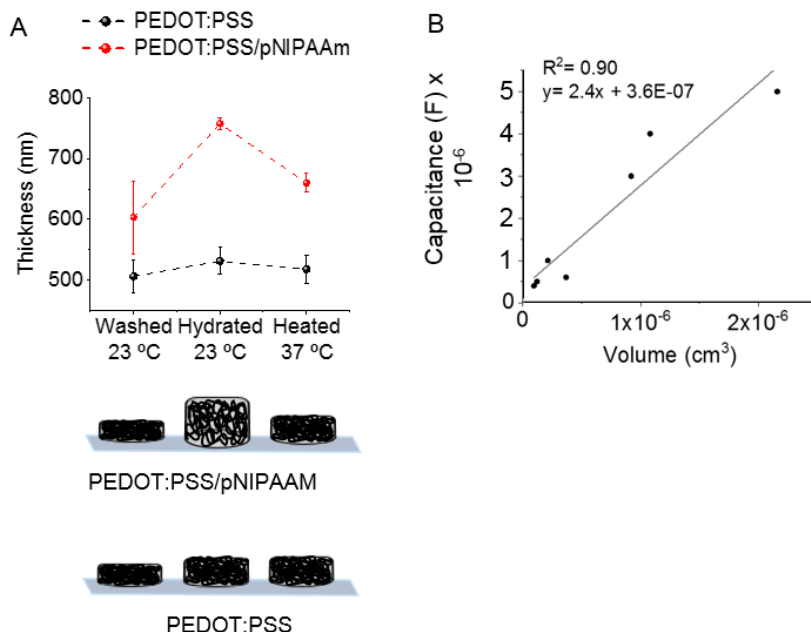


Figure 7.4. A) Thickness change of PEDOT:PSS and PEDOT:PSS/pNIPAAm after polymerisation and during a hydration/heating cycle (top), scheme of the thermo-actuation of PEDOT:PSS/pNIPAAm and PEDOT:PSS (bottom). Error bars correspond to the standard deviation from the mean for $n = 4$. B) Volume (cm^3) *versus* capacitance (F) for the PEDOT:PSS/pNIPAAm copolymer.

Furthermore, EIS measurements were performed on PEDOT:PSS and PEDOT:PSS/pNIPAAm both at 23 °C and 37 °C. PEDOT:PSS showed the same impedance profile for both temperatures, and no statistically different R_{el} values

(Figure 7.5A). In contrast, the impedance profile of PEDOT:PSS/pNIPAAm was different for the swelled state of the copolymer (23 °C) and the shrunk state (37 °C), with a statistically significant value decrease (33 %) of R_{el} for the shrunk state in comparison with the swelled state (Figure 7.5B). This suggests that, although the chemical composition of the copolymer is the same for both states, impedance drops for the shrunk copolymer at the mid-high frequency regime (> 10 Hz). In this frequency regime, the electronic transport dominates the impedance spectra of the system. Upon heating, the water is expelled from the polymer film and thus, the polymer film shrinks and the polymer chains become more packed. This might be the reason for the enhanced electronic transport in this material. Furthermore, the impedance of the shrunk PEDOT:PSS/pNIPAAm copolymer at low frequencies (< 10 Hz) is larger than for PEDOT:PSS, maybe due to the reduced ionic transport properties of the shrunk/contracted polymer film, which hinders ion transport. In addition, the hydrophobic pNIPAAm chains would also hinder the transport of hydrated ions within the polymer film⁶¹. C_{el} did not show any statistical differences for any of the two materials (Figure 7.5C).

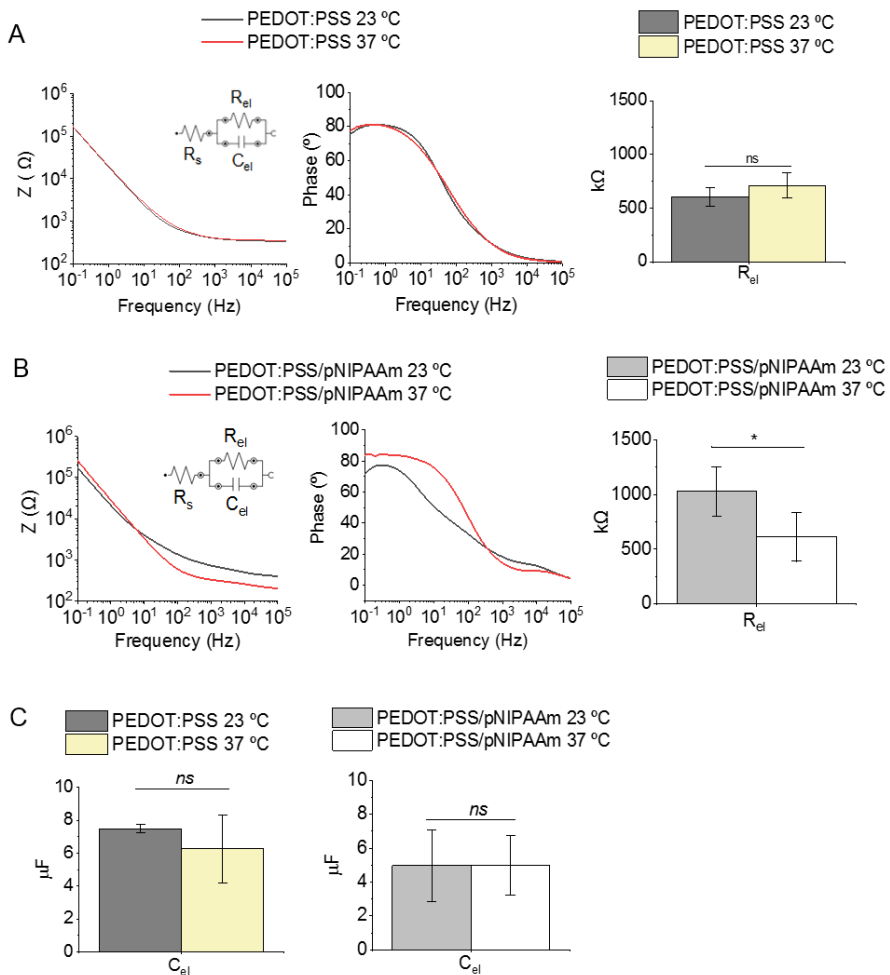


Figure 7.5. A) Impedance *versus* frequency (left), phase angle *versus* frequency (middle) and a plot displaying R_{el} (right) obtained from EIS measurements of the bare PEDOT:PSS at 23 °C and at 37 °C for a R(RC) circuit. No significantly different (ns) at the 0.05 level (one-way ANOVA $p = 0.2$). Error bars correspond to the standard deviation from the mean for $n = 4$. B) Impedance *versus* frequency (left), phase angle *versus* frequency (middle) and a plot displaying R_{el} (right) obtained from EIS measurements of swelled PEDOT:PSS/pNIPAAm at 23 °C and actuated PEDOT:PSS/pNIPAAm at 37 °C. * Significantly different at the 0.05 level

(one-way ANOVA, $p = 0.045$). Error bars correspond to the standard deviation from the mean for $n = 4$. C) C_{el} plotted for PEDOT:PSS at 23 °C and 37 °C; not significantly different (ns) at the 0.05 level (one-way ANOVA $p = 0.28$) (left) and C_{el} plotted for PEDOT:PSS/pNIPAAm at 23 °C and 37 °C; not significantly different (ns) at the 0.05 level (one-way ANOVA $p = 0.99$) (right). Error bars correspond to the standard deviation from the mean for $n = 4$.

PEDOT:PSS, pNIPAAm and PEDOT:PSS/pNIPAAm films were also characterised by Raman spectroscopy (see experimental section 7.4.6). The bands corresponding to PEDOT:PSS showed very high intensities, hindering the bands from the pNIPAAm in the copolymer (Figure 7.6A) as they have been signalled in the plot, in agreement with previous studies⁶²⁻⁶⁶. The Raman spectra for the pNIPAAm hydrogel was also in concordance with previous reports in literature^{67,68} (Figure 7.6B).

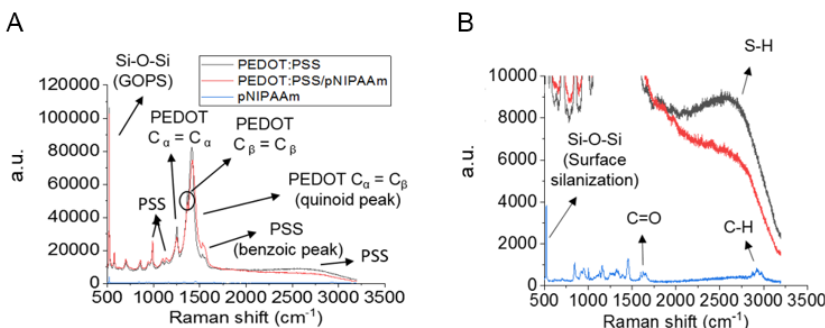


Figure 7.6. Raman spectroscopy PEDOT:PSS and pNIPAAm hydrogels and PEDOT:PSS/pNIPAAm copolymer. A) the whole spectra of peaks from 500 to 3500 nm and B) a zoom of the peaks of the pNIPAAm hydrogel in the range 0-12000 a.u.

7.2.3 Cell capture and release with PEDOT:PSS/pNIPAAm copolymer

In order to study the process of cell capture and release, PEDOT:PSS/pNIPAAm-coated electrodes of different shapes and sizes were first incubated with FN protein to embed the cell adhesion protein inside the polymer. Then, the PEDOT:PSS/pNIPAAm electrodes were incubated with the suspension of cells at 23 °C to allow cell capture, EIS measurements were performed, and optical microscopy images were acquired. Afterwards, the electrodes were heated to 37 °C for 20 min, above the LCST of pNIPAAm, to trigger the shrinking of the copolymer and the release of cells; then EIS measurements were carried out and optical microscopy images of the electrodes were taken (see experimental section 7.4.7).

Optical microscopy images confirmed that the cell capture and release process took place in all the electrode dimensions, however, the EIS measurements for the smaller electrodes showed that they were not sensitive enough to monitor the process (Figure 7.7)

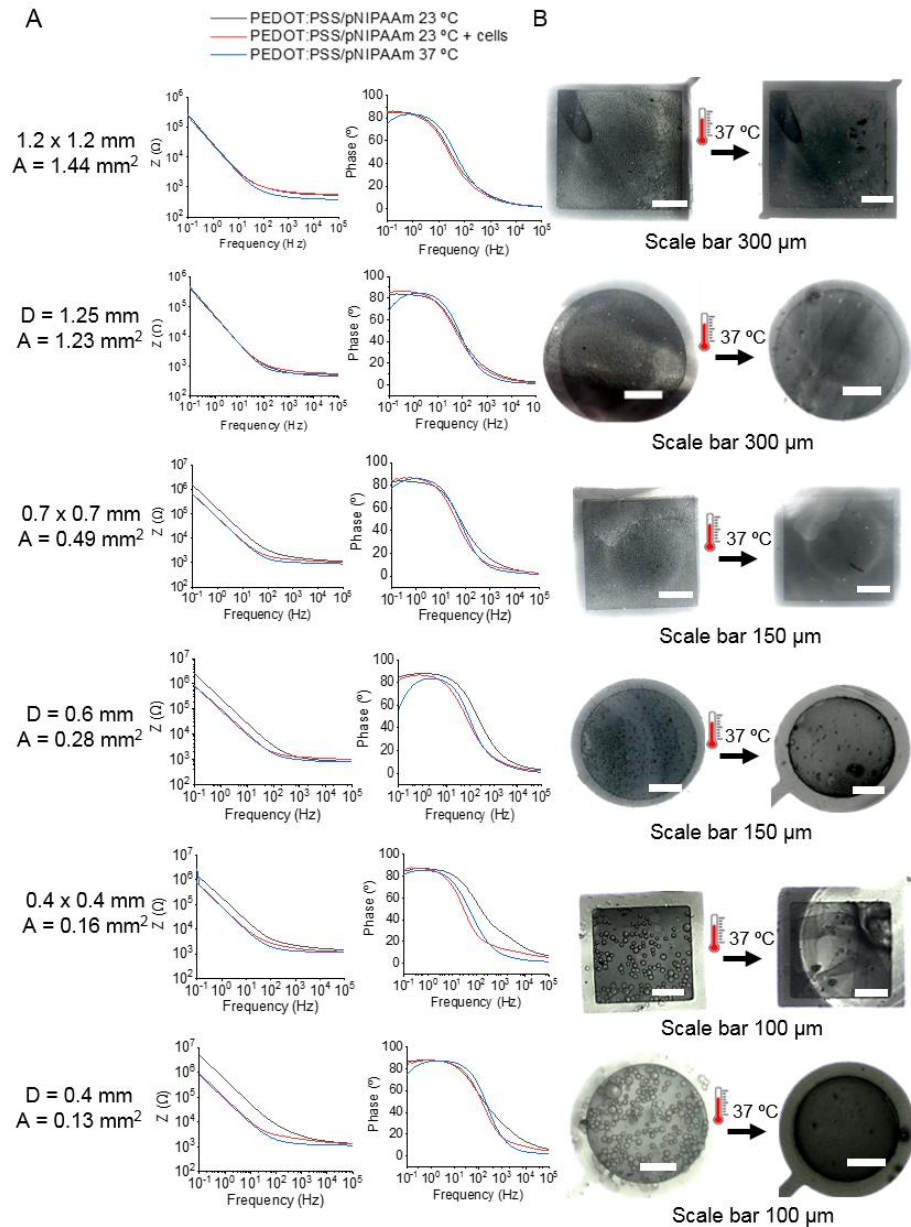


Figure 7.7. A) Impedance *versus* frequency and phase *versus* frequency plots of the cell capture and release with PEDOT:PSS/pNIPAAm on different electrode shape and sizes. B) Optical microscopy images of the captured cells (left) and after thermo-actuation (right) on different electrode shapes and sizes.

As mentioned before, the biggest electrodes (1.7 mm × 1.2 mm rectangles), were used for further experiments. After the incubation with cells, optical microscopy showed cell adhesion on the PEDOT:PSS/pNIPAAm electrodes, which were released after thermo-actuation (Figure 7.8A). The EIS data obtained displayed an increased impedance at the mid-high frequencies (> 10 Hz) for the samples with cells at 23 °C, with a subsequent recovery of these impedance values after the thermo-actuation of the copolymer (Figure 7.8B).

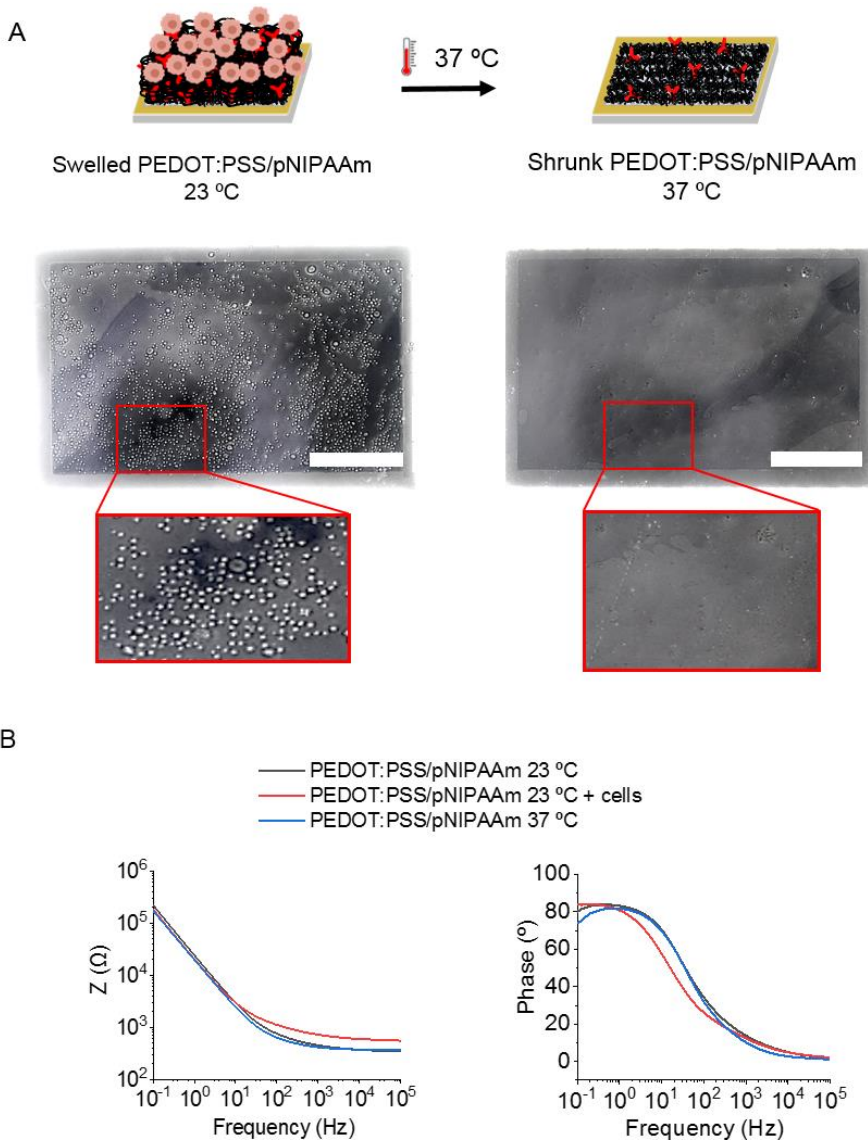


Figure 7.8. Cell capture and release data on PEDOT:PSS/pNIPAAm. A) (Top) Scheme of the actuation process to trigger cell release (top) and optical microscopy images (4x) of polymer coated electrodes before and after (bottom). Scale bars correspond to 400 μm . B) Impedance *versus* frequency and phase *versus* frequency plots of the cell capture and release with PEDOT:PSS/pNIPAAm.

The same experiment was conducted with electrodes coated with bare PEDOT:PSS. In this case, optical microscopy images showed that after incubation with cells, there was cell adhesion on the PEDOT:PSS, and after heating the electrodes at 37 °C, cells remained attached on the PEDOT:PSS (Figure 7.9A). The EIS monitoring of PEDOT:PSS electrodes showed that the impedance values before and after heating the polymer were similar (Figure 7.9B), confirming that cells did not release. These results were expected, since the polymer did not contain pNIPAAm, it could not be thermo-actuated and could not trigger cell release. This demonstrated that the thermo-response of PEDOT:PSS/pNIPAAm is what triggered cell release.

The density of cells captured on square electrodes coated with PEDOT:PSS/pNIPAAm or PEDOT:PSS was calculated from optical microscopy images by counting the number of cells in areas of 500 µm × 500 µm. The density of captured cells on PEDOT:PSS/pNIPAAm was 483 ± 61 (Figure 7.8A) and 175 ± 98 on PEDOT:PSS (Figure 7.9A). Moreover, PEDOT:PSS showed high variability in the density of captured cells for both, within the same electrode and between electrodes, while the cell coverage on PEDOT:PSS/pNIPAAm was more homogeneous for both cases.

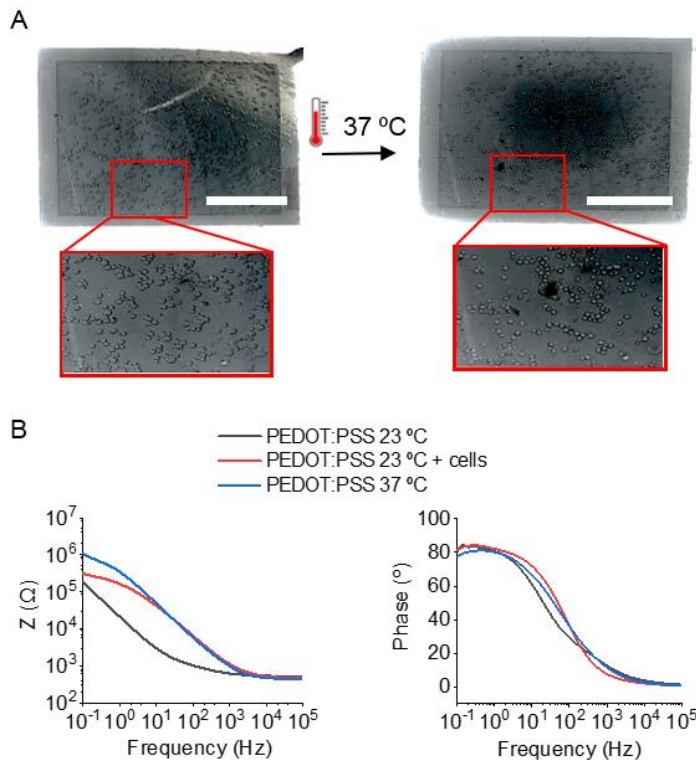


Figure 7.9. A) Optical microscopy images (4x) of PEDOT:PSS coated electrodes loaded with cells, before and after heating. Scale bars correspond to 400 μm . B) Impedance *versus* frequency and phase *versus* frequency plots of PEDOT:PSS at 23 °C, PEDOT:PSS with cells at 23 °C and PEDOT:PSS at 37 °C.

The experimental data of capture and release experiments was fitted to a R(RC)(RC) circuit; a R for the electrolyte and two parallel RC circuits, one for the electrode and another for the cell layer on top of the polymer film (Figure 7.10A). The corresponding R_{cells} values were calculated for the different stages of the process with PEDOT:PSS and PEDOT:PSS/pNIPAAm electrodes (Figure 7.9B). As shown in Figure 7.9B, the R_{cells} value of PEDOT:PSS/pNIPAAm was significantly reduced after heating the electrodes (actuation). This reduction of R_{cells} , corresponds to a 67 % drop value compared to the R_{cells} calculated after cell

capture, suggesting that cells were released from the electrodes. In contrast, the calculated R_{cells} for the PEDOT:PSS with captured cells was not statistically different before and after heating, obtaining values of $687 \pm 91 \text{ k}\Omega$ and $764 \pm 135 \text{ k}\Omega$, respectively (Figure 7.10B), confirming that cells remained on the electrodes after heating. Finally, the viability of the cells released was evaluated. Detached cells were collected in cell culture media and a trypan blue viability assay was performed. Only 6 % of the cells were stained with trypan blue, indicating that cell viability after the capture and release process was 94 % (Figure 7.10C).

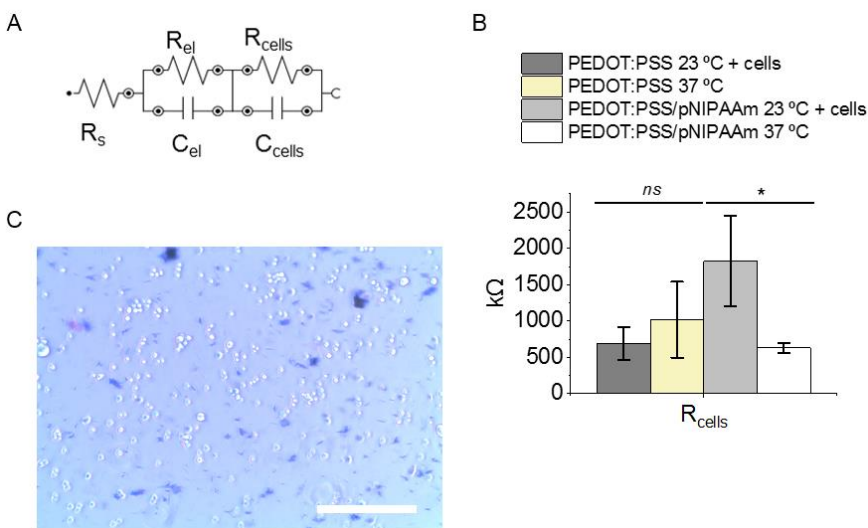


Figure 7.10. A) R(RC)(RC) electric circuit fitting for the cell capture and release system. B) R_{cells} plotted for PEDOT:PSS and PEDOT:PSS/pNIPAAm with cells at 23 °C and at 37 °C after heating. Error bars correspond to the standard deviation from the mean value for $n = 4$. Not significantly different (ns) at the 0.05 level (one-way ANOVA $p = 0.29$) and * significantly different at the 0.05 level (one-way ANOVA, $p = 0.009$). C) Optical microscopy image of the cells released, after adding trypan blue viability indicator (10x). Scale bar corresponds to 100 μm .

7.2.4 Characterisation of protein capture and release by fluorescence microscopy

Albumin from bovine serum (BSA) was used as a model protein^{62,63} to study the loading of the adhesion protein in the copolymer. The PEDOT:PSS, pNIPAAm and PEDOT:PSS/pNIPAAm polymeric layers were fabricated as described in the experimental section 7.4.8, and were then soaked in a 500 nM solution of the fluorescent labelled tetramethylrhodamine conjugated BSA (BSA-TAMRA) for 2 h. The protein uptake by the polymer layers was characterised doing fluorescence microscopy measurements of the polymers at room temperature after rinsing them with DI water, after incubation with the fluorescent protein, and after heating the samples for 20 min at 37 °C. The fluorescence intensity after incubation with the protein was 1000 times higher for PEDOT:PSS/pNIPAAm and 1500 times higher for pNIPAAm in comparison with PEDOT:PSS, indicating their higher protein uptake. After heating the polymer layers, the fluorescence signal did not change for PEDOT:PSS, while for PEDOT:PSS/pNIPAAm and pNIPAAm polymers, it decreased to 51% and 38%, respectively (Figure 7.11). These results indicated that PEDOT:PSS had a low uptake of BSA (and presumably of FN), what explained the lower adhesion of cells on the PEDOT:PSS coated electrodes compared with PEDOT:PSS/pNIPAAm electrodes. Additionally, the protein uptake by the PEDOT:PSS/pNIPAAm and pNIPAAm polymers was higher and after actuation part of the protein was released to the media.

Probably, the higher water uptake of the pNIPAAm copolymer due to the pNIPAAm helped accommodating large amounts of FN solution, increasing the presence of protein within the copolymer (Figure 7.11) and thus, creating more adhesion sites for cells.

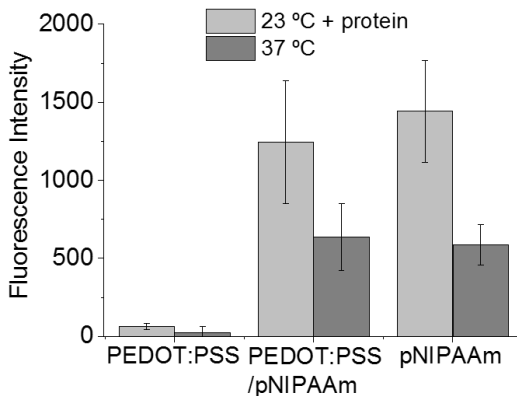


Figure 7.11. Fluorescence microscopy raw data for the capture and release of BSA-TAMRA on PEDOT: PSS, PEDOT:PSS/pNIPAAm and pNIPAAm polymeric layers. Error bars correspond to the standard deviation from the mean for $n = 5$.

7.3 Conclusions

In conclusion, in this chapter, a system for the non-invasive capture and release of cells and simultaneous monitoring has been developed using electrodes with a novel functional material made of PEDOT:PSS/pNIPAAm. The functional copolymer PEDOT:PSS/pNIPAAm was deposited on gold electrodes and functionalised with FN to promote the capture of cells. The novel copolymer maintained similar electrical properties to the ones of PEDOT:PSS, enabling the system to be sensitive enough to detect the target by EIS, while maintaining the thermo-actuation capability of the pNIPAAm. Therefore, PEDOT:PSS/pNIPAAm copolymer is functional for the temperature triggered release of hosting cells, as well as for the simultaneous monitoring of the process by EIS. This opens the possibility of using organic bioelectronics as sensors and actuators, as label-free devices to perform the detection and recovery of target species, leading to an easy monitoring of the process without labels, and with minimum user intervention. These results present the first step on the

development of more complex architectures that can act simultaneously as a sensor and actuator for different targets, while monitoring its performance electrically. Therefore, there is a great potential to adapt this platform, by changing the capturing specific molecule, to be used for the collection of other cells such as blood cells, CTCs, bacteria or even exosomes with relatively high temporal resolution. This type of measurement will open the floodgates to the fast diagnosis of cancer at the point-of-care in a clinic.

7.4 Experimental

7.4.1 Materials

Electrode fabrication: negative photoresist AZ4214E, positive photoresist AZ10XT and MIF726 developer and glass substrates were purchased from Microchemicals, Germany. Acetone, 2-propanol, 3-(trimethoxysilyl)propyl methacrylate, acetic acid and ethanol were obtained from Sigma Aldrich, UK, *p*-xilene from SCS, Kisko, USA and Micro-90 soap from Cole-Palmer, US.

Polymer formation: PDMS Sylgard™ 184 Silicone Elastomer Kit was from Dow, UK and PEDOT:PSS dispersion (1.3 % wt) Clevios™ PH1000, from Heraeus, Ossila, UK. GOPS, NIPAAm, DMPA and mBAAm were all from Merck, UK.

Cell capture and release: Sw480 colon adenocarcinoma cells were from ATCC, UK, and for their maintenance, Fetal Bovine Serum (FBS), glutamax, Penicillin/Streptomycin (PS), PBS and trypsin 2.5 % were obtained from Thermofisher, UK. Trypan blue, fibronectin adhesion protein and Phosphate Buffer Saline (PBS) were purchased from Sigma-Aldrich, UK.

Protein capture: BSA-TAMRA and PBS were purchased from Fisher Scientific,

Spain.

7.4.2 Electrode fabrication

In order to explore the most functional electrode size, 7 electrode designs were fabricated and their performance was studied. Figure 7.12 schematically shows the fabrication of the patterned gold electrodes. Briefly, the glass substrates were cleaned first, by sonicating them in micro-90 soap (3 % v/v) for 20 min and rinsed with DI water. Then, the glass substrates were sonicated in acetone and 2-propanol (50 %, v/v) for 20 min, and they were dehydrated at 220 °C for 10 min. A negative photolithography was carried out, so AZ4214E photoresist was spun at a maximum speed of 3000 rpm s⁻¹, over the glass substrates, followed by a soft bake of 2 min at 110 °C. Then, 6 pulses of 5 s of lightning (365 nm) with resting times of 3 s between cycles were performed with a MA/BA6 mask aligner (Karl Suss MicroTEc, Germany) to photopolymerise the resin through a mask. Afterwards, the patterned glass was introduced into a bath of MIF726 developer for 20 min to remove the non-polymerised resin. Finally, the patterned glass substrates, with the photoresist, were immersed in DI water for 5 min, and dried with compressed air.

Gold deposition followed the first photolithography process. The substrates were oxidised with Zepto one plasma cleaner (Diener electronic, Germany) (100 W, 30 % O₂) for 1 min, and a 10 nm high layer of titanium was deposited on the patterned glass using an E-beam evaporator in order to increase the binding of gold to the substrate. Subsequently, a gold layer with a height of 100 nm was deposited on the top of the titanium layer with the E-beam evaporator (Kurt J. Lesker Company, UK). To pattern the layers of titanium and gold, the metallised samples were introduced in acetone for 1 h in order to lift off the previously

patterned photoresist with the titanium and gold on the areas covered by it.

The fabrication continued with a parylene insulating deposition, comprised of two layers of parylene with soap in between. First, oxygen plasma (100 W, 30 % O₂) was used for 2 min to oxidise the surface patterned with the photoresist. Then, the substrates were immersed in a solution of 3 % of 3-(trimethoxysilyl)propyl methacrylate and 0.1 % of acetic acid in ethanol both from Sigma Aldrich, UK for 30 min. After that, the samples were rinsed with ethanol and baked for 1 h at 70 °C to finalise the functionalisation. To add the first layer of parylene, 1.5 g of *p*-xilene was lyophilised to create a parylene layer of 1.8 µm height. Micro-90 soap (3 % v/v) was spun at 3000 rpm s⁻¹ and, immediately after, a second layer of parylene was deposited on top, following the same protocol used for the first insulating layer.

For the second photolithography, positive photoresist AZ10XT was spun over the substrates at 3000 rpm s⁻¹ and then, soft baked for 2 min at 110 °C. Photopolymerisation was then carried out, applying 5 cycles of 5 soft lightning (365 nm) with resting times of 5 s between cycles, using the mask aligner to photopolymerise the resin through a mask. Afterwards, the patterned substrates were introduced into a bath of MIF726 developer for 5 min to remove the non-polymerised resin. Finally, the patterned glass substrates with the photoresist were immersed in DI water for 5 min, and dried with compressed air. Finally, reactive ion etcher plasma PROF 80 RIE (Oxford Instruments, UK) was used to remove the two layers on the top of the electrodes to bring them to the surface.

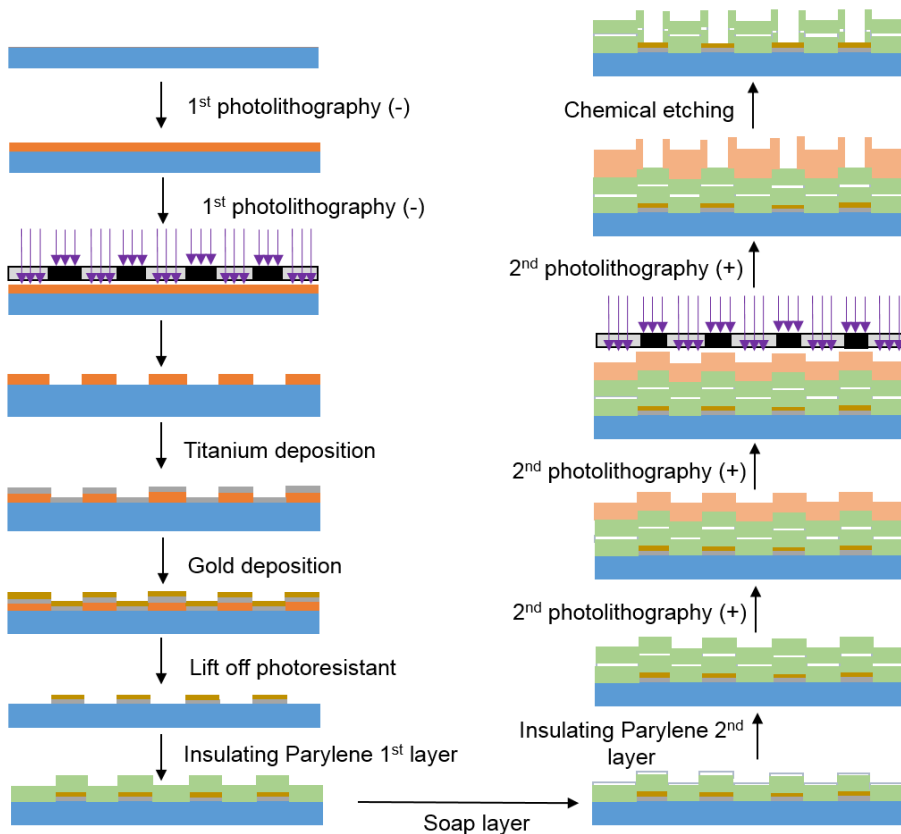


Figure 7.12. Scheme of the fabrication process of the patterned gold electrodes

7.4.3 PEDOT:PSS and PEDOT:PSS/pNIPAAm layer formation

A PDMS gasket was handmade fabricated to confine the liquid solutions on the patterned area, leaving exposed the reference electrodes. For that, PDMS elastomer and curing agent were poured on a glass dish with a 10:1 (v/v) ratio, this was degassed to remove air bubbles and then cured in an oven at 60 °C for 1 h.

PEDOT:PSS: 31 µL of GOPS were pipetted to 1 mL of a dispersion of PEDOT:PSS (1.3 % wt) and then sonicated for 20 min.

PEDOT:PSS/pNIPAAm: 2 mL of a PEDOT:PSS dispersion was mixed with 352 mg pNIPAAm, 30.9 mg DMPA and 30 mg of mBAAm at continuous stirring for 30 min. Then, 62 µL of GOPS were pipetted to the prepolymer mixture. The molar ratio was 1:2:5:80:2:4 for PEDOT:PSS:GOPS:pNIPAAm:DMPA:mBAAm.

To create the layers, the desired prepolymer solution was spun for 30 s at 1500 rpm s⁻¹ followed by 30 s at 3500 rpm s⁻¹ and baked at 70 °C for 2 min over the electrodes. After that, the layers were photopolymerised using the mask aligner MA/BA6, for 1 min at 365 nm, without a photomask. Then, hard bake was applied to the layers for 2 h at 120 °C. Once the polymerisation is complete, the layers were rinsed with ethanol and DI water to eliminate the non-polymerised monomers, resulting on a polymeric layer of 500 nm and 600 nm height for PEDOT:PSS and PEDOT:PSS/pNIPAAm respectively, according to the measurements performed using a DektakXT (Bruker, UK) profilometer.

7.4.4 Electric Impedance Spectroscopy measurements

The baseline for the different experiments was carried out by removing one of the parylene layers using an adhesive sheet to peel off. The electric impedance of four of the samples was measured in cell culturing media as the electrolyte solution, and all measurements were performed using a Pt wire (Warner Instruments) as the gate electrode. Impedance measurements were performed using a Metrohm PGSTAT101 potentiostat with customised NOVA 2.1 software, applying an AC voltage of 0.01 V a DC voltage of 0 mV *versus* open-circuit potential. From the data given by the potentiostat, the electric parameters were determined using NOVA 2.1 software.

7.4.5 Swelling/shrinking capability of PEDOT:PSS and PEDOT:PSS/pNIPAAm

The volume change triggered by the hydration/actuation of the copolymer PEDOT:PSS and PEDOT:PSS/pNIPAAm was measured in terms of thickness-change with a profilometer. The polymeric layers were measured with the profilometer after polymerisation and rinsing. Then, they were soaked with DI water for 10 min and the thickness was measured again. Finally, the samples were heated on a hotplate at 37 °C for 20 min and the thickness was measured again.

7.4.6 Characterisation of the PEDOT:PSS/pNIPAAm copolymer by Raman spectroscopy

In order to characterise the copolymer, Raman spectroscopy was carried out for bare PEDOT:PSS, pNIPAAm hydrogel and PEDOT:PSS/pNIPAAm copolymer.

PEDOT:PSS/pNIPAAm was synthesised as described in section 7.4.3, and PEDOT:PSS and pNIPAAm hydrogels were made as described in follows. To make pNIPAAm hydrogel, 2 mL DI H₂O, 452 mg pNIPAAm, 30.9 mg DMPA and 30 mg of DMPA were mixed in continuous stirring. For PEDOT:PSS hydrogel, 62 µL of GOPS were added to 2 mL of PEDOT:PSS dispersion in continuous stirring, and that was finally sonicated for 20 min. PEDOT:PSS and PEDOT:PSS/pNIPAAm were spun on silicon substrates (Wafer University) to create thin layers. For pNIPAAm hydrogel, a surface functionalisation step was previously required in order to keep the polymer covalently attached to the silicon. For that, the silicon pieces were oxidised with plasma for 10 min (Harrick PDC-32G-2 plasma cleaner) and vapour deposition of 3-(trimethoxysilyl)propyl

methacrylate (Sigma Aldrich, Spain) was carried out for 90 min. After that, 50 μL of pNIPAAm prepolymer were added on the functionalised silicon, and that was photopolymerised for 1 min under 25 mJ s^{-1} of UV light using UV LED masker UV-KUB 2 (Kloé). The samples of PEDOT:PSS, pNIPAAm and PEDOT:PSS/pNIPAAm were analysed after polymerisation, after incubating FN protein for 2 h and after incubation with protein and heating them at 37 $^{\circ}\text{C}$ for 20 min.

The characterisation of the polymers by Raman spectroscopy was done using A Renishaw spectrometer with an InVia confocal microscope.

7.4.7 Cell capture and release mechanisms

To perform cell capture and release experiments, the copolymer layers were first incubated with a solution 500 nM of FN in PBS for 2 h, and the samples were then rinsed with PBS. After incubating the protein, the upper layer of parylene was peeled off using an adhesive sheet, to avoid having FN adsorbed outside the electrode areas, Figure 7.13.

Cell capture:

Sw480 colon adenocarcinoma cells were suspended in cell culture media containing FBS (10 % v/v), glutamax (1 % v/v) and P/S (10 % v/v). Cells were trypsinized (trypsin 2.5 %) and the number of cells was adjusted to 650 000 cells mL^{-1} . The cell suspension was pipetted on the electrodes, which were surrounded by the PDMS gasket, and kept incubating in circular stirring using a microplate shaker (Corning, UK) for 3 h at room temperature. The suspension of cells was then removed, and the samples were washed with PBS 3 times. Fresh cell culturing media at room temperature was added and EIS measurements were

carried out to obtain the impedance data with the cells attached to the sensors as described in section 7.4.4.

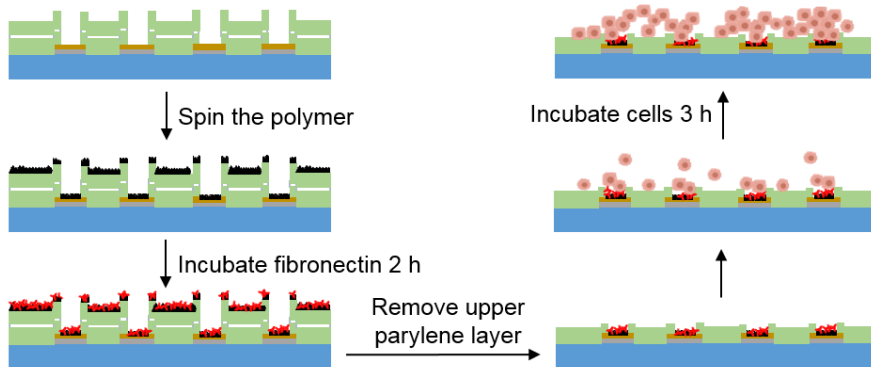


Figure 7.13. Illustration of the steps carried out for cell capture.

Cell release:

The substrates, containing the adhered cells, were heated on a hotplate controlling the temperature in media to 37 °C for 20 min. Then, the suspension with the detached cells was removed with a micropipette and replaced by fresh culture media. EIS measurements were performed.

In order to check the viability of the cells released from the functionalised electrodes, cells were recovered in 200 µL of cell culture media, and 200 µL of trypan blue were added to the released cell sample, containing the detached cells from the electrodes, and analysed by optical microscopy to assess viability.

7.4.8 Protein capture and release by fluorescence microscopy

To identify the presence of the protein in the copolymer during the cell capture and release, fluorescent BSA-TAMRA protein was used as a model molecule to

mimic FN behaviour. PEDOT:PSS and PEDOT:PSS/pNIPAAm layers were fabricated as described before, and for pNIPAAm layer, 452 mg of pNIPAAm, 30.9 mg DMPA and 30 mg mBAAm were dissolved in 2 mL DI H₂O. Once the polymers layers were done, they were incubated with a PBS solution 500 nM of BSA-TAMRA for 2 h at room temperature. After incubation with the protein the samples were washed 3 times with PBS and fluorescence microscopy was used to image the polymer substrate, specifically a Nikon Eclipse TE-2000-S inverted microscope coupled to an ANDOR Zyla sCMOS and a C-LHG1 100 W mercury lamp (570 nm filter). Then, the samples were actuated for 20 min at 37 °C and fluorescence was measured, keeping them protected from light to avoid fluorescent quenching.

In order to estimate the percentage of retained protein after actuation, the fluorescence intensity values were first normalised with respect to the corresponding blanks for each polymer (PEDOT:PSS, PEDOT:PSS/pNIPAAm or pNIPAAm). Then, the intensity obtained after heating the copolymer layers was compared to the intensity of the samples with 2 h of incubation with the fluorescent protein, and the percentage of the remaining protein after the actuation was calculated.

7.5 References

1. Ruan, H.; Wu, X.; Yang, C.; Li, Z.; Xia, Y.; Xue, T.; Shen, Z.; Wu, A. A supersensitive CTC analysis system based on triangular silver nanoprisms and SPION with function of capture, enrichment, detection, and release. *ACS Biomater. Sci. Eng.* 2018, **4**, 1073-1082.
2. Qian, W.; Zhang, Y.; Chen, W. Capturing cancer: emerging microfluidic technologies for the capture and characterization of circulating tumor cells. *Small* 2015, **11**, 3850-3872.
3. Gurkan, U. A.; Anand, T.; Tas, H.; Elkan, D.; Akay, A.; Keles, H. O.; Demirci, U. Controlled viable release of selectively captured label-free cells in microchannels. *Lab Chip* 2011, **11**, 3979-3989.
4. Hao, Y.; Liu, H.; Li, G.; Cui, H.; Jiang, L.; Wang, S. Photo and thermo dual-responsive copolymer surfaces for efficient cell capture and release. *ChemPhysChem* 2018, **19**, 2107-2112.
5. Zhan, W.; Wei, T.; Cao, L.; Hu, C.; Qu, Y.; Yu, Q.; Chen, H. Supramolecular platform with switchable multivalent affinity: photo-reversible capture and release of bacteria. *ACS Appl. Mater. Interfaces* 2017, **9**, 3505-3513.
6. Malic, L.; Zhang, X.; Brassard, D.; Clime, L.; Daoud, J.; Luebbert, C.; Barrere, V.; Boutin, A.; Bidawid, S.; Farber, J. Polymer-based microfluidic chip for rapid and efficient immunomagnetic capture and release of *Listeria monocytogenes*. *Lab Chip* 2015, **15**, 3994-4007.
7. Xia, Y.; Tang, Y.; Yu, X.; Wan, Y.; Chen, Y.; Lu, H.; Zheng, S. Label-Free Virus Capture and Release by a Microfluidic Device Integrated with Porous Silicon Nanowire Forest. *Small* 2017, **13**, 1603135.
8. Kang, Y.; Kim, Y. J.; Bu, J.; Cho, Y.; Han, S.; Moon, B. High-purity capture and release of circulating exosomes using an exosome-specific dual-patterned immunofiltration (ExoDIF) device. *Nanoscale* 2017, **9**, 13495-13505.
9. Hisey, C. L.; Dorayappan, K. D. P.; Cohn, D. E.; Selvendiran, K.; Hansford, D. J. Microfluidic affinity separation chip for selective capture and release of label-free ovarian cancer exosomes. *Lab Chip* 2018, **18**, 3144-3153.
10. Liu, S.; Chen, X.; Bao, L.; Liu, T.; Yuan, P.; Yang, X.; Qiu, X.; Gooding, J. J.; Bai, Y.; Xiao, J. Treatment of infarcted heart tissue via the capture and local delivery of circulating exosomes through antibody-conjugated magnetic nanoparticles. *Nat. Biomed. Eng.* 2020, **4**, 1063-1075.
11. Johnson, S. P.; Catania, J. M.; Harman, R. J.; Jensen, E. D. Adipose-derived stem cell collection and characterization in bottlenose dolphins (*Tursiops truncatus*). *Stem Cells Dev.* 2012, **21**, 2949-2957.

12. Lu, Y.; Ahmed, S.; Harari, F.; Vahter, M. Impact of Ficoll density gradient centrifugation on major and trace element concentrations in erythrocytes and blood plasma. *J. Trace Elem. Med. Biol.* 2015, 29, 249-254.
13. Gaysinskaya, V.; Soh, I. Y.; van der Heijden, Godfried W; Bortvin, A. Optimized flow cytometry isolation of murine spermatocytes. *Cytom. Part A* 2014, 85, 556-565.
14. Bhagwat, N.; Dulmage, K.; Pletcher, C. H.; Wang, L.; DeMuth, W.; Sen, M.; Balli, D.; Yee, S. S.; Sa, S.; Tong, F. An integrated flow cytometry-based platform for isolation and molecular characterization of circulating tumor single cells and clusters. *Sci. Rep.* 2018, 8, 1-14.
15. Legut, M.; Sanjana, N. E. Immunomagnetic cell sorting. *Nat. Biomed. Eng.* 2019, 3, 759-760.
16. Henry, E.; Holm, S. H.; Zhang, Z.; Beech, J. P.; Tegenfeldt, J. O.; Fedosov, D. A.; Gompper, G. Sorting cells by their dynamical properties. *Sci. Rep.* 2016, 6, 34375.
17. Yamada, M.; Seko, W.; Yanai, T.; Ninomiya, K.; Seki, M. Slanted, asymmetric microfluidic lattices as size-selective sieves for continuous particle/cell sorting. *Lab Chip* 2017, 17, 304-314.
18. Rabie, H.; Zhang, Y.; Pasquale, N.; Lagos, M. J.; Batson, P. E.; Lee, K. NIR Biosensing of Neurotransmitters in Stem Cell-Derived Neural Interface Using Advanced Core-Shell Upconversion Nanoparticles. *Adv Mater* 2019, 31, 1806991.
19. Fathi, F.; Rahbarghazi, R.; Rashidi, M. Label-free biosensors in the field of stem cell biology. *Biosens. Bioelectron.* 2018, 101, 188-198.
20. Shen, Q.; Xu, L.; Zhao, L.; Wu, D.; Fan, Y.; Zhou, Y.; OuYang, W.; Xu, X.; Zhang, Z.; Song, M. Specific capture and release of circulating tumor cells using aptamer-modified nanosubstrates. *Adv Mater* 2013, 25, 2368-2373.
21. Li, J.; Qi, C.; Lian, Z.; Han, Q.; Wang, X.; Cai, S.; Yang, R.; Wang, C. Cell-capture and release platform based on peptide-aptamer-modified nanowires. *ACS Appl. Mater. Interfaces* 2016, 8, 2511-2516.
22. Cao, J.; Zhao, X.; Younis, M. R.; Li, Z.; Xia, X.; Wang, C. Ultrasensitive capture, detection, and release of circulating tumor cells using a nanochannel-ion channel hybrid coupled with electrochemical detection technique. *Anal. Chem.* 2017, 89, 10957-10964.
23. Bombera, R.; Leroy, L.; Livache, T.; Roupioz, Y. DNA-directed capture of primary cells from a complex mixture and controlled orthogonal release monitored by SPR imaging. *Biosens. Bioelectron.* 2012, 33, 10-16.
24. Zhao, W.; Cui, C. H.; Bose, S.; Guo, D.; Shen, C.; Wong, W. P.; Halvorsen, K.; Farokhzad, O. C.; Teo, G. S.; Phillips, J. A.; Dorfman, D. M.; Karnik, R.; Karp, J. M. Bioinspired multivalent DNA network for capture and release of cells. *Proc. Natl. Acad. Sci. U. S. A.* 2012, 109, 19626-19631.

25. Umapathi, R.; Reddy, P. M.; Kumar, A.; Venkatesu, P.; Chang, C. The biological stimuli for governing the phase transition temperature of the “smart” polymer PNIPAM in water. *Colloid Surface B*. 2015, *135*, 588-595.
26. Gallagher, S.; Kavanagh, A.; Ziołkowski, B.; Florea, L.; MacFarlane, D. R.; Fraser, K.; Diamond, D. Ionic liquid modulation of swelling and LCST behavior of N-isopropylacrylamide polymer gels. *Phys. Chem. Chem. Phys.* 2014, *16*, 3610-3616.
27. Choi, A.; Seo, K. D.; Yoon, H.; Han, S. J.; Kim, D. S. Bulk poly (N-isopropylacrylamide)(PNIPAAm) thermoresponsive cell culture platform: toward a new horizon in cell sheet engineering. *Biomater. Sci.* 2019, *7*, 2277-2287.
28. Wang, L.; Liu, H.; Zhang, F.; Li, G.; Wang, S. Smart thin hydrogel coatings harnessing hydrophobicity and topography to capture and release cancer cells. *Small* 2016, *12*, 4697-4701.
29. Liu, H.; Liu, X.; Meng, J.; Zhang, P.; Yang, G.; Su, B.; Sun, K.; Chen, L.; Han, D.; Wang, S. Hydrophobic interaction-mediated capture and release of cancer cells on thermoresponsive nanostructured surfaces. *Adv Mater* 2013, *25*, 922-927.
30. Hou, S.; Zhao, H.; Zhao, L.; Shen, Q.; Wei, K. S.; Suh, D. Y.; Nakao, A.; Garcia, M. A.; Song, M.; Lee, T. Capture and stimulated release of circulating tumor cells on polymer-grafted silicon nanostructures. *Adv Mater* 2013, *25*, 1547-1551.
31. Reitinger, S.; Wissenwasser, J.; Kapferer, W.; Heer, R.; Lepperdinger, G. Electric impedance sensing in cell-substrates for rapid and selective multipotential differentiation capacity monitoring of human mesenchymal stem cells. *Biosens. Bioelectron.* 2012, *34*, 63-69.
32. Chawla, K.; Bürgel, S. C.; Schmidt, G. W.; Kaltenbach, H.; Rudolf, F.; Frey, O.; Hierlemann, A. Integrating impedance-based growth-rate monitoring into a microfluidic cell culture platform for live-cell microscopy. *Microsyst. Nanoeng.* 2018, *4*, 1-12.
33. Gao, T.; Li, L.; Wang, B.; Zhi, J.; Xiang, Y.; Li, G. Dynamic Electrochemical Control of Cell Capture-and-Release Based on Redox-Controlled Host–Guest Interactions. *Anal. Chem.* 2016, *88*, 9996-10001.
34. Rivnay, J.; Ramuz, M.; Leleux, P.; Hama, A.; Huerta, M.; Owens, R. M. Organic electrochemical transistors for cell-based impedance sensing. *Appl. Phys. Lett.* 2015, *106*, 043301.
35. Steinem, C.; Janshoff, A.; Galla, H.; Sieber, M. Impedance analysis of ion transport through gramicidin channels incorporated in solid supported lipid bilayers. *Bioelectrochem. Bioenerget.* 1997, *42*, 213-220.
36. Jimison, L. H.; Tria, S. A.; Khodagholy, D.; Gurfinkel, M.; Lanzarini, E.; Hama, A.; Malliaras, G. G.; Owens, R. M. Measurement of barrier tissue integrity with an organic electrochemical transistor. *Adv Mater* 2012, *24*, 5919-5923.
37. Ke, N.; Wang, X.; Xu, X.; Abassi, Y. A. The xCELLigence system for real-time and label-free monitoring of cell viability. In *Mammalian Cell Viability*. Springer: 2011; pp 33-43.

38. Bird, C.; Kirstein, S. Real-time, label-free monitoring of cellular invasion and migration with the xCELLigence system. *Nat. Methods* 2009, 6, v-vi.
39. Kumar, P.; Vriens, K.; Cornaglia, M.; Gijs, M.; Kokalj, T.; Thevissen, K.; Geeraerd, A.; Cammue, B.; Puers, R.; Lammertyn, J. Digital microfluidics for time-resolved cytotoxicity studies on single non-adherent yeast cells. *Lab Chip* 2015, 15, 1852-1860.
40. Stolwijk, J. A.; Wegener, J. Impedance-Based Assays Along the Life Span of Adherent Mammalian Cells In Vitro: From Initial Adhesion to Cell Death. 2019.
41. Curto, V.; Ferro, M.; Mariani, F.; Scavetta, E.; Owens, R. A planar impedance sensor for 3D spheroids. *Lab Chip* 2018, 18, 933-943.
42. Fan, Z.; Ouyang, J. Thermoelectric properties of PEDOT: PSS. *Adv. Electron. Mater.* 2019, 5, 1800769.
43. Xia, Y.; Ouyang, J. Significant different conductivities of the two grades of poly (3, 4-ethylenedioxythiophene): poly (styrenesulfonate), Clevios P and Clevios PH1000, arising from different molecular weights. *ACS Appl. Mater. Interfaces* 2012, 4, 4131-4140.
44. Del Agua, I.; Marina, S.; Pitsalidis, C.; Mantione, D.; Ferro, M.; Iandolo, D.; Sanchez-Sanchez, A.; Malliaras, G. G.; Owens, R. M.; Mecerreyes, D. Conducting polymer scaffolds based on poly (3, 4-ethylenedioxythiophene) and Xanthan gum for live-cell monitoring. *ACS omega* 2018, 3, 7424-7431.
45. Iandolo, D.; Sheard, J.; Levy, G. K.; Pitsalidis, C.; Tan, E.; Dennis, A.; Kim, J.; Markaki, A. E.; Widera, D.; Owens, R. M. Biomimetic and electroactive 3D scaffolds for human neural crest-derived stem cell expansion and osteogenic differentiation. *MRS Commun.* 2020, 10, 179-187.
46. Leibovitz, A.; Stinson, J. C.; McCombs, W. B.; McCoy, C. E.; Mazur, K. C.; Mabry, N. D. Classification of human colorectal adenocarcinoma cell lines. *Cancer Res.* 1976, 36, 4562-4569.
47. Hartman, J.; Edvardsson, K.; Lindberg, K.; Zhao, C.; Williams, C.; Strom, A.; Gustafsson, J. A. Tumor repressive functions of estrogen receptor beta in SW480 colon cancer cells. *Cancer Res.* 2009, 69, 6100-6106.
48. Wang, W.; Chen, P.; Hsiao, H.; Wang, H.; Liang, W.; Su, Y. Overexpression of the thymosin β -4 gene is associated with increased invasion of SW480 colon carcinoma cells and the distant metastasis of human colorectal carcinoma. *Oncogene* 2004, 23, 6666-6671.
49. Song, Y.; Shi, Y.; Huang, M.; Wang, W.; Wang, Y.; Cheng, J.; Lei, Z.; Zhu, Z.; Yang, C. Bioinspired Engineering of a Multivalent Aptamer-Functionalized Nanointerface to Enhance the Capture and Release of Circulating Tumor Cells. *Angew. Chem. Int.* 2019, 58, 2236-2240.
50. Cui, H.; Liu, Q.; Li, R.; Wei, X.; Sun, Y.; Wang, Z.; Zhang, L.; Zhao, X.; Hua, B.; Guo, S. ZnO nanowire-integrated bio-microchips for specific capture and non-destructive release of circulating tumor cells. *Nanoscale* 2020, 12, 1455-1463.

51. Bartolome, R.; Baderas, R.; Torres, S.; Fernandez-Aceñero, M. J.; Mendes, M.; García-Foncillas, J.; Lopez-Lucendo, M.; Casal, J. I. Cadherin-17 interacts with $\alpha 2\beta 1$ integrin to regulate cell proliferation and adhesion in colorectal cancer cells causing liver metastasis. *Oncogene* 2014, 33, 1658-1669.
52. Cantor, D. I.; Cheruku, H. R.; Nice, E. C.; Baker, M. S. Integrin $\alpha v\beta 6$ sets the stage for colorectal cancer metastasis. *Cancer Metastasis Rev.* 2015, 34, 715-734.
53. Liu, S.; Wang, J.; Niu, W.; Liu, E.; Wang, J.; Peng, C.; Lin, P.; Wang, B.; Khan, A. Q.; Gao, H. The $\beta 6$ -integrin-ERK/MAP kinase pathway contributes to chemo resistance in colon cancer. *Cancer Lett.* 2013, 328, 325-334.
54. Shen, H.; Ma, J. L.; Zhang, Y.; Deng, G. L.; Qu, Y. L.; Wu, X. L.; He, J. X.; Zhang, S.; Zeng, S. Integrin-linked kinase overexpression promotes epithelial-mesenchymal transition via nuclear factor-kappaB signaling in colorectal cancer cells. *World J. Gastroenterol.* 2016, 22, 3969-3977.
55. Gupta, S. K.; Oommen, S.; Aubry, M.; Williams, B. P.; Vlahakis, N. E. Integrin $\hat{I}\pm 9\hat{I}^2\hat{I}$ promotes malignant tumor growth and metastasis by potentiating epithelial-mesenchymal transition. *Oncogene* 2013, 32, 141-150.
56. Savva, A.; Wustoni, S.; Inal, S. Ionic-to-electronic coupling efficiency in PEDOT: PSS films operated in aqueous electrolytes. *J. Mater. Chem. C* 2018, 6, 12023-12030.
57. ElMahmoudy, M.; Inal, S.; Charrier, A.; Uguz, I.; Malliaras, G. G.; Sanaur, S. Tailoring the electrochemical and mechanical properties of PEDOT: PSS films for bioelectronics. *Macromol. Mater. Eng.* 2017, 302, 1600497.
58. Stavrinidou, E.; Leleux, P.; Rajaona, H.; Khodagholy, D.; Rivnay, J.; Lindau, M.; Sanaur, S.; Malliaras, G. G. Direct measurement of ion mobility in a conducting polymer. *Adv Mater* 2013, 25, 4488-4493.
59. Tudor, A.; Saez, J.; Florea, L.; Benito-Lopez, F.; Diamond, D. Poly (ionic liquid) thermo-responsive hydrogel microfluidic actuators. *Sens. Actuator B Chem.* 2017, 247, 749-755.
60. Proctor, C. M.; Rivnay, J.; Malliaras, G. G. Understanding volumetric capacitance in conducting polymers. *J. Polym. Sci. B: Polym. Phys.* 2016, 54, 1433-1436.
61. Zhou, Q.; Teng, W.; Jin, Y.; Sun, L.; Hu, P.; Li, H.; Wang, L.; Wang, J. Highly-conductive PEDOT: PSS hydrogel framework based hybrid fiber with high volumetric capacitance and excellent rate capability. *Electrochim. Acta* 2020, 334, 135530.
62. Chang, S. H.; Chiang, C.; Kao, F.; Tien, C.; Wu, C. Unraveling the enhanced electrical conductivity of PEDOT: PSS thin films for ITO-free organic photovoltaics. *IEEE Photonics J.* 2014, 6, 1-7.
63. Almeida, P. V.; Izumi, C.; Santos, H. F. D.; Sant'Ana, A. C. Spectroscopic characterization of pedot: pss conducting polymer by resonance raman and serrs spectroscopies. *Quím. Nova* 2019, 42, 1073-1080.
64. Garreau, S.; Duvail, J.; Louarn, G. Spectroelectrochemical studies of poly (3, 4-ethylenedioxythiophene) in aqueous medium. *Synth. Met.* 2001, 125, 325-329.

65. Hsieh, T.; Pan, S.; Huang, W.; Pan, H.; Ho, K.; Han, Y.; Chang, M. Improved performance of polymer solar cells featuring one-dimensional PEDOT nanocomposites in a modified buffer layer. *J. Electrochem. Soc.* 2011.
66. Farah, A. A.; Rutledge, S. A.; Schaarschmidt, A.; Lai, R.; Freedman, J. P.; Helmy, A. S. Conductivity enhancement of poly (3, 4-ethylenedioxythiophene)-poly (styrenesulfonate) films post-spincasting. *J. Appl. Phys.* 2012, 112, 113709.
67. Sanz, B.; Von Bilderling, C.; Tuninetti, J. S.; Pietrasanta, L.; Mijangos, C.; Longo, G. S.; Azzaroni, O.; Giussi, J. M. Thermally-induced softening of PNIPAm-based nanopillar arrays. *Soft Matter* 2017, 13, 2453-2464.
68. Wang, L.; Zhao, X.; Zhang, Y.; Zhang, W.; Ren, T.; Chen, Z.; Wang, F.; Yang, H. Fabrication of intelligent poly (N-isopropylacrylamide)/silver nanoparticle composite films with dynamic surface-enhanced Raman scattering effect. *RSC Adv.* 2015, 5, 40437-40443.
69. Swain, S. K.; Sarkar, D. Study of BSA protein adsorption/release on hydroxyapatite nanoparticles. *Appl. Surf. Sci.* 2013, 286, 99-103.
70. Naddaf, A.; Tsibranska, I.; Bart, H. Kinetics of BSA release from poly (N-isopropylacrylamide) hydrogels. *Chem. Eng. Process.* 2010, 49, 581-588.

8

Final Remarks and Future Work

8.1 Final Remarks and Future Work

As it was introduced in the first chapter, considerable advances have been made in the last decades towards the generation of integrated LOC for monitoring. Despite the advantages provided by the miniaturised microsystems, their use is still far from being extended to general consumers. Advances in the integration of components in LOC devices would boost the development of new microsystems as novel strategies for monitoring. This thesis demonstrates that the combination of materials science and microfabrication permits the development of novel integrated microsystems and provides new strategies for cellular and chemical monitoring to the research community.

For instance, the combination of a 3D printed smart architecture and UV curable ionogels enabled the precise integration of polymeric functional materials *in situ* within microfluidic devices, using UV light. The strategy developed in Chapter 3, stood out for its simplicity, providing a user-friendly and cost-effective approach for the integration of functional materials in 3D printed microfluidic devices. The anchoring capability of the used architecture eliminated the need of any surface functionalisation for the stable integration of sensing zones of reproducible dimensions. In that chapter, four sensors made of poly(*N*-isopropylacrylamide) (pNIPAAm) ionogels were integrated in a microfluidic device, comprising a colorimetric barcode readout for pH sensing, but this multiple-sensor design could be potentially used as well for multiplexing. Moreover, far from complex equipment, this microsystem required a simple camera for the interpretation of the colorimetric signal.

The design and integration of photopolymerisable sensors for the detection of other target analytes, such as lactate ¹, nitrate ² or even hazard chemical

compounds such as benzene and formaldehyde², within the microfluidic device presented in this chapter, will be the next step towards an easy to use multiplex LOC. The implementation of this smart microfluidic design for the integration of multiplex sensors, together with the easy colorimetric detection, will enable the development of portable and user-friendly integrated hybrid microfluidic devices for multiple and even, simultaneous analysis.

Moving deeper into the miniaturisation of sensors for integrated microsystems, Chapter 4 described a μ AA substrate, a strategy for the *in situ* and easy fabrication of high-density microsensor arrays, combining a Mylar® photomask as a versatile substrate with UV polymerisable sensors. This enabled the fabrication of high-density and well-positioned microsensor arrays in a single step, using just UV light. Within the materials used as functional materials to create the micropillar shaped microsensors, pNIPAAm ionogels showed higher reproducibility than hydrogels regarding micropillar density, shape and size. Besides, using a photomask as substrate for the fabrication of the ionogel microsensor array permitted the strong attachment of the structures to the substrate by UV grafting, with no need of surface functionalisation. Finally, the design of the μ AA facilitated the identification of the ROIs for imaging and thus, the automation of the optical readout. Further improvements of this system will focus on the sensitivity of the sensing element. For that, one of the future approaches relies on replacing the pH indicators by enzymes to create high density ionogel micropillars for the detection of bioprocesses. It is expected that, due to the bigger size of enzymes, leaching from the ionogel will be minimised in contrast to what it was documented in Chapter 4 for the pH indicators. Moreover, chemiluminescence, as presented in Chapter 2, is known to be more sensitive than colorimetry. Therefore, preliminary experiments have been carried out in this direction, to obtain chemiluminescent ionogels. The optimisation of

ionogel micropillars on μ AA substrates, will ensure a breakthrough in the fabrication of flexible sensing components with easy readout to be integrated in LOC devices.

The use of microstructured polymers can be extended to challenging application areas such as cell membrane related *in vitro* assays. As described in Chapter 5, the combination of materials science, microfabrication and microfluidics led to a hybrid microdevice for the high throughput formation and monitoring of lipid membrane NTs with controlled geometry. This device guaranteed a well-controlled flow for the formation of parallel, free-standing lipid NTs positioned on micropillars, avoiding the common micromanipulation procedures used for their production. Moreover, the micropillar configuration was reproduced with SU-8 photoresist and three different pNIPAAm ionogels with a resolution of 10 μ m, using a polymeric photomask. The microsystems enabled the controlled formation of lipid NTs, being the length of the NTs set by the interpillar distance, and the modulation of the NT radii by changing the material of the micropillar. Due to the functionality, easy to use and versatility of this microsystem, it is a promising tool for *in vitro* reconstitution assays. It was designed to provide to the research scientists with a flexible tool to work with membrane NTs, overcoming the main challenges of current technology during the generation and monitoring of membrane NTs. After demonstrating the performance of this platform, this device is ambitioned to be used by research groups for investigations on membrane NT *in vitro* assays, like in the work recently published in reference ³.

Cellular monitoring is essential to guarantee cell viability and obtain information of cellular behaviour. Miniaturised cellular monitoring systems provide new insights and strategies in this field, as demonstrated in Chapter 6, where the SCADA platform monitored cytotoxicity with single cell resolution. Due to the

single-cell arrays obtained by microcontact printing, the dot array occupancy or cell adhesion was quantified, which enabled the digitalisation of cellular death in presence of a toxic compound. This was performed by dynamically measuring cell adhesion over time in the presence of a toxic. Cell adhesion was correlated with cellular death or by using trypan blue to identify viability of adhered cells when the toxic compound killed cells, but inhibited their detachment. SCADA cytotoxicity assay provided information on death kinetics with single cell resolution, using SCADA alone or combined with conventional assays like trypan blue. Moreover, SCADA is a versatile platform that can be modified, by changing the composition, size and shape of the adhesion dots to adapt them to other cell types. The next challenge would be the complete implementation of this system within microfluidics and miniaturised optics and signal processing equipment (*e.g.* Raspberry Pi and its camera). This will make SCADA system a good candidate for commercialisation, following the steps of other commercialised platforms for cytotoxicity assessments, with digital measurements, single cell resolution and lower costs ^{4,5}, making quantitative cytotoxicity testing accessible and easy to do for any user in research and for any diagnostic applications.

The combination of more than one polymer, with different functionalities, supposes a step towards innovative enabling technologies. As described in Chapter 7, the combination of the temperature responsive pNIPAAm with the conducting PEDOT:PSS polymer led to a novel copolymer with both functionalities. This material was deposited on gold electrodes, and it was used for the capture and release of cancer cells with simultaneous bioelectronics monitoring. The novel copolymer integrated in this microsystem acted as an actuator, performing a temperature triggered cell release, and as a bioelectronics sensor, monitoring the capture and release processes by measuring cell adhesion

by electrochemical impedance spectroscopy. This chapter presented the first step towards the development of more complex architectures using a single component as simultaneous sensor and actuator, as an enabling technology for POC or diagnostic devices. This system was optimised and validated for one cancer cell line, and it could be modified for the specific capture and release of other cells, *e.g.* CTCs or blood cells, by just replacing the capture molecule. Further developments of this system would imply exploring new electrode architectures, cell types and samples, in order to investigate the capabilities of the system for cell isolation, cell sorting from complex samples or cell concentration. The validation of the system for such applications will suppose a breakthrough for new investigations and for health laboratories, deeply facilitating the collection of target cells and reducing considerably the handling of the samples during the process.

The work presented in this thesis demonstrates that the integration of functional materials into microfluidic structures produce novel technologies for chemical and cellular monitoring, moving towards cost-effectiveness and the acquisition of unknown data, by providing user-friendly microfluidic devices with high control at the microscale.

8.2 References

1. Khodagholy, D.; Curto, V. F.; Fraser, K. J.; Gurfinkel, M.; Byrne, R.; Diamond, D.; Malliaras, G. G.; Benito-Lopez, F.; Owens, R. M. Organic electrochemical transistor incorporating an ionogel as a solid state electrolyte for lactate sensing. *Journal of Materials Chemistry* 2012, 22, 4440-4443.
2. Gil-González, N.; Benito-Lopez, F.; Castaño, E.; Morant-Miñana, M. C. Imidazole-based ionogel as room temperature benzene and formaldehyde sensor. *Microchimica Acta* 2020, 187, 1-8.
3. Espadas, J.; Bocanegra, R.; Galvez, J. M. M.; Largo, E.; Baños-Mateos, S.; Arrasate, P.; Guisasola, J. O.; del Olmo, A. V.; Lillo, J. V.; Ibarra, B. GTP and lipids control self-assembly and functional promiscuity of Dynamin2 molecular machinery. *bioRxiv* 2021.
4. Urcan, E.; Haertel, U.; Styllou, M.; Hickel, R.; Scherthan, H.; Reichl, F. X. Real-time xCELLigence impedance analysis of the cytotoxicity of dental composite components on human gingival fibroblasts. *Dental materials* 2010, 26, 51-58.
5. Ke, N.; Wang, X.; Xu, X.; Abassi, Y. A. The xCELLigence system for real-time and label-free monitoring of cell viability. In *Mammalian Cell Viability*; Springer: 2011; pp 33-43.

MATERIALEN ZIENTZIA ETA MIKROFABRIKAZIOA: GAKO TRESNAK MONITORIZAZIO KIMIKO ETA ZELULARRA BURUTZEKO MIKROSISTEMAK GARATZEKO

Maite García Hernando^{1,2}

Zuzendariak: Assoc. Prof. Fernando Benito López¹

Ikerbasque Res. Prof. Lourdes Basabe Desmonts^{2,3}

¹Microfluidics Cluster UPV/EHU, Analytical Microsystems & Materials for Lab-on-a-Chip (AMMa-LOAC) Group, Analytical Chemistry Department, University of the Basque Country UPV/EHU, Spain.

²Microfluidics Cluster UPV/EHU, BIOMICS microfluidics Group, Lascaray Research Center, University of the Basque Country UPV/EHU, Vitoria-Gasteiz, Spain

³*Basque Foundation of Science, IKERBASQUE, María Díaz Haroko Kalea, 3, 48013 Bilbao, Spain*



2021

I

Gaur Egungo Erronkak Biosentsore Miniaturizatuen Garapenean

Gertaera biologikoen detekzio eta monitorizazioa esentziala da ikerkuntza laborategietan, industria farmazeutikoan, ingurugiro analisietarako eta osasun zaintzan. Biodeltekzio test hauen miniaturizazioak sentikortasuna hobetu, analisi denbora eta kostu ekonomikoak murriztu, manipulazioa ekidin eta automatizazioa eta detekzio multiplexatuak ahalbidetzen ditu. Aportazio hauei esker, test hauen tamaina murrizpenak informazioaren bilketa sistematikoa egiteko aukera ematen du, gertaera biologikoen monitorizazioa erraztuz. Bestalde, biosentsore miniaturizatuek, beste biodeltekzio tresna batzuekin lortu ezingo litzatekeen informazioa lortzea ahalbidetzen dute. Kapitulu honek, gailu biosentsore miniaturizatuak fabrikatzeko mikrofabrikazio teknika erabilienen ikuspuntu orokorra eman eta garatu berri diren gailu biosentsore miniaturizatu eta integratu batzuen azterketa egiten du, berauek detekzioa burutzeko transdukzio mekanismoaren arabera sailkatuz.

I.1 Sarrera

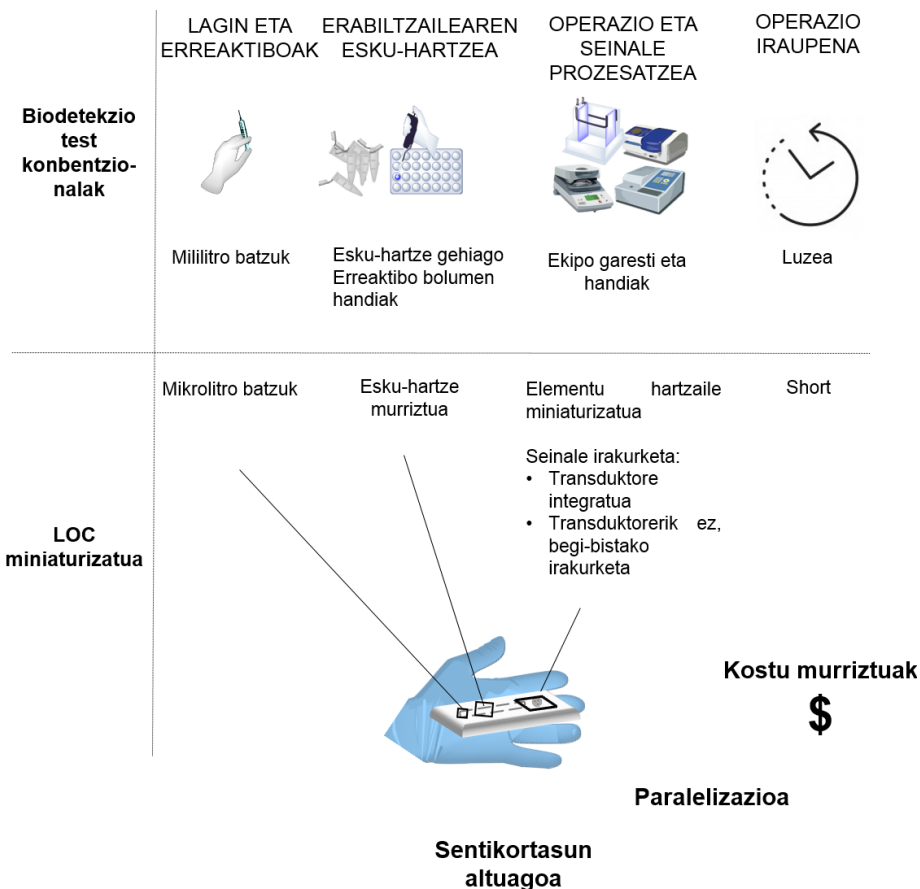
Biosensoreen funtzionamendua erreakzio edo molekula kimiko edo biologikoen detekzioan datza, eta funtsezko da erabilera askotarako, esaterako, farmakoen garapena, segurtasuna elikaduran, ingurugiro analisiak edo osasun zaintza¹. Gainera, biodetekzio neurketa sistematikoek gertaera biologiko edo biokimikoen monitorizazioa ahalbidetzen du, informazio garrantzitsuz hornituz, hala nola, kutsadura pikoak ingurugiro analisietan, orientazioa gaixotasunen prognosian edota jarduera biologikoen inguruari informazio ezezagunaren lorpena. Biosensore bat hartzale eta transduktore batez dago osatuta. Elementu hartzalea edo ezagutza elementua analitoarekin interakzionatzen duen elementua da, eta bio-ezagutzarako biomolekula bat darama txertatuta. Transduktorea, ordea, hartzaleak emandako informazio kimikoa hartu eta seinale fisiko-kimiko bihurtzen duen elementua da (seinale optiko, piezoelektriko, elektrokimikoa...) ^{1,2}.

Biodetekzio test konbentzionalek erreaktibo garestiak, analisi denbora luzeak eta pertsonal entrenatua behar dituzte normalean. Dena dela, test hauen integrazioa sistema miniaturizatuetan, “lab-on-a-chip” (LOC) direlakoetan, abantailatsua da hurrengo aspektuei dagokienez: eramangarritasuna, analisiaren iraupenaren eta lan espazioaren murrizpena, erreaktibo eta lagin bolumen txikien erabilpena, operazio erraza, manipulazio eta hondakinen produkzio murriztua, eta aldibereko detekzio ugari gauzatzeko aukera³⁻⁵ (I.1. irudia). Gainera, lagina jariakin fisiologikoak izanez gero, behar diren bolumen txikieei esker, pazientearen erosotasuna bultzatzen da. Ekarpen hauei esker, biosensore miniaturizatuek monitorizazioa errazten dute, analito, gertaera edo jarduera zehatzen neurketa sistematikoak burutzea erraztuz. Hortaz gain, gailu hauek mikro-eskalan eskaintzen duten kontrola dela eta, biosensore miniaturizatuek,

beste tresna batzuk erabiliz lortu ezingo litzatekeen informazioa lortzea ahalbidetzen dute, esate baterako, nanotubo lipidikoen sortako produkzio kontrolatua eta monitorizazioa (IV. Kapitulua)⁶ edo atxikipen zelulararen kuantifikazioa (V. Kapitulua)^{7,8}.

Mikroteknologiak mikro-eskalan erresoluzio altuko egituren fabrikazioa burutzeko aukera ematen du⁹, beraz aurrerapen anitz egin dira biosentsoreen miniaturizazioari dagokionez mikroteknologiaren garapenari esker. Adibidez, DNA formakuntzak^{10,11}, proteina formakuntzak^{7,12}, kristal fotonikoen formakuntzak^{13,14}, mintz proteinen detekzioa¹⁵, polimero formakuntzak^{16,17} eta material inteligenteak^{18,19} ari dira garatzen bio-detekzio erabilerarako. Biosentsore miniaturizatuen garapenean aurrerapenak eman diren arren, LOC gailu integratu batek elementu anitz barneratzen ditu, hala nola, ezagutze elementua ede elementu hartzailea, kontrol fluidikorako osagaiak edo transduktorea. Hori dela eta, mikrofabrikazio teknika multipleak behar dira hauek fabrikatzeko. Izan ere, zenbait erronka daude oraindik konpontzeke, esaterako, kontrol fluidikorako elementu²⁰ edo energia elektriko iturrien²¹ integrazioa. Honek, guztiz miniaturizatuta ez dauden gailu biosentsoreen garapena dakar²². Gainera, askotan, kanpo gailu konplexuak (mikroskopioak mikrosentsore optikoetarako edo ekipamendu elektronikoa sentsore elektrokimikoen kasuan etab.² behar izaten dira prozesamendua burutzeko, elementu hartzailetik jasotako informazioa, datu irakurgarri eta neurgarri bihurtzeko. Hau da, elementu hartzailearen miniaturizazioak eta detekzio metodoak (adibidez, begi-bistako detekzioak *versus* transduktore miniaturizatuen erabilera), biek, biodetekzio plataformen miniaturizazioa mugatzen dute. Erronka tekniko hauek direla eta, industrian eta laborategietan LOC gailuen erabilera ondo finkatzetik urrun dago oraindik.

Kapitulu honek biosentsore miniaturizatuei dagokienez egin diren aurrerapenak azertuko ditu, garatutako teknologien adibideak emanez, -sentsore motaren arabera sailkatuta. Erabiltzen diren mikrofabrikazio teknika erabilienak ere aurkeztuko dira, eta biosentsore miniaturizatuen integratziorako erabiltzen diren materialen ikuspuntu orokor bat emango da baita ere.



I.1. irudia. Biodetekzio test tradizionalen eta LOC biosentsore miniaturizatuen arteko konparaketa.

I.2 Elementu hartzailearen miniaturizazio eta integrazioa

Elementu hartzailearen tamaina murrizpenak ingurugiro kontrolatua eskaintzen du analito eta hartzailearen arteko interakzioa eman dadin, sentsore tradizionalen aurrean hurrengo abantailak eskainiz: errektibo eta lagin bolumen txikiagoak, ingurugiroaren manipulazio zehatza, jariakinen fluxuaren kontrol zehatza eta molekulen distribuzio homogeneoa sentsorean zehar⁴. Miniaturizazioak multiplexatua ere ahalbidetzen du, gune konkretu batean analito desberdinak detektatzeko mikro-sentsore ugari izatea posible izanez^{23,24}.

Biosentsoreen miniaturizazioan lehenengo pausoa egitura txikien fabrikazioa da, eta hau mikroteknologia erabiliz lor daiteke. Mikrofabrikazio teknika ugari daude erabilgarri, hauetako bakoitzak material batzuentzako egokia, ez gomendagarria, aldiz, beste batzuentzako.

I.2.1 Mikrofabrikazio teknikak

Mikrofabrikazioak mikrogailuetan osagai funtzionalen miniaturizazio eta integrazioa ahalbidetzen du, ondorioz, prozesu analitikoak burutzeko plataforma integratuak sortuz. Mikrofabrikazio tekniketan eman diren aurrerapenek biosentsore miniturizatu funtzionalen garapena bultzatu du.

I.2.1.1 Fotolitografia

Fotolitografia patroi geometriko bat fotomaskara batetik substratu batera transferitzean datza, UV argia erabiliz. Teknika honen erresoluzioa 100 nm-ra hel daiteke, eta bere efizientzia erabilitako argiaren propietateen araberakoa da.

Esaterako, 100-280 nm-ko tarteko UV argia erabiltzeak 50 nm-ko erresoluzioa

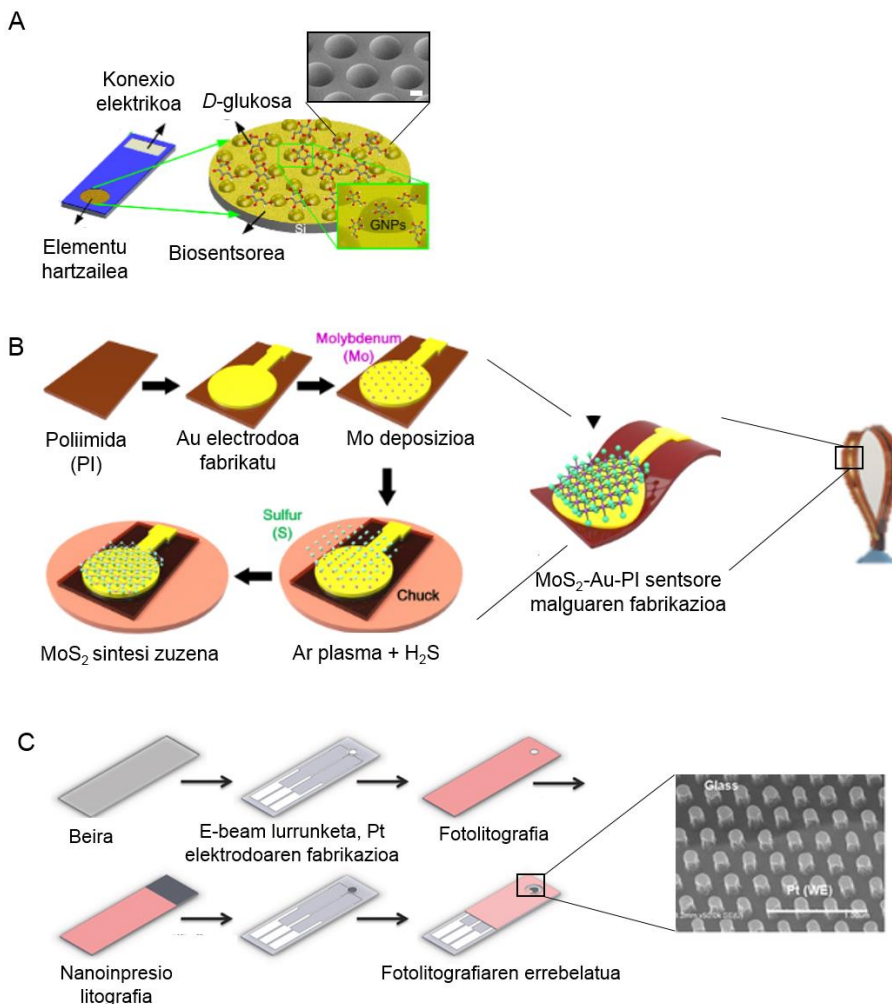
lortzea posible egiten du²⁵. Teknikak duen erresoluzioari esker, sentsoreen produkzio industrialaren ardatz izan da azken hamarkadetan, batez ere zirkuitu mikroelektronico integratuei dagokionean²⁶.

Hainbat lanek fotolitografiaz fabrikatutako biosentsore elektrokimiko miniaturizatuak aurkeztu dituzte analito itu desberdinatarako, metabolito fisiologikoak^{27,28}, azido nukleikoak^{29,30}, proteinak^{31,32} eta zelulak^{33,34} kasu. Biosentsore miniaturizatuen itu molekularik ezagunetarikoa glukosa da. Adibidetzat, Hsu *et al.* fotolitografiaz fabrikatutako egitura mikro-nano hibridoak garatu zitzuten, 3 µm diametroko zutabe formakuntzetan antolatuta²⁸ (I.2A. irudia). Egitura hauek, urrez estali zitzuten, glukosaren detekzio elektrokimikoa faboratuz, eta 9 µM-eko detekzio limitea lortuz.

Silizioa eta beira substratu material erabilienak dira fotolitografia egiteko. Silizioa bezalako material inorganikoen zurruntasun eta egonkortasun mekanikoa baliozkoak izan dira sentsoreen miniaturizazioan. Hala ere, osasun monitorizaziorako joera berrieik, jariakin interstiziala, izerdia, azala edo barne ehunak monitorizatzea dute helburu, beraz material malgu eta biobateragarrien erabilera halabeharrezkoa da. Esate baterako, inplantagarriak diren gailu sentsoreak azalarekin edota barne ehunekin kontaktuan daude, beraz, flexibleak izan behar dira, batetik, pazientearen erosotasuna bermatzeko, eta bestetik, analito ituaren ingurugiro biologikoa mimetizatzeko^{35,36}. Jantzigarriak diren sentsoreen ospea hazten ari da, glukosa^{37,38}, metal astunak³⁹, proteinak³² eta hormonak⁴⁰ bezalako biomarkatzaileen detekzio sistematikoaren bitartez osasuna monitorizatzeko tresna egokia baitira. Adibidetzat, Kim *et al.* MoS₂-poliimida elektrodo malguak garatu zitzuten PTH, T3 eta T4 hormonen detekzio elektrokimikorako⁴⁰. Fabrikatutako urrezko elektrodoa funtzionalizatu egin zen hormonen detekzio elektrokimikoa burutzeko, antigorputzekin sortzen dituzten

interakzio espezifikoez baliatuz (I.2B. irudia).

Fotolitografia litografia guztien artean teknikarik erabiliena den arren, beste litografia mota batzuk ere erabili dira mikrosistemen fabrikaziorako, hala nola, e-beam litografia ^{41,42}, bi fotoi litografia ⁴³ edo nanoinkrimaketa litografia ^{44,45}, beste batzuen artean ⁴⁶. Nanoinkrimaketa litografia metodo simplea da nanoegituren fabrikaziorako, beraz erabilia izan da elektrodoen gainazal azalera handitzeko, sentikortasuna handiagotzeko asmoz. Zehazki, platino elektrodoen gainean, UV bidez polimerizagarri eta eroaleak diren pirrol polimero nanoegiturak erabili ziren glukosaren detekziorako sentikortasuna hobetzeko ⁴⁴ (I.2C. irudia)

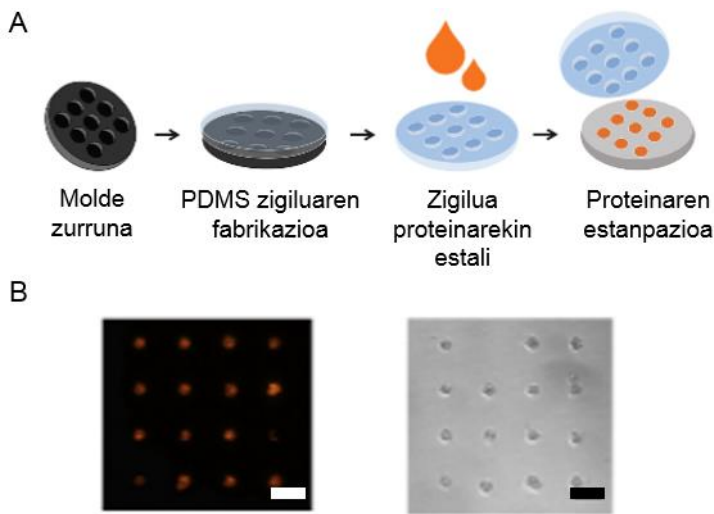


I.2. irudia. A) Fotolitografiaz fabrikatutako elektrodo hibrido micro/nano egituratuen eskema eta urea gehitu eta gero fabrikatutako laginaren mikroskopio elektronikoz (SEM) egindako argazkia. Eskala 5 μm ²⁸. B) MoS₂-ren sintesiaren irudikapena fotolitografiaz fabrikatutako Au-poliiimida elektrodo malgu baten gainean⁴⁰. C) Polipirrol elektrodoaren fabrikazioa nanonprimaketa fotolitografia erabiliz: ezkerrean, fabrikazioaren eskema eta eskuinean, elektrodoaren SEM argazkia. Eskala 1 μm ⁴⁴.

I.2.1.2 Litografia biguna

Litografia biguna litografia tradizionaletik dator, eta substratu zurren – normalean fotolitografiaz fabrikatutakoa- baten erreplika material malgu batean egitean datza⁴⁷. Litografia bigunaren agerpenak pauso handi bat suposatu zuen gailu biosentsore miniaturizatuen fabrikazioan, izan ere, erresoluzio-altuko egituren fabrikazio azkarra ahalbidetzen du biobateragarra den polidimetilsiloxano (PDMS) materialean^{48,49}. Litografia bigunaren abantaila nagusia gailu mikrofluidikoen prototipatu azkarrari lotuta dago, zeintzuk biodetekzioak gauzatzeko erabili daitezkeen, errektibo bolumen txikiagoren beharrarekin eta gastu ekonomiko murriztuekin^{3,4}.

Teknika honek mikro-kontaktu bidezko inprimaketaren garapena erraztu zuen, molekulak gainazal batean inprimatzeko, mikro-egiturak dituen PDMS gainazal baten estanpazioz. Mikro-kontaktu bidezko inprimaketaz biosentsoreak egiteko material anitz erabil daitezke, polimerotatik⁵⁰, proteinetara^{7,8,51} edota grafenora⁵². Diseinu zehatzek funtzionalitate berriak ekar ditzakete, esaterako, zelulaz kanpoko matrizeko proteina formakuntzak ikertu izan dira zelulen integrinen profilak aztertzeko. Horretarako, Pujana-Gonzalez *et al.* zelula indibidualak kokatzeko proteina formakuntzak gauzatu zituzten gainazal polimeriko batean, beraz, zelula batekin okupatuta zeuden proteina puntuen portzentaia kalkulatu zitekeen. Atxikipen zelularra monitorizatu zen atxikitutako zelula kopurua zenbatuz biomaterial ezberdinez osatutako puntuetaan. Honek ahalbidetu zuen biomaterial bakoitzerako atxikipen datu kuantitatiboak lortzea, eta hortaz, zelula-biomaterial interakzioak karakterizatzea⁸ (I.3. irudia).



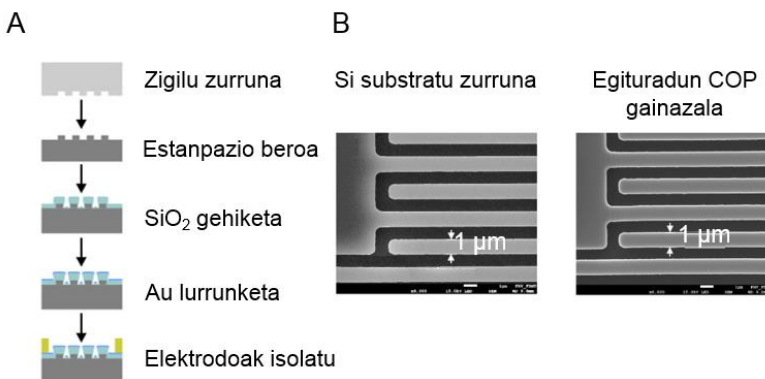
I.3. irudia. A) Zelulaz kanpoko matrizeko proteina formakuntzaren fabrikazioaren eskema. B) Ezkerean, proteina formakuntzaren fluoreszentzia mikroskopía argazkia, eta eskuinean, proteina formakuntzan osatutako zelula individualen formakuntzaren mikroskopía optiko irudia. Eskala 50 μm ⁸.

I.2.1.3 Estanpazio beroa

Estanpazio beroa substratu polimerikoetan erresoluzio altuko egiturak fabrikatzeko kostu baxuko teknika da, eta egituradun molde zurrun bat aurretik berotutako gainazal polimeriko baten estanpatzean datza⁵³. Molde zurruna normalean ondo finkatutako teknikak erabiliz fabrikatzen da aurretiaz, erresoluzio oso altuak (mikratik behera) lortuz, hau da, material eta ekipamendu garestiak erabiliz. Normalean, gainazal polimerikoan egiturak estanpatzen dituen zigilu zurruna behin eta berriz erabil daiteke egitura berdinak gainazal polimeriko anitzetan estanpatzeko. Estanpazio beroz fabrikatzeko protokolo egokien lorpenak erresoluzio altuko nano-egituren sorkuntza ahalbidetu du, bestelako pausoak ekidinez^{54,55}. Estanpazio beroa sentsoretzat jarduten duten elektrodoen fabrikaziorako erabiltzen da. Elektrodoen arteko gunea gero eta

txikiagoa izanik, orduan eta seinale altuagoak lortzen dira⁵⁶, beraz metodo honen bitartez garatutako erresoluzio altuko gailu elektronikoak prototipatu azkarrera hurbiltzen dira.

Estanpazio beroa metal deposizioarekin konbinatu izan da, gainazaleko erresonantzia magnetiko bidez (SPR) behi serum albumina (BSA) detektatzeko biosentsore bat fabrikatzeko polikarbonato substratu malgu batean⁵⁵. Partel *et al.* ere, urea gehitu zuten estanpazio beroz nano-tarteak dituzten elektrodo formakuntza interdigitatuak sortzeko, ziklo-olefina polimeroaren (COP) gainean⁵⁴ (I.4. irudia). Era honetan frogatu egin zuten sentsore integratuen fabrikazio azkarra eta kostu baxukoa posible zela estanpazio beroa erabiliz.



I.4. irudia. A) Elektrodo formakuntza interdigitatuaren fabrikazioaren eskema, dagokion pausoekin: siliziozko zigilu zurruna, honen estanpazio beroa COP-n, SiO₂-ren gehiketa, urearen gehiketa eta isolaketa geruzaren gehiketa elektrodoen ingurua pasibatzeko. B) Ezkerrean, siliziozko zigiluaren irudia eta eskuinean, COP gainazaleko egituren irudia estanpazio beroa eta gero⁵⁴.

I.2.1.4 Serigrafia

Serigrafia teknika substratu baten gainean material organiko edo inorganikoen

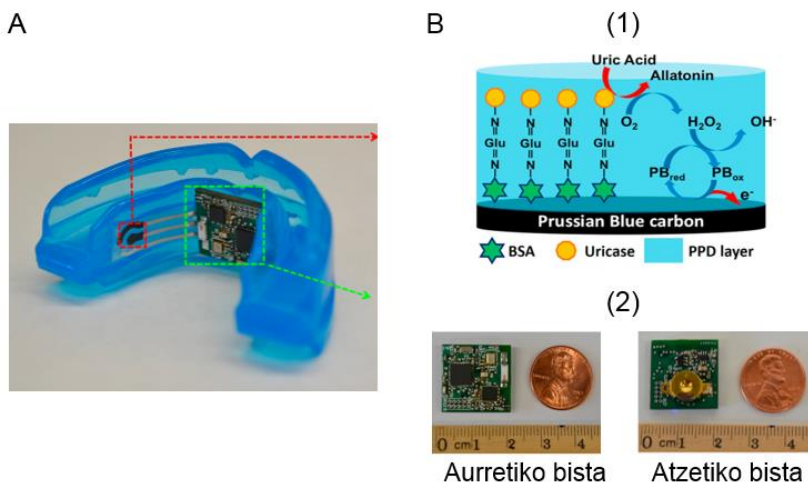
depositioan datza. Horretarako, pasta likido bat jartzen da sare baten barrena, substratura transferitu nahi den diseinua duen mascara bat erabiliz⁵⁷. Denbora luzez teknika hau helburu artistikoetarako erabili izan den arren, biosentsoreak fabrikatzeko tresna baliagarria izan da baita ere azken hamarkadetan⁵⁸. Honekin lortu daitekeen erresoluzioa 100 µm den arren - beste mikrofabrikazio teknika batzuek eskaintzen dutena baino eskasagoa-, teknika honek potentzial itzela dauka prototipatu eta produkzio industrialari dagokionez, eta analito fisiologikoak itu dituzten biosentsoreak fabrikatzeko erabilia izan da jada⁵⁹⁻⁶¹.

Serigrafia oso moldakorra da substratutzat erabili daitezkeen materialei dagokienez, horren adibide dira, zeramikak⁶², beirazko fibrak⁶³ edo polietileno tereftalato (PET)⁶⁴ eta polikarbonato malguak⁶⁵. Tinta eroaleak teknika honen bidez sentsoreak fabrikatzeko material erabilienak dira, substratu multipleen gainean sentsore elektrokimikoen produkzioa ahalbidetzen baitute, teknika litografiko tradizionalek baino protokolo errazagoak eskainiz, betiere, 100 µm baino txikiago diren egituren erresoluzioa arriskuan jarriz⁶⁶.

Adibidetzat, Kim *et al.* aho barrurako biosentsore bat garatu zuten, serigrafiaz fabrikatuta, azido urikoaren monitorizaziorako⁵⁹. “Prussian blue” eta grafitoz osatutako tinta erabili zuten 3 mm diametroko elektrodoa fabrikatzeko, eta usikasa entzima gehitu zioten honi, ondorioz, listuan azido urikoaren monitorizazio elektrokimikoa burutzeko gai zen biosentsorea lortuz, “wireless” data transmisioarekin (I.5. irudia). Lan berriago batean, egileek itu bera zutela, azido urikoaren monitorizazioa listuan, karbono tintadun elektrodoak fabrikatu zituzten serigrafiaz, eta berauei karbono nanotuboak eta urikasa entzima gehitu zizkieten azido urikoaren detekziorako⁶⁰.

Teknika hau baliagarria izan da baita ere tattoo antzeko biosentsore malguak garatzeko, izerdi eta jariakin intersticialaren aldibereko monitorizazioa burutzen

zutenak⁵⁷. Plataforma honek glukosa oxidasan oinarritutako elementu hartzaile elektrokimikoa zuen katodoan, glukosa jariakin interstizialean neurtzeko, eta alkohol oxidasan oinarritutako elementu hartzailea anodoan, izerdiko alkohola neurtzeko. Sistemak lortutako informazioa telefono mugikorrera bidaltzeko gai zen gainera, teknika hau biosentsoreen fabrikazio merke eta errazterako aukera egokia dela balioztatuz.



I.5. irudia. A) Serigrafiaz fabrikatutako aho barruko biosentsorearen argazkia. B) (1) Prussian blue eta karbonoz osatutako, eta urikasa duen elektrodoaren osagai geruzen eskema eta (2) zirkuitu anperometrikoaren argazkia: ezkerrean, aurretiko bista eta eskuinean, atzetiko bista⁵⁹.

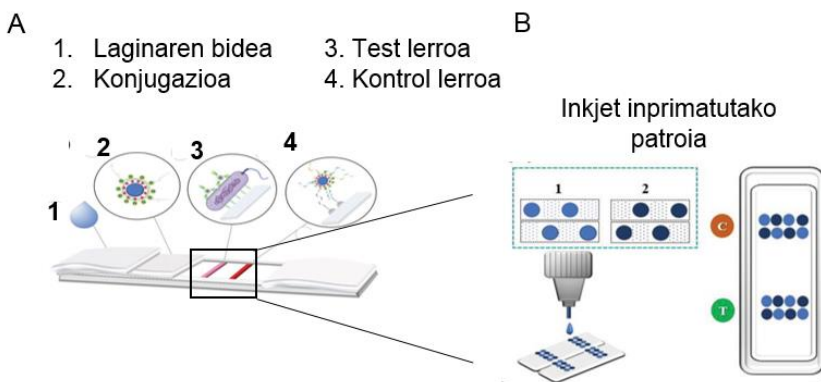
I.2.1.5 Inkjet inprimaketa

Inkjet inprimaketak ordenagailuko diseinuak inprimatzen ditu gainazal baten gainean tantak utziz, normalean porodun substratuak erabiliz. Egin ditzakeen tanten bolumen txikia dela eta ($10\text{-}20 \text{ pl tanta}^{-1}$), oso teknika interesgarria da mikro-biosentsoreak fabrikatzeko, gainera, tantak abiadura azkarrean utzi

ditzake gainazalean kontakturik egin gabe, eta substratu malguekin era erabil daiteke⁶⁸. Teknika honekin mikra azpiko erresoluzioa posible ez den arren, deposizio zehatza lortu izan da erresoluzio kokapenari dagokionez⁶⁹. Esate baterako, Beduk *et al.* poli(3,4-etilenodioxitofeno) poliestireno sulfonatoz eta ZnO-z (PEDOT:PSS/ZnO) osatutako sol-gel sentsore elektrokimikoa garatu zuten paperean, hidrazinaren detekziorako, 20 µm-ko erresoluziora helduz⁷⁰. Bestalde, inkjet inprimakera oso moldakorra da, hainbat material gehitu baitaitezke tantaka sentsore jarduteko⁷¹, hala nola, sol-gel materialak^{70,72}, material eroaleak^{73,74}, polimero inteligenteak⁷⁵, argi emaile diren diodoak^{76,77}, nanopartikulak⁷⁸⁻⁷⁹, metalak^{80,81} eta biomolekulak^{82,83}.

Fotolitografia eta inprimaketa beroa bezalako mikrofabrikazio tekniken erabilera finkatuta dago eta erresoluzio altua eskaintzen dute, baita errepikagarritasun eta efizientzia altuak ere. Dena dela, mikra azpiko erresoluzioa behar ez denean, inkjet inprimaketa aukera egokia da, sentsoreen fabrikazioa produkzio industrialera hurbilduz. Teknika hau erabili izan da thiram fungizidaren detekziorako SPR sentsore bat fabrikatzeko⁸⁴. Horretarako, kontzentrazio altuko urrezko nanopartikulen glizerol/etanol dispersioa erabili zen tintatzat kromatografia paper hidrofobikoan sentsoreak fabrikatzeko.

Biotintak ere inprima daitezke inkjet bidez biosentsoreen garapenarako. Adibidetzat, tinta aptameriko bat erabili zen *E.coli*-ren detekziorako test lateral bat garatzeko⁸³ (I.6. irudia). Erantzun kolorimetrikoa telefono mugikor batekin irakurtzen zelarik.



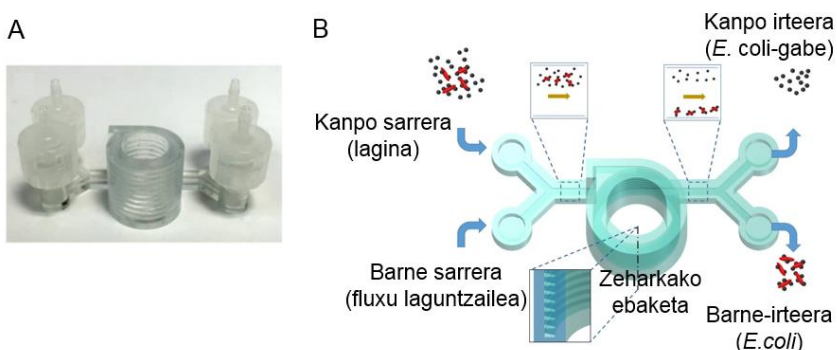
I.6. irudia. A) *E. coli*-ren detekziorako inkjet inprimaketaz fabrikatutako biosentsore lateralaren eskema. B) Sentsoretzat erabilitako tinta aptamerikoaren patroiaren irudikapena⁸³.

I.2.1.6 3D inprimaketa

3D inprimaketak CAD ordenagailu diseinuetatik hiru dimentsiotako objektuen fabrikazioa ahalbidetzen du. Azken urteetan teknika honek garatu duen erresoluzioa ($10 \mu\text{m}$) eta errepikakortasuna hobetu egin dira, eta erabili daitezkeen material aukerak areagotu ere; ondorioz, mikrosistemen fabrikaziorari dagokionez teknika honen populartasuna hazi egin da⁸⁵⁻⁸⁷. 3D inprimaketak gailuen barneko atal hutsak bezalako egitura konplexuen produkzioa ahalbidetzen du, baita prototipatu azkarra ere egin daitezkeen diseinu aldaketa erraz eta bizkorrei esker. Aurreko ekarpen hauek, fotolitografia edo inprimaketa beroa bezalako mikrofabrikazio teknika tradizionalen alboan abantailatsuak dira⁸⁵.

Aurreko mikrofabrikazio metodoak estrukturalak edo gainazalean patroiak inprimatzekoak dira, baina 3D inprimaketak ikuspuntu biak eskaintzen ditu. Diseinu egoki batek barne elementuak gauzatzea ahalbidetu dezake

mikrogailuen barne, esate baterako, injekzio balbulak ⁸⁸ edo prekontzentrazio/sailkapen osagaiak ^{89,90}. 3D inprimaketaz fabrikatutako kanal helikoidal eta antigorputzkin funtzionalizatutako nanopartikula magnetikoen konbinazioa erabili zen adibidez, indar inertzialen bidez esne laginetako bakteria patogenikoen detekzio eta banaketarako (I.7. irudia) ⁹⁰. Beste alde batetik, 3D inprimaketaz egindako arkitektura espezifiko eta material funtzional fotopolimerizagarrien arteko konbinazioak ikuspuntu erraza eskaintzen du gel materialak gailu mikrofluidikoen barne *in situ* era egonkorrean immobilizatzeko, II. Kapituluan azaldu bezala, material funtzionalen integrazioa erraztuz, eta fabrikazio kostuak murriztuz ⁹¹.



I.7. irudia. A) Patogenoen detekzio eta banaketarako 3D inprimaketaz fabrikatutako gailu mikrofluidikoaren argazkia. B) Indar inertzialak erabiliz bakterien banaketaren irudikapen eskematikoa ⁹⁰.

3D inprimaketa baliagarria da baita ere biosentsoreen elementu hartzalea zuzenean substratu baten gainazalean inprimatzeko, 3D inprimaketa bidezko elektronikan ^{92,93} edo 3D inprimatutako optikan bezala ^{94,95}. Bi hauek zientzia joera berria direnez, haurtzaroan daude oraindik, baina hauen populartasuna azkar ari da hazten. 3D inprimaketaz egindako elektronika oso interesgarria da elektrodoetan lor dezakeen erresoluzioagatik (15 μm kasu batzuetan),

fotomaskararik behar gabe, eta substratu malguetan erabiltzeko duen potentzialagatik^{96,97}. Esaterako, estrusiozko 3D inprimaketa erabili izan da potentziostato zirkuitu integratu eta miniaturizatu baten prototipoa fabrikatzeko⁹⁶. Zilar nanopartikulaz osatutako tinta likatsua erabiliz, zirkuitua substratu malgu batean fabrikatu zen, laktatoaren detekzio lineala lortuz 1 - 20 mM tartean. Teknika hau erabiltzeak, biosentsore elektrokimiko integratuen fabrikazioa erraztu zuen, fabrikazio industriala lortzeko bidean.

Halaber, 3D inprimaketaz fabrikatutako optikak zenbait desabantaila dauzka oraindik, guztiz gardenak eta leunak diren gainazalak sortzeko teknika honek dituen zailtasunak direla eta, honek argiaren islapenean eta transmisioan eragina izan baititzake⁹⁸. Hori horrela, Hinman *et al.* prisma bat fabrikatu zuten 3D inrpimaketaz, zeina zenbait lixatu pauso eta gero, bakterio toxinen detekzio plasmonikoa burutzeko gai izan zen, fabrikazio kostuak murritzuz eta osagai optikoen fabrikazioa erraztuz⁹⁵.

I.2.2 Materialen integrazioa biosentsore erabiltzeko

Materialek gako funtzioa betetzen dute ezagutza elementu bezala, analitoarekin ematen den interakzioaren informazio kimikoa bidaltzen baitiote transduktoreari. Material anitz erabil daitezke sentsoretzat, baina orokorrean, materialek kriterio tekniko, metrologiko eta ekonomiko zehatzak bete behar dituzte dagokien aplikaziorako egokiak izateko. Ezagutza elementua osatzen duten materialak hurrengo taldetan sailka daitezke.

I.2.2.1 Metalak

Metalak, elektrodoen oinarria direlarik, material erabiliena dira sentsoreetako elementu hartzalean erabiltzeko. Propietate elektriko eta eroale bikainak

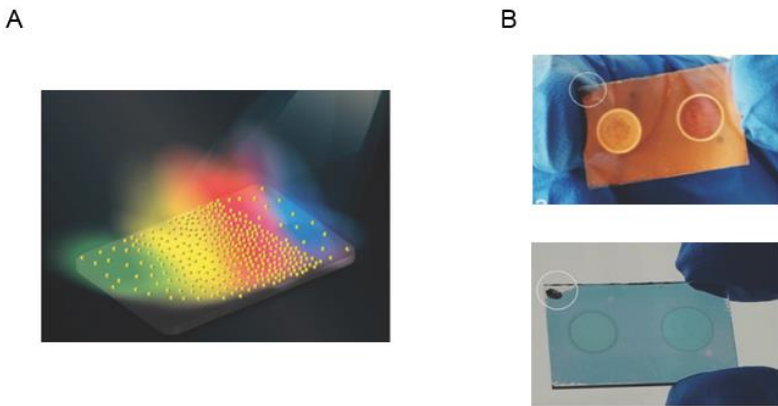
dituztelako dira hain erabiliak sentsore elektronikoetan. Horrez gain, xaflakortasuna eta harikortasuna bezalako propietate fisiko interesgarriak dituzte ere, zeinak metalen prozesamendua errazten duten fabrikazioari begira ⁹⁹. Duten eroankortasun, korrosioarekiko erresistentzia, gogortasun eta miniaturizazio ahalmenari esker, kobrea ¹⁰⁰, grafitoa ¹⁰¹, titanioa ¹⁰² eta zilarra ¹⁰³ bezalako metal tradizionalak erabilienak izan dira elektrodo miniaturizazioen fabrikaziorako. Dena dela, urreak afinitate handia dauka biomolekulekin, baita egonkortasun eta energia interfazial altuak, material interesgarria bihurtzen dutena biosentsore sentikorren fabrikaziorako ¹⁰⁴, beraz, ikertzaile gehienek, gaur egun, urrea erabiltzen dute biosentsore elektrodotzat.

Metalek, biosentsore elektrokimiko bezala, erabilera zabala izan dute metabolito ^{28,105} eta zelulen ^{33,106} detekziorako, baina aukera egokia dira baita ere DNA bezalako detekzio zailak burutzeko. Izatez, DNA molekulen etiketarik gabeko detekzio sentikor, selektibo eta azkarra erronka bat da oraindik, baina nanopartikulak ¹⁰⁷, karbono nanotuboak ¹⁰⁸, siliziozko nanohariak ¹⁰⁹, grafeno oxidoa ¹¹⁰ eta molibdeno disulfitoa (MoS_2) ²⁹ bezalako material metalikoen erabilera haten ari da. Horren adibide da Mei *et al.* azaldutako lana, DNA-ren detekziorako biosentsore ultrasentikor bat erakutsiz, MoS_2 -Z osatutako transistore baten oinarrituta ³¹. Horretarako, urrezko mikroelektrodoak fabrikatu eta gero, kanala MoS_2 eta fosforodiamidato morfolino oligoekin (PMO) estali zen. PMO-DNA hibridizazioa detektatu zen, selektibilitate eta errepikakortasun onak azalduz, detekzio limitea 6 fM-tan finkatu zelarik.

Interesgarria da baita ere, lagin biologikoek batzuetan berezko sentiberatasun magnetiko deuseztagarria erakusten dutela, eta hau neurtu egin daitekeela erresonantzia magnetiko nuklearra (NMR) erabiliz. Zentzu honetan, Huber *et al.* denge sukarra detektatu eta aldi berean minbizi zelulen profil molekularra

aztertzeko biosentsore azkarra azaldu zuten, erresonantzia sistema multi-kanal elektroniko hetero-nuklearra erabiliz, NMR bidez¹¹¹. Horrez gain, biosistema batzuk elektrikoki kitzika daitezke, eremu biomagnetikoak sortuz, eta elektrodo metalikoak hauek detekta ditzakete¹¹². Adibidetzat, pultsu magneto-inpedantzia sentsore bat erabiliz, guinea-txerrien muskuluen eremu magnetikoa monitorizatu, eta jasotako informazioa jarduera elektriko biologikoarekin korrelazionatu zen¹¹³.

Elektrodoak berak, sentikorrik eta eraginkorrik dira, baina hauek beste material batzuekin estaltzeak euren funtzionamendua hobetu dezake; estalki material horiek metalak edo bestelako materialak izan daitezke, sentsore híbridoak emanet. Esate baterako, metalezko egitura organikoak, moldakortasun estruktural handiko metal-polimero sareak dira, gainazal azalera eta adsortzio gaitasun handia dutenai¹¹⁴. Sarearen beraren eta molekula ostalari baten arteko interakzioari erantzun diezaiokete, urrezko elektrodoen sentikortasuna areagotuz^{115,116}. Bestalde, karbonozko nanomaterialak ere erabili ohi dira elektrodoen sentikortasuna handitzeko¹¹⁷. Grafenoa, hain zuzen ere, material eroale, garden eta malgua da, propietate elektrokimiko interesgarriekin, eta elektrodoen selektibilitatea areagotzeko aukera ona^{118,119}. Azkenik, metalek propietate plasmonikoak aurkeztu ditzakete baita ere. Esate baterako, Elbahri *et al.* metapartikula plasmonikoak (dipolo plasmonikoak) erabili zituzten giza serum exosomen begi bistako detekzioa lortzeko (I.8. irudia)¹²⁰.

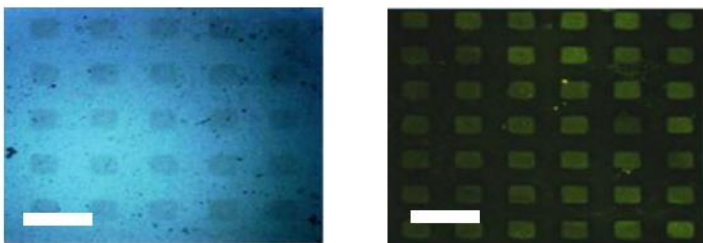


I.8. irudia. A) Nanopartikula plasmonikoek emandako koloreen irudikapen eskematikoa. B) Ezkerreko zirkuluan, Bowel gaixotasuna duen paziente baten exosomekin kontaktuan egon eta gero AU nano-taldeen irudia eta eskuineko zirkuluan, paziente osasuntsu baten exosomekin kontaktuan egon eta AU nano-taldeen irudia, bi modutan, islapena (goian) eta transmisioa (behean)¹²⁰.

I.2.2.2 Polimeroak

Biosentsoreak polimeroz osatuta egon daitezke baita ere. Polimeroek moldakortasun handia dute, eta propietate kimiko eta fisikoei dagokienez aukera anitz eskaintzen dituzte, hala nola, osagai biologikoekin interakzioak burutzeko gaitasuna, propietate biskoelastikoak, euren egituraren biomolekulak txertatzeko ahalmena¹²¹... Are gehiago, polimeroak mikro tamainako egiturak egiteko erabil daitezke, non erreakzio biokimikoak gertatu eta *in situ* detekta daitezkeen, Wang *et al.* azaldu bezala⁵⁰. Lan horretan, 100 µm diametroko azido poliakriliko irlak sortu ziren mikro-kontaktu inprimaketaz, eta Hepatitis-B-Birus eta Hepatitis-B-Birus antigenputzen arteko interakzioak fluoreszentzia mikroskopiaz eta SPR-z monitorizatzeko erabili ziren (I.9. irudia). Patroietan jarritako azido poliakriliko irlak birusaren detekzioaren amplifikazioa aurkeztu zuten patroirik gabeko (miniaturizatu gabeko) azido poliakrilikoarekin konparatuz, detekzio tarte linear

zabala lortuz.



I.9. irudia. Ezkerrean, azido poliakriliko irlak giza IgG-arekin inkubatu eta gero mikroskopia optiko irudia eta eskuinean, azido poliakriliko irlak giza IgG-arekin eta FITC-ahuntz-anti-H-IgG-rekin inkubatu eta gero mikroskopia fluoreszente irudia⁵⁰. Eskala 100 μm.

Sentsore polimerikoak moldakorrak dira baita seinale motari dagokionez ere. Duten egiturat esker, beste molekula batzuekin konbina daitezke, beraz biosentsore kolorimetriko¹²², fluoreszente¹²³ edo kimiolumineszente^{124,125} bihurtu daitezke. Bioelektronika organikoan ere dira erabiliak, elektrodo metaliko tradizionalekin batera biosentsore funtzioa hobetzeko^{126,127}, edo berauek bakarrik elektrodo bezala jardunez, biosentsore plataforma elektrokimiko malgu bezala¹²⁸. Zehazki, polimero semi-eroaleak erabilgarriak dira biosentsore elektrokimiko bezala^{32,129}, baina gaur egun monitorizazio mikrosistema malgu aurreratuagoak garatzeko joera da nagusi, larruazal artifiziala imitatzezkan, esaterako izerdian pH, urea eta azido laktikoa aldi berean detektatzeko¹³⁰.

Bestalde, material funtzionalak, edo konkretuki, material inteligenteak deritzenak, euren inguruan ematen diren aldaketan aurrean erreakzionatzen dute, era errepikakor eta espezifikoan¹³¹. Polimeroen familiaren barne, batzuk

estimulu edo kinada konkretuen aurrean erantzuten dutenez, interesgarriak dira biosentsoreen eremuan, hauen kinaden aurreko erantzuna neurtu egin daitekeelako, eta gertaera konkretuekin korrelazionatu. Polimero hauek eurek bakarrik erabil daitezke¹³², edo beste elementu sentsore batzuekin konbinatuta^{133,134}. Adibidetzat, fibra optikoak akrilamida hidrogelarekin estaltzeak, pH –aren SPR bidezko detekzioaren hobetzea ekarri zuen¹³³. Hori azaldu daiteke, hidrogela handitu egin zelako pH balio handiagotarako, ur absortzio handiagoa lortuz, eta ondorioz, errefrakzio indizeak txikiagotuz, pH neurketaren sentikortasuna handituz.

Horrez gain, funtzionalitate ezberdinak dituzten polimeroak konbinatu egin daitezke funtzionalitate multipledun material hibridoak lortzeko. VI. kapituluan, kopolimero garatu berri bat azaltzen da, zeina poli(N-isopropilakrilamida) (pNIPAAm) material termo-erantzulea eta PEDOT:PSS material eroalea konbinatu diren. Kopolimeroak, fibronektina proteinarekin funtzionalizatu zena, eragingailutzat jardun zuen, zelulen harrapatze eta kitzikatutako askapena gauzatzuz, eta baita biosentsoretzat ere, harrapatze eta askatze prozesua inpedantzia elektrokimiko espektroskopiaz monitorizatzuz. Aurretik aipatu bezala, polimeroek moldakortasun fisiko-kimiko bikaina daukate. Hala erakusten du kristal fotonikoen (PC), hau da, hutsune fotoniko bat duten nanoegitura optiko periodikoen, sorrerak¹³⁵. PC-k argia difraktatzen dute argi ikuskor espektroan, mikrometro azpiko tamaina dutenean, begi bistako sentsore kolorimetrikotzat jardunez¹³⁶. Esate baterako, poliestireno koloide sakabanatuez (100 nm diametroa) egindako koloide kristalino formakuntzak akrilamida-bisakrilamida sare batean txertatzean, glukosa biosentsore bat garatu zen¹⁴¹. Beste lan batean, Endo *et al.* nano-inprimaketa litografia erabili zuten polietilen glikol (PEG)-ean murgildutako COP materialean PC-ak sortzeko, listuan influenza virusaren detekzio reflektometrikoa gauzatzeko, 1 ng ml⁻¹-ko detekzio

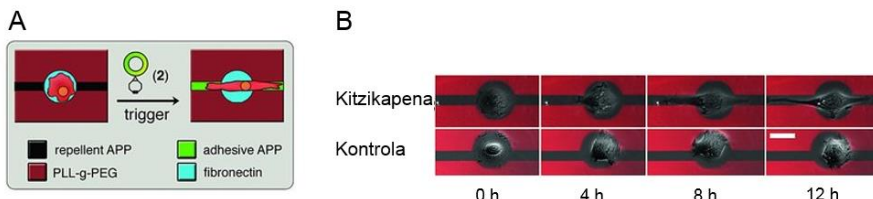
limitea lortuz¹³⁸.

Bestalde, polimeroek nano-eskalan abantailak eskaintzen dituzte baita ere euren prozesamenduari dagokionez, mikrofabrikazio aldetik, abantailatsua dena. Adibidetzat, polianilina nanopartikula dispersioak inkjet inprimaketa bidez prozesoa daitezke, elektrodoen gainean sortzen diren egitura polimerikoen lodiera eta tamaina kontrolatzuz^{139,140}.

I.2.2.3 Biomaterialak

Biomolekulak –proteinak, karbohidratoak eta azido nukleikoak- kate polimeriko edo sare konplexuak dira. Bata bestearekin afinitate handiko interakzioak dituzte, lotura kobalenteak ere sortuz. Biosentsore miniaturizatuek, normalean, ezagutza biomolekula hauetako bat izaten dute txertatuta, analito ituarekiko afinitate handia duena, era honetan detekziorako sentikortasuna eta selektibilitatea ziurtatzuz¹⁴¹. Ezagutza molekulak beste material sentsore batzuetan integra daitezke biomaterial sentsore hibridoak lortzeko¹⁴²⁻¹⁴⁴, edo zuzenean immobiliza daitezke gainazal batean^{7,8}, elementu hartzaile sentsorea osatzeko. Esaterako, elektrodoen funtzionalizazioa entzimekin oso metodo erabilia da biosentsoreei sentikortasuna eta selektibotasuna emateko¹⁴⁵. Are gehiago, entzimak kobalenteki lotu daitezke biopolimeroz estalitako elektrodoetan, entzimaren egonkortasuna eta funtzionalitatea bermatuz. Martin *et al.*, polidopamina film polimerikoak erabili zitzuten kolesterol oxidasa entzima platinozko elektrodo nano-egituratuetan lotura kobalentez lotzeko¹⁴². Biosentsore honek egonkortasun handia eta funtzionamendu egokia azaldu zituen kolesterolaren detekziorako, detekzio muga 10.5 µM -tan izanik. Beste alde batetik, nanopartikulak eraldatu izan dira baita ere biomolekulekin detekzio optikoa burutzeko, urezko nanopartikulak aptameroekin eraldatzuz¹⁴⁶.

Biomolekulak gainazalean zuzenean jartzeari dagokionez, biosentsoreak egiteko ere erabilia izan da, teknikaren arabera, erresoluzio altuak lortuz. Kasuan kasu, zelula indibidualentzako diseinatutako proteina patroiek datuak lortzeko bide berriak zabaltzen dituzte, detekzioaren interpretazioa zelula indibidualen kuantifikazioan oinarrituz⁷. Zelula bakoitza output indibidualtzat hartuz, sistemak datu kuantitatiboak jasotzen ditu, adibidez, proteinekiko afinitatearen detekzio optikoa^{8,147} edo toxizitate zelularra (ikusi V. kapitulua)⁷. Zelulen erantzunak zelulaz kanpoko matrizeko proteinekiko¹⁴⁸, zelulen polarizazioa¹⁴⁹, biomolekulen sekrezioa¹⁵⁰ eta migrazioa¹⁵¹ ere gainazaleko biomolekulak sentsoretzat hartzuz ikertu izan dira. Adibidetzat, Van Dongen *et al.* proteina mikro-patroiak erabili zituzten gainazal estalki dinamikotzat atxikipen zelularren, migrazioaren eta forma aldaketaren kontrolerako¹⁵² (I.10. irudia).



I.10. irudia. A) Poli-(L-lisina)-PEG eta azido-[polilisina-g-PEG] (APP), patroi bikoitzaren eskema, zeinetan zelulek migratu egin zuten biziklo[6.1.0]nonine-Arg-Gly-Asp peptido (2) -arekin kitzikatuak izan eta gero, forma aldaketa jasanez. B) RPE1 zelulen forma aldaketaren argazkiak denboran zehar (2) konposatura gehitu eta gero. Kontrol laginetan ez zen (2) konposatura gehitu. Eskala 25 μm¹⁵².

Are gehiago, molekula indibidualak gainazaletan jartzeak potentzial handia dauka biosentsoretzat erabiltzeko, espezifikotasun eta sentikortasun handiagoa oparoan, multiplexatu gaitasuna posible eginez¹⁵³. DNA-origami^{153,154}, elektroi

izpi litografia^{155,156} edo maskara koloidaleko litografia¹⁵⁷ bezalako teknika berriek jada posible egin dute biomolekula indibidualen kokapen zehatza. Zehazki, maskara koloidaleko litografia mahai gaineko metodoa da molekula indibidualak edozein materialen gainazalean kokatzeko (polimeroak, beira, metalak...), temperatura eta hezetasun baldintza berezirik behar gabe, eta diseinua erraz moldatzeko aukerarekin¹⁵⁷.

I.3 Seinalearen transduktzioaren integrazioa

Elementu transduktorea esentziala da elementu hartzaleak emandako detekzioaren emaitza irakurgarri bat lortzeko. Transduktzio ekipamenduen beharrak mugatu egiten du gailu sentsorearen miniaturizazioa, eta beraz, eramangarritasuna. Askotan, elementu hartzalearen miniaturizazioa lortzen den arren, kanpo tresnak behar izaten dira seinalearen transduktzioa burutzeko, sistema finalaren dimentsioak handitz, eta gailuaren erabilgarritasuna mugatuz.

Sentsoreetan bost transduktzio mekanismo nagusi erabili dira literaturan: optiko, elektrokimiko, piezoelektriko, magnetiko eta termometriko. Hauetako bakoitzak detekzio eta transduktzio baldintza ezberdinak bete behar dituzte, behean adierazten den bezala.

I.3.1 Biosentsore optikoak

Biosentsore optikoen erabilera oso arrunta da mikrosistemen garapenari dagokionez. Biosentsore optikoek transduktore optikoen beharra izan dezakete seinalea interpretatzeko, hala nola, errefraktometro, espektometro, interferometro, kamara/mikroskopio bat... beste batzuen artean. Ostera, biosentsore optiko batzuei dagokienez, begi bistaz ikus daitezkeen kolorimetria

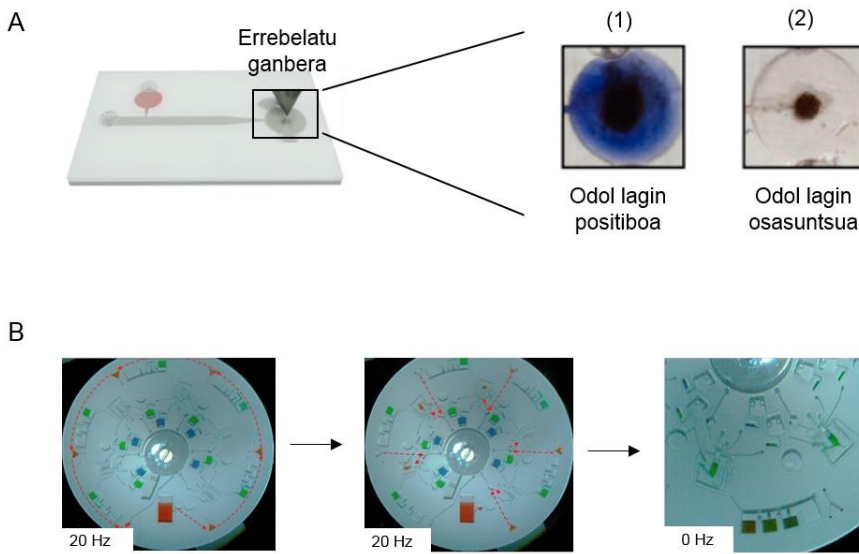
^{146,158}, fluoreszentzia ¹⁵⁹, luminiszentzia ^{114,160} edo plasmonika ^{120,161} sortzen duten erreakzioak ematen dituzte. Begi bistako detekzioari esker, ez litzateke kanpo irakurlerik beharko seinalearen interpretaziorako, biosentsore sistema osoaren tamaina osoa murriztuz. Hala ere, elementu hartzalearen miniaturizazioak begi bistako detekzioa zaildu egiten du, mikroskopio bat bezalako instrumentu baten erabilera bultzatzuz. Biosentsore optikoak hiru talde nagusitan sailkatzen dira, hurrengo transdukzio mekanismoaren arabera: absortzioa, lumineszentzia edo erresonantzia.

Absortzioan oinarritutako sentsoreak selektiboak eta erabiltarrak dira, baina hurrengo desabantailak dituzte: inguruko argiak neurketan egin dezakeen interferentzia, epe luzeko egonkortasuna eta tarte dinamiko mugatua ¹⁶². Zehazki, sentsore kolorimetrikoak biosentsore azkarretarako oso erabiliak dira ¹⁶³⁻¹⁶⁵. Kolorimetriak zenbait abantaila ditu beste metodo batzuen aurrean, hala nola, kostu baxua, begi bistako identifikazio kualitatibo edo semi-kuantitatiboa eta instrumentu simpleen erabilera (instrumenturik ez begi bistako detekziorako edota telefono mugikor bidezko datu analisirako moldapen potentziala. Seinale transdukziorako kanpo ekiporik behar duten beste absortzio metodoen aldean, kolorimetriak autonomia, eramangarritasuna, urrunezko sentsore funtzionamendua eta monitorizaziorako mikrosistema integratuen miniaturizazioa errazten ditu. Bestalde, sentsore kolorimetrikoen fabrikazioa teknika simpleekin bateragarria da (adibidez, inkjet inprimaketa, serigrafia...), eta sentsorearen funtzionamendua, datu jasotzea eta hauen analisia ez dira konplikatuak ¹⁶⁶. Esate baterako, Fraser *et al.* gailu mikrofluidiko bat garatu zuten malaria gaixotasunaren diagnosi kolorimetrikorako, aptameroei lotutako entzimetan oinarritutako testa gailuan integratuz ¹⁶⁴. Detekzioa telefono mugikor batekin monitorizatu zen (I.11A irudia).

Lumineszentzia material batek argia igortzean datza, erreakzio kimiko, UV argi edo kitzikapen elektrikoak bezalako iturrietatik hartutako energiaren ondorioz. Sentsore lumineszenteek, beraz, argia igortzen dute detekzio emaitzatzat. Behin energia iturriak materiala kitzikatu duela, kitzikatu gabeko egoerara bueltatzen da berriz ere, argia igorritz. Sentsore hauek normalean absortzioan oinarritutako sentsoreak baino sentikorragoak dira, gailuen miniaturizazio altuagoa ahalbidetuz. Zehazki, sentsore fluoreszenteak gailu miniaturizatuetan maiz erabiltzen dira, hauen seinalea hondo beltz batekiko zuzenean neurten delako, era honetan fluoreszentzia maila baxuak ere detektagarriak izanik¹⁶⁶. Fluoreszentzia biodetekzio testetan erabiltzen den teknika arruntena da; horren adibide da Natajaran *et al.*-en lana, zeinetan miokardio infartu zorrotzaren diagnostikorako gailu fluoreszente bat garatu zen¹⁷¹. Edonola ere, mikrosistema fluoreszenteek kanpo ekipamendu espezifikoen beharra dute, zeinak plataformaren tamainaren murrizpen osoa mugatzen duen, eta gainera, auto-fluoreszentzia duten materialek biosentsorearen funtzionamenduan eragin dezakete. Hondoko seinaleari dagokionez, sentsore lumineszenteen barne, kimiolumineszenteek seinale hobekuntza bikaina dute¹⁶⁷, beraz ahaleginak egin dira sistema mikrofluidikoetan test kimiolumineszenteak integratzeko¹⁶⁹⁻¹⁷¹. Hu *et al.* azaldutakoa azpimarragarria da, biosentsore kimiolumineszente eramangarria garatu baitzuten proteina C-erreaktiboa eta testosterona detektatzeko, errepikakortasun eta sentikortasun altuarekin¹⁷¹. Mikrofluidika digitala automatizatua ere kimiolumineszentziarekin konbinatua izan da¹⁷². Kasu honetan, gailu mikrofluidikoa mugikorreko aplikazio batekin guztiz kontrolatzen zen, lumineszentziarekin lotutako uniformetasun falta detektatzeko irudien prozesamendurako sistema barne.

Azkenik, plasmonika bezalako erresontzian oinarritutako sentsoreen erabilera hazten ari da, etiketarik gabeko detekzio gaitasuna baitu, sentikortasun

altuarekin eta denbora errealean monitorizazioa burutzeko¹⁷³. SPR fenomenoari dagokionez, gainazal metaliko bateko elektroiak argiarekin kitzikatzen dira, erreflexio indizean aldaketak emanez, eta aldaketa horiek espektrofotometro batekin^{174,175} edo begi bistaz^{176,177} irakur daitezke, miniaturizazio eta eramangarritasuna erraztuz^{178,179}. Esaterako, lab-on-a-disc gailu bat garatu zen IgG-ren detekzio kuantitatiboa SPR bidez detektatzeko, telefono mugikor bateko kamera erabiliz (I.11B irudia)¹⁷⁸. Lan honetan, egileek anti-IgG immobilizatu zuten lab-on-a-disc batean integratutako urrezko gainazalean, eta IgG-ren detekzioa burutu zuten gailu hau erabiliz, beste edozen biokonjugatu immobilizatz gero, bestelako biodetekzio batzuk egiteko moldapen potentzialarekin. Beste lan batean, Dipalo *et al.* hiPSC –etatik deribatutako zelula kardiakoen zelulaz kanpoko eta barneko gertaerak monitorizatzeko mikrosistema garatu zuten metaelektrodo plasmonikoak erabiliz¹⁸⁰. Horretarako, porodun elektrodo planarrak fabrikatu zituzten, funtzionalitate bakoitzarekin: batetik, elektrodo jarduera, eta bestetik, hiru dimentsiotako antena plasmonikoen jarduera optiko eta biologikoa imitatuz.



I.11. irudia. A) Malaria diagnosirako gailu kolorimetriko mikrofluidikoaren funtzionamenduaren irudikapena. Ezkerrean, aptameroekin estalitako perla magnetikoak magnetismo bidez garraiatu ziren ganberaraino, non aptamero eta parasioaren PfLDH proteinaren arteko interakzioaren ondorioz diformazan morearen sorrera eman eta kolorea sortzen zen. Eskuinean, bi odol laginen testen argazkiak, (1) *Plasmodium falciparum* positibo den odol lagina eta (2) paziente osasuntsu baten laginaren testaren emaitza¹⁶⁴. B) Lab-on-a-disc gailuaren funtzionamenduaren argazkiak, non kolore gorri, urdin eta berdeak erabili ziren lagin, garbiketa eta SPR neurketa bufferarentzat, hurrenez hurren. Ezkerrean, plasma alikuotatua, erdian, laginaren zentrifugazio bidezko ponpaketa, eta eskuinean, IgG –ren detekzioaren neurketa¹⁷⁸.

I.3.2 Biosentsore elektrokimikoak

Biosentsore elektrokimikoetan, analitoak elementu hartzalean erreakzionatzen du analitoaren kontzentrazioarekiko proportzionala den edo analito konkretu baterako berezkoa den seinale elektriko bat igorriz. Biosentsore elektrokimikoak

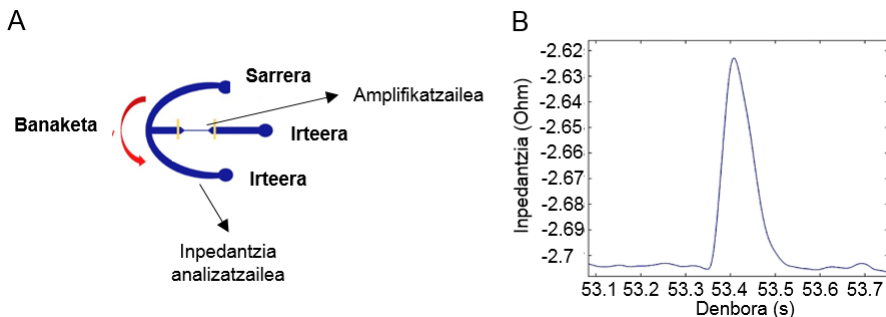
ondo finkatuta daude, eta hauen sendotasun, miniaturizazio erraztasun, sentikortasun altu eta etiketarik gabeko detekzio aukerengatik nabarmenzen dira¹⁸¹. Normalean, detekzioaren neurketa, anperometria, potentziometria edo inpedimetria bidez ematen da.

Anperometria potentzial konstante baten menpe korronte baten neurketan datza¹⁴⁵. Anperometriko biosentsore entzimatikoetan erabili da batez ere, elektrodoan ematen diren erredox erreakzioen emaitza neurtuz^{27,105}. Kaur *et al.* gailu mikrofluidiko anperometriko bat azaldu zuten kolesterolaren monitorizaziorako, nikel oxidoarekin eraldatutako platino elektrodoetan oinarrituz²⁷. Bestalde, 16S ARN erribosomikoa molekularen bezalako detekzio konplexuak lortu izan dira anperometriaz, aurretiazko amplifikazio pausoren beharrik gabe²³. Azken lan horretan, egileek patogenoak identifikatu zitzutzen 16S RNA erribosomikoen detekzioari esker, 16 sentsorez osatutako gailu anperometriko eramangarria (2.5 x 7.5 cm) erabiliz.

Potentziometrian, ordea, elektrolito batekin konektatuta dauden bi elektrodoren arteko potentzial diferentzia neurten da. Biosentsore potentziometrikoak sendoak, erabilerrazak eta sentikorrik dira¹⁸². Hori dela eta, immobilizatutako mikroorganismoen^{183,184} edo entzimen^{185,186} jarduera detektatzeko erabili izan dira. Horren adibide da propolian eta eztian fenolen detekzio kuantitatiborako bi geruzadun transduktorea¹⁸⁶. Zehazki, zero korronteko potentziometria erabili zen, beraz erredox potentzialean aldaketak neurtu beharrean, potentzial interfaziala neurtu zen¹⁸⁷. Zero korronteko potentziometriak DNA hibridizazioaren monitorizazio konplexua burutzea ahalbidetu zuen baita ere, analitoaren aurreko eraldaketen beharrik gabe, potentzial interfazialean oinarrituta bakarrik¹⁸⁸.

Azkenik, inpedimetrian, sistema bat korronte alternoaren menpe dagoenean,

honetan ematen den oposizio elektriko edo impedantzia neurtzen da. Biosentsore impedimentikoak biosistemekin bateragarriak dira normalean, erabiltzen dituzten tentsio baxuak direla eta, beraz, elektrodo/elektrolito interfasean ematen diren gertaera biologikoak monitoriza daitezke^{189,190}. Izatez, biosentsore mota hauek prozesu zelularren monitorizazio kuantitatiborako erabili izan dira^{191,192}, hau da, zelula^{34,106} eta proteina¹⁹³ espezifikoen detekziorako. Esaterako, Ghassemi *et al.* biosentsore impedimentiko bat garatu zuten, deformagarritasun impedantzia zitometrian oinarrituta, minbizi zelula zirkulatzileen detekzio eta kuantifikaziorako³⁴ (I.12 irudia).



I.12. irudia. A) Deformagarritasun impedantzia zitometria bidezko minbizi zelula zirkulatzileen analisirako gailuaren diseinua. B) Minbizi zelula indibidual baterako lortutako impedantzia balioa adierazten duen impedantzia *versus* denbora grafikoa³⁴.

I.3.3 Biosentsore piezoelektrikoak

Sentsore piezoelektrikoak tresna erabilgarriak dira etiketarik gabeko biosentsoretzat erabiltzeko, eta normalean kristal anisotropikoz osatuta daude. Bi elektrodok tentsio alterno bat sortzen dute biosentsorearen gainazalean, kristalaren frekuentzian oszilazioak eraginez. Analito bat kristalaren gainazalean atxikitzen denean, aldaketa bat ematen da oszilazio frekuentzian, eta hori da hain

zuzen ere detekzioarekin korrelacionatzeko neurtzen dena¹⁹⁴.

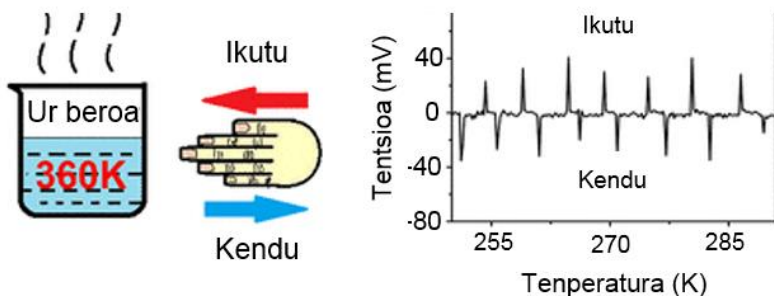
Kuartozko kristalezko mikrobalantza (QCM) biosentsore piezoelektriko miniaturizatuen artean arruntena da, duen fabrikazio finkatuari eta etiketarik gabeko detekzioari esker. QCM oso sentikorra den masa balantza bat da, mikro- eta nanogramo mailan neurketa zehatzak egitea ahalbidetzen duena. Kuartzozko disko mehe batez eta kontrako aldean elektrodoz dago osatuta, eta elektrodoetan zehar aplikatutako eremu elektriko alterno batek, oszilazioa eragiten du frekuentzia zehatz batean, kuartzozko kristalean. Kuartzozko kristalean masa gehitzeak edo kentzeak, oszilazio frekuentziaren aldaketa dakar, beraz, honen monitorizazioak gainazalean ematen diren interakzioen inguruko informazioa ematen du¹⁹⁵. QCM sistemak biosentsoretzat erabiliak izan dira jada, adibidez, E bitaminaren deribatu baten aurrean toxizitate zelularra neurtzeko, honen aurrean atxikipen zelularra monitorizatzu¹⁹⁶. Horrez gain, interakzio molekular dinamikoak monitoriza daitezke baita ere, Jin *et al.* demostratu bezala, DNA kaltetuaren eta proteina zelular batzuen arteko interakzio molekularrak denbora errealean neurtuz¹⁹⁷.

Bestalde, QCM-barreiatze sistemak QCM sentsoreen sentikortasuna areagotzen du (segundo bakoitzeko 200 datu puntu baino gehiagotan), eta horri esker, Asai *et al.* *Lupus Erythematosus* sistemikoaren diagnosia burutu zuten¹⁹⁸. Horretarako, QCM tradizional bati aluminio oxido nano-egitura anodikoak fabrikatu zizkioten (40, 60 eta 80 nm diametroko hutsuneak), elementu hartzailearen gainazala handiagotuz masa detekzioarako frekuentzia aldaketa areagotuz¹⁹⁹.

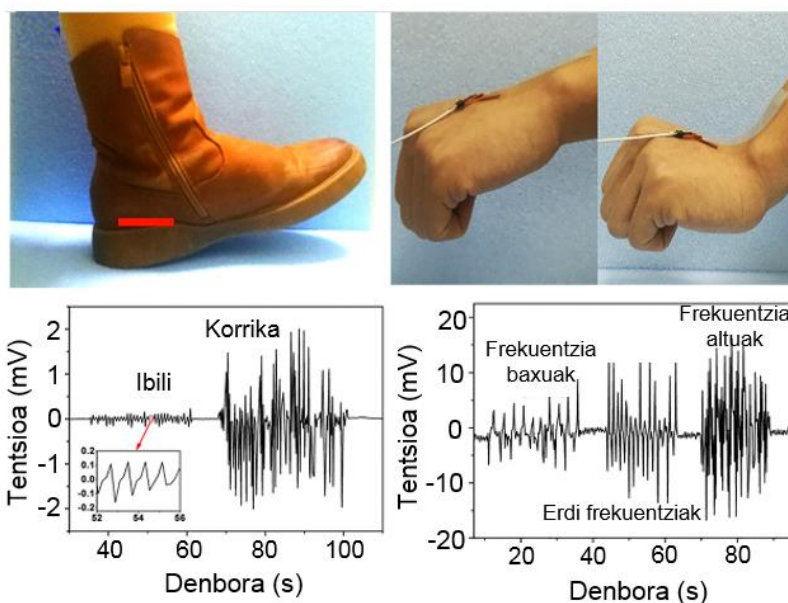
Biosentsore piezoelektrikoak erabiliak dira baita ere sentsore jantzigarritzat²⁰⁰ edo larruazal artifizialtzat^{201,202}, parametro fisiko eta kimikoak aldi berean neurtuz. Esaterako, gailu piezoelektriko jantzigarri eta autonomoa azaldu izan da larruazal elektronikotzat, denbora errealean odolarengan analisirako, sentsore

piezoelektrikoak emandako seinalea indar iturritzat erabiliz batetik, eta bestetik, proteina C-erreaktiboak detektatuz²⁰⁰. Beste lan interesgarri batean, Wang *et al.* elektrodo indibidual piezoelektriko bionikoa garatu zuten, presioa eta bero/hotza, aldi berean monitorizatzeko²⁰³ (I.13. irudia).

A



B



I.13. irudia. A) Ur beroa ikutu eta eskua kentzeko eskema, larruazal elektronikoa erabiliz. B) Taloi eta eskumuturrean larruazal elektronikoaren argazkiak, eta dagozkien grafikoak, ezkerrean ibiltzea eta korrika egitea (taloian) adieraziz, eta eskuinean, frekuentzia ezberdinei dagozkien tentsioen irudikapen grafikoa²⁰³.

I.3.4 Biosentsore magnetikoak

Biosentsore magnetikoek hurrengo abantailak eskaintzen dituzte: denboran zehar egonkortasuna, hondoko seinale interferentziarik ez, hurrunezko funtzionamendu potentziala eta sentikortasun altua²⁰⁴. Sentsore magnetiko batzuk sandwich erako erreakzioak dituzte oinarri, baina magnetoerresistentzian oinarritutako sentsoreak dira bereziki aipagarriak, biosentsore sendoak baitira, selektibotasun eta sentikortasun altuarekin²⁰⁵. Nanopartikula muin-oskol magnetoelektriko ferrielektrikoak erabili ziren minbizi zelulen NMR bidezko detekzioa burutzeko, minbizi zelula ezberdinen artean ezberdintzeko gaitasuna izanik²⁰⁶.

Mikrosistema biosentsoreei dagokienez, magnetismoaren beste abantailatzat, detekzioaren espezifikotasuna eta partikulak sentsorean zehar puntu konkretu bateraino garraiatzeko gaitasuna dira. Azken honi dagokionez, eremu magnetikoaren presentziak analitoaren eta hartzailaren arteko interakzioen azelerazioa dakar. Are gehiago, azken hamarkadetan, nanopartikula magnetikoen populartasuna ikerkuntzan esponentzialki hazi da, batez ere hipertermia tratamenduei^{207,208} eta itura bideratutako farmako askapenari^{209,210} dagokienez, edo baita kontraste agentetzat erabiliz erresonantzia magnetiko irudietarako ere^{211,212}.

Magnetoelektronika kontzeptua, aldiz, azken hamarkadetan azaldu den eta biosentsore gailu miniaturizatuetara begira etorkizun handiko tresna da^{206,213}. Gailu elektroniko integratuetan material ferromagnetiko baten gehiketan datza, eta honi esker sortzen diren gailuek magnetizazio egonkorra dute, eta “spin” egoerak tentsio edo korronte elektrikoarekin eragiteko aukera ematen dute²¹⁴. Adibidetzat, Xi *et al.* gailu magnetoelektriko bat azaldu zuten gibeleko burdinaren detekzio eta kuantifikaziorako²¹³. Hortaz gain, jaioberri den

magnetoelektronika malgua den eremu teknologikoa oparotasun handikoa dela uste da, sentsore magnetikoek ukimenik gabeko giza-makina interakzioetan izan dezakeen inpaktua dela eta²¹⁵. Nahiz eta eremu hau haurtzaroan dagoen oraindik, zenbait material ezagutzen dira jadanik larruazal artifizialak bezalako gailu magnetoelektroniko malguen garapenerako^{216,217}.

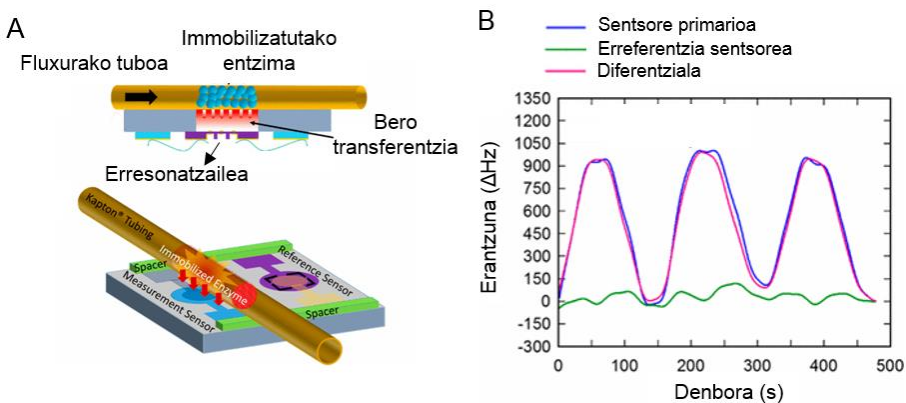
I.3.5 Biosentsore termometrikoak

Biosentsore termometrikoek beroa askatzen duen edozein erreakzio biologikoren tenperatura neurtzen dute, normalean, termistore sentikor bat erabiliz²¹⁸. Entzimak dituzten termistoreak biosentsore termometriko arruntenak dira, eta immobilizatuta dauden entzimen jardueraren ondoriozko beroa neurtzen dute^{219,220}. Biosentsore termometriko miniaturizatuen gainean lan gutxi atera diren arren, azken bost urteetan mikro-tamainako zenbait deskribatu izan dira²²¹⁻²²⁴.

Entzimen enkapsulazioa mikrokapsula polimerikoetan metodo aipagarria da aurkezten duen jarduera katalitikoaren efizientzia eta termometria bidezko detekzioa direla eta^{223,225}. Horren adibide da garatutako biosentsore termometriko ultrasentikor bat, Y formako kuartzko erresonatzaile batez osatuta dagoena, eta enkapsulatutako kreatinina deiminasa entzimen jarduera neurtuz, kreatinina kuantifikatzen duena²²³ (I.14. irudia). Dena dela, sentsore mota hauen desabantaila nagusia espezifikotasun falta da, izan ere, hauek entalpia aldaketak neurtzen dituzte, nahiz eta neurtutako entalpia aldaketak itu erreakzioak sortuak ez izan. Hori hobetzekotan, Wang *et al.* glukosaren neurketarako termopare sistema azaldu zuten, immobilizatutako glukosa oxidasaren jardueraren monitorizazioa burutzen zuena²²¹.

Jarduera entzimatikoaren neurketa sandwich erako immuno-sentsore termikoen bidez gauzatu daiteke baita ere²²². Esaterako, Bari *et al.* glukosa oxidasarekin

konjugatutako detekzio antigorputzak erabili zituzten tumore nekrosiren indikatzaile den α -faktorearen detekziorako, gailu mikrofluidiko batean²²⁵. Honen arabera, glukosa gehitzean, antigorputzei lotutako glukosa oxidasak glukosa oxidatu zuen, beroa askatuz, hau sentsore termometrikoarekin neurtuz.



I.14. irudia. A) Biosentsore termometrikoaren eskema. B) 25 mM kreatininaren aurrean sentsore primarioaren eta erreferentzia sentsorearen erantzunaren irudikapen grafikoa, baita bi sentsoreen erantzunen arteko diferentzia ere²²³.

I.4 Ondorioak

Aurrerapen teknologikoek berrikuntza sustatu dute biosentsore miniaturizatuetan, baita hauen LOC gailuetan integrazioa bultzatu ere. Sentsoreen parte diren elementu hartzale miniaturizatuen fabrikazio eta integrazioa aspaldi lortu zen litografia edo estanpazio bero teknikei esker, baina horretarako, ekipamendu garesti eta espezializatua beharrezkoa da, baita langile entreinatuak ere. Duela gutxiko mikrofabrikazio joerei dagokienez, serigrafia, inkjet inprimaketa eta 3D inprimaketa azpimarragarriak dira biosentsore miniaturizatuen fabrikaziorako teknika simple legez. Dena dela, mikroteknologia etengabe dago garapenean, erresoluzio altuagoak lortzen eta teknika bakoitzaren

erabilgarritasuna material ugarira zabaltzen, hartzale elementu edo sentsoretzat jardun dezaten.

Elementu hartzalearen miniaturizazioak gako funtzioa dauka lor daitekeen informazioari dagokionez. Esate baterako, material metalikoen miniaturizazioak elektrodo txikiagoren fabrikazioa ekarri du, 16S RNA molekulen bezalako detekzio konplexuak gauzatzeko gaitasuna lortuz. Hortaz gain, magnetoelektronikaren agerpena ere aipatu beharra dago, honi esker lortu baita eremu biomagnetiko biologiko intrintsekoen detekzioa, edo lagin biologikoen sentiberatasun magnetiko deuseztagarria erabili ahal izatea analitoen detekziorako. Polimeroei dagokienez, hauek mikro-eskalan patroietan kokatzeak sentikortasuna areagotzea eragin dezake. Hori ez ezik, hauen erabilera biosentsore elektronikoetan, bioelektronika malgu eremuari dagokienez bide berriak zabaldu ditu.

Biomaterialen edo biomolekulen integrazioa biosentsoreetan ezinbestekoa da. Batetik, biomolekulak beste material miniaturizatu batzuekin konbina daitezke analitoaren ezagutza eman dadin, edo biomolekulak berauek zuzenean koka daitezke substratu bateko gainazalean, era zuzen batean bio-ezagutza elementuak integratzeko. Ildo horretan, diseinu egokiek zelula indibidualen atxikipena ahalbidetu dezakete, zeinari esker gertaera zelularren kuantifikazioa lortu izan den, baina molekula bakarreko erresoluzioa ere posible da gaur egun, ikuspuntu oparoa eskainiz sentikortasun eta zehaztasunari begira.

Beste alde batetik, biosentsoreen tamaina murrizpenak elementu hartzalearen eta transduktorearen, bien, miniaturizazioa beharko luke. Sentsore motaren aukera egokia esentziala da biosentsore miniaturizatu oparoak garatzeko, sentsore mota bakoitzak ezaugarri ezberdinak baititu.

Sentsore elektrokimikoak erabilienak dira, euren moldakortasuna eta sentikortasunari esker. Serigrafia eta inket inprimaketaren erabilera azken boladan hazi egin da, elektrodoen fabrikazioa erraztu egiten baitute, batez ere gailu elektroniko malguei dagokienez. Bestalde, biosentsore optikoak aukera egokia dira baita ere, ematen duten seinalea begi bistaz detekta daitekelako askotan, transduktoreren beharrik gabe. Sentsore optikoen sentikortasuna altuagoa da egitura hartzale txikiagotarako, baina tamaina murrizpen honek begi bistako interpretazioa zaitzen du. Espresuki, plasmonika biosentsore funtzioetarako tresna sentikortzat hartzen da, begi bistako interpretazioa ere ahalbidetzen baitu. Biosentsore piezoelektrikoei dagokienez, sentikorrik eta efizienteak dira, baina hauen fabrikazioa garestia eta luzea da oraindik. Bestalde, biosentsore magnetikoen erabilera oso hedatuta ez dagoen arren, hauen popularitasuna hazi egin da azken hamarkadan, fabrikazioa errazten duten aurrerapen teknologikoei eta nanomaterial magnetikoen (minbiziaren aurkako terapiak, NMR...) agerpenari esker, baita elektronikarekin konbinatzeko gaitasunari esker ere, biosentsore magnetoelektroniko sentikor eta konpaktuak sortuz. Azkenik, biosentsore termometrikoak erabilera konkretuetarako interesarriak izan daitezkeen arren (adibidez, beroa askatzen duten bioerreakzioetarako), hauen erabilera biosentsore legez, ez da oso zabala.

Laburbilduz, aurrerapen handiak egin dira biosentsoreen miniaturizazioan, sentikortasun altuagoak eta erabilera errazak azalduz. Biosentsoretzat jardungo duten LOC gailu integratuak garatzeko bidean, orain arte garatu diren biosentsore miniaturizatu gehienak kanpo elementuak behar dituzte oraindik, hala nola, fluxu kontrolatzialeak, transduktoreak edo energia iturriak, beraz osagai hauen miniaturizazioa erronka bat da oraindik. Hala ere, garatu diren briosentsoreak, izan badira ezagutza zientifiko berria lortzeko tresna baliagarriak, hurrengo kapituluetan azaltzen direnak kasu.

I.5 Erreferentziak

1. Banica, F. Chemical sensors and biosensors: fundamentals and applications; John Wiley & Sons: 2012.
2. Fraden, J. Handbook of modern sensors: physics, designs, and applications; Springer Science & Business Media: 2004.
3. Vyawahare, S.; Griffiths, A. D.; Merten, C. A. Miniaturization and parallelization of biological and chemical assays in microfluidic devices. *Chem. Biol.* 2010, 17, 1052-1065.
4. Derkus, B. Applying the miniaturization technologies for biosensor design. *Biosens. Bioelectron.* 2016, 79, 901-913.
5. Soleymani, L.; Li, F. Mechanistic challenges and advantages of biosensor miniaturization into the nanoscale. *ACS sensors* 2017, 2, 458-467.
6. Galvez, J. M. M.; Garcia-Hernando, M.; Benito-Lopez, F.; Basabe-Desmonts, L.; Shnyrova, A. V. Microfluidic chip with pillar arrays for controlled production and observation of lipid membrane nanotubes. *Lab Chip* 2020, 20, 2748-2755.
7. Garcia-Hernando, M.; Calatayud-Sanchez, A.; Etxebarria-Elezgarai, J.; de Pancorbo, M.; Benito-Lopez, F.; Basabe-Desmonts, L. Optical Single Cell Resolution Cytotoxicity Biosensor Based on Single Cell Adhesion Dot Arrays. *Anal. Chem.* 2020, 9658-9665.
8. Gonzalez-Pujana, A.; Santos-Vizcaino, E.; García-Hernando, M.; Hernaez-Estrada, B.; de Pancorbo, M. M.; Benito-Lopez, F.; Igartua, M.; Basabe-Desmonts, L.; Hernandez, R. M. Extracellular matrix protein microarray-based biosensor with single cell resolution: Integrin profiling and characterization of cell-biomaterial interactions. *Sens. Actuator B Chem.* 2019, 299, 126954.
9. Lee, S. J.; Sundararajan, N. Microfabrication for microfluidics; Artech house: 2010.
10. Nawattanapaiboon, K.; Kiatpathomchai, W.; Santanirand, P.; Vongsakulyanon, A.; Amarit, R.; Somboonkaew, A.; Sutapun, B.; Srikririn, T. SPR-DNA array for detection of methicillin-resistant *Staphylococcus aureus* (MRSA) in combination with loop-mediated isothermal amplification. *Biosens. Bioelectron.* 2015, 74, 335-340.
11. Abbott, J.; Ham, D.; Xu, G. All-Electrical Graphene DNA Sensor Array. In *Biosensors and Biodetection* Springer: 2017; pp 169-187.
12. Gogalic, S.; Sauer, U.; Doppler, S.; Preininger, C. Investigating Colorimetric Protein Array Assay Schemes for Detection of Recurrence of Bladder Cancer. *Biosensors* 2018, 8, 10.
13. Chakravarty, S.; Tang, N.; Yan, H.; Yang, C.; Zou, Y.; Shen, Q.; Chen, R. Photonic crystal microarray sensing of breast cancer cell line lysates 2014.
14. Zhang, Y.; Zhao, Y.; Zhou, T.; Wu, Q. Applications and developments of on-chip biochemical sensors based on optofluidic photonic crystal cavities. *Lab Chip* 2018, 18, 57-74.

15. Wittenberg, N. J.; Im, H.; Johnson, T. W.; Xu, X.; Warrington, A. E.; Rodriguez, M.; Oh, S. Facile assembly of micro-and nanoarrays for sensing with natural cell membranes. *ACS nano* 2011, 5, 7555-7564.
16. Peveler, W. J.; Landis, R. F.; Yazdani, M.; Day, J. W.; Modi, R.; Carmalt, C. J.; Rosenberg, W. M.; Rotello, V. M. A rapid and robust diagnostic for liver fibrosis using a multichannel polymer sensor array. *Adv Mater* 2018, 30, 1800634.
17. Ngernpimai, S.; Geng, Y.; Makabenta, J. M.; Landis, R. F.; Keshri, P.; Gupta, A.; Li, C.; Chompoosor, A.; Rotello, V. M. Rapid identification of biofilms using a robust multichannel polymer sensor array. *ACS Appl. Mater. Interfaces* 2019, 11, 11202-11208.
18. Wang, L.; Jackman, J. A.; Tan, E.; Park, J. H.; Potroz, M. G.; Hwang, E. T.; Cho, N. High-performance, flexible electronic skin sensor incorporating natural microcapsule actuators. *Nano Energy* 2017, 36, 38-45.
19. Shen, J.; Pang, J.; Xu, G.; Xin, X.; Yang, Y.; Luan, X.; Yuan, S. Smart stimuli-responsive fluorescent vesicular sensor based on inclusion complexation of cyclodextrins with Tyloxapol. *RSC Adv.* 2016, 6, 11683-11690.
20. Ter Schiphorst, J.; Saez, J.; Diamond, D.; Benito-Lopez, F.; Schenning, A. P. Light-responsive polymers for microfluidic applications. *Lab Chip* 2018, 18, 699-709.
21. Dinh, T.; Nguyen, T.; Phan, H.; Nguyen, T.; Dau, V. T.; Nguyen, N.; Dao, D. V. Advances in rational design and materials of high-performance stretchable electromechanical sensors. *Small* 2020, 16, 1905707.
22. Temiz, Y.; Lovchik, R. D.; Kaigala, G. V.; Delamarche, E. Lab-on-a-chip devices: How to close and plug the lab? *Microelectron. Eng.* 2015, 132, 156-175.
23. Gao, J.; Jeffries, L.; Mach, K. E.; Craft, D. W.; Thomas, N. J.; Gau, V.; Liao, J. C.; Wong, P. K. A multiplex electrochemical biosensor for bloodstream infection diagnosis. *SLAS Technol.* 2017, 22, 466-474.
24. Huertas, C. S.; Domínguez-Zotes, S.; Lechuga, L. M. Analysis of alternative splicing events for cancer diagnosis using a multiplexing nanophotonic biosensor. *Sci. Rep.* 2017, 7, 1-8.
25. Andrews, D.; Nann, T.; Lipson, R. H. Comprehensive nanoscience and nanotechnology; Academic press: 2019.
26. Panzarasa, G.; Soliveri, G. Photocatalytic Lithography. *Appl. Sci.* 2019, 9, 1266.
27. Kaur, G.; Tomar, M.; Gupta, V. Development of a microfluidic electrochemical biosensor: Prospect for point-of-care cholesterol monitoring. *Sens. Actuator B Chem.* 2018, 261, 460-466.
28. Hsu, C.; Su, F.; Peng, P.; Young, H.; Liao, S.; Wang, G. Highly sensitive non-enzymatic electrochemical glucose biosensor using a photolithography fabricated micro/nano hybrid structured electrode. *Sens. Actuator B Chem.* 2016, 230, 559-565.

29. Mei, J.; Li, Y.; Zhang, H.; Xiao, M.; Ning, Y.; Zhang, Z.; Zhang, G. Molybdenum disulfide field-effect transistor biosensor for ultrasensitive detection of DNA by employing morpholino as probe. *Biosens. Bioelectron.* 2018, 110, 71-77.
30. Xu, S.; Zhan, J.; Man, B.; Jiang, S.; Yue, W.; Gao, S.; Guo, C.; Liu, H.; Li, Z.; Wang, J. Real-time reliable determination of binding kinetics of DNA hybridization using a multi-channel graphene biosensor. *Nat. Commun.* 2017, 8, 14902.
31. Tran, T.; Clark, K.; Ma, W.; Mulchandani, A. Detection of a secreted protein biomarker for citrus Huanglongbing using a single-walled carbon nanotubes-based chemiresistive biosensor. *Biosens. Bioelectron.* 2020, 147, 111766.
32. Xu, M.; Yadavalli, V. K. Flexible biosensors for the impedimetric detection of protein targets using silk-conductive polymer biocomposites. *ACS sensors* 2019, 4, 1040-1047.
33. An, L.; Wang, G.; Han, Y.; Li, T.; Jin, P.; Liu, S. Electrochemical biosensor for cancer cell detection based on a surface 3D micro-array. *Lab Chip* 2018, 18, 335-342.
34. Ghassemi, P.; Ren, X.; Foster, B. M.; Kerr, B. A.; Agah, M. Post-enrichment circulating tumor cell detection and enumeration via deformability impedance cytometry. *Biosens. Bioelectron.* 2020, 150, 111868.
35. Someya, T.; Bao, Z.; Malliaras, G. G. The rise of plastic bioelectronics. *Nature* 2016, 540, 379-385.
36. Klauk, H. *Organic electronics II: more materials and applications*; John Wiley & Sons: 2012; Vol. 2.
37. Kudo, H.; Sawada, T.; Kazawa, E.; Yoshida, H.; Iwasaki, Y.; Mitsubayashi, K. A flexible and wearable glucose sensor based on functional polymers with Soft-MEMS techniques. *Biosens. Bioelectron.* 2006, 22, 558-562.
38. Xuan, X.; Yoon, H. S.; Park, J. Y. A wearable electrochemical glucose sensor based on simple and low-cost fabrication supported micro-patterned reduced graphene oxide nanocomposite electrode on flexible substrate. *Biosens. Bioelectron.* 2018, 109, 75-82.
39. Gao, W.; Nyein, H. Y.; Shahpar, Z.; Fahad, H. M.; Chen, K.; Emaminejad, S.; Gao, Y.; Tai, L.; Ota, H.; Wu, E. Wearable microsensor array for multiplexed heavy metal monitoring of body fluids. *Acs Sensors* 2016, 1, 866-874.
40. Kim, H.; Kim, H. Y.; Seok, H.; KANADE, V. K.; Yoo, H.; Park, K.; Lee, J.; Lee, M.; Kim, T. Flexible MoS₂-Polyimide Electrode for Electrochemical Biosensors and their Applications for the highly sensitive Quantification of Endocrine Hormones: PTH, T3, and T4. *Anal. Chem.* 2020.
41. Huang, H.; Ger, T.; Lin, Y.; Wei, Z. Single cell detection using a magnetic zigzag nanowire biosensor. *Lab Chip* 2013, 13, 3098-3104.
42. Presnova, G.; Presnov, D.; Krupenin, V.; Grigorenko, V.; Trifonov, A.; Andreeva, I.; Ignatenko, O.; Egorov, A.; Rubtsova, M. Biosensor based on a silicon nanowire field-effect transistor functionalized by gold nanoparticles for the highly sensitive determination of prostate specific antigen. *Biosens. Bioelectron.* 2017, 88, 283-289.

43. Bakhtina, N. A.; Loeffelmann, U.; MacKinnon, N.; Korvink, J. G. Two-Photon Nanolithography Enhances the Performance of an Ionic Liquid–Polymer Composite Sensor. *Adv. Funct. Mater.* 2015, 25, 1683–1693.
44. Ahn, J.; Kwon, S.; Jung, S.; Lee, W. S.; Jeong, J.; Lim, H.; Shin, Y.; Lee, J. Fabrication of Pyrrole-Based Electrochemical Biosensor Platform Using Nanoimprint Lithography. *Adv. Mater. Interfaces* 2018, 5, 1701593.
45. Mohapatra, S.; Kumari, S.; Moirangthem, R. S. Fabrication of a cost-effective polymer nanograting as a disposable plasmonic biosensor using nanoimprint lithography. *Mater. Res. Express* 2017, 4, 076202.
46. Vazquez-Mena, O.; Sannomiya, T.; Tosun, M.; Villanueva, L. G.; Savu, V.; Voros, J.; Brugger, J. High-resolution resistless nanopatterning on polymer and flexible substrates for plasmonic biosensing using stencil masks. *ACS nano* 2012, 6, 5474–5481.
47. Xia, Y.; Whitesides, G. M. Soft lithography. *Annu. Rev. Mater. Sci.* 1998, 28, 153–184.
48. Fischer, R.; Steinert, S.; Fröber, U.; Voges, D.; Stubenrauch, M.; Hofmann, G.; Witte, H. Cell cultures in microsystems: Biocompatibility aspects. *Biotechnol. Bioeng.* 2011, 108, 687–693.
49. Bélanger, M.; Marois, Y. Hemocompatibility, biocompatibility, inflammatory and in vivo studies of primary reference materials low-density polyethylene and polydimethylsiloxane: A review. *J. Biomed. Mater. Res.* 2001, 58, 467–477.
50. Wang, Y.; Cui, Y.; Cheng, Z.; Song, L.; Wang, Z.; Han, B.; Zhu, J. Poly (acrylic acid) brushes pattern as a 3D functional biosensor surface for microchips. *Appl. Surf. Sci.* 2013, 266, 313–318.
51. Hu, S.; Chen, T.; Zhao, Y.; Wang, Z.; Lam, R. H. Protein–substrate adhesion in microcontact printing regulates cell behavior. *Langmuir* 2018, 34, 1750–1759.
52. Tsai, S.; Goshia, T.; Chen, Y.; Kagiri, A.; Sibal, A.; Chiu, M.; Gadre, A.; Tung, V.; Chin, W. High-throughput label-free microcontact printing graphene-based biosensor for valley fever. *Colloids Surf. B Biointerfaces* 2018, 170, 219–223.
53. Worgull, M. Hot embossing: theory and technology of microreplication; William Andrew: 2009.
54. Partel, S.; Kasemann, S.; Matylitskaya, V.; Thanner, C.; Dincer, C.; Urban, G. A simple fabrication process for disposable interdigitated electrode arrays with nanogaps for lab-on-a-chip applications. *Microelectron. Eng.* 2017, 173, 27–32.
55. Lee, K.; Wu, T.; Hsu, H.; Yang, S.; Wei, P. Low-cost and rapid fabrication of metallic nanostructures for sensitive biosensors using hot-embossing and dielectric-heating nanoimprint methods. *Sensors* 2017, 17, 1548.
56. Partel, S.; Dincer, C.; Kasemann, S.; Kieninger, J.; Edlinger, J.; Urban, G. Lift-off free fabrication approach for periodic structures with tunable nano gaps for interdigitated electrode arrays. *ACS nano* 2016, 10, 1086–1092.

57. MacDougall, A. Screen printing today: The basics; ST Books, a division of Media Group International: 2008.
58. Tudorache, M.; Bala, C. Biosensors based on screen-printing technology, and their applications in environmental and food analysis. *Anal. Bioanal. Chem.* 2007, 388, 565-578.
59. Kim, J.; Imani, S.; de Araujo, W. R.; Warchall, J.; Valdés-Ramírez, G.; Paixão, T. R.; Mercier, P. P.; Wang, J. Wearable salivary uric acid mouthguard biosensor with integrated wireless electronics. *Biosens. Bioelectron.* 2015, 74, 1061-1068.
60. Shi, W.; Li, J.; Wu, J.; Wei, Q.; Chen, C.; Bao, N.; Yu, C.; Gu, H. An electrochemical biosensor based on multi-wall carbon nanotube-modified screen-printed electrode immobilized by uricase for the detection of salivary uric acid. *Anal. Bioanal. Chem.* 2020, 1-9.
61. Jiang, D.; Chu, Z.; Peng, J.; Jin, W. Screen-printed biosensor chips with Prussian blue nanocubes for the detection of physiological analytes. *Sens. Actuator. B Chem.* 2016, 228, 679-687.
62. Rantala, T.; Pirttiaho, L.; Lantto, V. Simulation studies of non-ohmic conductance behaviour in SnO₂ thick-film gas sensors. *Sens. Actuator B Chem.* 1993, 16, 323-327.
63. Galán-Vidal, C. A.; Muñoz, J.; Domínguez, C.; Alegret, S. Glucose biosensor based on a reagentless graphite-epoxy screen-printable biocomposite. *Sens. Actuator B Chem.* 1997, 45, 55-62.
64. Hu, F.; Liu, T.; Pang, J.; Chu, Z.; Jin, W. Facile preparation of porous Co₃O₄ nanocubes for directly screen-printing an ultrasensitive glutamate biosensor microchip. *Sens. Actuator B Chem.* 2020, 306, 127587.
65. Burrell, M. C.; Tilley, M. G. Surface chemistry of polycarbonate film and adhesion of ultraviolet-cured inks. *J. Vac. Sci. Technol.* 1994, 12, 2507-2514.
66. Gonzalez-Macia, L.; Killard, A. Screen printing and other scalable point of care (POC) biosensor processing technologies. In *Medical Biosensors for Point of Care (POC) Applications* Elsevier: 2017; pp 69-98.
67. Kim, J.; Sempionatto, J. R.; Imani, S.; Hartel, M. C.; Barfidokht, A.; Tang, G.; Campbell, A. S.; Mercier, P. P.; Wang, J. Simultaneous monitoring of sweat and interstitial fluid using a single wearable biosensor platform. *Adv. Sci.* 2018, 5, 1800880.
68. Wilson Jr, W. C.; Boland, T. Cell and organ printing 1: protein and cell printers. *Anat. Rec.* 2003, 272, 491-496.
69. Barron, J.; Wu, P.; Ladouceur, H.; Ringeisen, B. Biological laser printing: a novel technique for creating heterogeneous 3-dimensional cell patterns. *Biomed. Microdevices* 2004, 6, 139-147.
70. Beduk, T.; Bihar, E.; Surya, S. G.; Castillo, A. N.; Inal, S.; Salama, K. N. A paper-based inkjet-printed PEDOT: PSS/ZnO sol-gel hydrazine sensor. *Sens. Actuator B Chem.* 2020, 306, 127539.

71. Calvert, P. Inkjet printing for materials and devices. *Chem. Mater.* 2001, 13, 3299-3305.
72. Hossain, S. Z.; Luckham, R. E.; Smith, A. M.; Lebert, J. M.; Davies, L. M.; Pelton, R. H.; Filipe, C. D.; Brennan, J. D. Development of a bioactive paper sensor for detection of neurotoxins using piezoelectric inkjet printing of sol-gel-derived bioinks. *Anal. Chem.* 2009, 81, 5474-5483.
73. Yoshioka, Y.; Jabbour, G. E. Inkjet printing of oxidants for patterning of nanometer-thick conducting polymer electrodes. *Adv Mater* 2006, 18, 1307-1312.
74. Pöldsalu, I.; Harjo, M.; Tamm, T.; Uibu, M.; Peikolainen, A.; Kiefer, R. Inkjet-printed hybrid conducting polymer-activated carbon aerogel linear actuators driven in an organic electrolyte. *Sens. Actuator B Chem.* 2017, 250, 44-51.
75. Tijero, M.; Díez-Ahedo, R.; Benito-Lopez, F.; Basabe-Desmonts, L.; Castro-López, V.; Valero, A. Biomolecule storage on non-modified thermoplastic microfluidic chip by ink-jet printing of ionogels. *Biomicrofluidics* 2015, 9, 044124.
76. Chang, S.; Liu, J.; Bharathan, J.; Yang, Y.; Onohara, J.; Kido, J. Multicolor organic light-emitting diodes processed by hybrid inkjet printing. *Adv Mater* 1999, 11, 734-737.
77. Liu, Y.; Li, F.; Xu, Z.; Zheng, C.; Guo, T.; Xie, X.; Qian, L.; Fu, D.; Yan, X. Efficient all-solution processed quantum dot light emitting diodes based on inkjet printing technique. *ACS Appl. Mater. Interfaces* 2017, 9, 25506-25512.
78. Jang, J.; Ha, J.; Cho, J. Fabrication of water-dispersible polyaniline-poly(4-styrenesulfonate) nanoparticles for inkjet-printed chemical-sensor applications. *Adv Mater* 2007, 19, 1772-1775.
79. Lee, H.; Harden-Chaters, W.; Han, S. D.; Zhan, S.; Li, B.; Bang, S. Y.; Choi, H. W.; Lee, S.; Hou, B.; Occhipinti, L. G. Nano-to-Microporous Networks via Inkjet Printing of ZnO Nanoparticles/Graphene Hybrid for Ultraviolet Photodetectors. *ACS Appl. Nano Mater.* 2020, 3, 4454-4464.
80. Trotter, M.; Juric, D.; Bagherian, Z.; Borst, N.; Gläser, K.; Meissner, T.; von Stetten, F. v.; Zimmermann, A. Inkjet-Printing of Nanoparticle Gold and Silver Ink on Cyclic Olefin Copolymer for DNA-Sensing Applications. *Sensors* 2020, 20, 1333.
81. Jensen, G. C.; Krause, C. E.; Sotzing, G. A.; Rusling, J. F. Inkjet-printed gold nanoparticle electrochemical arrays on plastic. Application to immunodetection of a cancer biomarker protein. *Phys. Chem. Chem. Phys.* 2011, 13, 4888-4894.
82. Creran, B.; Li, X.; Duncan, B.; Kim, C. S.; Moyano, D. F.; Rotello, V. M. Detection of bacteria using inkjet-printed enzymatic test strips. *ACS Appl. Mater. Interfaces* 2014, 6, 19525-19530.
83. Díaz-Amaya, S.; Zhao, M.; Lin, L.; Ostos, C.; Allebach, J. P.; Chiu, G. T.; Deering, A. J.; Stanciu, L. A. Inkjet Printed Nanopatterned Aptamer-Based Sensors for Improved Optical Detection of Foodborne Pathogens. *Small* 2019, 15, 1805342.

84. Godoy, N.; García-Lojo, D.; Sigoli, F.; Pérez-Juste, J.; Pastoriza-Santos, I.; Mazali, I. Ultrasensitive inkjet-printed based SERS sensor combining a high-performance gold nanosphere ink and hydrophobic paper. *Sens. Actuator B Chem.* 2020, 128412.
85. Amin, R.; Knowlton, S.; Hart, A.; Yenilmez, B.; Ghaderinezhad, F.; Katebifar, S.; Messina, M.; Khademhosseini, A.; Tasoglu, S. 3D-printed microfluidic devices. *Biofabrication* 2016, 8, 022001.
86. Bustillos, J.; Montero, D.; Nautiyal, P.; Loganathan, A.; Boesl, B.; Agarwal, A. Integration of graphene in poly (lactic) acid by 3D printing to develop creep and wear-resistant hierarchical nanocomposites. *Polym. Compos.* 2018, 39, 3877-3888.
87. Muralidharan, A.; Uzcategui, A. C.; McLeod, R. R.; Bryant, S. J. Stereolithographic 3D Printing for Deterministic Control over Integration in Dual-Material Composites. *Adv. Mater. Technol.* 2019, 4, 1900592.
88. Su, C.; Hsia, S.; Sun, Y. Three-dimensional printed sample load/inject valves enabling online monitoring of extracellular calcium and zinc ions in living rat brains. *Anal. Chim. Acta* 2014, 838, 58-63.
89. Su, C.; Peng, P.; Sun, Y. Fully 3D-printed preconcentrator for selective extraction of trace elements in seawater. *Anal. Chem.* 2015, 87, 6945-6950.
90. Lee, W.; Kwon, D.; Choi, W.; Jung, G. Y.; Au, A. K.; Folch, A.; Jeon, S. 3D-printed microfluidic device for the detection of pathogenic bacteria using size-based separation in helical channel with trapezoid cross-section. *Sci. Rep.* 2015, 5, 7717.
91. Etxebarria-Elezgarai, J.; García-Hernando, M.; Basabe-Desmonts, L.; Benito-Lopez, F. In In 3D printed high quality bechtop microfluidic devices integrating smart materials as sensors; 21st International Conference on Miniaturized Systems for Chemistry and Life Sciences, MicroTAS 2017; 2020, pp 305-306.
92. Park, J. S.; Kim, T.; Kim, W. S. Conductive cellulose composites with low percolation threshold for 3D printed electronics. *Sci. Rep.* 2017, 7, 1-10.
93. Yin, M.; Xiao, L.; Liu, Q.; Kwon, S.; Zhang, Y.; Sharma, P. R.; Jin, L.; Li, X.; Xu, B. 3D printed microheater sensor-integrated, Drug-Encapsulated microneedle patch system for pain management. *Adv. Healthc. Mater.* 2019, 8, 1901170.
94. Udoфia, E. N.; Zhou, W. 3D Printed optics with a soft and stretchable optical material. *Addit. Manuf.* 2020, 31, 100912.
95. Hinman, S. S.; McKeating, K. S.; Cheng, Q. Plasmonic sensing with 3D printed optics. *Anal. Chem.* 2017, 89, 12626-12630.
96. Dong, Y.; Min, X.; Kim, W. S. A 3-D-printed integrated PCB-based electrochemical sensor system. *IEEE Sens. J.* 2018, 18, 2959-2966.
97. Siebert, L.; Lupan, O.; Mirabelli, M.; Ababii, N.; Terasa, M.; Kaps, S.; Cretu, V.; Vahl, A.; Faupel, F.; Adelung, R. 3D-Printed chemiresistive sensor array on nanowire CuO/Cu₂O/Cu heterojunction nets. *ACS Appl. Mater. Interfaces* 2019, 11, 25508-25515.

98. Sharafeldin, M.; Jones, A.; Rusling, J. F. 3D-printed biosensor arrays for medical diagnostics. *Micromachines* 2018, 9, 394.
99. Mortimer Charles, E. Chemistry: A Conceptual Approach. 1975.
100. De Oliveira, I. M.; Pla-Roca, M.; Escriche, L.; Casabó, J.; Zine, N.; Bausells, J.; Teixidor, F.; Crespo, E.; Errachid, A.; Samitier, J. Novel all-solid-state copper (II) microelectrode based on a dithiomacrocycle as a neutral carrier. *Electrochim. Acta* 2006, 51, 5070-5074.
101. Luo, J.; Zhang, M.; Pang, D. Selective and sensitive determination of uric acid at DNA-modified graphite powder microelectrodes. *Sens. Actuator B Chem.* 2005, 106, 358-362.
102. McCarthy, P.; Rao, M.; Otto, K. Simultaneous recording of rat auditory cortex and thalamus via a titanium-based, microfabricated, microelectrode device. *J. Neural Eng.* 2011, 8, 046007.
103. Yang, H.; Rahman, M. T.; Du, D.; Panat, R.; Lin, Y. 3-D printed adjustable microelectrode arrays for electrochemical sensing and biosensing. *Sens. Actuator B Chem.* 2016, 230, 600-606.
104. Abdulbari, H. A.; Basheer, E. A. Electrochemical biosensors: electrode development, materials, design, and fabrication. *ChemBioEng Reviews* 2017, 4, 92-105.
105. Mi, S.; Xia, J.; Xu, Y.; Du, Z.; Sun, W. An integrated microchannel biosensor platform to analyse low density lactate metabolism in HepG2 cells in vitro. *RSC Adv.* 2019, 9, 9006-9013.
106. Abdolahad, M.; Taghinejad, M.; Taghinejad, H.; Janmaleki, M.; Mohajerzadeh, S. A vertically aligned carbon nanotube-based impedance sensing biosensor for rapid and high sensitive detection of cancer cells. *Lab Chip* 2012, 12, 1183-1190.
107. Cai, B.; Huang, L.; Zhang, H.; Sun, Z.; Zhang, Z.; Zhang, G. Gold nanoparticles-decorated graphene field-effect transistor biosensor for femtomolar MicroRNA detection. *Biosens. Bioelectron.* 2015, 74, 329-334.
108. Li, J.; Lee, E. Functionalized multi-wall carbon nanotubes as an efficient additive for electrochemical DNA sensor. *Sens. Actuator B Chem.* 2017, 239, 652-659.
109. Hameed, M. F. O.; Saadeldin, A. S.; Elkaramany, E. M.; Obayya, S. Silicon Nanowires for DNA Sensing. In Computational Photonic Sensors Springer: 2019; pp 321-342.
110. Lu, C.; Huang, P. J.; Liu, B.; Ying, Y.; Liu, J. Comparison of graphene oxide and reduced graphene oxide for DNA adsorption and sensing. *Langmuir* 2016, 32, 10776-10783.
111. Huber, S.; Min, C.; Staat, C.; Oh, J.; Castro, C. M.; Haase, A.; Weissleder, R.; Gleich, B.; Lee, H. Multichannel digital heteronuclear magnetic resonance biosensor. *Biosens. Bioelectron.* 2019, 126, 240-248.
112. Wang, T.; Zhou, Y.; Lei, C.; Luo, J.; Xie, S.; Pu, H. Magnetic impedance biosensor: A review. *Biosens. Bioelectron.* 2017, 90, 418-435.

113. Nakayama, S.; Atsuta, S.; Shinmi, T.; Uchiyama, T. Pulse-driven magnetoimpedance sensor detection of biomagnetic fields in musculatures with spontaneous electric activity. *Biosens. Bioelectron.* 2011, 27, 34-39.
114. Zhang, Q.; Wang, C.; Lv, Y. Luminescent switch sensors for the detection of biomolecules based on metal-organic frameworks. *Analyst* 2018, 143, 4221-4229.
115. Venkatasubramanian, A.; Lee, J.; Stavila, V.; Robinson, A.; Allendorf, M. D.; Hesketh, P. J. MOF@ MEMS: Design optimization for high sensitivity chemical detection. *Sens. Actuator B Chem.* 2012, 168, 256-262.
116. Chen, Q.; Li, X.; Min, X.; Cheng, D.; Zhou, J.; Li, Y.; Xie, Z.; Liu, P.; Cai, W.; Zhang, C. Determination of catechol and hydroquinone with high sensitivity using MOF-graphene composites modified electrode. *J Electroanal Chem* 2017, 789, 114-122.
117. Yang, C.; Denno, M. E.; Pyakurel, P.; Venton, B. J. Recent trends in carbon nanomaterial-based electrochemical sensors for biomolecules: A review. *Anal. Chim. Acta* 2015, 887, 17-37.
118. Kudr, J.; Zhao, L.; Nguyen, E. P.; Arola, H.; Nevanen, T. K.; Adam, V.; Zitka, O.; Merkoçi, A. Inkjet-printed electrochemically reduced graphene oxide microelectrode as a platform for HT-2 mycotoxin immunoenzymatic biosensing. *Biosensors and Bioelectronics* 2020, 156, 112109.
119. Chang, Y.; Venton, B. J. Optimization of graphene oxide-modified carbon-fiber microelectrode for dopamine detection. *Anal. Methods* 2020.
120. Elbahri, M.; Abdelaziz, M.; Homaeigohar, S.; Elsharawy, A.; Keshavarz Hedayati, M.; Röder, C.; El Haj Assad, M.; Abdelaziz, R. Plasmonic Metaparticles on a Blackbody Create Vivid Reflective Colors for Naked-Eye Environmental and Clinical Biodetection. *Adv Mater* 2018, 30, 1704442.
121. Cichosz, S.; Masek, A.; Zaborski, M. Polymer-based sensors: A review. *Polym. Test.* 2018, 67, 342-348.
122. Huang, J.; Li, M.; Zhang, P.; Zhang, P.; Ding, L. Temperature controlling fiber optic glucose sensor based on hydrogel-immobilized GOD complex. *Sens. Actuator B: Chem.* 2016, 237, 24-29.
123. Dong, S.; Ji, W.; Ma, Z.; Zhu, Z.; Ding, N.; Nie, J.; Du, B. Thermosensitive Fluorescent Microgels for Selective and Sensitive Detection of Fe₃ and Mn₂ in Aqueous Solutions. *ACS Appl. Polym. Mater.* 2020.
124. Shen, H.; Liu, B.; Liu, D.; Zhu, X.; Wei, X.; Yu, L.; Shen, Q.; Qu, P.; Xu, M. Lanthanide coordination polymer-based biosensor for citrate detection in urine. *Anal. Methods* 2019, 11, 1405-1409.
125. Wang, Z.; Qian, Y.; Wei, X.; Zhang, Y.; Wu, G.; Lu, X. An “on-off” electrochemiluminescence biosensor based on molecularly imprinted polymer and recycling amplifications for determination of dopamine. *Electrochim. Acta* 2017, 250, 309-319.

126. Liu, W.; Li, H.; Yu, S.; Zhang, J.; Zheng, W.; Niu, L.; Li, G. Poly (3, 6-diamino-9-ethylcarbazole) based molecularly imprinted polymer sensor for ultra-sensitive and selective detection of 17- β -estradiol in biological fluids. *Biosens. Bioelectron.* 2018, 104, 79-86.
127. Inal, S.; Rivnay, J.; Suiu, A.; Malliaras, G. G.; McCulloch, I. Conjugated polymers in bioelectronics. *Acc. Chem. Res.* 2018, 51, 1368-1376.
128. Pal, R. K.; Farghaly, A. A.; Wang, C.; Collinson, M. M.; Kundu, S. C.; Yadavalli, V. K. Conducting polymer-silk biocomposites for flexible and biodegradable electrochemical sensors. *Biosens. Bioelectron.* 2016, 81, 294-302.
129. Antensteiner, M.; Khorrami, M.; Fallahianbijan, F.; Borhan, A.; Abidian, M. R. Conducting polymer microcups for organic bioelectronics and drug delivery applications. *Adv Mater* 2017, 29, 1702576.
130. Gao, B.; Wang, X.; Li, T.; Feng, Z.; Wang, C.; Gu, Z. Gecko-Inspired Paper Artificial Skin for Intimate Skin Contact and Multisensing. *Adv. Mater. Technol.* 2019, 4, 1800392.
131. Bogue, R. Smart materials: a review of recent developments. *Assem. Autom.* 2012.
132. Lee, M. E.; Armani, A. M. Flexible UV exposure sensor based on UV responsive polymer. *ACS Sensors* 2016, 1, 1251-1255.
133. Zhao, Y.; Lei, M.; Liu, S.; Zhao, Q. Smart hydrogel-based optical fiber SPR sensor for pH measurements. *Sens. Actuator B Chem.* 2018, 261, 226-232.
134. Wang, T.; Liu, J.; Nie, F. Non-dye cell viability monitoring by using pH-responsive inverse opal hydrogels. *J. Mater. Chem. B* 2018, 6, 1055-1065.
135. Yablonovitch, E. Photonic band-gap crystals. *J. Phys. Condens. Matter* 1993, 5, 2443.
136. Endo, T.; Ozawa, S.; Okuda, N.; Yanagida, Y.; Tanaka, S.; Hatsuzawa, T. Reflectometric detection of influenza virus in human saliva using nanoimprint lithography-based flexible two-dimensional photonic crystal biosensor. *Sens. Actuator B Chem.* 2010, 148, 269-276.
137. Ben-Moshe, M.; Alexeev, V. L.; Asher, S. A. Fast responsive crystalline colloidal array photonic crystal glucose sensors. *Anal. Chem.* 2006, 78, 5149-5157.
138. Endo, T.; Ozawa, S.; Okuda, N.; Yanagida, Y.; Tanaka, S.; Hatsuzawa, T. Reflectometric detection of influenza virus in human saliva using nanoimprint lithography-based flexible two-dimensional photonic crystal biosensor. *Sens. Actuator B Chem.* 2010, 148, 269-276.
139. O'Reilly, E.; Kelly, M.; Morrin, A.; Smyth, M. R.; Killard, A. J. Chronocoulometric determination of urea in human serum using an inkjet printed biosensor. *Anal. Chim. Acta* 2011, 697, 98-102.
140. Hibbard, T.; Crowley, K.; Killard, A. J. Direct measurement of ammonia in simulated human breath using an inkjet-printed polyaniline nanoparticle sensor. *Anal. Chim. Acta* 2013, 779, 56-63.

141. Zang, F.; Fan, X. Z.; Gerasopoulos, K. D.; Ben-Yoav, H.; Brown, A. D.; Culver, J. N.; Ghodssi, R. In In Scale-down effects: Towards miniaturization of an electrochemical sensor using biomolecules; *SENSORS, 2013 IEEE*; IEEE: 2013, pp 1-4.
142. Martín, M.; Salazar, P.; Álvarez, R.; Palmero, A.; López-Santos, C.; González-Mora, J. L.; González-Elipe, A. R. Cholesterol biosensing with a polydopamine-modified nanostructured platinum electrode prepared by oblique angle physical vacuum deposition. *Sens. Actuator B Chem.* 2017, 240, 37-45.
143. Moreira, F. T.; Dutra, R. A.; Noronha, J. P.; Sales, M. G. F. Electrochemical biosensor based on biomimetic material for myoglobin detection. *Electrochim. Acta* 2013, 107, 481-487.
144. Draghici, C.; Mikhalevich, V.; Gunkel-Grabole, G.; Kowal, J.; Meier, W.; Palivan, C. G. Biomimetic planar polymer membranes decorated with enzymes as functional surfaces. *Langmuir* 2018, 34, 9015-9024.
145. Dzyadevych, S.; Arkhypova, V.; Soldatkin, A.; El'Skaya, A.; Martelet, C.; Jaffrezic-Renault, N. Amperometric enzyme biosensors: Past, present and future. *Irbm* 2008, 29, 171-180.
146. Jiang, Y.; Shi, M.; Liu, Y.; Wan, S.; Cui, C.; Zhang, L.; Tan, W. Aptamer/AuNP biosensor for colorimetric profiling of exosomal proteins. *Angew. Chem. Int.* 2017, 56, 11916-11920.
147. Jose, B.; McCluskey, P.; Gilmartin, N.; Somers, M.; Kenny, D.; Ricco, A. J.; Kent, N. J.; Basabe-Desmonts, L. Self-powered microfluidic device for rapid assay of antiplatelet drugs. *Langmuir* 2016, 32, 2820-2828.
148. Melero, C.; Kolmogorova, A.; Atherton, P.; Derby, B.; Reid, A.; Jansen, K.; Ballestrem, C. Light-Induced Molecular Adsorption of Proteins Using the PRIMO System for Micro-Patterning to Study Cell Responses to Extracellular Matrix Proteins. *JoVE* 2019, e60092.
149. Zhang, Y.; De Mets, R.; Monzel, C.; Acharya, V.; Toh, P.; Chin, J. F. L.; Van Hul, N.; Ng, I. C.; Yu, H.; Ng, S. S. Biomimetic niches reveal the minimal cues to trigger apical lumen formation in single hepatocytes. *Nat. Mater.* 2020, 1-10.
150. Khan, E. S.; Sankaran, S.; Paez, J. I.; Muth, C.; Han, M. K.; del Campo, A. Photoactivatable Hsp47: a tool to regulate collagen secretion and assembly. *Adv. Sci.* 2019, 6, 1801982.
151. Pavlou, G.; Touquet, B.; Vigetti, L.; Renesto, P.; Bougdour, A.; Debarre, D.; Balland, M.; Tardieu, I. Coupling Polar Adhesion with Traction, Spring and Torque Forces Allows High Speed Helical Migration of the Protozoan Parasite Toxoplasma. *ACS Nano* 2020.
152. van Dongen, S. F.; Maiuri, P.; Marie, E.; Tribet, C.; Piel, M. Triggering cell adhesion, migration or shape change with a dynamic surface coating. *Adv Mater* 2013, 25, 1687-1691.

153. Koirala, D.; Shrestha, P.; Emura, T.; Hidaka, K.; Mandal, S.; Endo, M.; Sugiyama, H.; Mao, H. Single-Molecule Mechanochemical Sensing Using DNA Origami Nanostructures. *Angew. Chem.* 2014, 126, 8275-8279.
154. Sajfutdinow, M.; Uhlig, K.; Prager, A.; Schneider, C.; Abel, B.; Smith, D. Nanoscale patterning of self-assembled monolayer (SAM)-functionalised substrates with single molecule contact printing. *Nanoscale* 2017, 9, 15098-15106.
155. Spitzberg, J. D.; Zrehen, A.; van Kooten, X. F.; Meller, A. Plasmonic-Nanopore Biosensors for Superior Single-Molecule Detection. *Adv Mater* 2019, 31, 1900422.
156. Sun, H.; Jiang, Z.; Xin, N.; Guo, X.; Hou, S.; Liao, J. Efficient Fabrication of Stable Graphene-Molecule-Graphene Single-Molecule Junctions at Room Temperature. *ChemPhysChem* 2018, 19, 2258-2265.
157. Lum, W.; Gautam, D.; Chen, J.; Sagle, L. B. Single molecule protein patterning using hole mask colloidal lithography. *Nanoscale* 2019, 11, 16228-16234.
158. Chen, Z.; Lin, Y.; Ma, X.; Guo, L.; Qiu, B.; Chen, G.; Lin, Z. Multicolor biosensor for fish freshness assessment with the naked eye. *Sens. Actuator B Chem.* 2017, 252, 201-208.
159. Hou, L.; Qin, Y.; Li, J.; Qin, S.; Huang, Y.; Lin, T.; Guo, L.; Ye, F.; Zhao, S. A ratiometric multicolor fluorescence biosensor for visual detection of alkaline phosphatase activity via a smartphone. *Biosens. Bioelectron.* 2019, 143, 111605.
160. Peng, T.; Wang, J.; Zhao, S.; Zeng, Y.; Zheng, P.; Liang, D.; Mari, G. M.; Jiang, H. Highly luminescent green-emitting Au nanocluster-based multiplex lateral flow immunoassay for ultrasensitive detection of clenbuterol and ractopamine. *Anal. Chim. Acta* 2018, 1040, 143-149.
161. Karami, C.; Mehr, S. Y.; Deymehkar, E.; Taher, M. A. Naked eye detection of Cr 3 and Co 2 ions by Gold nanoparticle modified with azomethine. *Plasmonics* 2018, 13, 537-544.
162. Lobnik, A.; Turel, M.; Urek, Š Optical chemical sensors: design and applications; InTech Rijeka, Croatia: 2012.
163. Nam, J.; Jung, I.; Kim, B.; Lee, S.; Kim, S.; Lee, K.; Shin, D. A colorimetric hydrogel biosensor for rapid detection of nitrite ions. *Sens. Actuator B Chem.* 2018, 270, 112-118.
164. Fraser, L. A.; Kinghorn, A. B.; Dirkzwager, R. M.; Liang, S.; Cheung, Y.; Lim, B.; Shiu, S. C.; Tang, M. S.; Andrew, D.; Manitta, J. A portable microfluidic Aptamer-Tethered Enzyme Capture (APTEC) biosensor for malaria diagnosis. *Biosens. Bioelectron.* 2018, 100, 591-596.
165. Liu, X.; Huang, D.; Lai, C.; Qin, L.; Zeng, G.; Xu, P.; Li, B.; Yi, H.; Zhang, M. Peroxidase-Like Activity of Smart Nanomaterials and Their Advanced Application in Colorimetric Glucose Biosensors. *Small* 2019, 15, 1900133.

166. Kangas, M. J.; Burks, R. M.; Atwater, J.; Lukowicz, R. M.; Williams, P.; Holmes, A. E. Colorimetric sensor arrays for the detection and identification of chemical weapons and explosives. *Crit. Rev. Anal. Chem.* 2017, 47, 138-153.
167. Natarajan, S.; Su, F.; Jayaraj, J.; Shah, M. I. I.; Huang, Y. A paper microfluidics-based fluorescent lateral flow immunoassay for point-of-care diagnostics of non-communicable diseases. *Analyst* 2019, 144, 6291-6303.
168. Dodeigne, C.; Thunus, L.; Lejeune, R. Chemiluminescence as diagnostic tool. A review. *Talanta* 2000, 51, 415-439.
169. Inpota, P.; Nacapricha, D.; Sunintaboon, P.; Sripumkhai, W.; Jeamsaksiri, W.; Wilairat, P.; Chantiwas, R. Chemiluminescence detection with microfluidics for innovative in situ measurement of unbound cobalt ions in dynamic equilibrium with bound ions in binding study with polyethyleneimine and its functionalized nanoparticles. *Talanta* 2018, 188, 606-613.
170. Al Mughairey, B.; Al-Lawati, H. A.; Suliman, F. O. Characterization and application of nanocolloidal Mn (IV) in a chemiluminescence system for estimating the total phenolic content in pomegranate juices using a nanodroplet microfluidics platform. *Sens. Actuator B Chem.* 2018, 277, 517-525.
171. Hu, B.; Li, J.; Mou, L.; Liu, Y.; Deng, J.; Qian, W.; Sun, J.; Cha, R.; Jiang, X. An automated and portable microfluidic chemiluminescence immunoassay for quantitative detection of biomarkers. *Lab Chip* 2017, 17, 2225-2234.
172. Zeng, Z.; Zhang, K.; Wang, W.; Xu, W.; Zhou, J. Portable electrowetting digital microfluidics analysis platform for chemiluminescence sensing. *IEEE Sens. J.* 2016, 16, 4531-4536.
173. Li, M.; Cushing, S. K.; Wu, N. Plasmon-enhanced optical sensors: a review. *Analyst* 2015, 140, 386-406.
174. Fu, C.; Hu, C.; Liu, Y.; Xu, S.; Xu, W. Bioidentification of biotin/avidin using surface plasmon resonance and surface-enhanced Raman scattering (SPR-SERS) spectroscopy. *Anal. Methods* 2012, 4, 3107-3110.
175. Barroso, J.; Ortega-Gomez, A.; Calatayud-Sanchez, A.; Zubia, J.; Benito-Lopez, F.; Villatoro, J.; Basabe-Desmonts, L. Selective ultrasensitive optical fiber nanosensors based on plasmon resonance energy transfer. *ACS sensors* 2020.
176. Moitra, P.; Alafeef, M.; Dighe, K.; Frieman, M.; Pan, D. Selective Naked-Eye Detection of SARS-CoV-2 Mediated by N Gene Targeted Antisense Oligonucleotide Capped Plasmonic Nanoparticles. *ACS nano* 2020.
177. Ismail, M.; Khan, M.; Akhtar, K.; Seo, J.; Khan, M. A.; Asiri, A. M.; Khan, S. B. Phytosynthesis of silver nanoparticles; naked eye cellulose filter paper dual mechanism sensor for mercury ions and ammonia in aqueous solution. *J. Mater. Sci. Mater. Electron.* 2019, 30, 7367-7383.
178. Miyazaki, C. M.; Kinahan, D. J.; Mishra, R.; Mangwanya, F.; Kilcawley, N.; Ferreira, M.; Ducrée, J. Label-free, spatially multiplexed SPR detection of immunoassays on a

- highly integrated centrifugal Lab-on-a-Disc platform. *Biosens. Bioelectron.* 2018, 119, 86-93.
179. Špringer, T.; Piliarik, M.; Homola, J. Surface plasmon resonance sensor with dispersionless microfluidics for direct detection of nucleic acids at the low femtomole level. *Sens. Actuator B Chem.* 2010, 145, 588-591.
180. Dipalo, M.; Melle, G.; Lovato, L.; Jacassi, A.; Santoro, F.; Caprettini, V.; Schirato, A.; Alabastri, A.; Garoli, D.; Bruno, G. Plasmonic meta-electrodes allow intracellular recordings at network level on high-density CMOS-multi-electrode arrays. *Nat. Nanotechnol.* 2018, 13, 965-971.
181. Wilson, M. S. Electrochemical immunosensors for the simultaneous detection of two tumor markers. *Anal. Chem.* 2005, 77, 1496-1502.
182. Ding, J.; Qin, W. Recent advances in potentiometric biosensors. *TrAC Trends in Anal. Chem.* 2020, 124, 115803.
183. Ebrahimi, E.; Yazdian, F.; Amoabediny, G.; Shariati, M. R.; Janfada, B.; Saber, M. A microbial biosensor for hydrogen sulfide monitoring based on potentiometry. *Process Biochemistry* 2014, 49, 1393-1401.
184. Rotariu, L.; Bala, C.; Magearu, V. New potentiometric microbial biosensor for ethanol determination in alcoholic beverages. *Anal. Chim. Acta* 2004, 513, 119-123.
185. Yang, Z.; Zhang, C.; Zhang, J.; Bai, W. Potentiometric glucose biosensor based on core-shell Fe₃O₄-enzyme-polypyrrole nanoparticles. *Biosens. Bioelectron.* 2014, 51, 268-273.
186. Draghi, P. F.; Fernandes, J. C. B. Label-free potentiometric biosensor based on solid-contact for determination of total phenols in honey and propolis. *Talanta* 2017, 164, 413-417.
187. Gao, W.; Song, J. Towards surface acid-base property of the carboxylic multi-walled carbon nanotubes by zero current potentiometry. *Electrochim. Commun.* 2009, 11, 1285-1288.
188. Wu, N.; Gao, W.; He, X.; Chang, Z.; Xu, M. Direct electrochemical sensor for label-free DNA detection based on zero current potentiometry. *Biosens. Bioelectron.* 2013, 39, 210-214.
189. Rivnay, J.; Ramuz, M.; Leleux, P.; Hama, A.; Huerta, M.; Owens, R. M. Organic electrochemical transistors for cell-based impedance sensing. *Appl. Phys. Lett.* 2015, 106, 8_1.
190. Steinem, C.; Janshoff, A.; Galla, H.; Sieber, M. Impedance analysis of ion transport through gramicidin channels incorporated in solid supported lipid bilayers. *Bioelectrochem. Bioenerget.* 1997, 42, 213-220.
191. Bird, C.; Kirstein, S. Real-time, label-free monitoring of cellular invasion and migration with the xCELLigence system. *Nat. Methods* 2009, 6, v-vi.

192. Stolwijk, J. A.; Wegener, J. STOLWIJK, Judith A.; WEGENER, Joachim. Impedance-Based Assays Along the Life Span of Adherent Mammalian Cells In Vitro: From Initial Adhesion to Cell Death. En Label-Free Monitoring of Cells in vitro. Springer, Cham, 2019. p. 1-75.
193. Lee, J. A.; Hwang, S.; Kwak, J.; Park, S. I.; Lee, S. S.; Lee, K. An electrochemical impedance biosensor with aptamer-modified pyrolyzed carbon electrode for label-free protein detection. *Sens. Actuator B: Chem.* 2008, 129, 372-379.
194. Pohanka, M. Overview of piezoelectric biosensors, immunosensors and DNA sensors and their applications. *Materials* 2018, 11, 448.
195. Skládal, P. Piezoelectric biosensors. *TrAC Trends Anal. Chem.* 2016, 79, 127-133.
196. Fohlerová, Z.; Turánek, J.; Skládal, P. The cell adhesion and cytotoxicity effects of the derivate of vitamin E compared for two cell lines using a piezoelectric biosensor. *Sens. Actuator B Chem.* 2012, 174, 153-157.
197. Jin, Y.; Xie, Y.; Wu, K.; Huang, Y.; Wang, F.; Zhao, R. Probing the dynamic interaction between damaged DNA and a cellular responsive protein using a piezoelectric mass biosensor. *ACS Appl. Mater. Interfaces* 2017, 9, 8490-8497.
198. Hussain, M.; Northoff, H.; Gehring, F. K. QCM-D providing new horizon in the domain of sensitivity range and information for haemostasis of human plasma. *Biosens. Bioelectron.* 2015, 66, 579-584.
199. Asai, N.; Shimizu, T.; Shingubara, S.; Ito, T. Fabrication of highly sensitive QCM sensor using AAO nanoholes and its application in biosensing. *Sens. Actuator B Chem.* 2018, 276, 534-539.
200. Lei, Y.; Zhao, T.; He, H.; Zhong, T.; Guan, H.; Xing, L.; Liu, B.; Xue, X. A self-powered electronic-skin for detecting CRP level in body fluid based on the piezoelectric-biosensing coupling effect of GaN nanowire. *Smart Mater. Struct.* 2019, 28, 105001.
201. Gogurla, N.; Roy, B.; Kim, S. Self-powered artificial skin made of engineered silk protein hydrogel. *Nano Energy* 2020, 105242.
202. Chung, S. Y.; Lee, H.; Lee, T. I.; Kim, Y. S. A wearable piezoelectric bending motion sensor for simultaneous detection of bending curvature and speed. *Rsc Adv.* 2017, 7, 2520-2526.
203. Wang, X.; Song, W.; You, M.; Zhang, J.; Yu, M.; Fan, Z.; Ramakrishna, S.; Long, Y. Bionic single-electrode electronic skin unit based on piezoelectric nanogenerator. *Acs Nano* 2018, 12, 8588-8596.
204. Nabaei, V.; Chandrawati, R.; Heidari, H. Magnetic biosensors: Modelling and simulation. *Biosens. and Bioelectron.* 2018, 103, 69-86.
205. Krishna, V. D.; Wu, K.; Perez, A. M.; Wang, J. Giant magnetoresistance-based biosensor for detection of influenza A virus. *Front. Microbiol.* 2016, 7, 400.
206. Nagesetti, A.; Rodzinski, A.; Stimpson, E.; Stewart, T.; Khanal, C.; Wang, P.; Guduru, R.; Liang, P.; Agoulnik, I.; Horstmyer, J. Multiferroic coreshell magnetoelectric

- nanoparticles as NMR sensitive nanoprobes for cancer cell detection. *Sci. Rep.* 2017, 7, 1-9.
207. Jordan, A.; Scholz, R.; Wust, P.; Fähling, H.; Felix, R. Magnetic fluid hyperthermia (MFH): Cancer treatment with AC magnetic field induced excitation of biocompatible superparamagnetic nanoparticles. *J Magn Magn Mater* 1999, 201, 413-419.
208. Das, P.; Colombo, M.; Prosperi, D. Recent advances in magnetic fluid hyperthermia for cancer therapy. *Colloid Surf. B* 2019, 174, 42-55.
209. Arruebo, M.; Fernández-Pacheco, R.; Ibarra, M. R.; Santamaría, J. Magnetic nanoparticles for drug delivery. *Nano today* 2007, 2, 22-32.
210. Gao, X.; Zhai, M.; Guan, W.; Liu, J.; Liu, Z.; Damirin, A. Controllable synthesis of a smart multifunctional nanoscale metal-organic framework for magnetic resonance/optical imaging and targeted drug delivery. *ACS Appl. Mater. Interfaces* 2017, 9, 3455-3462.
211. Rohrer, M.; Bauer, H.; Mintorovitch, J.; Requardt, M.; Weinmann, H. Comparison of magnetic properties of MRI contrast media solutions at different magnetic field strengths. *Invest. Radiol.* 2005, 40, 715-724.
212. Du, Y.; Liu, X.; Liang, Q.; Liang, X.; Tian, J. Optimization and design of magnetic ferrite nanoparticles with uniform tumor distribution for highly sensitive MRI/MPI performance and improved magnetic hyperthermia therapy. *Nano letters* 2019, 19, 3618-3626.
213. Xi, H.; Qian, X.; Lu, M.; Mei, L.; Rupprecht, S.; Yang, Q. X.; Zhang, Q. A room temperature ultrasensitive magnetoelectric susceptometer for quantitative tissue iron detection. *Sci. Rep.* 2016, 6, 29740.
214. Johnson, M. Introduction to magnetoelectronics. In *Magnetoelectronics* Elsevier: 2004; pp 1-65.
215. Melzer, M.; Kaltenbrunner, M.; Makarov, D.; Karnaushenko, D.; Karnaushenko, D.; Sekitani, T.; Someya, T.; Schmidt, O. G. Imperceptible magnetoelectronics. *Nat. Commun.* 2015, 6, 1-8.
216. Makarov, D.; Melzer, M.; Karnaushenko, D.; Schmidt, O. G. Shapeable magnetoelectronics. *Appl. Phys. Rev.* 2016, 3, 011101.
217. Sagar, R. U. R.; Galluzzi, M.; García-Peña, A.; Bhat, M. A.; Zhang, M.; Stadler, F. J. Large unsaturated room temperature negative magnetoresistance in graphene foam composite for wearable and flexible magnetoelectronics. *Nano Research* 2019, 12, 101-107.
218. Ramanathan, K.; Danielsson, B. Principles and applications of thermal biosensors. *Biosens. Bioelectron.* 2001, 16, 417-423.
219. Xu, N.; Bai, J.; Peng, Y.; Qie, Z.; Liu, Z.; Tang, H.; Liu, C.; Gao, Z.; Ning, B. Pretreatment-free detection of diazepam in beverages based on a thermometric biosensor. *Sens. Actuator B Chem.* 2017, 241, 504-512.

220. Yakovleva, M.; Buzas, O.; Matsumura, H.; Samejima, M.; Igarashi, K.; Larsson, P.; Gorton, L.; Danielsson, B. A novel combined thermometric and amperometric biosensor for lactose determination based on immobilised cellobiose dehydrogenase. *Biosens. Bioelectron.* 2012, 31, 251-256.
221. Wang, Z.; Kimura, M.; Ono, T. Manufacturing and characterization of simple cantilever thermal biosensor with Si-Metal thermocouple structure for enzymatic reaction detection. *Thermochim. Acta* 2018, 668, 110-115.
222. Bari, S. M. I.; Reis, L. G.; Nestorova, G. G. Calorimetric sandwich-type immunosensor for quantification of TNF- α . *Biosens. Bioelectron.* 2019, 126, 82-87.
223. Gaddes, D.; Reeves, W. B.; Tadigadapa, S. Calorimetric biosensing system for quantification of urinary creatinine. *ACS sensors* 2017, 2, 796-802.
224. Kazura, E.; Mernaugh, R.; Baudenbacher, F. A Capillary-Perfused, Nanocalorimeter Platform for Thermometric Enzyme-Linked Immunosorbent Assay with Femtomole Sensitivity. *Biosensors* 2020, 10, 71.
225. Wang, Z.; Kimura, M.; Inomata, N.; Ono, T. In In A freestanding microfluidic-based thermocouple biosensor for enzyme-catalyzed reaction analysis; 2016 IEEE 11th Annual International Conference on Nano/Micro Engineered and Molecular Systems (NEMS); IEEE: 2016, pp 58-61.

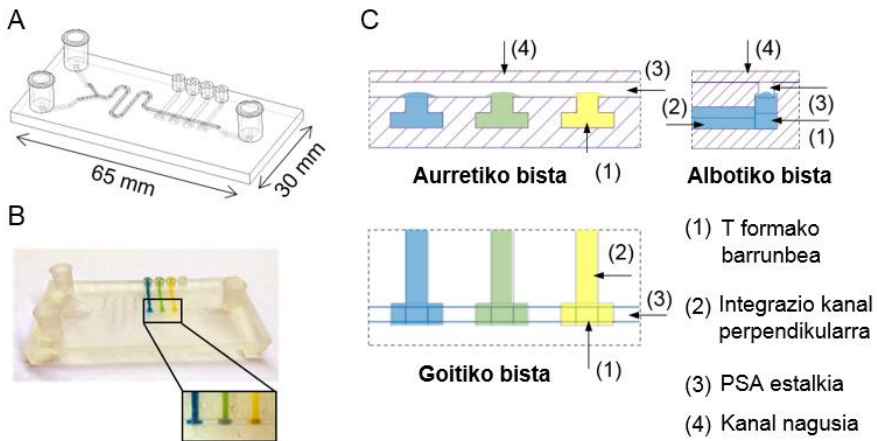
II

Material Funtzional Polimerikoen Integrazioa 3D Inprimaketaz Fabrikatutako Gailu Mikrofluidikoetan

Kapitulu honek gailu mikrofluidikoetan material funtzionalak integratzeko arkitektura kontzeptu berria dakar, 3D inprimaketa konbentzionalez eginiko egitura espezifikoak eta *in situ* polimerizazioa oinarri. Proposamen honek material funtzional polimerikoen integrazio egonkorra ahalbidetzen du gailu mikrofluidikoen posizio konkretuetan, muntaian zehar eman ohi diren erroreak ekidinez. Metodo hau balioztatzeko, 3D inprimaketaz fabrikatutako gailu mikrofluidiko bateko kanal nagusian, ionogelez osatutako lau sentsore integratu ziren pH detekzioaren irakurketarako barra-kode kolorimetriko bat lortuz. Erabilitako arkitekturak material funtzionalen atxikipena areagotu zuen kanal mikrofluidikoan, ionogelen konposizio kimikoak eraginik izan gabe.

*Kapitulu honen zatiak hurrengoan publikatuak izan dira: Etxebarria-Elezgarai, J., Garcia-Hernando, M., Basabe-Desmonts, L., & Benito-Lopez, F. 3D printed high quality benchtop microfluidic devices integrating smart materials as sensors, paper presented at the 21th International Conference on Miniaturized Systems for Chemistry and Life Sciences, Micro-TAS 2017, 2020, pp. 305 – 306.

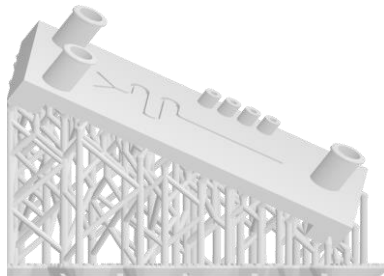
II.1 Eskema nagusia



II.1. irudia. A) Gailu mikrofluidikoaren 3D diseinua. B) 3D inprimaketaz fabrikatutako gailuaren argazkia pH detekziorako ionogelak integratuta. C) Integrazio sistemaren irudikapena, kanal mikrofluidiko nagusia, T formako barrunbeak eta integrazio kanal perpendikularrak (urreko biak konektatz) eta presioari sentikorra den itsasgarria (PSA), adieraziz.

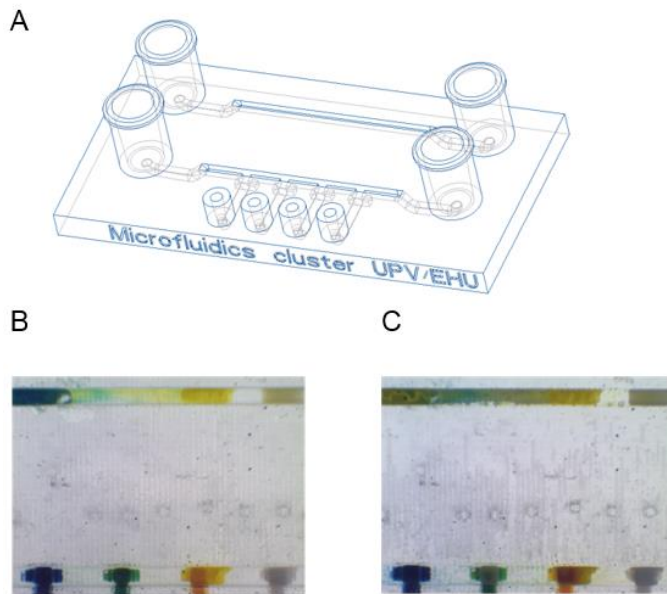
II.2 Emaitzak

II.2.1 Gailu mikrofluidikoaren fabrikazioa



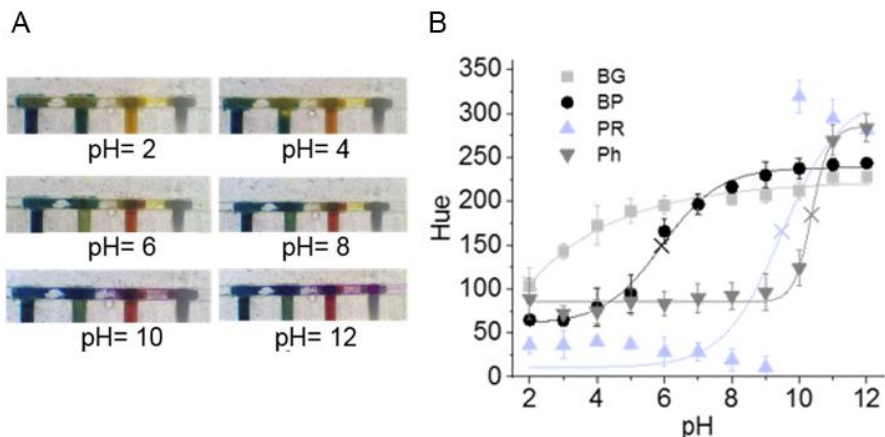
II.2. irudia. Inprimatutako eredu baten irudia, euskarri estrukturak eta ereduaren orientazio aproposa adieraziz. Euskarriek eraikitze plataformarekiko hurbilen dauden gailuaren behe geruzen konpresio tentsioak ekiditen dituzte. Eredua estruktura kritikoenak eta barne kanal luzeenak gorantz jarrita ageri dira, polimerizatu gabeko erretxina drainatu dadin.

II.2.2 pH detekziorako ionogel sentsoreen integrazioa 3D inprimaketaz egindako gailu mikrofluidikoan



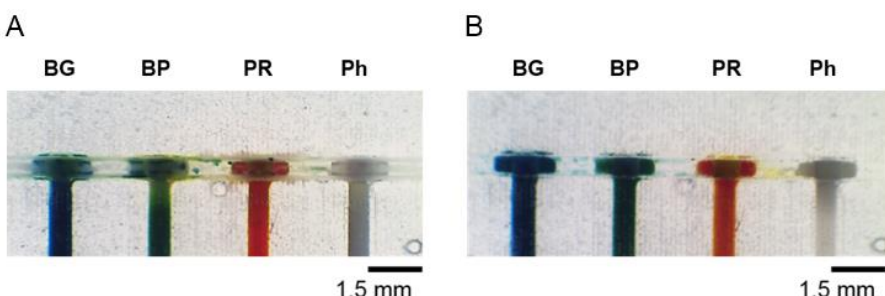
II.3. irudia. A) Gailu mikrofluidikoaren 3D ereduaren irudikapena, konparazio helburu diren bi kanalak erakutsiz: goian, kanal laukizuzen simplea eta behean, T formako integrazio egiturako kanala. B) Materialen integrazioa adierazten duen irudia behin polimerizazioa gauzatuta, ur distilatuarekin garbitu eta gero. C) Materialen integrazioa azaltzen duen irudia 2 minutu igaro ondoren $600 \mu\text{l min}^{-1}$ fluxuaren menpe (pH 6).

II.2.3 pH detekzioa gailu mikrofluidiko hibrido integratua erabiliz



II.4. irudia. A) Gailu mikrofluidikoan integraturiko lau ionogel sentsoreren irudia, pH 2-12 tartean sei pH balio ezberdinetarako. Sentsore bakoitzak pH indikatzaile bat dauka gehituta sentsore funtzioa emateko, ezkerretik eskuinera, bromokresol berdea (BG), bromokresol morea (BP), fenol gorria (PR) eta fenolftaleina (Ph). B) Ionogel sentsore bakoitzerako Hue (H) balioen irudikapen grafikoa pH 2-12 tarteko pH balio desberdinetarako. Errore barrak $n = 3$ laginen bataz bestekoaren desbiderapen estandarrari dagozkie. (X) ionogel bakoitzaren pK_a balioari dagokio, ikusi 3.2.5. atala.

II.2.4 3D gailu mikrofluidikoaren pH detekzio ahalmenaren egiaztapena



II.5. irudia. A) Gailu mikrofluidikoan integraturako pH sentsoreez osatutako

barra-kode kolorimetrikoaren argazkia, lau sentsoreak 15 minutuz ur distilatuan hidratatu ondoren. B) Gailu mikrofluidikoan integratutako pH sentsoreez osatutako barra-kode kolorimetrikoaren argazkia HCl eta NaOH arteko erreakzio ekimolarra serpentinean burutu eta produktua ionogel sentsore ataletik pasatu eta gero.

Disoluzioaren pH balioa funtzi sigmoidala aplikatuz lortu zen, pH indikatzileen jokabide sigmoidala dela eta, $HI \rightleftharpoons H^+ + I^-$, pK_a kontretu batekin.

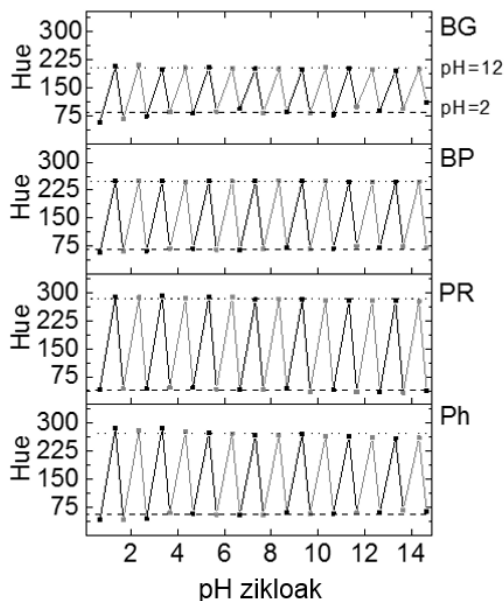
$$pH = pK_a + \log\left(\frac{[I^-]}{[HI]}\right)$$

II.1. taula. BG, BP, PR eta Ph kalibrazio kurben datuak.

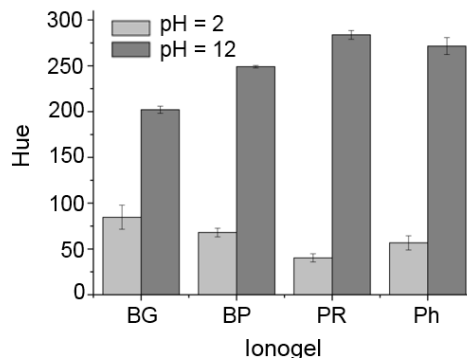
Egokitasun koefizientea	BG	BP	PR	Ph
A	-303402.4	59.9	10.7	86.99
B	222.6	238.5	319.0	284.7
C	-19.3	5.9	9.5	10.4
D	0.16	0.50	0.50	1.66
R^2	0.9615	0.9902	-	0.9887
pka	2	5.9	9.5	10.4
Hue (azido/base erreakzioa)	211	206	25	87
pH (solver)	7.5	7.2	6.9	6.8

Emaitzan arabera, MATLAB-ekin lortutako pH balioa hurrengoa izan zen sentsore desberdinatarako: 7.5 BG, 7.2 BP, 6.9 PR eta 6.8 Ph, hauen bataz bestekoa 7.1 izanik. Neurtutako balio hau, pH neurtzaile komertzial batekin lortutakoarekin konparatuz (pH 7.0), sentsore honen zehaztasuna 0.1 izan zen.

II.2.5 Sentsore mikrofluidikoaren berrerabilera



II.6. irudia. pH 2 eta pH 12 duten disoluzioak sentsorean zehar 14 aldiz pasatzean lortutako Hue balioen irudikapen grafikoa (ziklo bat soluzio azidoa eta gero basikoa pasatzeari dagokio). Ionogel sentsoreak soluzio bakoitzarekin kontaktuan 2 minuto egon eta gero lortu ziren Hue balioak, BG, BP, PR eta Ph sentsoreen kolorea azalera guztian zehar homogeneoa izateko. Marradun eta puntudun zuzenek ziklo bakoitzean sentsore bakoitzak emandako Hue balioaren bataz bestekoa adierazten dute pH 2 eta pH 12 neurketetarako, hurrenez hurren.



II.7. irudia. pH 2 eta pH 12 neurketetarako errepikagarritasun probak 14 ziklotan zehar. Errore barra $n = 3$ laginen bataz bestekoaren desbiderapen estandarrari dagozkie.

II.3 Ondorioak

Kapitulu honetan proposatutako estrategiak material funtzionalen integrazioa du helburu, 3D inprimaketaz fabrikatutako gailu mikrofluidikoetan. Estrategia honek arkitektura espezifiko bat eta material funtzionalen *in situ* polimerizazioa konbinatzen ditu, 3D inprimaketaz fabrikatutako gailu mikrofluidikoetan material funtzionalak (kasu honetan pH sentsoretzat jarduteko prestatutako ionogelak) integratzeko. Bereziki azpimarragarriena da, honi esker material funtzionalen integrazio prozesua erraztu egiten dela, posizio zehaztapenik galdu gabe, eta gainera erabiltzaileak ez duela gaitasun berezirik izan behar, edozein adar zientifikoko erabiltzaileek teknika hau erabiltzeko gai izatea ahalbidetuz.

Diseinatutako arkitekturak erakusten duen aingura fisiko ahalmenari esker, ionogel sentsoreen atxikipena areagotu egin zen, kanalaren gainazalari inolako tratamendu kimiko edo funtzionalizaziorik egin beharrik gabe. Mikrosentsoreen posizioari dagokionez egonkortasuna eta zehaztasuna bermatzea lortu zen.

Gainera, sentsoreen dimentsio errepikagarriek mutaia akatsak ekidin eta sentsoreen funtzionamendu eta seinalearen interpretazioa hobetu zuten. Bestalde, proposatutako arkitektura espezifikoari esker, material funtzionalak *in situ* polimeriza daitezke (adibidez argi ultramore bidez), 3D inprimagailuetan aldaketak egin beharrik gabe, horrek dakartzan kostu eta esfortzuak ekidinez. Hori horrela, integrazioaren frogapena burutu zen lau pH sentsore optiko ezberdin -konposizio ezberdinarekin- miniaturizatuz eta integratuz. Sentsore bakoitza pH tarte ezberdin batean erantzuteko diseinatu zen, lauak konbinatzuz, pHa 2 - 12 tartean detektatu ahal izateko.

Mikrokanal batean sentsore anitz integratu ahal izateak multiplexatzeko aukera ematen du. Baino proposatutako sistema honen aukerak hemendik haratago doaz. Izan ere, diseinuan aldaketa txikiak eginez material funtzional ugari integratu deitezke, sentsore funtziotzaz gain aktuatzaire elementuak ere integratzea ahalbidetuz. Elementu hauetako bat minimizatu eta integratzeko gaitasuna elementuaren beraren eta 3D inprimagailuaren ezaugarrien araberakoa izango da, izan ere, sentsore edo aktuatzaire mota bakoitzak funtzionaltasun egokia bermatzen duen miniturizazio maximo bat agertzen du.

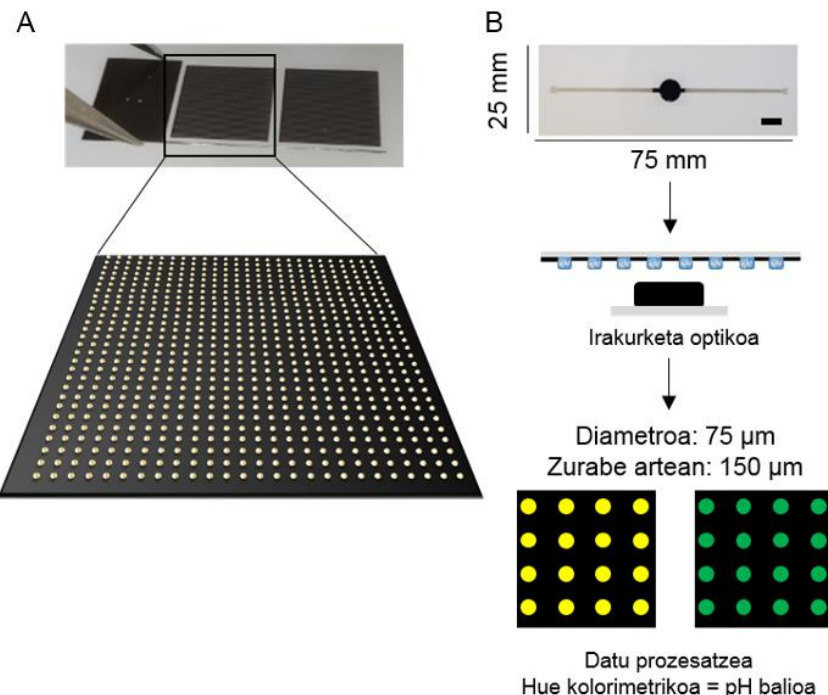
Azkenik, erabilitako fabrikazioak 3D inprimaketa duenez oinarri, hurrengo abantailak aurkezten ditu: fabrikazio azkarra, kostu murrizpena eta beraz, fabrikazio prozesuaren efizientziaren areagotzea, eta geometria konplexuak era errazean fabrikatzeko ahalmena, prototipoen fabrikaziorako diseinuaren optimizazioa erraztuz. Guzti honek, aurretik aipatutako integrazioaren simplifikazioari lotuta, prototipotik produkturako trantsizioaren azelerazioa dakar, arrazoizko kostu batekin.

III

Mikrosentsore Anitzeko Formakuntzak Gauzatzeko “Mikro Irekitzedun Formakuntza” Substratua

Lab-on-a-Chip gailuen garapenak askotan arkitektura mikrofluidikoen barnean sentsoreak integratzea eskatzen du. Hori dela eta, sentsore mota eta sentsore arkitektura egokien garapena nahitaezkoa da. Bereziki, polimeroak etorkizun handiko materialak dira sentsore modura jarduteko, fabrikazio protokolo merke eta azkarra ahalbidetu eta gailu mikrofluidikoetan integratzeko potentzial handia dutelako. Kapitulu honek mikrosentsore ugariz osatutako sentsore-matrizeak fabrikatzeko metodologia azaltzen du, argiz polimeriza daitezkeen polimeroak sentsoretzat erabiliz. Mylar® fotomaskarak erabili ziren substratutzat fabrikazio zuzena lortzeko, mikro-irekitze formakuntza izena harturik. Honen frogapena pH detekziorako ionogel mikrosentsore kolorimetrikoak erabiliz gauzatu zen. Ikuspuntu berritzaire honek lab-on-a-chip gailuetan integratu daitezkeen sentsore kimikoak fabrikatzeko potentziala dauka.

III. 1 Eskema nagusia

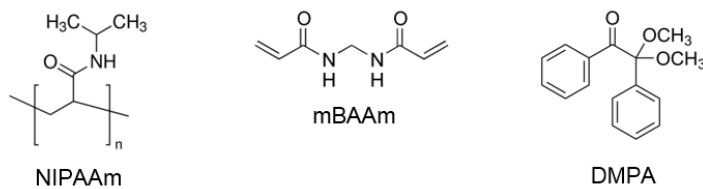


III.1. irudia. A) Mylar® fotomaskararen irudia, $D = 75 \mu\text{m}$ diametroko zirkulu gardenez osatutako matrize patroiarekin. B) Goian, gailu mikrofluidikoan integratutako mikrosentsoreen argazkia. Zirkuluaren diametroa 1 cm eta kanalaren zabalera 1 mm da. Erregela 10 mm. Erdian, mikrosentsoreak dituen substratuaren irakurketa optikoa. Behean, mikrosentsore formakuntzaren irudikapena bi pH-ren detekziorako (horia pH azidoa, berdea pH basikoa).

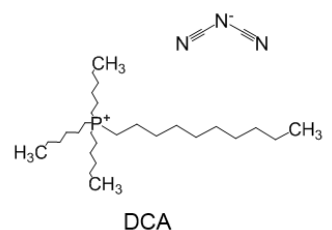
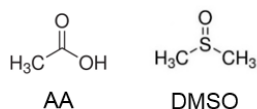
III.2 Emaitzak

III.2.1 Mikrozutabe formakuntzaren fabrikazioa

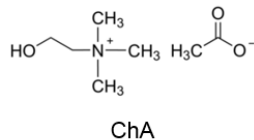
A



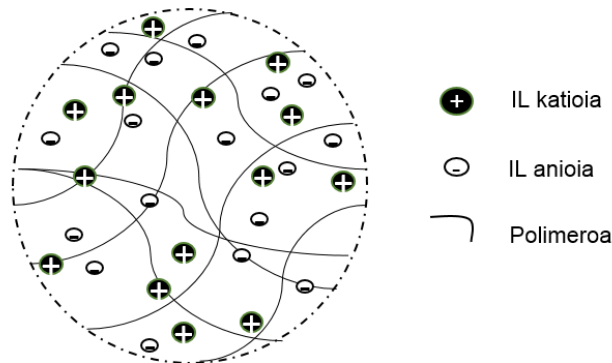
Disolbatzaile konbentzionalak



ILs

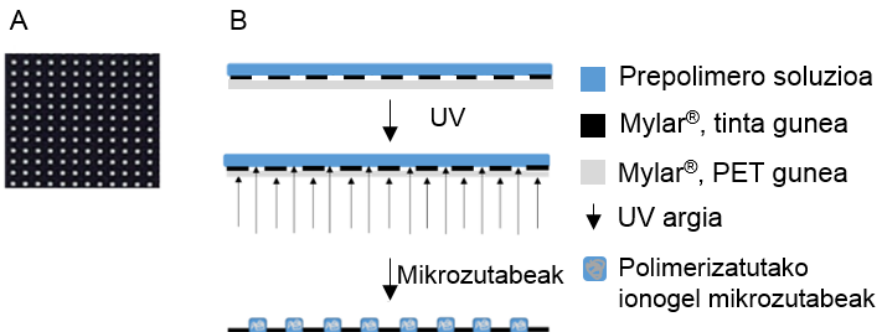


B

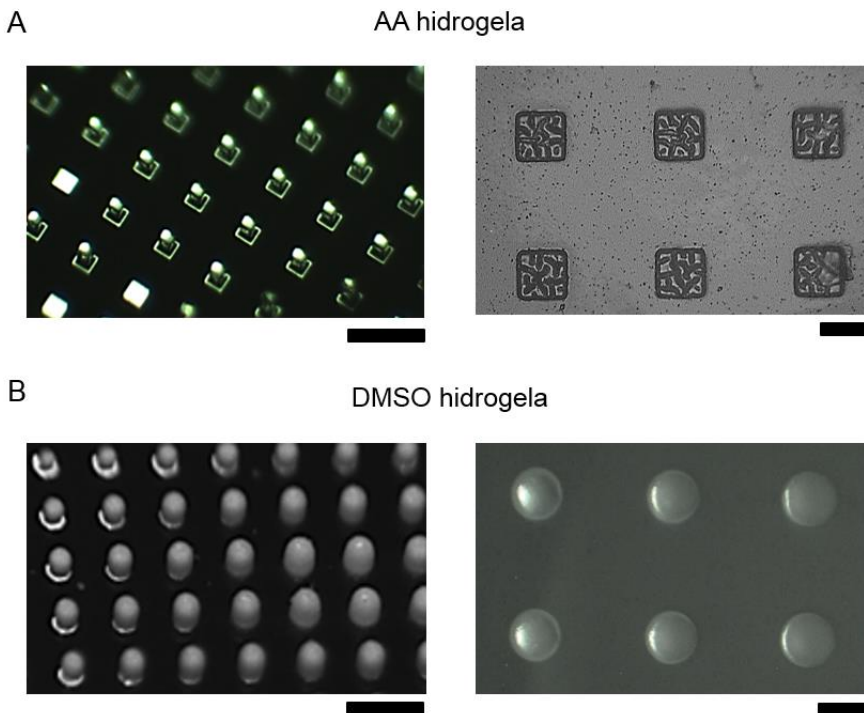


III.2. irudia. A) Polimero ezberdinez egindako mikrozutabeak osatzeko matrize polimerikoen osagaien eta disolbatzaileen molekulen eskema: poli(N-isopropilakrilamida) (NIPAAm, monomeroa), N,N'-Metilenebisakrilamida (mBAAm, elkargurutzatzalea), 2,2-dimetoxi-2-fenilazetofenona (DMPA, foto-

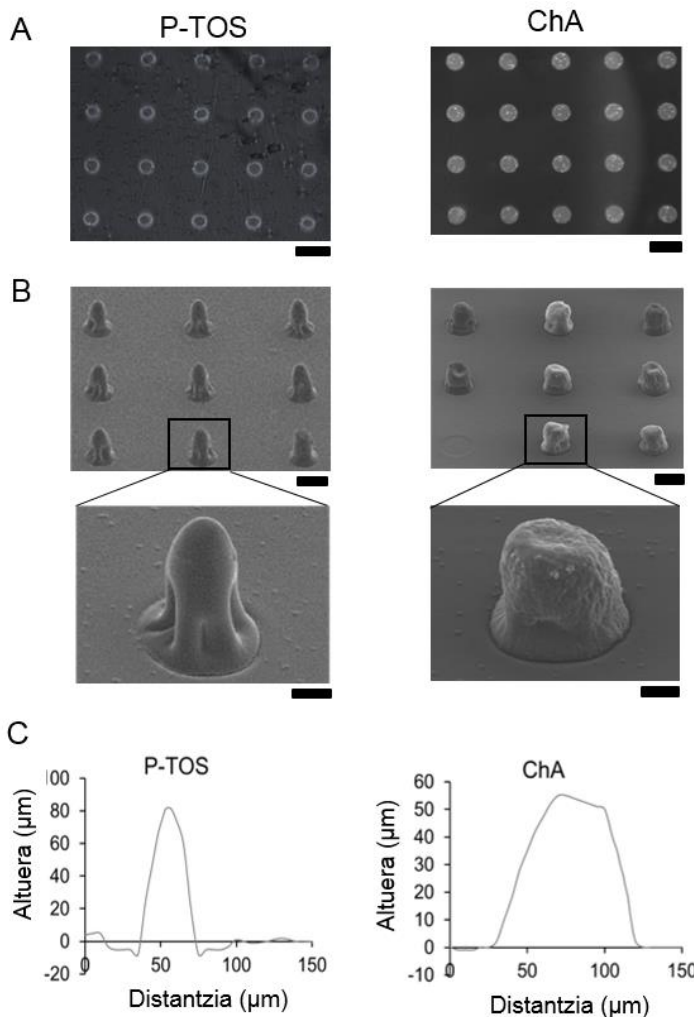
haslea), dimetil sulfoxido (DMSO), azido azetiko (AA), eta trihexiltetradezilfosfonio dizianamida (DCA), tetrabutilfosfonio p-toluenosulfonato (P-TOS) eta kolina azetato (ChA) likido ionikoak (IL). B) Ionogel sare polimeriko baten irudikapen grafikoa.



III.3. irudia. A) Mylar® substratuaren irudikapena. B) Irekitzedun substratuaren (fotomaskararen) tintadun aldean mikrozutabe polimerikoak UV polimerizazioz osatzeko metodoaren eskema grafikoa.

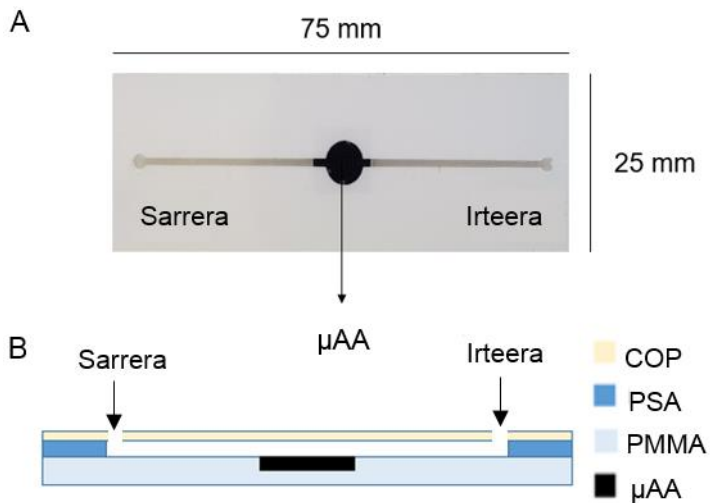


III.4. irudia. A) AA hidrogelez osatutako mikrozutabeen argazkiak, ezkerrean lupa eta eskuinean, mikroskopio optikoa erabiliz. B) DMSO hidrogelez osatutako mikrozutabeen argazkiak, ezkerrean, lupa eta eskuinean, mikroskopio optikoa erabiliz. Eskala 100 μm . Mikrozutabe guztiak irekitzedun substratuan fabrikatu ziren.

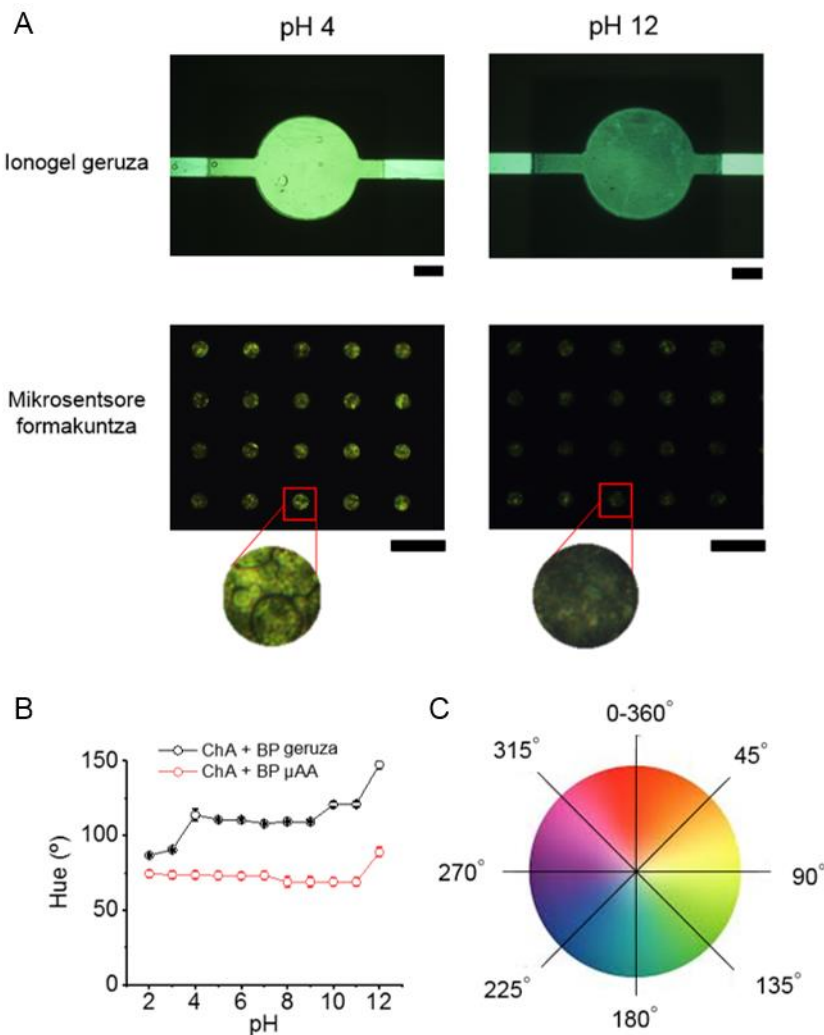


III.5. irudia. A) Irekitzedun substratuan fabrikatutako P-TOS (ezkerra) eta ChA (eskuina) ionogel mikrozutabeei dagozkien mikroskopia optiko irudiak. Eskala 150 μm . B) Irekitzedun substratuan fabrikatutako P-TOS (ezkerra) eta ChA (eskuina) ionogel mikrozutabeei dagozkien mikroskopia elektronikoa (SEM) irudiak (1000X handipena). Eskala 75 μm dira ionogel formakuntzarako eta 20 μm mikrozutabe indibidualen handipenerako. C) Perfilometro optikoarekin neurtutako ionogel mikrozutabe indibidual baten profila: P-TOS (ezkerra) eta ChA (eskuina).

III.2.2 pH detekzio kolorimetrikoa



III.6. irudia. A) Irekitzedun substratuaren karakterizazio kolorimetrikoa fluxu jarraian gauzatzeko gailu mikrofluidikoaren argazkia. B) Gailu mikrofluidikoa osatzen duten material geruzen irudikapen grafikoa, osagaiak hurrengoak direla: olefina zikliko polimeroa (COP), presioari sentikorra den itsasgarria (PSA) polimetilmetakrilato (PMMA) eta irekitzedun substratua.



III.7. irudia. A) Mikroskopia optikoaz ateratako irudiak. Goian, bromokresol more (BP) pH indikatzailea integratuta duten ionogel geruzen argazkiak pH 4 eta pH 12 soluzioak gailu mikrofluidikoan zehar pasaraztean (erregela 2 mm) eta behean, BP pH indikatzailea integratuta duten ionogel mikrozutabeak irekitzedun substratuan (erregela 200 μm). B) pH 2 – 12 tartean ionogel sentsoreen erantzuna irudikatzen duen grafikoa. Errorre barrak $n = 20$ laginen bataz bestekoaren desbiderapen estandarrari dagozkie. C) HSV neurketa kolorimetriko sistemako Hue parametroari dagokion diagrama.

III.3 Ondorioak

Kapitulu honek mikrosentsore ugariz osatutako sentsore-matrizeak substratu malgu batean fabrikatzeko mikrofabrikazio teknika berria aurkezten du, lab-on-a-chip (LOC) gailuetan integratzeko potentziala duena. Mylar® fotomaskara malgua substratutzat erabiltzea du oinarri, espezifikoki diseinatutako gune garden eta beltzez osatuta dagoena. Substratu hau sentsoretzat erabili daitezkeen material UV-polimerizagarriekin konbinatuta (pH detekziorako eraldatutako ionogelak kasu), mikrozutabe sentsoreen formakuntzak lortu ziren pauso bakarrean.

Material desberdinak frogatu ziren mikrosentsoreen 3D egitura sortzeko, hidrogelak eta ionogelak, mikrozutabe anitzen formakuntzak sortzeko hauen egokitasuna ikertzeko asmoz. P-TOS eta ChA ionogeletek eman zitzuten emaitza onenak, mikrozutabe kopuru, forma eta tamainari dagokienez, errepikagarritasun altuena adieraziz. ChA-z egindako mikrozutabeak simetrikoenak izan ziren, mikroskopia optikoa erabiltzean mikrozutabeen azaleran fokuratzea, eta beraz, kolorimetria bidezko analisia, bermatuz.

Bestalde, ionogelaren polimerizazioa fotomaskaran zehar egiteak ionogel mikrozutabeen substratuarekiko atxikipena indartu zuen gainazal tratamendu kimikoen beharrik gabe. Era berean, fotomaskarak irudi analisiaren automatizazioa erraztu zuen ondo definitutako gune garden eta beltzak zirela eta, eta inguruko azalera beltzak optika hobetu zuen, analisi kolorimetrikoetan ematen den inguruko zarata seinalea ekidinez.

Sentsoretzat jarduteko, ionogelari pH indikatzaile bat gehitu zitzaison. Lortutako emaitzen arabera, pH sentsoreek emaitza ezberdina erakutzi zuten ionogela azalera handiko geruza bezela zegoenean edo mikrozutabeetan egituratuta

zegoenean. Bestalde, mikrozutabeen dimentsio txikiak direla eta, ionogelean zehar molekulen difusio eta mugikortasuna errazten denez, BP pH indikatzailearen ionogeletik irteera eragin ahako litzateke, eta beraz, sentsore hauen sentikortasuna murriztu. Hala ere, pH detekziorako erantzun denbora 4 minutukoa izan zen ionogel geruzarako, mikrozutabe sentsoreentzat berehalakoa (< 0.5 s) izan zen bitartean.

Kapitulu honek fotomaskarak substratutzat erabiliz mikrosentsoreen fabrikazio merke eta erraza lortzeko lehenengo pausoa suposatzen du, mikrosentsore formakuntzak egiteko ionogelen potentziala adierazten duelarik. Mikrozutabe sentsoreen garapena oraindik haurtzaroan dago, hala ere, nire ustetan honek potentzial itzela dauka mikrosentsore anitzeko formakuntzak era azkar eta kostu baxuarekin fabrikatzeko. Are gehiago, optimizazio batzuk eginda -pH indikatzailea moduko sentsoretzat diharduen molekulak matrize polimerikoan lotura kobalentez integratzea edo entzimak bezalako molekula handiagoak gehituz- tresna oso baliagarria izan daiteke LOC gailuetan integragarri den elementu sentsore malgu bezala.

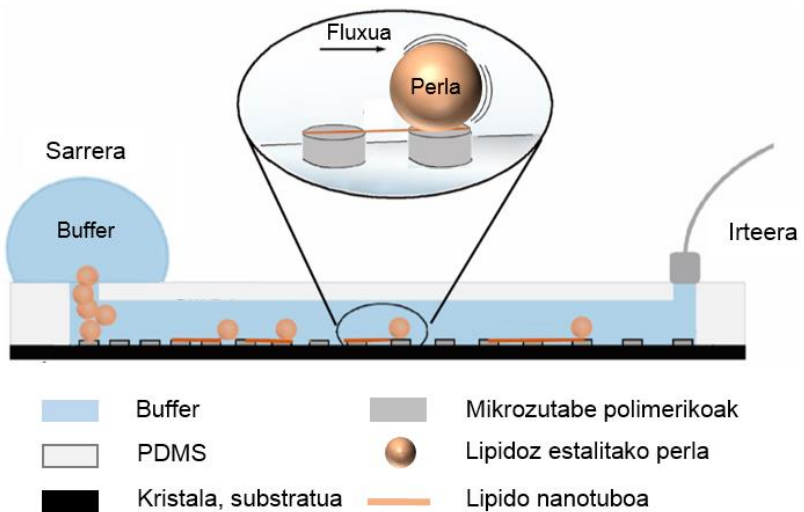
IV

Mikrozutabe Polimerikoak eta Mikrofluidika Nanotubo Lipidikoen Sorkuntza eta Monitorizaziorako

Nanotubo lipidikoen erabilera oso hedatuta dago *in vitro* ikerketetan prozesu zelularren eredutzat. Nanotuboak normalean, banan-banan sortzen dira teknika sofistikatuak erabiliz, beraz, hauek era kontrolatuan eta sortan produzitu eta monitorizatzeko metodoak behar dira. Kapitulu honetan, nanotuboak sortzeko eta monitorizatzeko lab-on-a-chip gailu bat proposatzen da, material ezberdinako mikrozutabe integratuekin. Mikrofluidika eta materialen zientzia konbinatuz nanotubo lipidiko ugariren aldibereko produkzioa eman zen, nanotuboien muturrak mikrozutabe polimerikoetan atxikita zeudela, eta gorputza, suspensioan, nanotuboien luzera eta erradioa kontrolatzea lortuz.

*Kapitulu honetan deskribatutako lana Biofisika institutuko (CSIC,UPV/EHU) Anna Shnyrovaren taldearekin bat egin da. Honen zatiak argitaratu dira: Galvez, J. M. M., Garcia-Hernando, M., Benito-Lopez, F., Basabe-Desmonts, L. & Shnyrova, A. V. Microfluidic chip with pillar arrays for controlled production and observation of lipid membrane nanotubes. *Lab Chip*. 2020, 2748-2755.

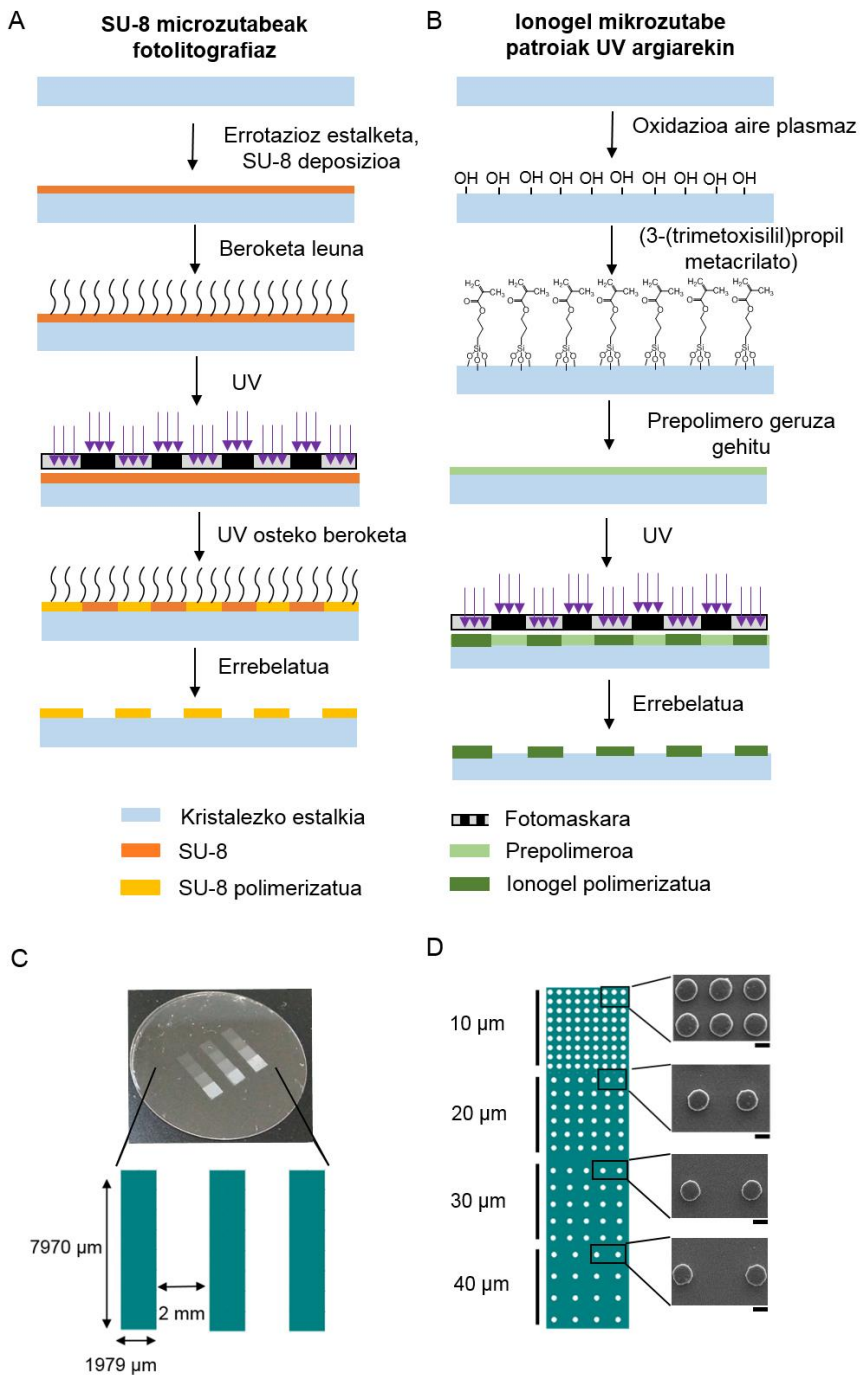
IV.1 Eskema nagusia



IV.1. irudia. Nanotubo (NT) lipidikoak sortzeko gailu mikrofluidikoaren irudikapena. PDMS: polidimetilsiloxano elastomeroa.

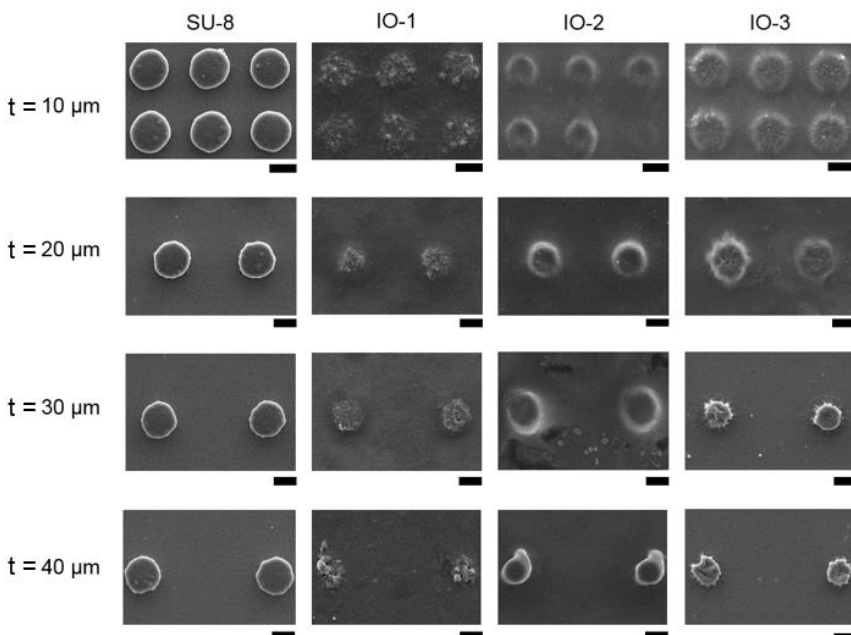
IV.2 Emaitzak

IV.2.1 Mikrozutabe formakuntzen fabrikazioa

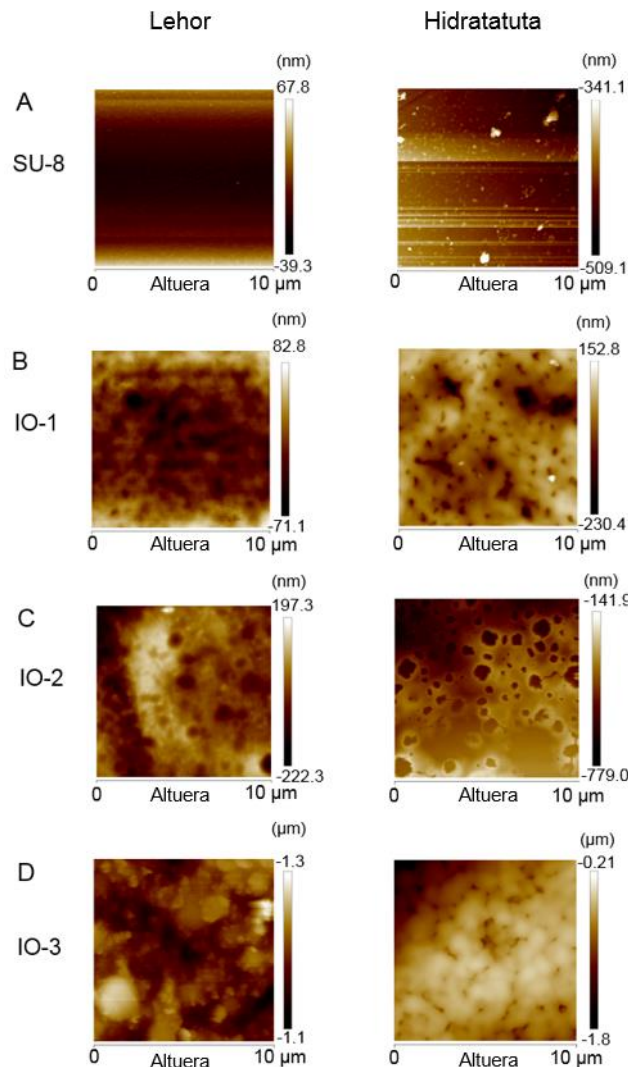


IV.2. irudia. A) Fotolitografia bidez SU-8 erretxina negatiboz egindako

mikrozutabeen fabrikazioaren eskema. B) Ionogel mikrozutabeen fabrikazioaren eskema. C) SU-8 polimerozko mikrozutabeak integratuta dituen beirazko substratuaren argazkia. Beirazko substratua gailu mikrofluidikoa sortzeko erabiliko da eta hiru gune laukizuzen nagusiz osatua dago, hauetako bakoitza kanal mikrofluidiko aske bat izango delarik. Handitutako irudikapenak formakuntzen dimentsio orokorrak adierazten ditu. D) Cirudian ageri diren hiru gune laukizuzenetako baten handipenaren irudikapena, mikrozutabeen lau diseinu ezberdin ageri direlarik, eta eskuinaldean mikrozutabe polimerikoen eskaneatze mikroskopia elektroniko (SEM) irudiak azaltzen direlarik, eskala 10 μm . Lau diseinuek mikrozutabeen diametro bera dute, 15 μm -ko diametrodun mikrozutabeak, 10, 20, 30 eta 40 μm -ko t tarteez bananduta, hurrenez-hurren.

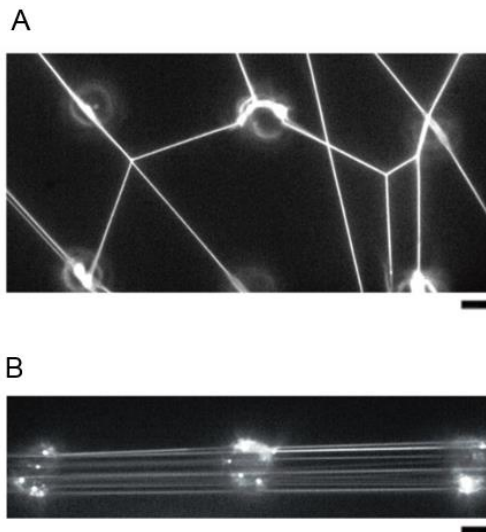


IV.3. irudia. SU-8, ionogel 1 (IO-1), ionogel 2 (IO-2) eta ionogel 3 (IO-3) materialez egindako 15 μm -ko diametroko mikrozutabeen SEM irudiak, haien arteko t distantziak 10, 20, 30 eta 40 μm direlarik. Eskala 15 μm .

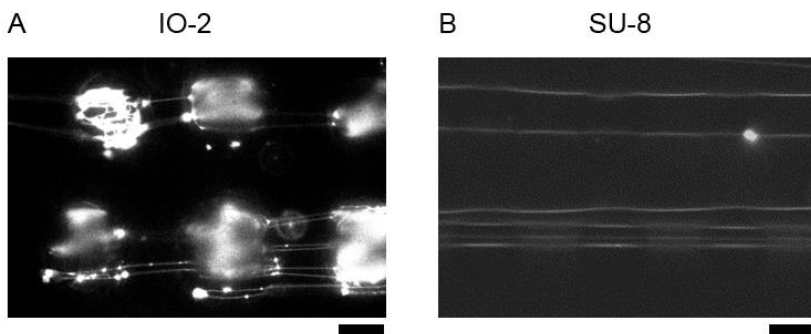


IV.4. irudia. Mikrozutabeak sortzeko erabilitako lau materialen gainazalaren indar atomikoko mikroskopia (AFM) irudiak, A) SU-8, B) IO-1, C) IO-2 eta D) IO-3, lehor daudenean (ezkerra) eta hidratatuta (eskuina).

IV.2.2 Mikrozutabeen arteko lipidozko nanotuboen (NT) sorkuntza

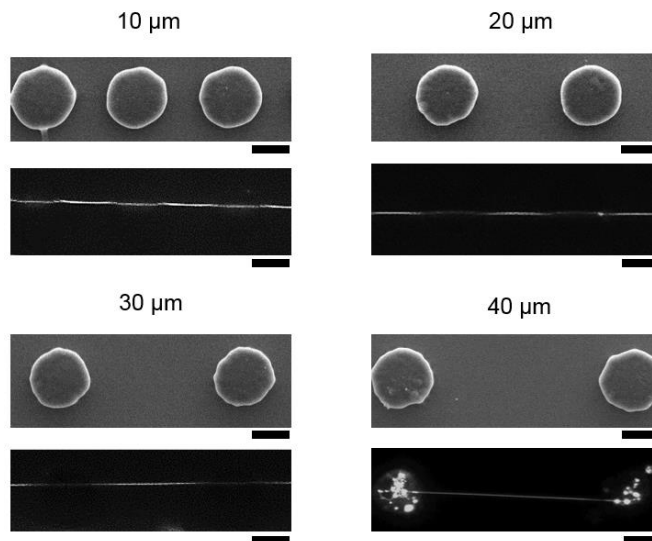


IV.5. irudia. A) Inklinazio metodoaren bidez sortutako mikrozutabeen arteko NT lipidiko sarearen fluoreszentzia mikroskopia irudiak. B) Fluxu negatiboa erabiliz sortutako mikrozutabeen arteko NT lipidiko paraleloen fluoreszentzia mikroskopia irudiak. Eskala 10 μm .

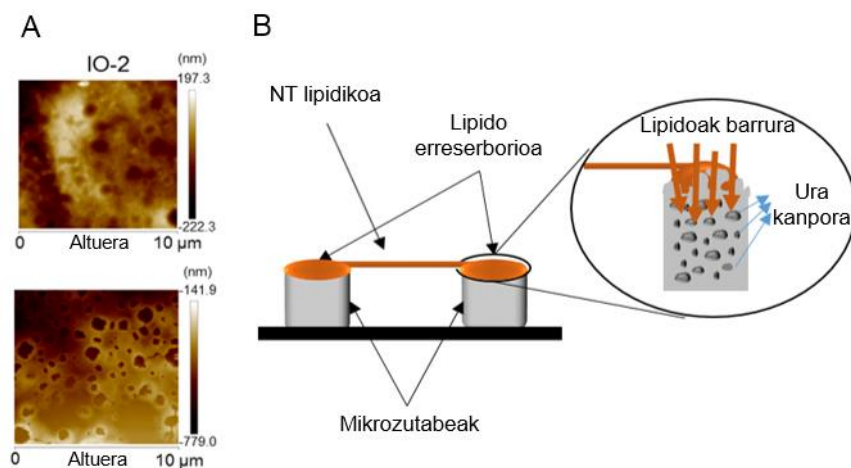


IV.6. irudia. A) IO-2 mikrozutabeetan sortutako NT lipidiko paraleloen fluoreszentzia mikroskopia irudiak. B) SU-8 -zko mikrozutabeetan sortutako NT

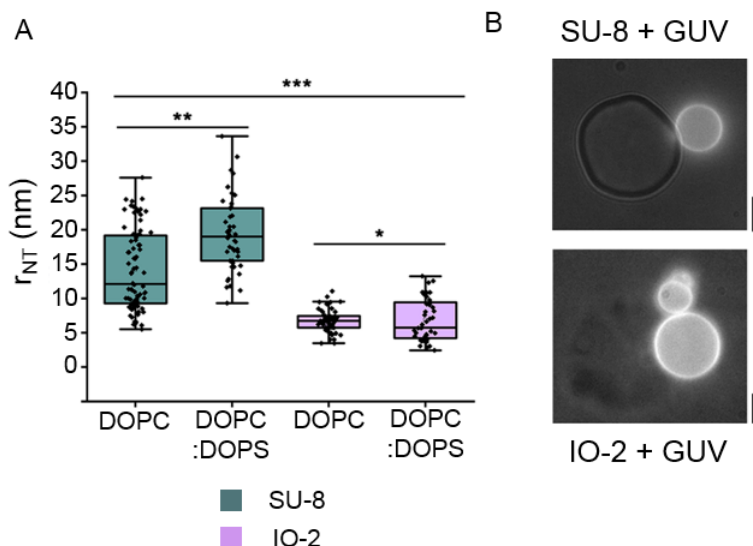
lipidiko paraleloen fluoreszentsia mikroskopia irudiak. Eskala 10 μm .



IV.7. irudia. Ondoz ondoko eta distantzia ezberdinetara dauden bi SU-8 mikrozutabeee atxikitutako NT lipidikoen irudiak. Eskala 10 μm .



IV.8. irudia. A) IO-2 materialaren gainazalaren AFM irudiak lehor (goian) eta hidratatuta (behean) dagoenean. B) Lipido/IO-2 mikrozutabearren interfazearen eskema.



IV.9. irudia. A) NT lipidikoen erradioak mintzaren konposizioaren eta mintzak mikrozutabeen materialarekin duen interakzioaren funtzioko irudikatzen dituen grafikoa. Errore barrak hurrengo n laginen bataz bestekoaren desbiderapen estandarrari dagokie DOPC/SU-8, n = 81; DOPC:DOPS/SU-8, n= 46; DOPC/IO-2, n = 63 eta DOPC:DOPS/IO-2, n = 45. Esangura estatistikoa: *** Ezberdintasun esanguratsua 0.05 mailan (Two-way ANOVA (substratu eta lipido konposizioak kontutan hartuta), $p = 1.88 \cdot 10^{-18}$); ** Ezberdintasun esanguratsua 0.05 mailan (One-way ANOVA, $p = 3.2 \cdot 10^{-6}$); * Ezberdintasun ez esanguratsua 0.05 mailan (One-way ANOVA, $p = 0.71$). B) Geruza bakarreko besikula erraldoien (GUV) atxikipena SU-8 (goian) eta IO-2 (behean) mikrozutabeetara. Eskala 5 μm .

IV.3 Ondorioak

NT lipidikoak sortzeko eta monitorizatzeko gaur egun erabiltzen diren teknikak ez bezala, aurkeztutako gailu mikrofluidikoak NT lipidiko ugari modu erraz eta azkarrean sortzea ahalbidetzen du, gailuak integratuta dauzkan mikrozutabez osatutako matrizeei esker. NT lipidikoak sortzeko erabiltzen diren

mikromanipulazio teknika konbentzionalen aldean, kapitulu honetan aurkeztu den metodologiak ez du mikromanipulaziorik behar sortutako NT lipidikoen luzera kontrolatzeko, eta are gehiago, hauen erradioa kontrolatzeko aukera ematen du. Perlen errotazioaren, mikrozutabez osatutako matrizeen dimentsioen eta mikrofluidikaren konbinazioak, denbora gutxian, NT lipidiko anitz sortzeko metodologia erraz eta moldakorra eskaintzen du.

Mikrofluidikak fluxu errejimenaren kontrola ahalbidetzen du, baita NT -en fabrikazio eta analisiaren automatizazioa erraztu. Halaber, prozesu osoa mikrokanalaren barne ematen da, beharrezko erreaktiboen bolumena murriztuz.

Mikrozutabeetan sortutako NT lipidikoak dindilizka daude mikrozutabeen artean, beste elementuekin – substratua, esaterako - interakzioaren ondorioz eman zitezkeen artefaktuak ekidinez. Bestalde, mikrozutabeen altuera txikiak (zuzenean kristalezko estalki batean fabrikatuak), NT lipidikoen monitorizazioa ahalbidetzen du fluoreszentzia mikroskopiaz, handipen handiko objektiboak erabiliz.

Ionogelak material bikainak izan daitezke argi bidezko patroiak egiteko, beraz, kapitulu honek frogatu egiten du material hauekin erresoluzio altuko ($15\ \mu\text{m}$) egiturak lor daitezkeela, eta hauek egonkorra direla hilabete ugaritan zehar eta erabilera anitzerako. Ionogel familiaren aldakortasunak eta hauen egokitasunak argi bidezko patroiak sortzeko, gainazalak kimikoki aldatzeko prozedurekin bat, sistema honi moldakortasun altua eskaintzen diote. Izan ere, aurkeztutako mikrosistemak NT lipidikoek mikrozutabe polimerikoekin duten interakzioaren indarra molda dezake, eta ondorioz, sortutako NT -en erradioa. Erabiltzeko erraza den sistema miniaturizatu hau, tresna oso baliagarria izango da kurbadura altuko mintz prozesuak ikertzeko *in vitro* proba askotarako.

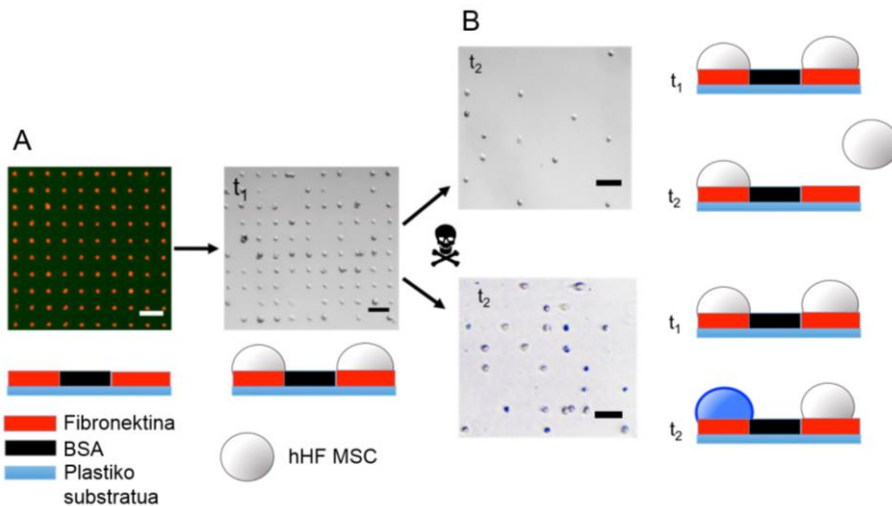
V

Toxizitate zelularra zelula indibidual erresoluzioarekin antzemateko biosentsore optikoa

Kapitulu honetan zelulen heriotzaren jarraipena egiteko erresoluzio altuko metodologia aurkezten da. Zelulen bideragarritasuna neurtzeko zelulen kuantifikazio optiko eta dinamikoa du ardatz, zelula indibidualen atxikipenerako diseinatutako fibronektina puntuen formakuntzez baliatuz. Sistema honek heriotza zelularren monitorizazioa ahalbidetzen du bi ikuspuntuz baliatuz. Batetik, zelulen heriotzaren monitorizazio kuantitatibo eta dinamikoa egin daiteke, zelulen substratutik askapena kuantifikatz eta heriotzarekin korrelazionatz. Beste alde batetik, zelulak hil baina hauen askapena ekiditen duten konposatu toxikoen efektua heriotza zelularrean monitorizatu daiteke.

* Kapitulu honen zatiak hurrengoan publikatuak izan dira: Garcia-Hernando, M., Calatayud-Sanchez, A., Etxebarria-Elezgarai, J., de Pancorbo, M. M., Benito-Lopez, F., Basabe-Desmonts, L. Optical single cell resolution cytotoxicity biosensor based on single cell adhesion dot arrays. *Anal. Chem.* 2020, 92, 9658-9665.

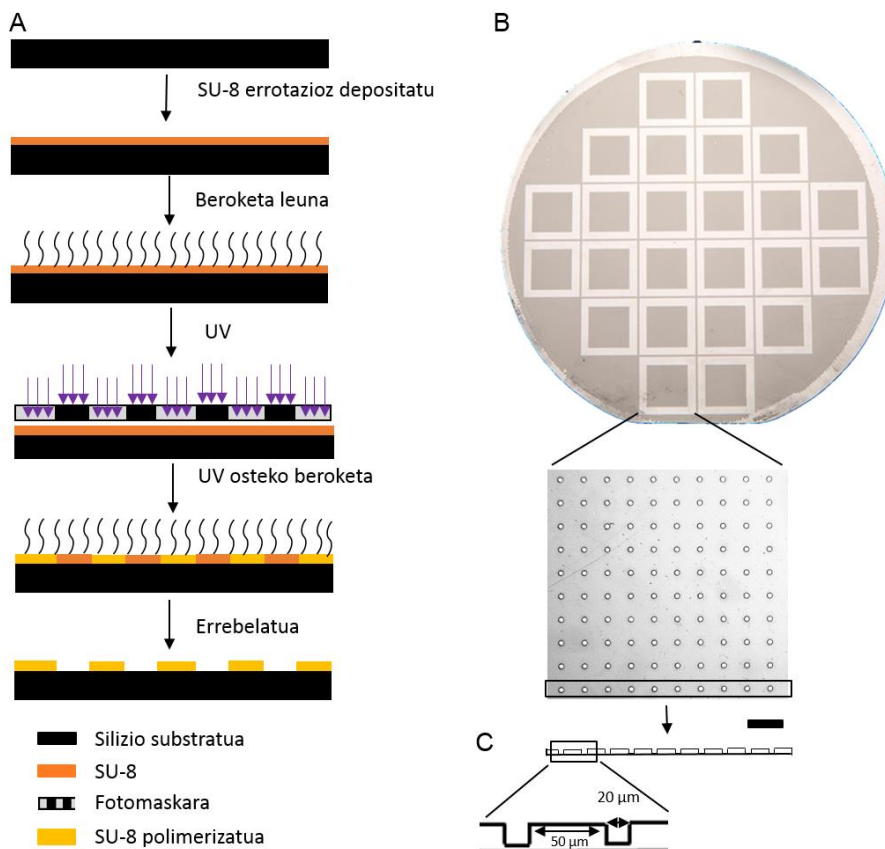
V.1 Eskema nagusia



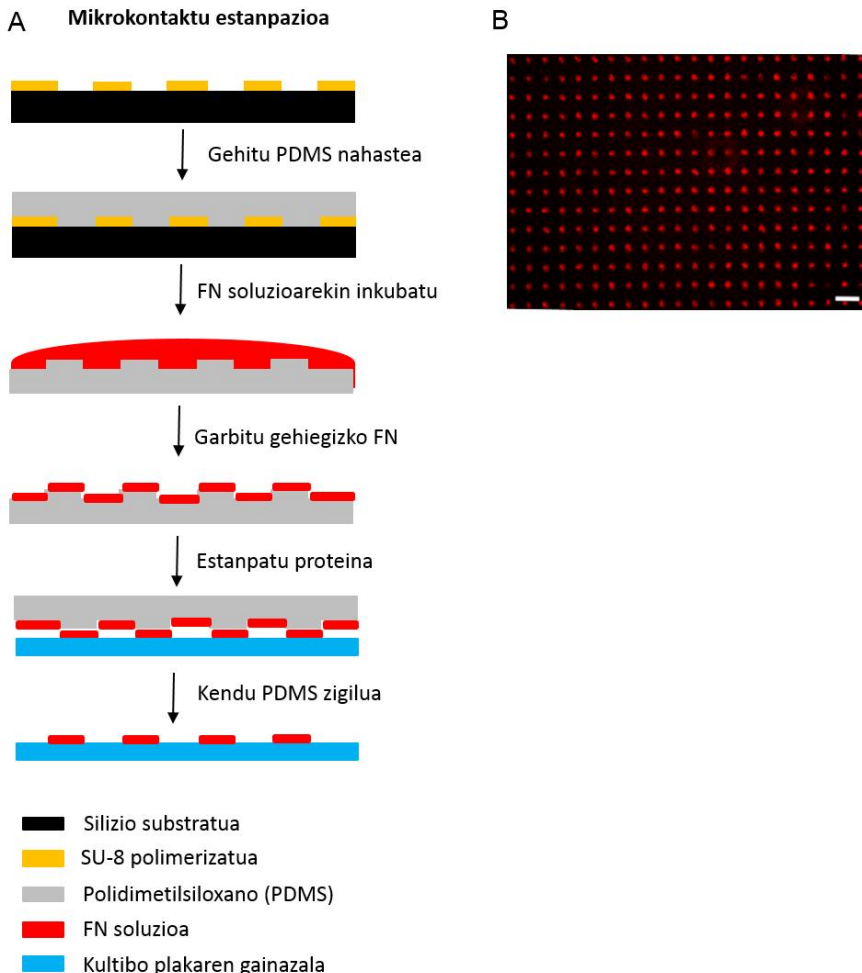
V.2. irudia. Zelula indibidualak atxikitzeko puntuen formakuntza, ingelesez single cell adhesion dot array (SCADA) zelulen toxizitate testaren eskema. A) Ezkerrean, fibronektina (FN) puntuen formakuntzaz osatutako FN-SCADA substratu baten fluoreszentzia mikroskopia irudia; eta eskuinean, FN-SCADA substratua ile folikuluko zelula ama mesenkimalen (hHF-MSCs) inkubatu eta gero lortutako zelula indibidualen formakuntzaren mikroskopia optiko irudia. BSA behi serum albumina, blokeo agenteari dagokio. B) Zelulez saturatutako SCADA substratuak zelulen heriotza eragiten duten bi konposatu toxikoren presentzian egon eta geroko mikroskopia optiko irudiak: goian, konposatu toxikoak zelulen substratutik askapena eragindako monitorizazioa, eta behean, konposatu toxikoak eragindako heriotza zelularra behatzeko zelulen bideragarritasuna ebaluatzeko trypan blue tindaketa eginez gauzatutako monitorizazioa. Eskala 100 μ m.

V.2 Emaitzak

V.2.1 Fibronektina patroien produkzioa



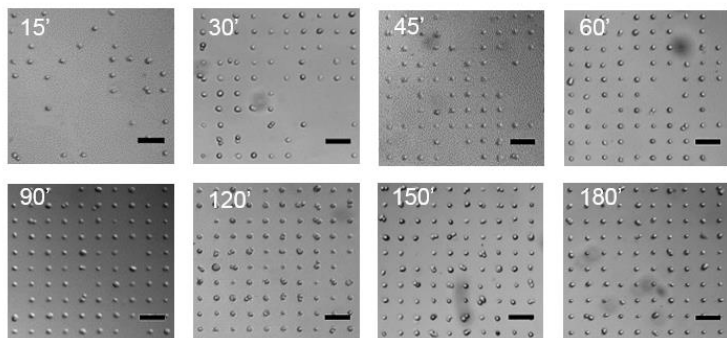
V.2. irudia. A) Fotolitografia teknikaren irudikapen grafikoa. B) Fabrikatutako silizio moldearen argazkia eta dagokion mikropatroiarengan mikroskopio optiko irudia. Mikropatroia 20 μm -ko diametroko eta 50 μm -z banatutako zuloez dago osatuta. Eskala 100 μm .



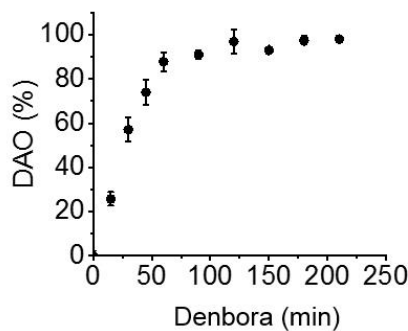
V.3. irudia. A) Mikrokontaktu bidezko estanpazioaren eskema grafikoa. B) Zelula indibidualen atxikipenerako proteina patroi uniforme baten fluoreszentzia mikroskopia irudia. Eskala 100 μm .

V.2.2 Zelulen proteina substratuekiko atxikipen eta askapenaren monitorizazioa zelula indibidual erresoluzioarekin

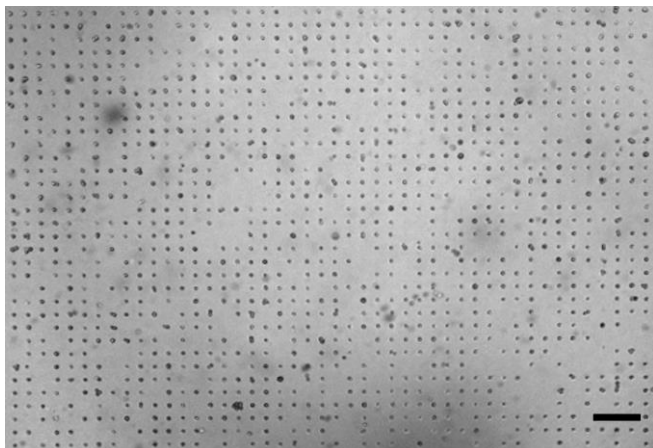
A



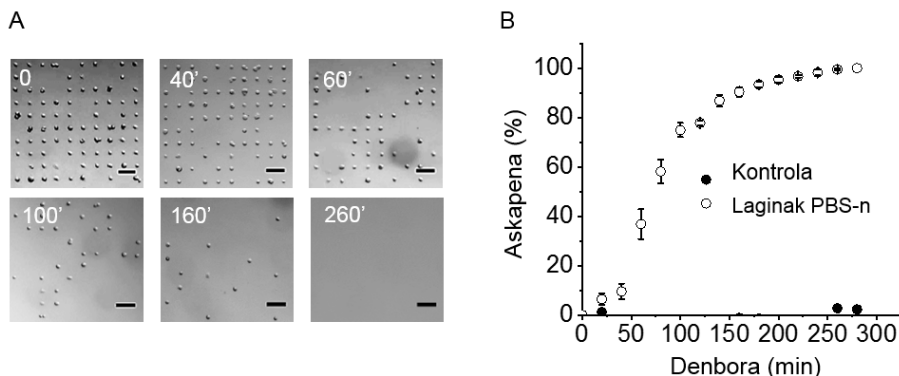
B



Irudi V.4. SCADA substratuetan zelula indibidualen atxikipena. A) Zelula indibidualen formakuntzen mikroskopia optiko irudiak denbora puntu desberdinatan: 15, 30, 45, 60, 90, 120, 180 eta 210 min. B) DAO *versus* denbora grafikoa. DAO, formakuntza puntuen okupazioa, ingelesetik Dot Array Occupancy. Eskala 100 μm . Errore barrek hurrengo $n = 3$ laginen bataz bestekoaren desbiderapen estandarrari dagokie.

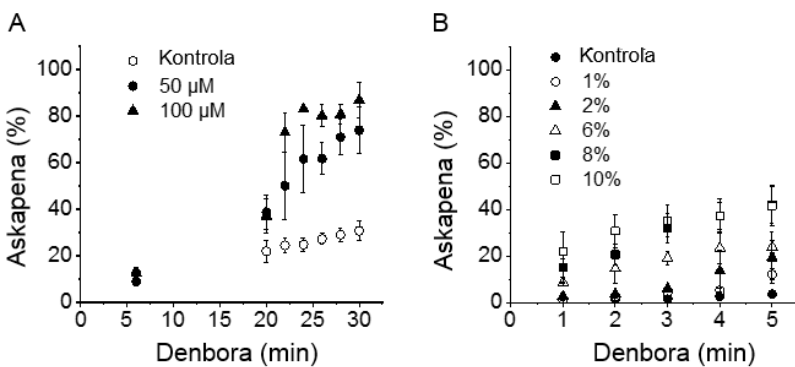


V.5. irudia. Fibronektina punto formakuntzak hHF-MSCs-ekin inkubatu eta gero ateratako mikroskopia optiko irudia, 1758 proteina puntuz eta 1298 zelulez osatuta. Eskala 250 μm .



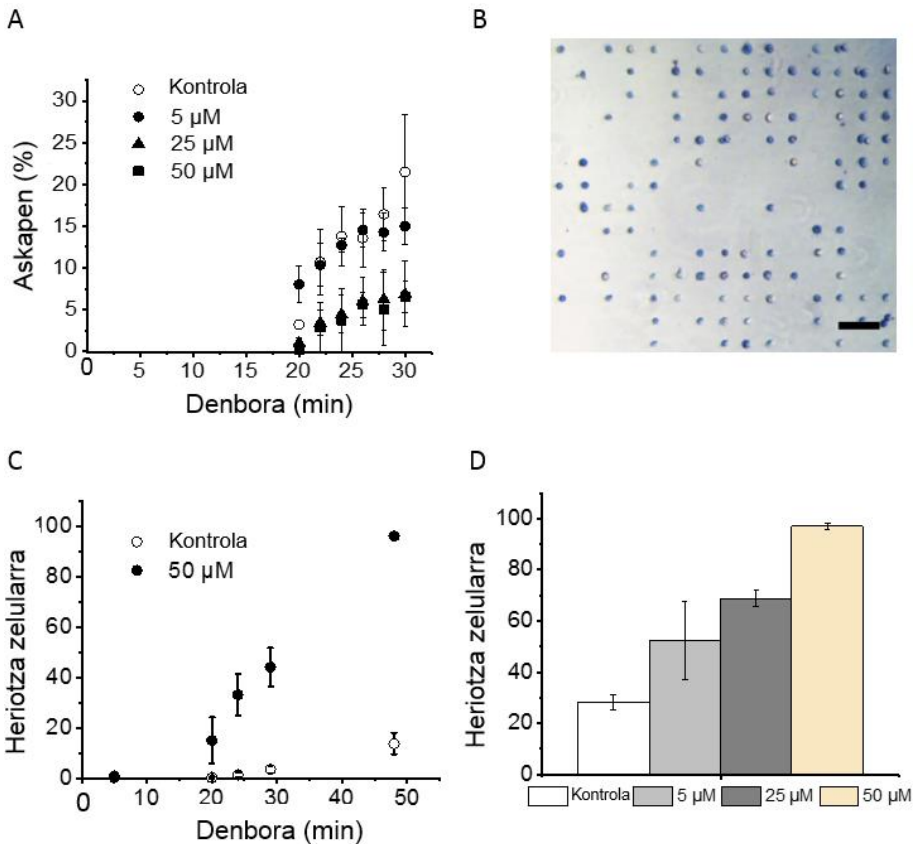
V.6. irudia. SCADA substratuetan atxikituta dauden zelulen askapen dinamikoa. A) Zelula indibidualen askapenaren mikroskopia optiko argazkiak fosfatodun gatz buffer (PBS, ingelesetik phosphate buffer saline) presentzian, hurrengo denbora puntuetaan: 0, 40, 60, 100, 160 eta 260 min. Eskala 100 μm . B) hHF-MSCs -en askapena *versus* PBS -ren presentzian igarotako dendora. Errore barrak hurrengo n = 3 laginen bataz bestekoaren desbiderapen estandarrari dagokie.

V.2.3 K_2CrO_4 eta DMSO konposatuuen toxizitate zelular testa etiketa gabeko SCADA erabiliz.



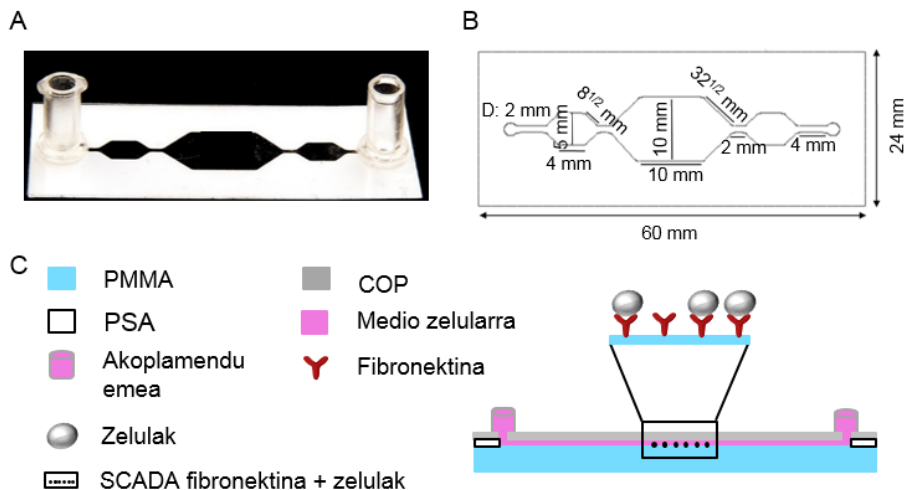
V.7. irudia. A) Zelula askapenaren zinetika K_2CrO_4 50 eta 100 μ M-en presentzian 30 ordu tan zehar. Errore barrek hurrengo n = 3 laginen bataz bestekoaren desbiderapen estandarrari dagokie. B) Zelula askapenaren zinetika DMSO % 1, 2, 4, 6, 8 eta 10-en presentzian 5 ordu tan zehar. Errore barrek hurrengo n = 3 laginen bataz bestekoaren desbiderapen estandarrari dagokie.

V.2.4 SCADA zelulen bideragarritasun test kolorimetrikoak

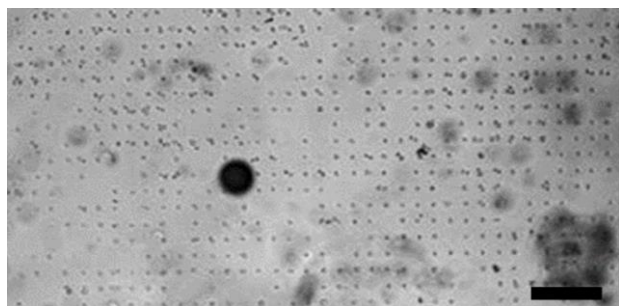


V.8. irudia. Heriotza zelularra HgSO_4 konposatuarekin inkubatu eta gero. A) hHF-MSC zelulen askapenaren zinetika HgSO_4 5, 25 eta 50 μM -en presentzian 30 ordutan zehar. B) hHF-MSC zelulak dituen FN-SCADA substratuaren mikroskopia optiko irudia, HgSO_4 25 μM -ekin 48 orduz egon eta gero, eta trypan blue zelula hilen tindaketa erabilita. Eskala 100 μm . C) Heriotza zelularren irudikapen grafikoa, HgSO_4 50 μM -en presentzian 48 ordutan zehar egonik. D) Heriotza zelularren irudikapen grafikoa, HgSO_4 5, 25 eta 50 μM -en presentzian 48 orduz egon eta gero. Errore barrek hurrengo n = 3 laginen bataz bestekoaren desbiderapen estandarrari dagokie.

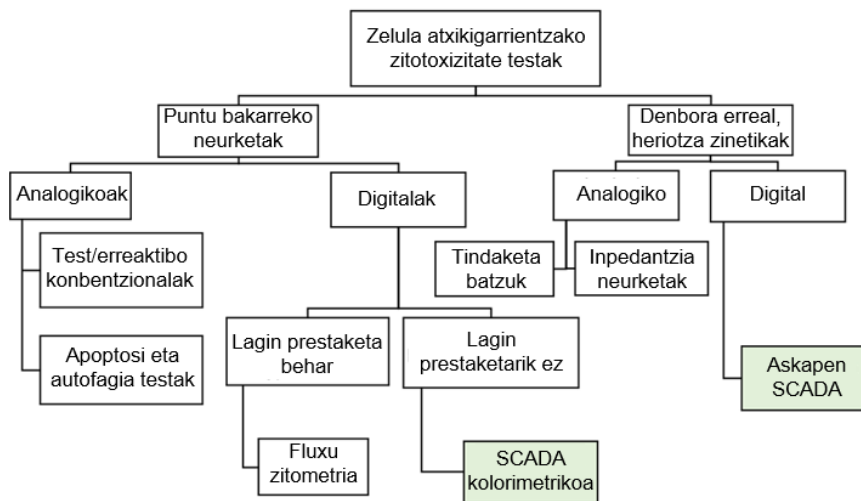
V.2.5 SCADA on Chip



V.9. irudia. A) Gailu mikrofluidiko muntatuaren argazkia. B) Gailu mikrofluidikoaren goitiko biota, dagozkion dimentsioekin C) Gailu mikrofluidiko hibridoaren albotiko bistaren irudikapena. Hiru material geruzaz dago osatuta: polimetilmetakrilato (PMMA), presioari sentikorra den itsasgarria (PSA) kanalaren altuera eta diseinua finkatzeko, eta olefina zikliko polimeroa (COP) kanala zigilatzeko. Irudikapena ez dago eskalan. Handipena SCADA guneari dagokio.



V.10. irudia. Gailu mikrofluidikoan zelula indibidualen atxikipenaren mikroskopia optiko irudia, zelulak 15 min inkubatu eta gero. Eskala 300 μm .



V.11. irudia. Zelulen toxizitatea eta bideragarritasun zelularra neurtzeko existitzen diren tresnen sailkapena, ematen duten informazioaren arabera sailkatuta. SCADA-k heriotza zelularren neurketa digitala ahalbidetzen du, laginaren prestaketa pausorik behar gabe konposatu toxikoaren presentzian egon eta gero.

V.3 Ondorioak

Kapitulu honek heriotza zelularra monitorizatzeko erresoluzio altuko SCADA metodologiaren oinarriak aurkezten ditu, tresna optikoak erabiliz zelulen bideragarritasunaren kuantifikazio dinamiko eta digitalean oinarritzen dena. Batetik, zelulen askapenaren monitorizazio dinamikoa ahalbidetzen du, eta bestetik, zelulen askapena induzitzen ez duten konposatu toxikoen hilgarritasunaren detekzioa. SCADA sistemaren zehaztasuna, zenbatzeko modu binario edo digitalean datza, eta hori lortzeko, zelula individualentzako atxikipen puntuak erabiltzen ditu. Puntu positiboak (zelula dago edo zelula

tindatuta dago) zenbatu egin daitezke, eta zelulen atxikipenerako eskuragai dauden puntu kopuru totalaz zatitzu, ehunekoa kalkula daiteke, DAO izanik atxikipen zelularren okupazioaren ehunekoa kuantifikatzen duen unitatea. Atxikipen puntu bakoitza, besteekiko askea da, beraz zelula individual batek berau okupatzeko aukera berdina da atxikipen puntu denentzat, hurrengo kode digitala ahalbidetuz: okupatua/libre, tindatuta/tindatu gabe, positibo/negatibo edo 0/1. SCADA toxizitate zelularra monitorizatzeko teknika ez inbaditzalea da, eta beraz era sentikorrean heriotza zelularra monitorizatzea ahalbidetzen du, tresna optikoak soilik erabilita.

Zelulen toxizitate testa bi konposatu kimikorekin egiaztatu zen, K_2CrO_4 eta DMSO, hauen toxizitate zinetikak monitorizatuz. SCADA substratuek, lehenengo aldiz ahalbidetu zuten DMSO eta K_2CrO_4 konposatu toxikoek hHF-MSC zeluletan eragiten zuten heriotza monitorizatzea, tresna optikoak baino ez erabilita. Bestalde, $HgSO_4$ konposatuak zelulak hil baina hauen askapena sustatzen ez zuenez, honek hHF-MSC zeluletan sortutako heriotza zelularra monitorizatu zen SCADA trypan blue tindaketarekin konbinatuta eta tresna optikoak erabiliz.

SCADA sistemaren erabilera zelula tipo ugariri eta heriotza test ugariri hedatiteke, erabilitako atxikipen matrizearen konfigurazioa aldatuz: puntuen forma, kopurua edota konposizioa. Metodologia hau gailu mikrofluidikoetan integratzea lortu eta tresna optiko simpleekin erabilgarria izateko disenatu zenez, SCADAk toxizitate zelularren neurketa zehatzetan inpaktua izango duelakoan nago, bai oinarrizko ikerkuntzaren esparruan, baita erabilera komertzialeko eremuetan ere.

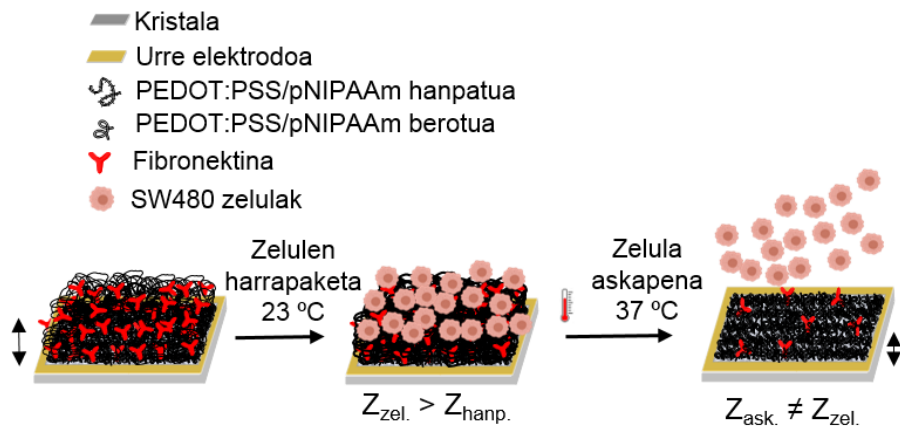
VI

Elektrodo Inteligente eta Funtzionalak Zelulen Harrapaketa eta Askapenerako eta Aldibereko Monitorizaziorako

Kapitulu honek material funtzionalen konbinaketan oinarritutako mikrosistema bat aurkezten du, zelulen harrapaketa eta askapena burutu eta aldi berean prozesu horren monitorizazioa burutzeko gai dena. Poli(*N*-isopropilakrilamida) termo-erantzuna duen materiala eta eroalea den poli(3,4-etilendioxitofeno) poliestireno sulfonatu materialak konbinatu ziren, inteligentea eta eroalea zen kopolimeroa osatuz. Hau elektrodoetan jarri, eta fibronektina proteina gehitu zitzaison zelulen harrapaketa induitzeko. Kopolimeroak konformazio aldaketa jasan zuen temperaturari erantzunez, eragingailutzat jardunez, ondorioz zelulen askapena sustatz. Era berean, kopolimeroak sentsore gisa ziharduen, zelulen harrapaketa eta askapena impedantzia elektrokimiko espektroskopiaz monitorizatz.

* Kapitulu honen zatiak hurrengoan publikatzeko bidaliak izan dira, Biosensors and Bioelectronics: Garcia-Hernando, M., Saez, J., Savva, A., Basabe-Desmonts, L., Owens, RM. & Benito-Lopez, F. An electroactive and Thermo-responsive Material for the Capture and Release of Cells.

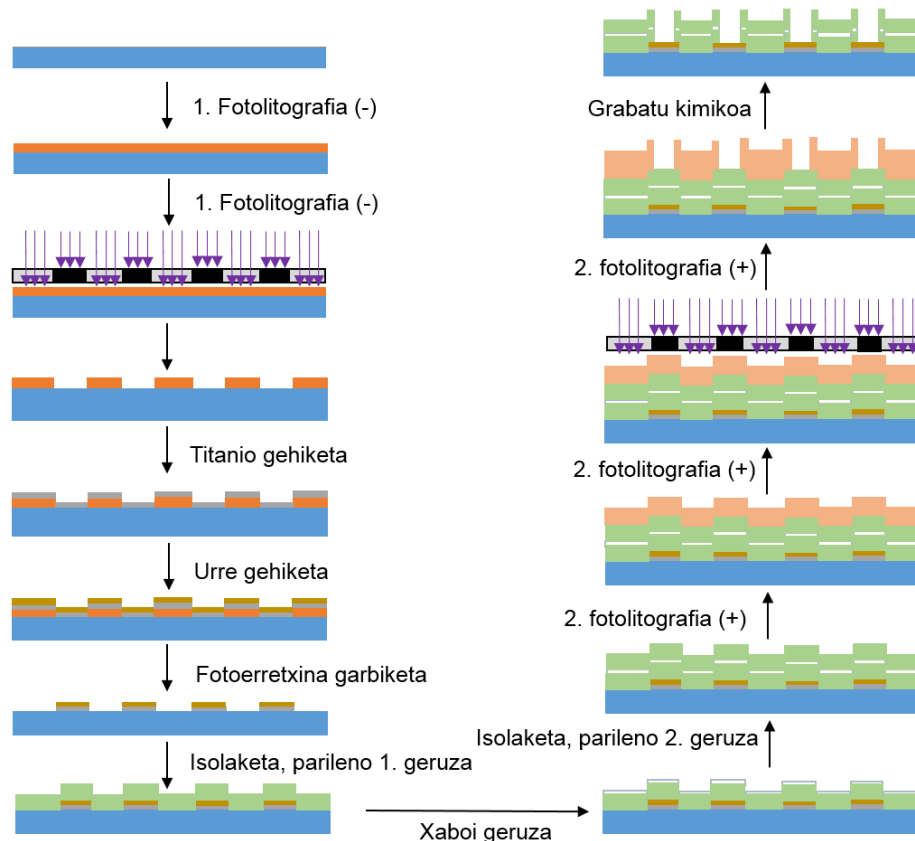
VI.1 Eskema nagusia



VI.1. irudia. Zelulen harrapaketa eta askapen prozesua eta aldibereko monitorizazio elektrikoaren eskema, poli(3,4-etilendioxitofeno) poliestireno sulfonatu/poli(*N*-isopropilakrilamida) (PEDOT:PSS/pNIPAAm) kopolimero hibrido funtzionala oinarri. Ezker eta eskuineko geziak PEDOT:PSS/pNIPAAm hanpatu edo hidratatuari (ezkerra) eta PEDOT:PSS/pNIPAAm berotuari (eskuina) dagokie.

VI.2 Emaitzak

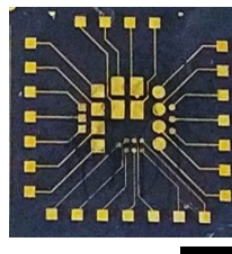
VI.2.1 Elektrodoen fabrikazioa



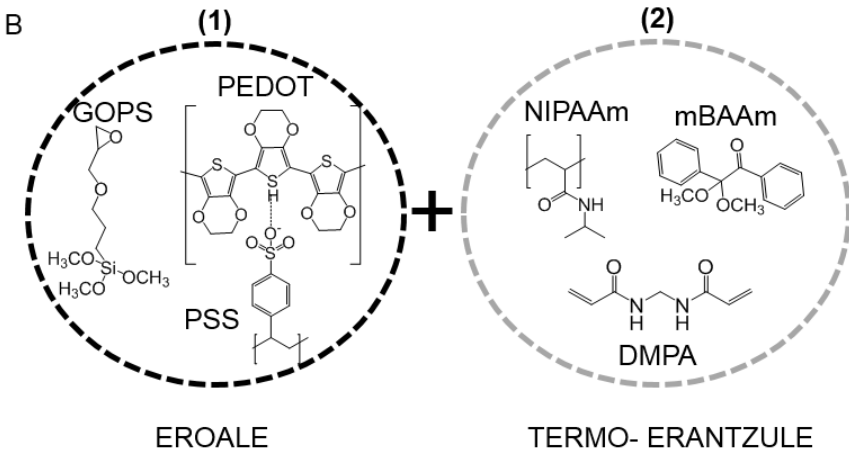
VI.2. irudia. Urrezko elektrodoen fabrikazio prozesuaren irudikapen eskematikoa.

VI.2.2 Inpedantzia elektrokimiko espektroskopia (EIS) bidezko karakterizazioa

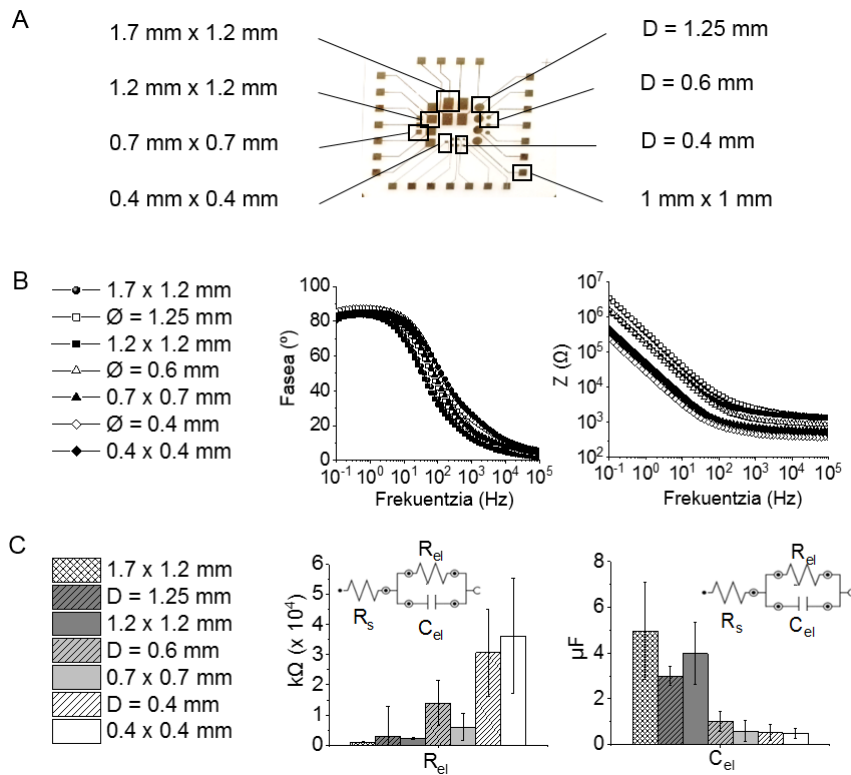
A



B

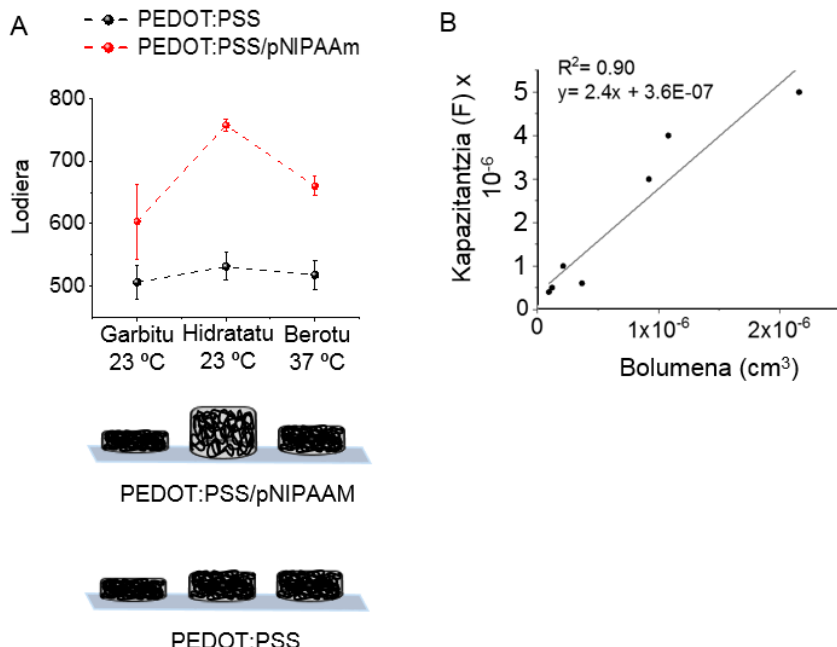


VI.3. irudia. A) Fotolitografiaz fabrikatutako 24 urre-elektrodoz osatutako beirazko substratuaren argazkia. Eskala 5 mm. B) Hurrengo osagaien estruktura kimikoak (1) polimero eroalea: PEDOT eta PSS, glizidoxi propiltrimetoxisilano (GOPS) termo-haslea eta (2) termo-erantzuna duen polimeroa, NIPAAm monomeroa, N,N'-metilenbisakrilamida (mBAAm) elkargurutzatzalea eta 2,2-dimetoxi-2-fenilazetofenona (DMPA) foto-haslea.

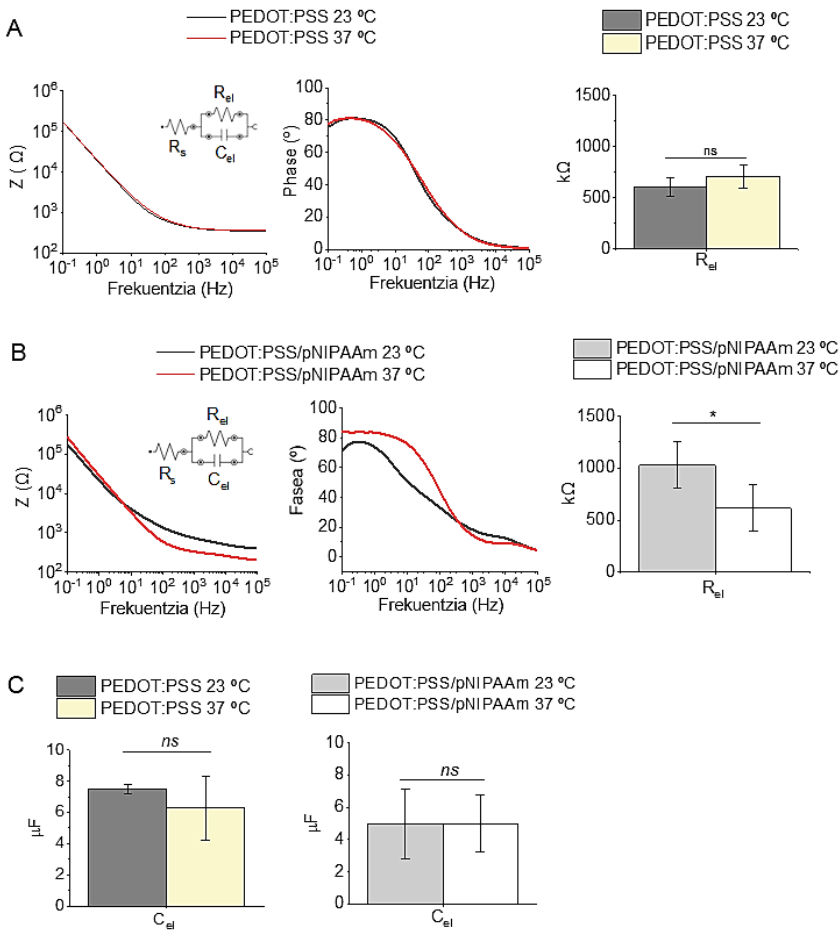


VI.4. irudia. A) Elektrodoen argazkia, dimentsio ezberdinak 7 diseinuz osatua. B) Inpedantzia *versus* frekuentzia (erdian) eta fsea *versus* frekuentzia (eskuina) grafikak, PEDOT:PSS/pNIPAAm tamaina ezberdinak elektrodoen EIS datuak irudikatuz. C) PEDOT:PSS/pNIPAAm elektrodo guztiak EIS neurketetik lortutako R_{el} eta C_{el} parametro elektrikoen irudikapena. Errore barra $n = 3$ laginen bataz bestekoaren desbiderapen estandarrari dagozkie. Grafikoen barneko irudiak PEDOT:PSS/pNIPAAm kopolimeroaren EIS neurketetako datuei dagozkien R(RC) zirkuituaren irudikapena dira.

VI.2.3 Kopolimeroaren termo-erantzunaren eta propietate eroalearen karakterizazioa



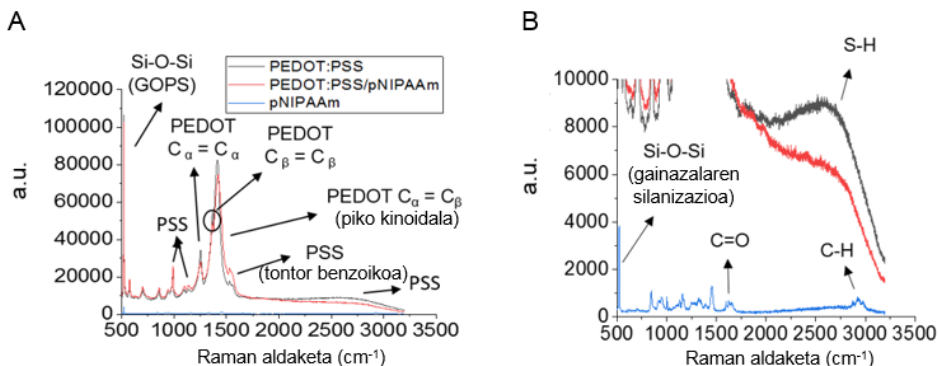
VI.5. irudia. A) Goian, PEDOT:PSS eta PEDOT:PSS/pNIPAAm materialen lodieraren aldaketa, polimerizazioa eta gero, eta hidratazio/beroketa ziklo baten ondoren. Errore barrik $n = 4$ laginen bataz bestekoaren desbiderapen estandarrari dagozkie. Behean, PEDOT:PSS/pNIPAAm eta PEDOT:PSS materialen hidratazio/beroketa zikloaren eskema. B) PEDOT:PSS/pNIPAAm kopolimeroari dagokion bolumena (cm^3) *versus* kapazitantzia (F) grafikoa.



VI.6. irudia. A) PEDOT:PSS 23 °C eta PEDOT:PSS 37 °C materialen EIS neurketen impedantzia *versus* frekuentzia (ezkerra), fasea *versus* frekuentzia (erdian) eta EIS datuei dagokien R(RC) zirkuiturako lortutako R_{el} irudikatzen duen grafikoa. Ez dago aldaketa esanguratsurik (ns) 0.05 mailan (one-way ANOVA $p = 0.2$). Errore barrak $n = 4$ laginen bataz bestekoaren desbiderapen estandarrari dagozkie. B) PEDOT:PSS/pNIPAAm 23 °C eta PEDOT:PSS 37 °C materialen EIS neurketen impedantzia *versus* frekuentzia (ezkerra), fasea *versus* frekuentzia (erdian) eta EIS datuei dagokien R(RC) zirkuiturako lortutako R_{el} irudikatzen duen grafikoa.

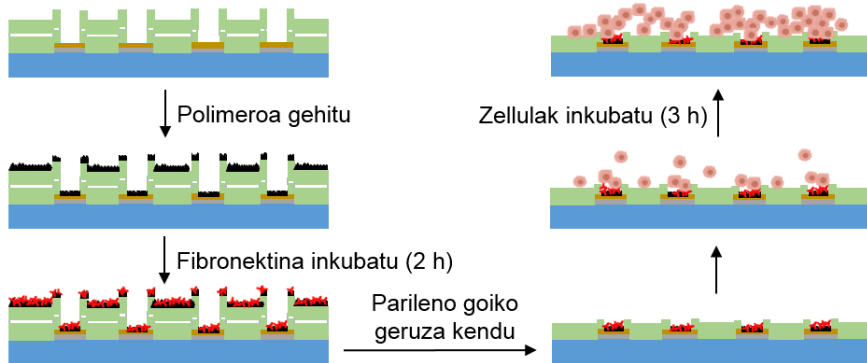
*Aldaketa esanguratsua 0.05 mailan (one-way ANOVA $p = 0.045$). Errore barrak

$n = 4$ laginen bataz bestekoaren desbiderapen estandarrari dagozkie. C) PEDOT:PSS 23 °C eta 37 °C materialei dagokien C_{el} parametroaren irudikapen grafikoa; ez dago aldaketa esanguratsurik (ns) 0.05 mailan (one-way ANOVA $p = 0.28$) (ezkerra) and PEDOT:PSS/pNIPAAm 23 °C eta 37 °C materialei dagokien C_{el} parametroaren irudikapen grafikoa; ez dago aldaketa esanguratsurik (ns) 0.05 mailan (one-way ANOVA $p = 0.99$) (eskuina). Errore barrak $n = 4$ laginen bataz bestekoaren desbiderapen estandarrari dagozkie.

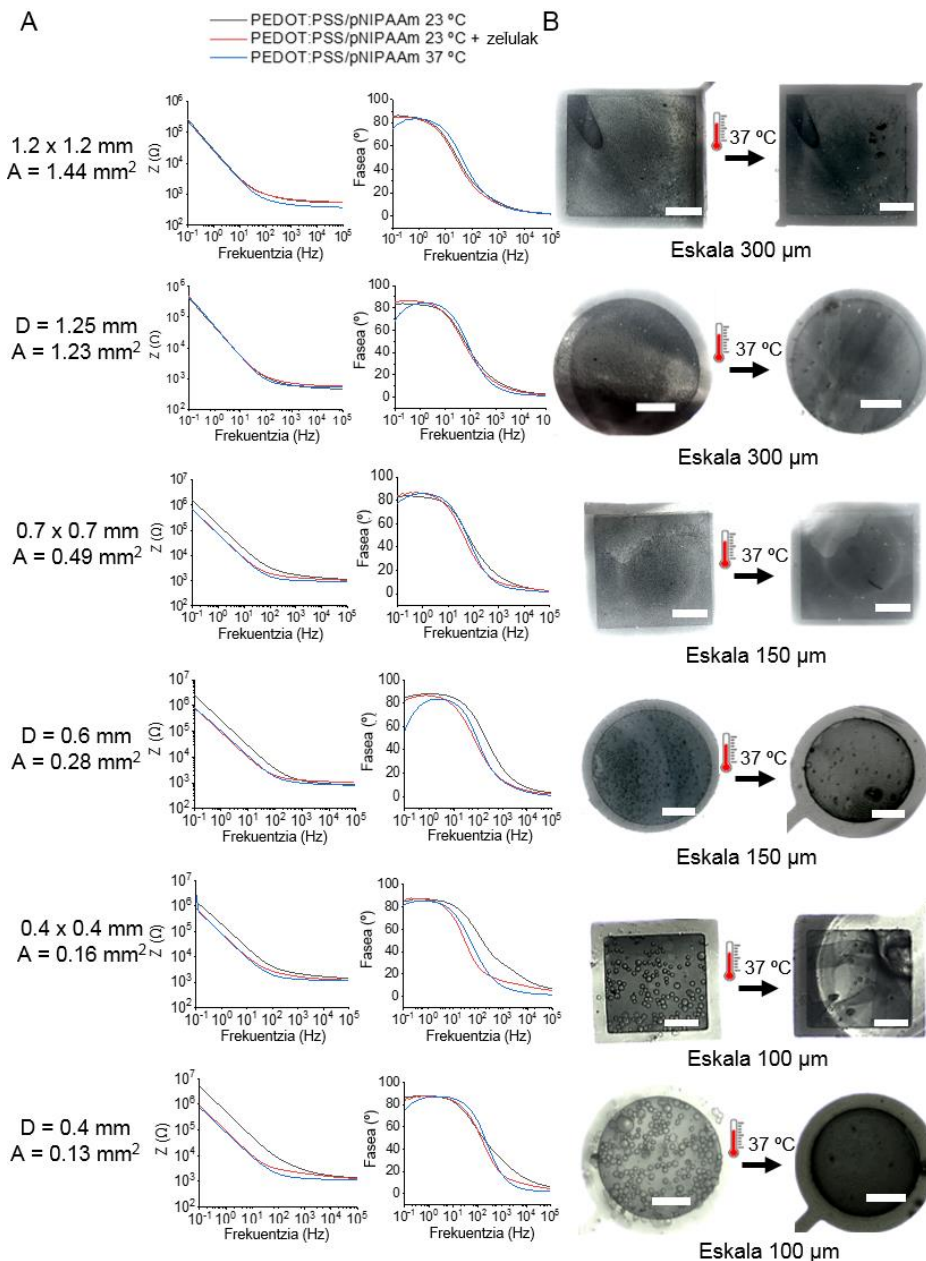


VI.7 irudia. PEDOT:PSS and pNIPAAm hidrogelen eta PEDOT:PSS/pNIPAAm kopolimeroaren Raman espektroskopia. A) Pikoen espektro osoa, 500 – 3500 nm tartean. B) pNIPAAm hidrogelaren pikoen espektroaren handipena 0-10000 a.u. tartean.

VI.2.4 Zelulen harrapaketa eta askapena PEDOT:PSS/pNIPAAm kopolimeroa erabiliz

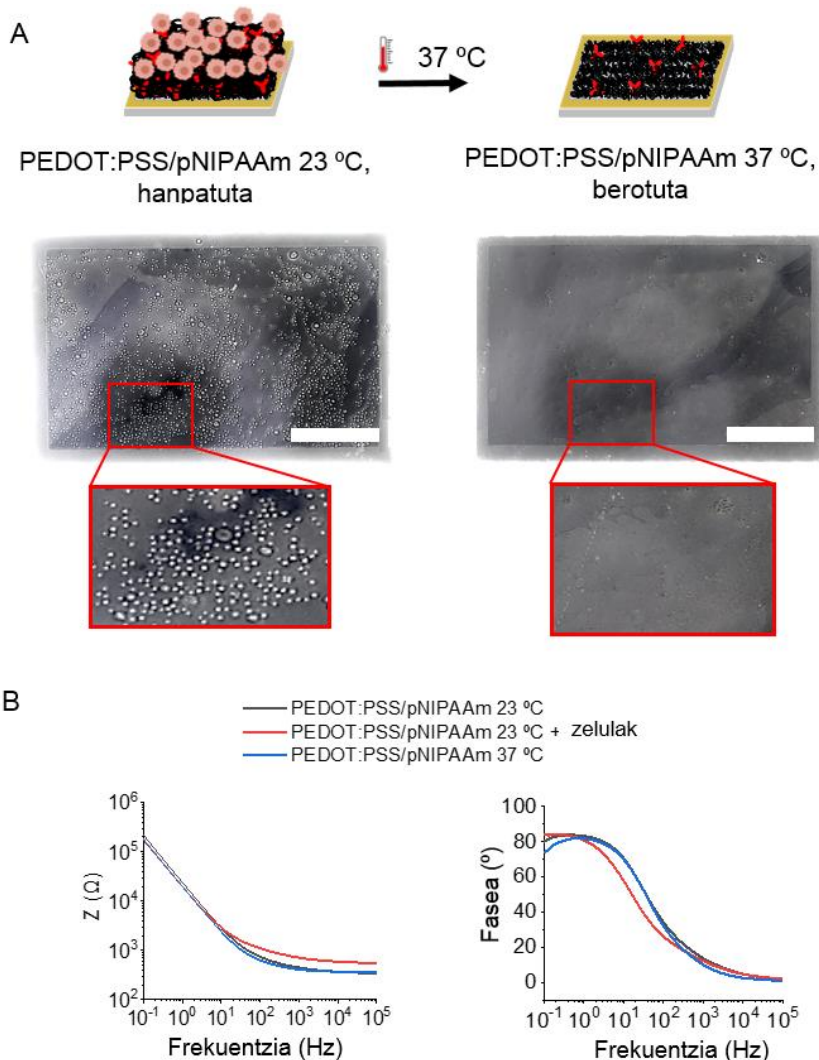


VI.8. irudia. Zelulen harrapaketa burutzeko pausoen irudikapen grafikoa.



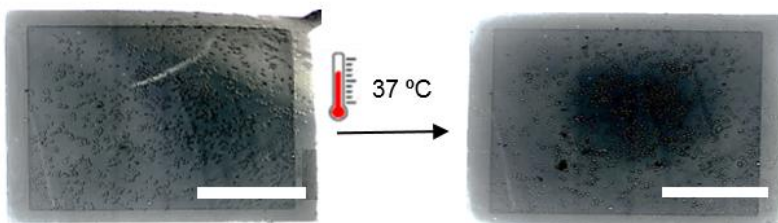
VI.9. irudia. A) Dimentsio ezberdinako PEDOT:PSS/pNIPAAm elektrodoetan zelulen harrapaketa eta askapenaren impedantzia *versus* frekuentzia (ezkerra) eta fasea *versus* frekuentzia (eskuina) grafikoak. B) PEDOT:PSS/pNIPAAm elektrodoetan zelulen harrapaketa (23 °C) (ezkerra) eta askapen (37 °C)

prozesuen (eskuina) mikroskopia optiko irudiak.

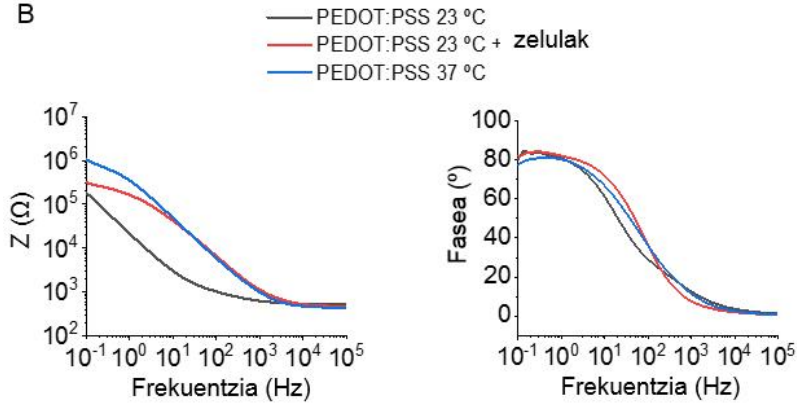


VI.10. irudia. PEDOT:PSS/pNIPAAm elektrodoetan zelulen harrapazte eta askapena. A) Zelulen askapenaren eskema goian, eta PEDOT:PSS/pNIPAAm elektrodoen mikroskopia optiko irudiak behean, zelulen askapena induzitu baino lehen eta ondoren. Eskala 400 μm . B) PEDOT:PSS/pNIPAAm 23 °C, PEDOT:PSS/pNIPAAm 23 °C zelulekin eta PEDOT:PSS 37 °C elektrodoen impedantzia *versus* frekuentzia eta fasea *versus* frekuentzia grafikoak.

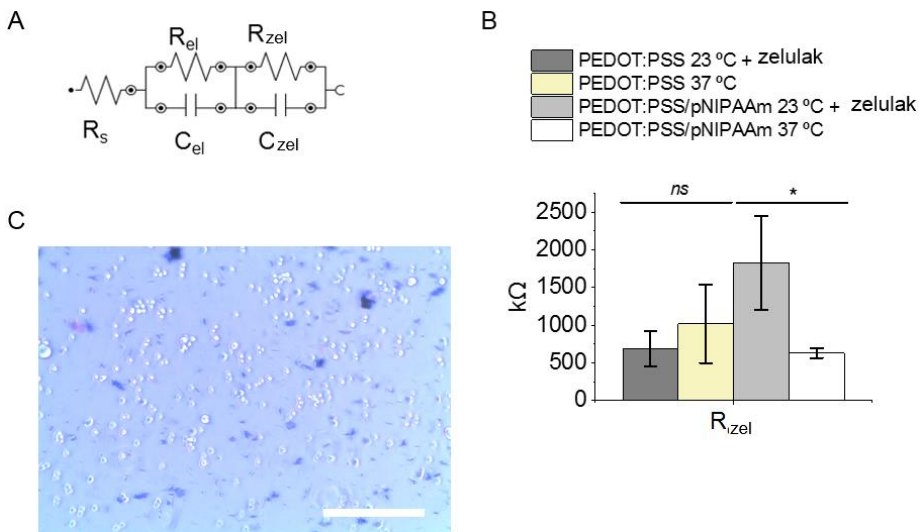
A



B

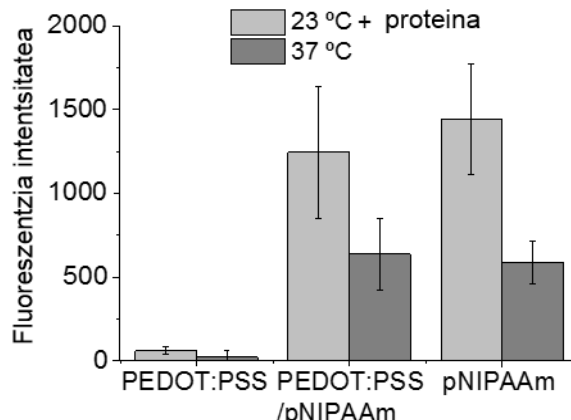


VI.11. irudia. A) PEDOT:PSS elektrodoen mikroskopia optiko irudiak zelulak harrapatuta daudenean, berotu baino lehen (ezkerra) eta gero (eskuina). Eskala 400 μm . B) PEDOT:PSS 23 °C-tan, PEDOT:PSS zelulekin 23 °C-tan eta PEDOT:PSS 37 °C-tan elektrodoen impedantzia *versus* frekuentzia eta fase *versus* frekuentzia grafikoak.



VI.12. irudia. A) Zelulen harrapaketa eta askapenari dagokion $R(RC)(RC)$ zirkuitu elektrikoa. B) PEDOT:PSS eta PEDOT:PSS/pNIPAAm materialak, zelulekin harrapatuta, 23 °C eta 37 °C-tan kalkulatutako R_{cells} parametroaren grafikoa. Errore barrak $n = 4$ lagenen bataz bestekoaren desbiderapen estandarrari dagozkie. Ez dago aldaketa esanguratsuk (ns) 0.05 mailan (one-way ANOVA $p = 0.29$) eta *aldaketa esanguratsua 0.05 mailan (one-way ANOVA, $p = 0.009$). C) Askatutako zelulei trypan blue bideragarritasun zelularrerako erreaktiboa gehitu eta geroko mikroskopia optiko irudia. Eskala 100 μm .

VI.2.5 Proteinen harrapatze eta askapenaren karakterizazioa fluoreszentzia mikroskopiaz



VI.13. irudia. PEDOT:PSS, PEDOT:PSS/pNIPAAm eta pNIPAAm geruza polimerikoetan tetrametilrodamina etiketa fluoreszentea duen behi serum albumina (BSA-TAMRA) proteinaren harrapaketa eta askapenaren fluoreszentzia mikroskopia datuak. Errore barrak $n = 5$ laginen bataz bestekoaren desbiderapen estandarrari dagozkie.

VI.3 Ondorioak

Laburbilduz, kapitulu honetan zelulen harrapatze eta askapenerako sistema ez inbaditzaile bat garatu da, prozesu honen aldibereko monitorizazioa gauzatzeko ahalmena duena. Horretarako, urrezko elektrodoak PEDOT:PSS/pNIPAAm material funtzional batekin konbinatu ziren. Kopolimero funtzional hau elektrodoen gainean jarri zen, eta FN proteina gehitu zitzaion zelulak atxiki zitezen. Kopolimero berriak PEDOT:PSS materialaren antzeko propietate elektrikoak mantendu zituen, EIS bidezko monitorizazioa ahalbidetuz, baita pNIPAAm materialaren termo-erantzun ahalmena ere. Beraz,

VI. Kapitulua

PEDOT:PSS/pNIPAAm kopolimeroa funtzionala zen tenperaturak induzitutako zelulen askapena burutzeko, baita EIS bidezko aldiberekoko monitorizazioa gauzatzeko ere.

Sistema honek bioelektronika organikoa aldi berean sentsoretzat eta eragingailutzat erabili ahal izateko bideak zabaltzen ditu, espezie ezberdinaren detekzio eta berreskurapenean inpaktu izanik, erabiltailearen esku-hartzea minimizatz. Emaitza hauek arkitektura konplexuagoak garatzeko lehenengo pausoak besterik ez dira, eta aldi berean sentsore eta eragingailuen erabilera eskaintzen duten helburu ezberdinatarako sistema berritzaila eratzeko oinarri gisa balio dute. Honezkerro, plataforma hau eraldatzeko potentziala handia da, harrapatze-molekula espezifikoa beste batengatik ordezkatu liteke, adibidez, beste zelula batzuen harrapaketa bideratzeko, esate baterako, odol zelulak, tumore zelula zirkulatzailak, bakteriak edota exosomak. Mota honetako analisiak klinikan, gailu eramangarriez baliatuz, minbiziaren diagnosi azkarrari atea zabaltzen dizkiote.

VII

Oharrak eta Etorkizuneko Lana

VII.1 Oharrak eta Etorkizuneko Lana

Lehenengo kapituluan azaldu bezala, Aurrerapen handiak egin dira azken hamarkadetan monitorizaziorako lab-on-a-chip (LOC) gailuen garapenari dagokionez. Nahiz eta mikrosistema miniaturizatuek abantaila anitz eskaintzen dituzten, hauen erabilera kontsumitzale orokorrera heltzetik urrun dago oraindik. LOC gailuetan osagai funtzionalak integratzeko ahalmenak, monitorizazio kimiko eta zelularrako estrategia berritzaileen garapena bultz dezake. Ildo horretan, tesi honek materialen zientzia eta mikrofabrikazioaren arteko konbinazioak aztertu ditu, eta monitorizaziorako estrategia berriean oinarrituz, mikrosistema integratuen garapen eta funtzionamendu egokirako adibide ezberdinak egiatzatu ditu.

Esaterako, 3D inprimaketaz fabrikatutako arkitektura inteligente bat eta UV bidez polimerizagarriak diren ionogelak konbinatuz, material funtzional polimerikoak gailu mikrofluidikoetan *in situ* eta modu zehatzean integratzea lortu zen, UV argia bakarrik erabiliz. Garatutako estrategia hau simplea izateaz gain, erabilera errazeko eta kostu baxuko metodoa eskaintzen du 3D inprimaketaz egindako gailu mikrofluidikoetan material funtzionalak integratzeko. Erabilitako arkitekturak eskaintzen duen aingura gaitasunak dimentsio errepikagarridun sentsore polimerikoen integrazio egonkorra ahalbidetzen du gainazal funtzionalizazio prozedurarik behar gabe. Kapitulu horretan, poli(*N*-isopropilakrilamida) (pNIPAAm) ionogelez osatutako lau sentsore integratu ziren gailu mikrofluidiko batean, pH detekziorako barra-kode itxurako irakurketa kolorimetrikoa lortuz. Dena dela, lau hauen artean pH detekziorako barra-kode irakurketaz gain, sentsore multipleen diseinu hau multiplex detekziorako erabili ahalko litzateke, sentsore bakoitzak detekzio helburu ezberdinatarako diseinatuz.

Gailu mikrofluidiko horretan argiz polimerizagarriak diren eta beste analito batzuk detektatzeko prest dauden sentsore multipleak integratzea da hurrengo pausoa, LOC multiplex eta erabilerrazak garatzeko bidean; esaterako, laktato¹, nitrato² edo bentzenoa eta formaldehidoa bezalako konposatu kimiko arriskutsuak³ detektatzeko. Sentsore multiplex-en integratzaileko diseinu mikrofluidiko inteligente honen implementazioak, detekzio kolorimetriko simplearekin batera, erabilera errazeko gailu eramangarrien garapena ahalbidetuko du analisi multiple eta akaso, aldiberekoak, burutzeko.

Mikrosistema integratuei begira, sentsoreen miniaturizazioan gehiago murgilduz, III. Kapituluak mikrosentsoreak kokatzeko irekitzedun substratua deskribatzen du. Mikro-sentsore matrizeak *in situ* fabrikatzeko teknika erraztuanik, Mylar® fotomaskara moldaerraza eta UV bidez polimerizagarriak diren eta sentsoreatzat erabil daitezkeen materialak ditu oinarri. Honek ahalbidetu zuen zehatz kokatutako mikrosentsore anitzen formakuntzak sortzea, pauso bakar batean, eta UV argia bakarrik erabiliz. Mikrozutabe formako mikrosentsoreak sortzeko material funtzionaltzat probatutako materialen artean, pNIPAAm ionogelek hidrogelek baino erreproduzgarritasun altuagoa aurkeztu zuten, mikrozutabeen dentsitate, forma eta tamainari dagokienez. Gainera, ionogel mikrosentsoreen fabrikaziorako substratutzat fotomaskara bat erabiltzeari esker, egituren atxikipen handia lortu zen substratuan, UV “grafting” edo txertaketa zela medio, gainazal funtzionalizazio teknikarik behar izan gabe. Azkenik, fotomaskara substratuaren diseinuak detekzio guneen identifikazioa erraztu zuen, irudi analisia eta irakurketa optikoaren automatizazioa ahalbidetuz. Sistema honen hurrengo hobekuntzak elementu sentsorearen sentikortasunean enfokatuko dira. Horretarako, ikuspuntuetako bat pH indikatzaileak entzimekin ordezkatzean datza, bioproszesuen detekziorako ionogel mikrozutabe anitzak sortzeko. Hala, entzimen tamaina

handiagoa dela eta, espero da hauek ionogeletatik ez isurtzea, III. Kapituluan pH indikatzaileekin dokumentatu zen ez bezala. Bestalde, I. Kapituluan azaldu bezala, kimiolumineszentzia kolorimetria baino sentikorragoa omen da. Hortaz, aurretiazko esperimentu batzuk burutu dira ionogel kimiolumineszenteak garatzeko. Mylard® substratuetan ionogel mikrozutabeen optimizazioak, LOC gailuetan integratzeko osagai sentsore malguen fabrikazioan aurrerakuntza ziurtatuko du.

Polimero mikroegiturak mintz zelularrekin lotutako *in vitro* testak bezalako erabilera erronkarietara heda daitezke. IV. Kapituluan azaldu bezala, materialen zientzia, mikrofabrikazioa eta mikrofluidikaren konbinazioaren ondorioz, geometria kontrolatuko nanotubo (NT) lipidikoen sortako formazio eta monitorizaziorako gailu hibridoa garatu zen. Gailu honek, mikrozutabeetan zehazki kokatutako NT lipidiko paraleloak sortzeko fluxu kontrolatua bermatu zuen, hauen formaziorako erabiltzen ohi diren mikromanipulazio prozedurak ekidinez. Mikrozutabeen konfigurazioa lau materialein errepikatu zen, SU-8 batetik, eta bestetik, hiru pNIPAAm ionogel ezberdineki, fotomaskara polimeriko bat erabiliz, eta 10 µm-ko erresoluzioa lortuz. Mikrosistema hauetan NT lipidikoen formazio kontrolatua ahalbidetu zuten, NT-en luzera mikrozutabeen distantziak finkatzen zuelarik, eta NT-en erradioa mikrozutabeko materialak modulatzen zuela. Mikrosistema hauen funtzionaltasuna, erabiltzeko erraztasuna eta moldakortasuna direla eta, mintz zelularren *in vitro* berreraikitze testak gauzatzeko tresna oparoa da. Plataforma hau ikerlariak mintz NT-ekin lan egiteko tresna moldakorraz hornitzeko diseinatua izan da, NT lipidikoen formazio eta monitorizaziorako erabiltzen diren teknika tradizionalek dituzten erronka nagusiak gaindituz. Plataforma honen funtzionaltasuna frogatu eta gero, espero da NT lipidikoen *in vitro* testak erabiltzen dituzten ikerkuntza taldeek gailu hau erabiliko dutela.

Monitorizazio zelularra nahitaezkoa da bideragarritasun zelularra eta zelulen portaeraren gainean informazioa lortzeko. Monitorizazio zelularrerako sistema miniaturizatuek ideia eta estrategia berriak agerrazten dituzte, V. Kapituluan frogatu zen bezala, non SCADA plataformak toxizitate zelularra zelula indibidual erresoluzioarekin monitorizatzeko erabili zen. Mikrokontaktu inprimaketaz sortutako zelula indibidualen formakuntzei esker, formakuntza puntuen okupazioa edo atxikipen zelularra kuantifikatu zen, konposatu toxikoen presentzian heriotza zelularraren digitalizazioa ahalbidetuz. Hau burutzeko, zelulen atxikipena era dinamikoan neurtu zen denboran zehar, askapen zelularra heriotza zelularrarekin korrelazionatuz batetik, edo trypan blue konposatura gehituz bestetik, konposatu toxikoak zelulak hil baina hauen askapena inhibitu zutenean. SCADA toxizitate zelularrerako testak heriotza zelularraren zinetikak zelula indibidual erresoluzioarekin ezagutzea ahalbidetzen du, SCADA bakarrik erabiliz edo trypan blue bezalako test konbentzionalekin konbinatuz. Hortaz gain, SCADA plataformaari aldaketak egin diezazkioke, esaterako, formakuntzako puntuen konposizioa, forma edo tamaina aldatu beste zelula tipo batzuetara moldatzeko. Sistema honen gailu mikrofluidiko batean implementazio osoa izango litzateke hurrengo erronka, tresna optiko eta seinalearen prozesamendurako ekipo miniaturizatuak erabiliz (adibidez, Raspberry Pi eta berari dagokion kamera). Honek SCADA aukera egokia bihurtuko luke merkaturatzeari dagokionez, zelulen toxizitatea neurtzeko beste plataforma komertzializatuen pausoak jarraituz, eta hauen aldean neurketa digitalak, zelula indibidual erresoluzioa eta kostu txikiagoak erakutsiz ^{4 5}. Era honetan, ikerkuntza edo diagnostiko erabileretan dabiltsan edozein erabiltzaileen eskura jarriko litzateke toxizitate zelular kuantitatiboa burutzeko tresna erabilterraza eta eskuragarria.

Bestalde, funtzionaltasun desberdinak dituzten polimero bat baino gehiagoren

arteko konbinazioak aurrerapauso bat suposatzen du monitorizazio teknologia berritzaleak garatzeko bidean. VI. kapituluan deskribatu bezala, temperaturari erantzuten dion pNIPAAm polimeroa eta poli(3,4-etilenodioxitofeno) poliestireno sulfonato (PEDOT:PSS) material eroalearen arteko konbinaziotik bi funtzioak dituen kopolimero berria sortu zen. Material hauurrezko elektrodoen gainean utzi eta gero, minbizi zelulen harrapaketa eta askapenerako eta honen aldibereko monitorizazio bioelektronikorako erabili zen. Mikrosistema horetan integratutako kopolimero berriak eragingailutzat jardun zuen batetik, temperaturak sustatutako zelulen askapena bermatuz, eta sentsore bioelektronikotzat bestetik, zelulen harrapaketa eta askapen prozesua monitorizatz, atxikipen zelularra impedantzia elektrokimiko espektroskopiaz detektatuz. Kapitulu honek aldibereko eragingailu eta sentsoretzat diharduten eta arkitektura konplexuagoa duten osagaien garapenaren bidean lehenengo pausoa da, etorkizuneko diagnostikorako gailuetan erabiltzeko oparoa. Sistema hau minbizi lerro zelular baterako optimizatu eta balioetsi zen, eta beste zelula espezifiko batzuen harrapaketa eta askapenerako erabiltzeko moldatu ahalko litzateke, esaterako tumore zelula zirkulatzaileak, odol zelulak... fibronektina harapatze molekula beste batengatik ordezkatuz. Plataforma honen hurrengo hobekuntzak elektrodo arkitektura berriak eta beste zelula eta lagin tipo batzuk esploratzean datzate. Era horretan, sistemaren gaitasuna ikertuko da beste erabilera batzuetarako, hala nola, zelulen isolaketa, zelulen sailkapena lagin konplexuetatik edota zelulen kontzentrazioa. Erabilera horietarako sistema honen balioespena aurrerapena izango da osasun laborategietan ikerkuntza berriean erabiltzeko, zelula ituen bilketa erraztuz eta biltze prozesuan zehar laginen manipulazioa murriztuz.

Tesi horretan aurkeztutako lanak balioztatu egiten du egitura mikrofluidikoetan material funtzionalen integrazioak monitorizazio kimiko eta zelularrako

teknologia berriak sorrarazten dituela, monitorizazio estrategia berriak eskainiz. Gainera, kostu murrizpena eta datu ezezagunen eskuratzea bermatzen da, erabilterrazak diren eta mikro-eskalan kontrola garantizatzen duten plataforma miniaturizatuei esker.

VII.2 Erreferentziak

1. Khodagholy, D.; Curto, V. F.; Fraser, K. J.; Gurfinkel, M.; Byrne, R.; Diamond, D.; Malliaras, G. G.; Benito-Lopez, F.; Owens, R. M. Organic electrochemical transistor incorporating an ionogel as a solid state electrolyte for lactate sensing. *J. Mater. Chem.* 2012, 22, 4440-4443.
2. Saez, J.; Arana, G.; Fernandez-Cuadrado, L.; Benito-Lopez, F. Ionogel-based Nitrite and Nitrate Sensor for Water Control at the Point-of-Need. *Procedia Eng.* 2016, 168, 518-521.
3. Gil-González, N.; Benito-Lopez, F.; Castaño, E.; Morant-Miñana, M. C. Imidazole-based ionogel as room temperature benzene and formaldehyde sensor. *Microchim. Acta* 2020, 187, 1-8.
4. Urcan, E.; Haertel, U.; Styllou, M.; Hickel, R.; Scherthan, H.; Reichl, F. X. Real-time xCELLigence impedance analysis of the cytotoxicity of dental composite components on human gingival fibroblasts. *Dent. Mater.* 2010, 26, 51-58.
5. Ke, N.; Wang, X.; Xu, X.; Abassi, Y. A. The xCELLigence system for real-time and label-free monitoring of cell viability. In *Mammalian Cell Viability* Springer: 2011; pp 33-43.

Acknowledgements

When I go back in my memory to my early days at the Microfluidics Cluster, I remember spending the whole summer looking forward to start the journey. I was starting a PhD, it was so exciting! I also remember how extremely lost I felt during the first months, and now, after four years, here I am, ready to end the adventure. At this point, I would like to thank every person who has somehow contributed to my thesis (and to my mental sanity during it).

First, to my supervisors, Fernando and Lourdes, thank you for this opportunity. Me gustaría agradecerlos enormemente la confianza en mí desde el principio y durante estos años, en ocasiones en que ni siquiera yo la tenía. Por vuestra paciencia y por darme toda la autonomía, dejando vuestro despacho y mente abiertos para mis frustraciones; por las veces que he acudido a vosotros arrastrando los pies y he vuelto dando saltos de esperanza.

Because normal is boring, to my group, the special Microfluidics Cluster UPV/EHU, and to the ones that were ever part of it, Enrique, Alba, Yara, Jon, Raquel, Sandra, Udara, Vahid... Sara, que si bien llevas poco tiempo, te has ganado un sitio con tu buen rollo contagioso, ¡que nunca te lo quiten! Gracias a todos por demostrar el compañerismo, por las risas espontáneas que cierran la puerta de zoología, por aguantar el pescaíto y sobre todo por los últimos meses en los que habéis conseguido amenizar mis bucles. ¡Ah! Ojo al hot plate, a ver quién lo va a apagar si no estoy yo ☺. Yara, nunca podré agradecerte lo suficiente el congreso en Basel.

A Anna y Juanma, parte del Shnyrova Lab, gracias por el trabajo en colaboración. Especialmente Juanma, ha sido un placer trabajar contigo.

I also want to thank the Bioelectronics (BEST) group from Cambridge University, especially Dr. Roisin Owens, who took me in her group for some months. To all the group, thank you for taking me as one of yours during my visit, but particularly Achilleas, I am so grateful for your help and support during my visit!

A mis coffee boys, capaces de alegrarte la mañana más gris. Manu, el “*good morning in the morning*” que mejor sienta, fogonazo de luz sureña en los días ingleses. Iñazio, ipurtargi euskalduna Cambridgen, goizeroko “*egun on maitia*” gustokoena. Eskerrik asko barrengatik, garagardo botila huts pilaketengatik.

Janire, ¡cómo no! Gracias por poner microcosas en mis manos por primera vez (¡cómo te la jugaste!), no te acordarás, pero me tuviste mi primera semana quitando protectores con toda la gracia de la que fui capaz, al estilo Eduardo manostijeras, mientras nos conocíamos mejor (la mejor bienvenida al grupo). También por los tres meses de aventura juntas, por los *sin pijama*, las *floreh asuleh y quilateh*, los break ingleses y todas las confidencias, por ser apoyo lejos de casa.

Jaio, zeu beti gogoan, paragrafotxo hau aspaldi daramat lantzen, zeuri eskerrak nola eman pentsatzen, barruan dudana ondo transmititzeko nahian, ta ezinean. Elkarri ezagutzen hasi ginen bazkalosteko kafe bat eskutan ta udaberriko eguzki izpien babespean. Hartaz geroztik, momentu eskas eta onetan, eskerrik asko bihotz-bihotzez niretzat egotearren, beti zentzuzko gomendiorik botatzeko prest. Esker anitz zeure eskutara heldu zen umemokoa (ni neu!) hartzearren eta, muxutruk, lan egiten irakastearren. Esan beharrik ere ez dago, famau zazela!

A Mai, siempre recordándome que puedo con todo, gracias por celebrar conmigo cada logro (¡un vino!) y cada batacazo (¡DOS VINOS!). Ainho, Jone, zeuek be aguantatu izan nauzuena... eskerrik asko, batez ere diseinu grafikoek inguruko brainstorming-ak eskaintzeagatik! Anetxu, siempre en paralelo, siempre

compartiendo etapa, gracias por los intercambios de audios eternos que arreglan conflictos mundiales. Ana, Lauri, Malu e Iraia, lo más parecido a una familia durante este tiempo de convivencia. Ana, gracias por las conversaciones, el proyecto fallido de obrador casero... Iraia, superviviente de un confinamiento con mi tesis y conmigo (¡eres una gudari!) por los sábados de pelí, palomitas y cata de pan. Roberto, gracias por ser el *landlord* que cualquiera querría, por tratarme como a una hija, por nutrirme con la huerta en casa y por las fotazas de estudio.

A mis hermanos, Iñi y Leire, gracias por ir antes que yo en el camino, guiándome en el mío, cada uno a vuestra manera. Iñi, por el momento clave en que me hiciste empoderarme, cuando me hiciste creer en mí con la mayor naturalidad (es más, sé que ni te acuerdas de ello). Leire, *sis*, gracias por enseñarme que la vida son más de 8 horas al día, gran lección de vida. Y gracias a los dos por darme esos bichillos que alegran a cualquiera. A aita y ama, que tanto os debo, a los que más, esto es también vuestro. Gracias por inculcarme la pasión por el trabajo, el sacrificio y el compromiso; por estar siempre en cada momento, en los buenos y los malos. En definitiva, gracias por intentar comprenderme en cada paso del camino, darme la mano cuando he tropezado y ser mi colchón, nunca os lo podré agradecer lo suficiente.

Al meu Gerard, gràcies infinites per ser la meva calma, un suport incondicional, per ajudar-me a treure el millor de mi mateixa, i ser, i descobrir el meu yang. Tot i que obris i tanquis la llum, que sempre vinguis i mai vagis, sense tu aquesta etapa hauria estat el doble de dura. Gràcies per l'esforç, per fer que 420 km siguin a prop, per ser el meu equip sempre!

Por último, a mis guindillas, ellos que son luz, y que cada vez que parpadeo han crecido más de lo que me gustaría, ojalá fuerais Peter Pan. Sois mis personas vitamina, pura alegría, capaces de suavizar cada mal momento con un abrazo,

una partida a la petanca, un “ikiko!”, una peli entre superamigas... Habéis aportado más de lo que os podríais imaginar, en estos cuatro años en los que izeko Maite os ha disfrutado a tope.

Pese a la incertidumbre del futuro, solo espero que esté donde esté, pueda apreciar y disfrutar cada paso del camino, y seguir encontrándome con personas, que como muchas de las citadas, dejen huella de la buena.